Petahertz optoelectronics via attosecond control of solids

Dmitry Zimin

München 2021

Petahertz optoelectronics via attosecond control of solids

Dmitry Zimin

Dissertation
an der Fakultät für Physik
der Ludwig–Maximilians–Universität
München

vorgelegt von
Dmitry Zimin
aus Togliatti, Russland

München, 30.07.2021

Erstgutachter: Prof. Dr. Ferenc Krausz
Zweitgutachter: Prof. Dr. Mikhail (Misha) Ivanov
Tag der mündlichen Prüfung: 27.09.2021

for Academia without suppression of young scientists

1471413

Contents

Abstract

Fast evolving technologies require faster data processing. Modern electronics possess physical limits for computation speed. To circumvent these limits new scientific approaches are required. Light is the fastest information carrier, therefore optoelectronic light-matter interaction can be potentially employed as a method towards much faster computation. In order to exploit light-matter interactions in the attosecond (1×10^{-18} s) temporal and petahertz (1×10^{15} Hz) frequency domains, three main conditions should be fulfilled: a) techniques capable of detecting such fast processes must be available, b) physical mechanisms with an attosecond response time should be found and characterized, c) the methodology for storing and controlling of the information by means of these fast processes should be developed. This dissertation addresses these conditions and demonstrates the applicability of optoelectronics towards attosecond and petahertz domains.

The thesis reports on novel approaches for the sampling of pulsed optical waveforms with attosecond temporal resolution and petahertz detection bandwidth, as well as their applications for time-resolved studies of attosecond non-equilibrium dynamics in solids and gases. It is demonstrated that the light-matter-light scheme of the optoelectronic interaction can be used to manipulate optical pulses waveforms, while optical pulses, in turn, can manipulate properties of matter.

The temporal confinement of high-order non-linear excitation of charge carriers in dielectrics and gases is employed as a temporal gate for the sampling of pulsed waveforms. Non-symmetric displacement of photo-excited charges leads to polarization of a medium. Metal electrodes in the vicinity of the created polarization produce a measurable current. Gas pressure and distance to an electrode allow for control of the magnitude of the generated current and the detection sensitivity. The optimum signal in the air as the interaction medium is observed at around several mbar pressure. When the current signal is measured from two electrodes opposing each other, a 180-degree phase shift is observed, indicating that the polarization of a medium is the main mechanism responsible for the detected signal.

Ultra-broadband photonic detection at near-petahertz and petahertz frequencies is demonstrated based on a heterodyne detection scheme. Pulsed waveform characterization with unstabilized carrier-envelope phase is demonstrated.

The three-channel optical synthesizer is characterized by the novel methodology. Temporal confinement of the sampling channel allows extending the detection bandwidth of the electro-optic field sampling technique, for the first time, towards the visible spectral

domain.

Technological advances are applied to study and control non-steady-state dynamics in solids. The information encoded in the changes of optical pulse waveforms provides access to ultrafast processes occurring in a sample medium. The very first moments of a medium excitation and formation of optical properties are studied directly in the time domain.

The dynamics of the formation of the non-equilibrium refractive index of a medium as well as thermalization of a non-equilibrium charge carrier distribution is studied in detail. The time delay associated with the plasma screening and non-linear excitation of a medium is observed experimentally and confirmed theoretically. Transient and long-lasting switching and modulation of optical properties are studied for silicon, diamond, and fused silica solids.

The manipulation of pulsed optical waveforms based on light-matter-light interaction is demonstrated. The temporal confinement of the photo-excitation of a medium by an injection pulse is employed as a switch to induce localized and controllable changes on a pulse waveform. The control of the switching event in combination with the interacting test pulse provides a scheme towards manipulation of optical pulse waveforms as well as material properties in ultrafast time scale.

Zusammenfassung

Durch die rasche technologische Entwicklung, wird eine schnellere Datenverarbeitung notwendig. Die moderne Elektronik hat jedoch physikalische Grenzen in Bezug auf die Rechengeschwindigkeit. Um diese Limitierungen zu umgehen, sind neue wissenschaftliche Ansätze gefragt. Licht ist der schnellste Informationsträger. Diese Eigenschaft macht die optoelektronische Licht-Materie-Wechselwirkung zu einer möglichen Methode für viel schnellere Berechnungen. Um Licht-Materie-Wechselwirkungen in einem Zeitbereich von Attosekunden (1×10^{-18} s) und in einem Frequenzbereich von Petahertz (1×10^{15} Hz) nutzen zu können, müssen folgende drei Hauptbedingungen erfüllt sein: a) Techniken, die so schnelle Prozesse detektieren können, müssen verfügbar sein, b) physikalische Mechanismen mit einer Antwortzeit im Attosekundenbereich müssen sowohl gefunden, als auch charakterisiert werden, c) die Methodik zur Speicherung und Steuerung von Informationen, die durch derart schnelle Prozesse generiert werden, muss entwickelt werden. In der hier vorliegenden Dissertation wurden die drei genannten Bedingungen behandelt und außerdem die Anwendbarkeit der Optoelektronik im Attosekunden- und Petahertzbereich demonstriert.

Diese Dissertation berichtet über neuartige Ansätze zur Abtastung der Wellenformen von optischen Laserimpulsen mit einer zeitlichen Auflösung im Bereich von Attosekunden und einer Detektionsbandbreite im Petahertzbereich. Außerdem behandelt sie, deren Anwendung für zeitaufgelöste Untersuchungen von Nichtgleichgewichtsdynamiken auf Attosekunden-Zeitskala in Festkörpern und Gasen. Es wird demonstriert, dass das Licht-Materie-Licht-Schema der optoelektronischen Wechselwirkung genutzt werden kann, um die Wellenformen optischer Pulse zu manipulieren, während optische Pulse wiederum Eigenschaften von Materie manipulieren können.

Die zeitliche Begrenzung der Anregung von Ladungsträgern in Dielektrika und Gasen mittels hoch-nichtlinearen Prozessen wird als zeitliches Tor für die Abtastung von gepulsten Wellenform eingesetzt. Die nicht-symmetrische Verschiebung photoangeregter Ladungen führt zur Polarisation eines Mediums. Metallische Elektroden, die sich in nächster Umgebung zu dieser erzeugten Polarisation befinden, erzeugen messbaren Strom. Der Gasdruck einerseits und der Abstand zu den Elektroden andererseits, ermöglichen es, die Stärke des erzeugten Stroms zu regulieren und erhöhen zudem die Detektionsempfindlichkeit. Das optimale Signal für Luft als Interaktionsmedium wird bei einem Druck von einigen mbar beobachtet. Wenn der erzeugte Strom an zwei einander gegenüberliegenden Elektroden gemessen wird, wird eine Phasenverschiebung von 180 Grad beobachtet. Das weißt darauf

hin, dass die Polarisation eines Mediums der Hauptmechanismus ist, der für das erfasste Signal verantwortlich ist.

Die ultrabreitbandige Messung von Photonen im PHz-nahen und PHz Frequenzbereichen, wird auf Grundlage der Heterodyn-Detektionsschema demonstriert. Auch die Charakterisierung der gepulsten Wellenformen mittels Pulsen, deren Träger-Einhüllenden-Frequenz nicht stabilisiert ist, wird demonstriertgezeigt.

Der dreikanalige, optische Synthesizer wird durch neuartige Verfahren charakterisiert. Durch zeitliche Begrenzung des Abtastkanals wird es zum allerersten Mal möglich, die Detektionsbandbreite der elektrooptischen Feldabtastung in Richtung des sichtbaren Spektralbereich auszudehnen.

Die technologischen Fortschritte werden angewandt, um Dynamiken in Festkörpern außerhalb des Gleichgewichtszustands zu erforschen und zu kontrollieren. Dabei geben die Informationen, welche in den Änderungen der optischen Wellenform gespeichert sind, Aufschluss über die extrem schnellen Prozesse, welche in der Probe stattfinden. So können die allerersten Augenblicke der Anregung des Mediums und die Ausbildung der optischen Eigenschaften direkt im Zeitbereich untersucht werden.

Die Dynamik der Ausbildung des Brechungsindex, sowie die Thermalisierung von Ladungsträgern in einem Ungleichgewichtszustand werden im Detail untersucht. Außerdem wird die zeitliche Verzögerung, welche durch eine vom erzeugten Plasma verursachte Abschirmung verursacht wird, experimentell beobachtet und auch theoretische bestätigt. Für Silizium, Diamant und Quarzglas werden transiente und langanhaltende Veränderungen und Modulationen der optischen Eigenschaften untersucht.

Die Manipulation von gepulsten optischen Wellenformen mittels Licht- und Materiewechselwirkung wird gezeigt. Dabei wird die zeitliche Beschränkung der Anregung eines Mediums mit einem Injektionsimpuls verwendet, um lokale und kontrollierbare Veränderungen in einer Test-Wellenform hervorzurufen. Die Kontrolle über das Umschaltereignis in Kombination mit dem wechselwirkenden Puls, bietet ein Schema zur Manipulation optischer Pulswellenformen, sowie Materialeigenschaften in ultraschneller Zeitskala.

List of Publications and Conference Contributions

Peer-Reviewed publications

D. Zimin, M. Weidman, J. Schötz, M. F Kling, V. S. Yakovlev, F. Krausz, N. Karpowicz. *Petahertz-scale nonlinear photoconductive sampling in air. Optica*, Vol. 8, Issue 5, pp. **586-590** (2021).

S. Sederberg, **D. Zimin**, S. Keiber, F. Siegrist, M. S. Wismer, V. S. Yakovlev, I. Floss, C. Lemell, J. Burgdörfer, M. Schultze, F. Krausz, N. Karpowicz. *Attosecond optoelectronic field measurement in solids. Nature Communications*, 11, **430** (2020).

M. Qasim, **D. A. Zimin**, V. S. Yakovlev. *Optical gain in solids after ultrafast strong-field excitation. Phys. Rev. Lett. 127, 087401.*

D. A. Zimin, S. Sederberg, S. Keiber, F. Siegrist, M. Wismer, V. S. Yakovlev, I. Floss, C. Lemell, J. Burgdorfer, M. Schultze, F. Krausz, N. Karpowicz. *Attosecond control of charged carriers and waveform sampling in solids. Nonlinear Optics*, NTu3A. **7**, (2019).

M. Kubullek, Z. Wang, K. von der Brelje, **D. Zimin**, P. Rosenberger, J. Schötz, M. Neuhaus, S. Sederberg, A. Staudte, N. Karpowicz, M. F. Kling, B. Bergues. *Single-shot carrier–envelope-phase measurement in ambient air. Optica*, Vol. 7, Issue 1, pp. **35-39** (2020).

J. Schötz, L. Seiffert, A. Maliakkal, J. Blöchl, **D. Zimin**, P. Rosenberger, B. Bergues, P. Hommelhoff, F. Krausz, T. Fennel, M. F. Kling. *Onset of charge interaction in strong-field photoemission from nanometric needle tips. Nanophotonics, vol. 10, no. 14, 2021, pp. 3769-3775.*

E. Ridente, M. Mamaikin, N Altwaijry, **D. Zimin**, M. Kling, V. Pervak, M. Weidman, F. Krausz, N. Karpowicz. *Electro-optic characterization of synthesized infrared-visible light fields. Nature Communications (accepted).*

M. Ossiander, K. Golyari, K. Scharl, L. Lehnert, F. Siegrist, J. Bürger, **D. Zimin**, J. Gessner, M. Weidman, I. Floss, V. Smejkal, S. Donsa, C. Lemell, F. Libisch, N. Karpowicz, J. Burgdörfer, F. Krausz, M. Schultze. *The speed limit of optoelectronics. Nature Communications (accepted).*

D. Zimin, V. S. Yakovlev, N. Karpowicz. *Ultra-broadband photonic sampling of optical waveforms. Submitted to Nature Photonics (in review). https://arxiv.org/abs/2111.09864.*

J. Schoetz, A. Maliakkal, J. Blöchl, **D. Zimin**, Z. Wang, P. Rosenberger, M. Alharbi, A. Azzeer, M. Weidman, V. Yakovlev, B. Bergues. *The emergence of macroscopic currents in photoconductive sampling of optical fields . Submitted to Nature Communications (in review).*

D. Zimin, N. Karpowicz, M. Qasim, M. Weidman, F. Krausz, V. S. Yakovlev. *1-femtosecond-scale Drude-Lorentz response in photoexcited solids. Submitted to Nature (in review).*

D. Zimin, M. Qasim, N. Karpowicz, F. Krausz, V. S. Yakovlev. *Ultrafast thermalization of charge carriers in semiconductors and dielectrics. In preparation.*

D. Zimin, V. S. Yakovlev, F. Krausz, N. Karpowicz. *Material-dependent study of attosecond light-matter energy transfer in solids. In preparation.*

D. Zimin, V. S. Yakovlev, F. Krausz, N. Karpowicz. *Characterization of optical pulses with CEP-unstabilized transients. In preparation.*

Conference contributions

D. Zimin, S. Sederberg, S. Keiber, F. Siegrist, M. S. Wismer, V. S. Yakovlev, I. Floss, C. Lemell, J. Burgdörfer, M. Schultze, F. Krausz, N. Karpowicz. *Attosecond field measurement and charge control in solids. CLEO Europe 2019.* Oral presentation.

D. Zimin, S. Sederberg, S. Keiber, F. Siegrist, M. S. Wismer, V. S. Yakovlev, I. Floss, C. Lemell, J. Burgdörfer, M. Schultze, F. Krausz, N. Karpowicz. *Gating of optical waveforms by attosecond charge control in solids. Ultrafast Optics XII (UFO 2019).* Oral presentation.

D. Zimin, S. Sederberg, S. Keiber, F. Siegrist, M. S. Wismer, V. S. Yakovlev, I. Floss, C. Lemell, J. Burgdörfer, M. Schultze, F. Krausz, N. Karpowicz. *Optoelectronic measurements of light fields by sub-cycle carrier injection in dielectrics. SPIE Photonics Europe 2018.* Oral presentation.

K. Golyari, M. Ossiander, K. Scharl, L. Lehnert, F. Siegrist, **D. Zimin**, M. Weidman, I. Floss, V. Smejkal, C. Lemell, J. Burgdörfer, M. Schultze, F. Krausz. *Attosecond Vacuum-Ultraviolet Photoconductive Switching in Dielectrics. 31st International Conference on Photonic, Electronic and Atomic Collisions (The 22nd International Conference on Ultrafast Phenomena 2020.* Co-author.

D. Zimin, S. Sederberg, S. Keiber, F. Siegrist, M. S. Wismer, V. S. Yakovlev, I. Floss, C. Lemell, J. Burgdörfer, M. Schultze, F. Krausz, N. Karpowicz. *Sampling of light waveforms by sub-cycle carrier injection and control in solids. CHILI 2019.* Oral presentation.

D. Zimin, S. Sederberg, S. Keiber, F. Siegrist, M. S. Wismer, V. S. Yakovlev, I. Floss, C. Lemell, J. Burgdörfer, M. Schultze, F. Krausz, N. Karpowicz. *Non-linear attosecond photo-conductive charge control in solids. Nanophotonics and Micro/Nano Optics International Conference 2019.* Oral presentation.

D. Zimin, S. Sederberg, S. Keiber, F. Siegrist, M. S. Wismer, V. S. Yakovlev, I. Floss, C. Lemell, J. Burgdörfer, M. Schultze, F. Krausz, N. Karpowicz. *Attosecond optoelectronic metrology. 31st International Conference on Photonic, Electronic and Atomic Collisions (ICPEAC XXXI).* Poster presentation.

List of Abbreviations

BNC - Bayonet Neill–Concelman
CEP - carrier-envelope phase
CLC - coulomb-laser coupling
CPA - chirped pulse amplifier
CVD - chemical vapor deposition
DC - direct current
DFG - difference frequency generation
EOS - electro-optic sampling
FWM - four-wave mixing
GPIB - general purpose interface bus
HCF - hollow-core fibre
NIR - near infra-red
NOS - non-linear optical sampling
NPS - non-linear photo-conductive sampling
PCB - printed circuit board
RMS - root mean square
SFG - sum-frequency generation
SHG - second harmonic generation
SNR - signal-to-noise ratio
SPM - self-phase modulation
TDDFT - time-dependent density-functional theory
THG - third harmonic generation
UVFS - Ultra-violate fused silica
XPM - cross-phase modulation
XUV - extreme ultraviolet

List of Figures

Introduction

The exponential growth of computing power predicted by Gordon Moore[8] requires faster and smaller electronic components. However, the laws of quantum mechanics put a fundamental limitation on how small these components can be, and therefore how fast they can operate. The light-matter interaction is considered to be a potential direction to circumvent these speed limits[9, 10, 11].

One of the approaches is based on quantum computing[12, 13, 14, 15, 16]. However, quantum computing requires a high degree of coherence[17, 18, 19] which is difficult to achieve due to the influence of the environment. Another approach is to use fast processes as temporal gates[20, 21] to control and measure physical observables.

Many physical processes are so fast that can take place in femtosecond (1×10^{-15} s), attosecond, or zeptosecond (1×10^{-21} s) time scales. However to control such fast phenomena one requires a comparably fast 'switch'. A short electromagnetic pulse can serve this purpose[22]. The invention of pulsed lasers allowed confinement of the burst of light into femtosecond or even attosecond-scale durations[23]. For instance, it has been shown that light pulses produced by high harmonic generation[24, 25, 26, 27, 28, 29, 30, 31] can be confined to the attosecond-scale temporal window[23, 32, 33]. The first generation and measurement[34] of isolated attosecond pulses therefore has lead to the birth of *attosesond physics*[23, 34]. In a frequency domain, such spark of electromagnetic wave consists of a broadband spectrum approaching or even exceeding petahertz frequencies.

If properties of light can be measured and controlled, so as sub-femtosecond changes in properties of matter can be measured and controlled via light-matter interaction[35, 36, 37]. Hence, characterization of light pulses is essential for studying and controlling fast physical processes. Multiple characterization techniques[38, 39, 40] have been recently developed. In a frequency domain, the characterization of light transients can be reduced to only two quantities: spectral amplitudes (spectral intensities) and spectral phases. If these quantities can be measured and controlled the electromagnetic transient can be used as a tool for light-matter interaction.

Multiple attempts have been made to access and control physical processes in attosecond or femtosecond time scales[41, 42, 43, 44, 45, 46]. The 'attosecond transient absorption'[47] approach allows accessing fast processes such as excitation of charge carriers with attosecond temporal resolution[37, 44, 48]. Another recent approach is based on the analysis of a high-harmonic generation spectra[49, 50, 51, 52, 53]. However, both types of methodologies are sensitive only to changes in spectral intensities, while the spectral phase information is practically lost. Although attempts have been made to acquire the

phase information[54].

The optical field sampling approach[55, 56, 57], on the contrary, allows the study of such fast physical phenomena[58, 59, 60, 61] preserving information about spectral amplitudes and spectral phases. One of the breakthrough techniques is an attosecond streak camera. It allows observation of light transients with attosecond temporal resolution in real time[62]. In this method isolated attosecond pulses are used as a temporal gate for the photo-ionization of a medium, resulting in the emission of electrons with finite kinetic energy. If attosecond pulses are superimposed with a driving electric field of a pulse to be measured, the photo-excited electrons will experience a change of the kinetic energy upon interaction with the driving field. The change in the electron kinetic energy will be proportional to the vector potential of the driving field from the moment of the photo-excitation[23]. Measuring the final electron kinetic energy as a function of a delay between attosecond and driving pulses, therefore, allows measuring the vector potential of the driving field directly. The simple relation between the vector potential and an electric field of the driving pulse, therefore, provides real-time access to the drive pulse waveform.

If the pulse waveform is known, it can be used as a reference to study physical processes provided such processes cause a modification of the pulse waveform. Such concept was applied to study non-linear polarization and energy transfer in a dielectric medium[7]. The changes imprinted on the pulse waveform, therefore, provide information about processes that caused these modifications. If the pulse waveform changes are resolved in time, the physical processes which caused these modifications are also resolved in time, although can not always be decoupled. The ability to measure optical pulse waveforms already paved the way towards the study and control of very fast phenomena in atoms and molecules[63, 64, 43] as well as solids[65].

The faster is a physical process in time the larger is the spectral bandwidth of the detection required to resolve it. In addition to that, since *changes* of a waveform are of the most interest, high dynamic range and high sensitivity of the technique are required. Although optical field sampling based on attosecond streaking provides a detection bandwidth approaching petahertz frequencies[35], it lacks sufficient sensitivity to access physical processes that produce weak signals. On the contrary electro-optic sampling[66, 67, 55, 57] provides similar optical field detection with much higher sensitivity, however lacks a sufficient detection bandwidth to access processes occurring on an attosecond time scale.

The aim of this thesis work is to extend optical field sampling metrology towards petahertz detection bandwidth with high sensitivity and to apply it for the study and control of attosecond scale processes for the purpose of advancing future optoelectronics.

Chapter 1 provides a theoretical background essential for the scientific work presented in this thesis.

Chapter 2 describes several novel methods for the optical field sampling with attosecond temporal resolution and high sensitivity exceeding several orders of magnitude of the signal-to-noise ratio. It demonstrates that the study and control of fast processes in nature can now be achieved with conventional and rather inexpensive laser systems on a simple table-top setup.

Chapter 3 describes the application of the novel metrology for the characterization

of a high-frequency channel of the optical synthesizer. This characterization allowed for the first time to extend boundaries of the conventional electro-optic sampling towards the visible spectral range.

The techniques are then applied for time-resolved studies of attosecond scale processes, such as light-matter energy transfer and non-linear polarization (chapter 5) in solids. It is demonstrated that transient and non-transient energy transfers can be confined to an attosecond-scale temporal window within a sub-cycle of a pulse.

Chapter 4 demonstrates that the comparison of pulsed waveforms measured with different types of techniques allows extracting information associated with the non-linear photo-excitation and the formation of the Coulomb plasma screening field inside a medium.

The last chapter 6 presents a detailed study of the formation and manipulation of non-equilibrium properties of solids in ultrafast time scales. In addition, it is shown that the control of such non-equilibrium dynamics allows localized manipulation of optical pulse waveforms.

The new studies and metrology presented in this thesis, therefore, aim to advance modern optoelectronics towards attosecond and petahertz domains.

Chapter 1

Theoretical background

This chapter introduces an essential theoretical background for physical mechanisms as well as technological approaches employed in this thesis.

Section 1.1 reviews the linear electromagnetic latter-matter interaction described by James Clerk Maxwell[68]. The relation between medium polarization and electromagnetic waves is introduced in terms of the wave-equation and linear susceptibility of a medium.

Sections 1.2 and 1.3 extend the theory of the linear interaction towards transient and non-transient non-linear optical effects.

Section 1.4 provides a theoretical background for light-matter energy transfer taking into account non-instantaneous response of a medium.

Section 1.5 provides a quantum mechanical theory for the optical properties of a medium based on the distribution of charge carriers within the energy structure.

The last two sections of the chapter describe two main concepts of the optical pulse waveform characterization: homodyne and heterodyne detection (section 1.6) as well as a gated detection (section 1.7).

All sections of this chapter serve as a basis for the research described in this thesis.

1.1 Electromagnetic light-matter interaction

One of the four fundamental interactions in physics is electromagnetic interaction. In classical electromagnetism such interaction can be described by Maxwell's equations:

$$\nabla \cdot \mathbf{D} = \frac{\rho}{\epsilon_0}, \tag{1.1}$$

$$\nabla \cdot \mathbf{B} = 0, \tag{1.2}$$

$$\nabla \times \mathbf{E} = -\frac{\partial \mathbf{B}}{\partial t}, \tag{1.3}$$

$$\nabla \times \mathbf{H} = \mu_0 \left(\mathbf{J} + \frac{\partial \mathbf{D}}{\partial t} \right). \tag{1.4}$$

Here $\epsilon_0 \approx 8.854 \cdot 10^{-12}$ F/m is the vacuum permittivity and $\mu_0 \approx 1.256 \cdot 10^{-6}$ H/m is the vacuum permeability. $\mathbf{E}$ is an electric field and $\mathbf{H}$ is a magnetic field strength. $\mathbf{E}$ and $\mathbf{H}$ are external fields that are not associated with intrinsic properties of a medium. $\mathbf{J}$ and ρ are current and charge densities, which may or may not be present in a medium. Bold notations represent vector quantities.

Since Maxwell's equations are microscopic and classical, phenomenological quantities called polarization field $\mathbf{P}$ and magnetization field $\mathbf{M}$ are introduced to account for intrinsic atomic electric and magnetic fields associated with free and bound charge carriers inside a medium, as well as spins and magnetic moments of charge carriers.

The total electric and magnetic fields, taking into account atomic intrinsic fields, are therefore called *electric displacement field*:

$$\mathbf{D} = \epsilon_0 \mathbf{E} + \mathbf{P}, \tag{1.5}$$

and *magnetic induction field* or just *magnetic field*:

$$\mathbf{B} = \mu_0 \mathbf{H} + \mu_0 \mathbf{M}. \tag{1.6}$$

The time-dependent polarization field $\mathbf{P}$ creates a polarization current density:

$$\mathbf{J}_p = \frac{\partial \mathbf{P}}{\partial t}. \tag{1.7}$$

On the other hand, the space dependent magnetization field creates a magnetization current density:

$$\mathbf{J}_m = \nabla \times \mathbf{M}. \tag{1.8}$$

The term $\mathbf{J}$ in the eq. 1.4 is a free-charge current density.

Therefore electromagnetic interaction with any medium can be described by Maxwell's equations provided that intrinsic polarization field $\mathbf{P}$, intrinsic magnetization field $\mathbf{M}$ and free-charge current density within a medium are known.

Everyday electronic applications and devices such as computers rely on modification and control of some properties of a medium, represented by quantities in eq. 1.1 - 1.6.

In the case of optoelectronic applications these quantities are modified by the interaction of a medium with electromagnetic waves such as light. If the electric field $\mathbf{E}$ exerts an electric force

$$\mathbf{F}_E = e\mathbf{E} \tag{1.9}$$

on a particle with charge e, and this force is not large enough to accelerate a particle to velocities (ν) comparable to the speed of light (which is usually the case, unless under extreme conditions such as in particle accelerators), the magnetic force

$$\mathbf{F}_B = e(\nu \times \mathbf{B}) \tag{1.10}$$

exerted by a magnetic field **B** is always much smaller than exerted electric force. Therefore a typical interaction of a medium with an incident light is mainly dominated by electric field and sufficiently described if only polarization **P** of a medium is considered.

Multiple particles can create stable systems with certain energy eigenstates. These states can be approximately determined by an appropriate version of the Schrödinger equation. The simplest form of this equation is the time-independent Schrödinger equation:

$$\hat{H}|\Psi\rangle = E|\Psi\rangle. \tag{1.11}$$

If a wave function Ψ and a Hamiltonian operator $\hat{H}$ of a system are known, for instance for a single non-relativistic particle positioned by a vector $\mathbf{r}$ with respect to positive nuclei, the energy eigenstates E can be determined by solving the linear partial differential equation:

$$\left[-\frac{\hbar^2}{2m}\nabla^2 + V(\mathbf{r})\right]\Psi(\mathbf{r}) = E\Psi(\mathbf{r}). \tag{1.12}$$

Each eigenstate solution of the eq. 1.12 corresponds to a certain wavefunction. The wavefunction itself provides the spatial probability density function $|\Psi|^2$. If the probability density function posses a rotational symmetry, an average macroscopic intrinsic polarization of a medium will average to zero. This however might not be the case in, for instance, pyroelectric materials which maintain non-zero macroscopic polarization.

Regardless of the type of medium, the space separation between charge carriers maintains the stability of a system. However, if the system is exposed to an external static electric field the distribution of particles in space will be altered from its stable state. Under influence of the external field, the particles may become closer to each other or further from each other. This displacement from an equilibrium position will produce an additional polarization of a medium.

Internal fields, such as a Coulomb field, which bound medium together poses different strengths for different distances between interacting particles since the magnitude of a Coulomb force F between two charges q_1 and q_2 is inversely proportional to the square of the distance r between these charges:

$$|F(r)| = \frac{|q_1||q_2|}{r^2}. \tag{1.13}$$

The dependence of the force between two particles on the distance between them is therefore non-linear. This implies that if the distance between two interacting particles will be doubled, the field strength which these particles will experience will not necessarily be reduced by half. Or alternatively, if the static electric field, to which the medium is exposed will be doubled, the space separation between particles in the medium will, in general, not necessarily be increased by a factor of two.

The proportionality factors between the applied electric field and displacement of charge carriers are determined by the internal forces within the medium, and therefore material

specific. Depending on an atomic structure of a medium, the relation between an applied field and displacement of charge carriers may also be medium orientation dependent.

If a medium is exposed to a time-varying electric field (instead of static), such as electromagnetic wave, the displacement of charge carriers will also vary in time accordingly, but the displacement will not be necessarily linearly proportional to the incident electric field.

Incident electric field induces a polarization in a medium, according to a proportionality factor χ called *electric susceptibility*:

$$\mathbf{P} = \epsilon_0 \chi \mathbf{E}. \tag{1.14}$$

This proportionality factor however, in general, is a function of the incident electric field $\mathbf{E}$ and can be well approximated by a constant at rather low electric fields. This regime is refereed as *linear optics*.

If an incident electric field is much weaker than the fields that maintain the medium in a stable state, the applied external field can be considered as a small perturbation. Within such approximation, employing a perturbation theory[69], the relation between the incident electric field and induced medium polarization can be in general written in the Taylor power series:

$$\mathbf{P}(t) = \epsilon_0 \left[\chi^{(1)}\mathbf{E}(t) + \chi^{(2)}\mathbf{E}^2(t) + \chi^{(3)}\mathbf{E}^3(t) + ...\right] = \mathbf{P}^{(1)}(t) + \mathbf{P}^{(2)}(t) + \mathbf{P}^{(3)}(t) + ... \tag{1.15}$$

The $\chi^{(1)}\mathbf{E}(t)$ term of the eq. 1.15 corresponds to the linear response of a medium to an applied electric field, which results in a linear polarization $\mathbf{P}^{(1)}(t)$. All other terms $\chi^{(2)}\mathbf{E}^2(t)$, $\chi^{(3)}\mathbf{E}^3(t)$ etc. account for non-linear response of a medium and corresponding non-linear polarizations $\mathbf{P}^{(2)}(t)$, $\mathbf{P}^{(3)}(t)$ etc. In general in anisotropic materials, the susceptibility might be not uniform in different spatial directions. Therefore the general mathematical term of a susceptibility $\chi^{(n)}$ is a (n + 1)-degree tensor.

The regime where higher order terms of the Taylor expansion start to play an important role is refereed as *non-linear optics*.

For homogeneous, isotropic and polarizable medium, the electric field wave equation takes the following form[70]:

$$\nabla^2\mathbf{E} - \frac{1}{c_0^2}\frac{\partial^2\mathbf{E}}{\partial t^2} = \mu_0 \frac{\partial^2\mathbf{P}}{\partial t^2}. \tag{1.16}$$

Therefore if polarization created in a medium is varying in time it will result in the creation of a propagating electromagnetic wave. This is consistent with Larmor's theorem of electromagnetism that states that accelerating charges generate electromagnetic radiation.

In case of the linear polarization, the frequencies of generated light will be the same as frequencies of incident light. However, the frequencies of light generated by a non-linear polarization might differ from the frequencies of an incident light, as described in sections 1.2 and 1.3 of this thesis.

Optical phenomena which can be described by the linear polarization are a part of *linear optics*. However, all other phenomena which can be described by a non-linear polarization, are a part of *non-linear optics*. The *non-linear order* is defined by the exponent of the electric field in the non-linear polarization expression.

If a medium is exposed to an electric field comparable in magnitude to the field which bounds medium together, such as a Coulomb field, the perturbation approximation is no longer valid and eq. 1.15 can not be used for description of such non-linear effects. This regime is called a *non-perturbative regime of nonlinear optics*.

Some non-linear effects are present only during the time of interaction with an incident field and cause only temporary modification of a medium. Such effects are termed *transient* in this thesis. However, other non-linear effects cause either permanent modification of a medium or long-lasting modification, which is present even after the incident electric field is no longer applied. These effects are termed *non-transient* in this thesis.

A combination of linear and non-linear responses to the incident electric and magnetic fields determine optical properties of a medium, such as refraction, reflection, absorption, transmittance, birefringence, dichroism, dispersion, etc. Many of the optical phenomena can be described by a unique phenomenological quantity that is specific for every material. Such quantity is called *refractive index*. The optical properties of a medium can be observed and controlled if the refractive index of the material can be measured and modified in a controllable way. Therefore refractive index provides a unique tool to alter and control the optical properties of any medium.

In summary, light-matter interaction can be described by Maxwell's equations, which are based on a polarization created in a medium. The proportionality factor between an incident electric field and created polarization is called susceptibility. The response of a medium to the applied electric field can be linear or non-linear, transient or non-transient, and instantaneous or non-instantaneous.

1.2 Transient non-linear optics

Eqs. 1.15 and 1.16 imply that due to the non-linear polarization of a medium, the new light can be generated or the properties of the incident light can be modified.

Considering only the lowest order of non-linearity (second-order), and only two frequencies ω_1 and ω_2 interacting with a medium, the resulting polarization will take the following form[71]:

$$\begin{aligned}\mathbf{P}^{(2)}(t) = \epsilon_0\chi^{(2)}[E_1^2 e^{-2i\omega_1 t} + E_2^2 e^{-2i\omega_2 t} + 2E_1E_2e^{-i(\omega_1+\omega_2)t} \\ +2E_1E_2^* e^{-i(\omega_1-\omega_2)t} + c.c.] + 2\epsilon_0\chi^{(2)}\left[E_1E_1^* + E_2E_2^*\right].\end{aligned} \tag{1.17}$$

Here E_1 and E_2 are the complex amplitudes, $*$ is a complex conjugate of a quantity, while *c.c.* is a complex conjugate of the former expression. From this equation, we can identify terms that describe specific types of non-linear phenomena:

$$\begin{aligned}\mathbf{P}(2\omega_1) &= \epsilon_0\chi^{(2)}E_1^2e^{-2i\omega_1 t},\\ \mathbf{P}(2\omega_2) &= \epsilon_0\chi^{(2)}E_2^2e^{-2i\omega_2 t},\end{aligned}\quad \text{(SHG)} \tag{1.18}$$

$$\mathbf{P}(\omega_1+\omega_2) = 2\epsilon_0\chi^{(2)}E_1E_2e^{-i(\omega_1+\omega_2)t}, \quad \text{(SFG)} \tag{1.19}$$

$$\begin{aligned}\mathbf{P}(\omega_1-\omega_2) &= 2\epsilon_0\chi^{(2)}E_1E_2^*e^{-i(\omega_1-\omega_2)t},\\ \mathbf{P}(\omega_2-\omega_1) &= 2\epsilon_0\chi^{(2)}E_1^*E_2e^{-i(\omega_2-\omega_1)t},\end{aligned}\quad \text{(DFG)} \tag{1.20}$$

$$\mathbf{P}(0) = 2\epsilon_0\chi^{(2)}\left[E_1E_1^* + E_2E_2^*\right]. \quad \text{(OR)} \tag{1.21}$$

When only the third-order non-linearity and only three incident light frequencies ω_1, ω_2, ω_3 are considered, the polarization will take the following form[71]:

$$\mathbf{P}^{(3)}(t) = \sum_n P(\omega_n)e^{-i\omega_n t}. \tag{1.22}$$

Here $P(\omega_n)$ are complex amplitudes of created polarizations. In total, the third order polarization described by eq. 1.22 will consist of 22 different frequencies ω_n. However, these frequencies can be identified with three distinct types of non-linear phenomena:

$$\begin{aligned}\mathbf{P}(\omega_1) &= \epsilon_0\chi^{(3)}\left[3E_1E_1^* + 6E_2E_2^* + 6E_3E_3^*\right]E_1e^{-i\omega_1 t},\\ \mathbf{P}(\omega_2) &= \epsilon_0\chi^{(3)}\left[6E_1E_1^* + 3E_2E_2^* + 6E_3E_3^*\right]E_2e^{-i\omega_2 t},\\ \mathbf{P}(\omega_3) &= \epsilon_0\chi^{(3)}\left[6E_1E_1^* + 6E_2E_2^* + 3E_3E_3^*\right]E_3e^{-i\omega_3 t},\end{aligned}\quad \text{(SPM or XPM)} \tag{1.23}$$

$$\begin{aligned}\mathbf{P}(3\omega_1) &= \epsilon_0\chi^{(3)}E_1^3e^{-i3\omega_1 t},\\ \mathbf{P}(3\omega_2) &= \epsilon_0\chi^{(3)}E_2^3e^{-i3\omega_2 t},\\ \mathbf{P}(3\omega_3) &= \epsilon_0\chi^{(3)}E_3^3e^{-i3\omega_3 t},\end{aligned}\quad \text{(THG)} \tag{1.24}$$

$$\begin{aligned}\mathbf{P}(\omega_1+\omega_2+\omega_3) &= 6\epsilon_0\chi^{(3)}E_1E_2E_3e^{-i(\omega_1+\omega_2+\omega_3)t},\\ \mathbf{P}(2\omega_1+\omega_2) &= 3\epsilon_0\chi^{(3)}E_1^2E_2e^{-i(2\omega_1+\omega_2)t},\\ \mathbf{P}(2\omega_2+\omega_1) &= 3\epsilon_0\chi^{(3)}E_2^2E_1e^{-i(2\omega_2+\omega_1)t},\\ \mathbf{P}(2\omega_3+\omega_1) &= 3\epsilon_0\chi^{(3)}E_3^2E_1e^{-i(2\omega_3+\omega_1)t},\\ \mathbf{P}(2\omega_1+\omega_3) &= 3\epsilon_0\chi^{(3)}E_1^2E_3e^{-i(2\omega_1+\omega_3)t},\\ \mathbf{P}(2\omega_2+\omega_3) &= 3\epsilon_0\chi^{(3)}E_2^2E_3e^{-i(2\omega_2+\omega_3)t},\\ \mathbf{P}(2\omega_3+\omega_2) &= 3\epsilon_0\chi^{(3)}E_3^2E_2e^{-i(2\omega_1+\omega_2)t},\end{aligned}\quad \text{(FWM + + +)} \tag{1.25}$$

$$
\begin{aligned}
\mathbf{P}(\omega_1+\omega_2-\omega_3) &= 6\epsilon_0\chi^{(3)}E_1E_2E_3^*e^{-i(\omega_1+\omega_2-\omega_3)t},\\
\mathbf{P}(\omega_1+\omega_3-\omega_2) &= 6\epsilon_0\chi^{(3)}E_1E_3E_2^*e^{-i(\omega_1+\omega_3-\omega_2)t},\\
\mathbf{P}(\omega_2+\omega_3-\omega_1) &= 6\epsilon_0\chi^{(3)}E_2E_3E_1^*e^{-i(\omega_2+\omega_3-\omega_1)t},\\
\mathbf{P}(2\omega_1-\omega_2) &= 3\epsilon_0\chi^{(3)}E_1^2E_2^*e^{-i(2\omega_1-\omega_2)t},\\
\mathbf{P}(2\omega_2-\omega_1) &= 3\epsilon_0\chi^{(3)}E_2^2E_1^*e^{-i(2\omega_2-\omega_1)t}, \qquad \text{(FWM + + –)}\\
\mathbf{P}(2\omega_3-\omega_1) &= 3\epsilon_0\chi^{(3)}E_3^2E_1^*e^{-i(2\omega_3-\omega_1)t},\\
\mathbf{P}(2\omega_1-\omega_3) &= 3\epsilon_0\chi^{(3)}E_1^2E_3^*e^{-i(2\omega_1-\omega_3)t},\\
\mathbf{P}(2\omega_2-\omega_3) &= 3\epsilon_0\chi^{(3)}E_2^2E_3^*e^{-i(2\omega_2-\omega_3)t},\\
\mathbf{P}(2\omega_3-\omega_2) &= 3\epsilon_0\chi^{(3)}E_3^2E_2^*e^{-i(2\omega_3-\omega_2)t},
\end{aligned}
\tag{1.26}
$$

$$
\begin{aligned}
\mathbf{P}(\omega_1-\omega_2-\omega_3) &= 6\epsilon_0\chi^{(3)}E_1E_2^*E_3^*e^{-i(\omega_1-\omega_2-\omega_3)t},\\
\mathbf{P}(\omega_2-\omega_1-\omega_3) &= 6\epsilon_0\chi^{(3)}E_1^*E_3^*E_2e^{-i(\omega_2-\omega_1-\omega_3)t},\\
\mathbf{P}(\omega_3-\omega_2-\omega_1) &= 6\epsilon_0\chi^{(3)}E_2^*E_3E_1^*e^{-i(\omega_3-\omega_2-\omega_1)t},\\
\mathbf{P}(\omega_1-2\omega_2) &= 3\epsilon_0\chi^{(3)}E_1(E_2^*)^2e^{-i(\omega_1-2\omega_2)t},\\
\mathbf{P}(\omega_1-2\omega_3) &= 3\epsilon_0\chi^{(3)}E_1(E_3^*)^2e^{-i(\omega_1-2\omega_3)t}, \qquad \text{(FWM – – +)}\\
\mathbf{P}(\omega_2-2\omega_1) &= 3\epsilon_0\chi^{(3)}E_2(E_1^*)^2e^{-i(\omega_2-2\omega_1)t},\\
\mathbf{P}(\omega_2-2\omega_3) &= 3\epsilon_0\chi^{(3)}E_2(E_3^*)^2e^{-i(\omega_2-2\omega_3)t},\\
\mathbf{P}(\omega_3-2\omega_1) &= 3\epsilon_0\chi^{(3)}E_3(E_1^*)^2e^{-i(\omega_3-2\omega_1)t},\\
\mathbf{P}(\omega_3-2\omega_2) &= 3\epsilon_0\chi^{(3)}E_3(E_2^*)^2e^{-i(\omega_3-2\omega_2)t}.
\end{aligned}
\tag{1.27}
$$

In summary, second and third non-linearity orders provide seven main types of transient optical non-linear phenomena: SHG, SFG, DFG, OR, SPM or XPM, THG, FWM. As will be shown in section 2.2 of this thesis, a combination of these non-linear processes can be used for electric field sampling of optical pulse waveforms with multi-PHz detection bandwidth and attosecond temporal resolution.

1.3 Non-transient non-linear optics

When an incident electric field becomes comparable in magnitude to the internal fields inside a medium, it may cause either permanent or long-lasting modifications. For instance, the atomic field strength of a Hydrogen atom can be estimated based on the Bohr radius:

$$E_{at} = \frac{e}{4\pi\epsilon_0 a_0^2} = 51.4(\text{V/Å}), \tag{1.28}$$

where e is the electron charge, ϵ_0 is the vacuum permittivity, a_0 is the Bohr radius of the Hydrogen atom. Some of the effects however may occur at field strengths far below this

value. For instance color-center formation.

Since these modifications can last even after the applied field is removed, they are considered as non-transient, and the process can not be described by eq. 1.15.

The long-lasting modifications are due to the redistribution of charge carriers in a medium within energy levels. Since each energy level (or energy band) has an intrinsic lifetime, it takes some time for the medium to return to its original equilibrium state.

The permanent modifications of a medium, however, can be either due to the breakage of chemical bonds or due to the phase transition. For instance, carbon can exist in the phase of graphite, diamond, and graphene. The exact phase of each particular carbon specimen is determined by the environmental condition to which this specimen is exposed.

For optoelectronic applications, the temporary modifications are of the most importance since they allow altering medium properties in a reversible manner.

The temporary modifications of a medium during the light-matter interaction occur mainly either due to the multi-photon absorption of incident photons or due to the tunnelling between energy levels. Which process dominates is determined by the Keldysh parameter[72]:

$$\gamma = \frac{\omega\sqrt{2mI_0}}{eF} \quad \text{(Gases)}, \tag{1.29}$$

$$\gamma = \frac{\omega\sqrt{mE_g}}{eF} \quad \text{(Solids)}, \tag{1.30}$$

$$\gamma = \frac{\omega\sqrt{m\Phi}}{eF} \quad \text{(Metal surfaces)}. \tag{1.31}$$

Here F is a field strength of the incident wave, I_0 is the ionization potential of a gas medium, m is the reduced electron effective mass, E_g is the band gap of the transition between energy bands, Φ is the work function of a metal surface, ω is the angular frequency of an incident wave, e is the electron charge.

If γ is much smaller than 1, the transition is dominated by the tunnelling ionization. On the other hand, if γ is much larger than 1, then the multi-photon absorption regime dominates (Fig. 1.1).

Since for both, multi-photon absorption and tunnelling ionization rather strong fields are required, the type of the transition is mainly dominated by the frequency of the incident wave.

In summary, non-transient effects lead to permanent or long-lasting changes inside the medium. The origin of the non-transient changes is mainly due to the multi-photon absorption or tunnelling ionization. Which process dominates can be estimated by the Keldysh parameter γ.

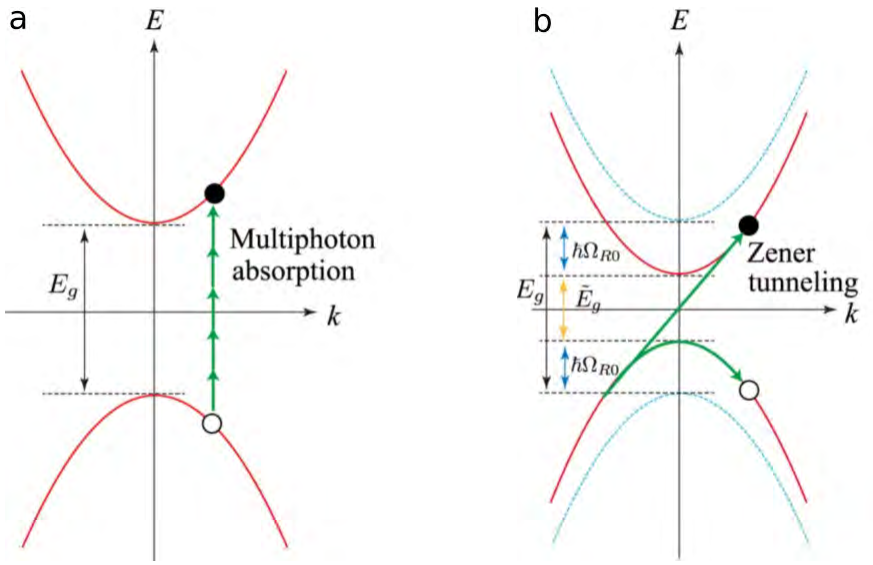

Figure 1.1: Schematic representation of the multi-photon absorption (**a**) and Zener tunnelling (**b**) regimes. Adopted from [1].

1.4 Non-instantaneous response and light-matter energy transfer

In sections 1.1 and 1.2 it was assumed that susceptibilities of a medium are the same for all frequencies of an incident light. Or in other words, the displacement of a charge carrier and therefore a polarization created in a medium depends only on an *instantaneous* value of the incident electric field.

In general however, the displacement x of charge carriers with a charge q, under influence of an incidence field is governed by the equation of motion for a damped harmonic oscillator:

$$m\frac{d^2}{dt^2}x + b\frac{d}{dt}x + Dx = qEe^{(i\omega t)}, \tag{1.32}$$

where E is a complex amplitude of the applied electric field with a frequency ω, m is the mass of a charge carrier and t is time. The term $m\frac{d^2}{dt^2}x$ represents an acceleration of a charge carrier by the applied electric field, $b\frac{d}{dt}x$ accounts for damping of the oscillatory motion due to, for instance, interaction of the oscillator with a surrounding medium. The strength of the damping is defined by the constant b. The term Dx describes the restoring force on the charge carrier in a bound system. The strength of the restoring force is defined by the constant D.

Using the ansatz $x = x_0e^{i\omega t}$[73] one can obtain the solution for the differential equation 1.32:

$$x_0 = \frac{qE}{m\left(\omega_0^2 - \omega^2 + i\gamma\omega\right)}, \tag{1.33}$$

where $\gamma = \frac{b}{m}$ and $\omega_0^2 = \frac{D}{m}$. The displacement x allows calculation of the medium polarization

$$P = Nqx, \tag{1.34}$$

where N is the number of dipoles in a medium per unit volume. Knowing the medium polarization and incident electric field allows calculating the linear susceptibility of a medium ($\chi^{(1)} = P/E$):

$$\chi^{(1)}(\omega) = \frac{Nq^2}{\epsilon_0 m\left(\omega_0^2 - \omega^2 + i\gamma\omega\right)}. \tag{1.35}$$

Eq. 1.35 shows that the optical susceptibility is, in general, frequency-dependent and a complex-valued quantity. The frequency dependence of the susceptibility leads to non-instantaneous polarization response, and as a consequence, to the medium *dispersion*. The imaginary part of the susceptibility corresponds to medium *absorption* since in the phasor representation of the oscillating electric field propagating through the medium with a complex refractive index $n' = n + i\kappa$, leads to the multiplication of the complex amplitude by an attenuating term

$$E = E_0 e^{-k\kappa z} e^{i(\omega t - nkz)}, \tag{1.36}$$

where z is the medium propagation length and k is the wave vector. The larger is the distance z which electric field propagates through the medium, the smaller is the amplitude of the electric field becomes.

Equation 1.35 also shows that quasi-free and bound charge carriers provide different polarization responses[74] because the restoring force which is present in the case of bound carriers is absent in the case of free carriers. The polarization response of carriers that are exposed to a restoring force is referred to as *Lorentz response* and described by eq. 1.35. On the other hand, the polarization response with absent restoring force is referred to as *Drude response* and can be described in the integral form as

$$\chi^{(1)}(\omega) = -\frac{\omega_{pl}^2}{\omega^2 + i\gamma\omega}, \tag{1.37}$$

where

$$\omega_{pl} = \sqrt{\frac{q^2 N}{\epsilon_0 m}} \tag{1.38}$$

is called *plasma frequency*[73].

In addition, the polarization field can be defined as the time integral of the current density (eq. 1.7). The current density is proportional to velocity of a charge carrier:

$$J = \frac{I}{A} = \frac{q}{tA} = \frac{vq}{xA}, \tag{1.39}$$

where I is a total current, A is a surface area, q is a total charge, v is a velocity of the charge carrier, t is time and x is a unit of distance. This last expression is merely a velocity times charge density.

If free and bound charge carriers with the same charge q travel through the same distance x, the current density response to the applied electric field depends on the velocity of the charge carrier. For the bound charge carriers the time-dependent position of the carrier is governed by eq. 1.15. For the case of the weak applied field, the polarization response is linear and determined by the first-order term of the eq. 1.15. The velocity v of charge carriers can then be written as

$$v_b(t) = \frac{\chi^{(1)}}{qN}\frac{d}{dt}E(t), \tag{1.40}$$

where $E(t)$ is the applied electric field and N is a charge density. For free charge carriers on the other hand, the time-dependent position of the carrier is governed by the equation of motion (eq. 1.32). The velocity v of charge carriers at time t can then be written as

$$v_f(t) = \frac{q}{m}\int_{-\infty}^{t} E(t')\,dt', \tag{1.41}$$

If the incident electric field is monochromatic with a single frequency ω, it can be represented as $E(t) = Esin(\omega t)$. The velocity of the bound carriers is then

$$v_b(t) = \frac{\chi^{(1)}}{qN}\left(E \cdot \omega \cdot cos(\omega t)\right), \tag{1.42}$$

while of the free carriers is

$$v_f(t) = \frac{q}{m}\left(-\frac{E}{\omega} \cdot cos(\omega t)\right). \tag{1.43}$$

Substituting eq. 1.42 and 1.43 in eq. 1.39 and then to eq. 1.7 shows that the created polarization in a medium is linearly proportional to the velocity of charge carriers. For bound carriers (in the absence of absorption) $P_b \propto Esin(\omega t)$, while for free carriers (in the absence of damping) $P_f \propto -\frac{E}{\omega^2}sin(\omega t)$. Therefore the polarization response of bound and free charge carriers in the case of absent absorption and damping, is not in phase and oppose each other.

In solids however, the bonding of multiple atoms results in the formation of energy bands, in which charge carriers are described by the Bloch function[75]. The crystal potential of the Bloch function results in a quasi-free electron/hole crystal momentum to be linearly proportional to the *vector potential* of the incident light. Such dependence is known as *acceleration theorem*[76]:

$$\begin{aligned} \frac{d(\hbar k)}{dt} &= qE(t), \\ \hbar k(t) = m_{eff} v_{qf}(t) &= q \int_{-\infty}^{t} E(t')\, dt'. \end{aligned} \tag{1.44}$$

Equation 1.44 shows that the velocity of quasi-free charge carriers in solids is proportional to the electric field of the incident light, with introduced effective mass of a charge carrier (under parabolic approximation of a band dispersion relation) in the same manner as for charge carriers in free space.

The creation of the medium polarization requires work to be performed by the incident light. If the incident light is polarized along x-axis, and the polarization of a medium is homogeneous, the performed work can be written as

$$W(t) = \int_{-\infty}^{t} J(t')V(t')\, dt' = x \int_{-\infty}^{t} J(t')E(t')\, dt' = x \int_{-\infty}^{t} E(t') \cdot \frac{d}{dt'} P(t')\, dt', \tag{1.45}$$

where J is a total current, V is a voltage and P is a medium polarization. Therefore the work made by the incident light is proportional to the time evolution of the incident electric field and the change of the created polarization.

According to the eq. 1.15, and as described in the section 1.2 of this thesis, the total polarization can be decomposed on linear and non-linear parts with respect to the incident electric field. Therefore the total work is a linear sum of works performed due to linear and non-linear polarizations of a medium.

The *time-resolved* non-linear polarization can be determined when the same electromagnetic pulse is transmitted through a thin medium at high and low field strengths, provided that the pulse waveform can be measured. At low incident field strength the non-linear polarization is negligible and under this assumption, the total polarization consists of only the linear contribution. At high incident field strength, on the other hand, the non-linear polarization can not be neglected and the total polarization consists of linear and non-linear contributions. When the normalized transmitted pulse waveform measured at low field strength is subtracted from the normalized transmitted pulse waveform measured at high field strength, the linear polarization is subtracted and the difference between two waveforms provides time-resolved non-linear polarization. In the frequency domain, the non-linear polarization can be expressed as[7]

$$P_{\omega}^{(NL)}(\frac{l}{2}) = \frac{2 \cdot i \cdot n(\omega)\epsilon_0 c}{\omega l} \Delta E_{\omega} e^{ik_{\omega} l/2}, \tag{1.46}$$

where l is a length of an interacting medium, n is a complex refractive index at a frequency ω, ϵ_0 is the vacuum permittivity, c is the speed of light, k is the wave-vector and ΔE is the change of the field amplitude at a frequency ω.

Performed by the incident light work causes charge carriers to gain or lose their kinetic energy, while the incident field loses or gains the same amount of energy in order for energy to be conserved. The total free charge carrier kinetic energy can be written as

$$E_k(t) = \frac{p^2}{2m} = \frac{q^2}{2m}\left[\int_{-\infty}^{t} E(t')\,dt'\right]^2 = \frac{q^2}{2m}A(t)^2, \tag{1.47}$$

while for the quasi-free charge carriers in solids within the parabolic approximation:

$$E_k(t) = \frac{(\hbar k)^2}{2m} = \frac{q^2}{2m_{eff}}\left[\int_{-\infty}^{t} E(t')\,dt'\right]^2 = \frac{q^2}{2m_{eff}}A(t')^2. \tag{1.48}$$

In summary, the polarization response of a medium to an applied electric field is in general non-instantaneous and leads to dispersion and absorption by the medium. Incident on a medium light interacts with free (or quasi-free) and bound charge carriers creating medium polarization. The polarization created by free (or quasi-free) carriers opposes polarization created by bound carriers within the approximation that neglects the absorption and damping of a medium. Created polarization causes work and transfer of energy performed by the incident light. Since the polarization can be linear and non-linear, the total work and energy transfer consist of linear and non-linear components. The non-linear work and energy transfer can be determined if the non-linear polarization is known, while the non-linear polarization can be determined from the field-resolved measurement of the incident pulse in the linear and non-linear regimes.

1.5 Optical properties of a medium

So far the optical properties of a medium where explained based on phenomenological quantities such as susceptibility and refractive index. These quantities however are the consequence of distribution of charge carriers within a medium, which is described by the carrier wave-functions that satisfy the time-dependent Schrödinger equation:

$$i\hbar\frac{\partial\psi}{\partial t} = \hat{H}\psi. \tag{1.49}$$

Here $\hbar$ is the Planck's constant, ψ is the wave-function of a quantum mechanical system, and $\hat{H}$ is the Hamiltonian operator of the system. When a medium is exposed to an electric field, the total Hamiltonian operator will consist of the Hamiltonian of a free atom and the interaction Hamiltonian:

$$\hat{H} = \hat{H}_0 - \hat{\boldsymbol{\mu}} \cdot \mathbf{E}(t), \tag{1.50}$$

where $\hat{\boldsymbol{\mu}} = -e\hat{\mathbf{r}}$ is the electric dipole moment operator, e is an electron charge and $\hat{\mathbf{r}}$ is a position operator.

If the interaction Hamiltonian is much smaller than the Hamiltonian of a free atom, the perturbation theory can be used to obtain the wave-function of the system in terms of unperturbed wave-functions and power series that account for the perturbation:

$$\psi(\mathbf{r},t) = \psi^{(0)}(\mathbf{r},t) + \lambda\psi^{(1)}(\mathbf{r},t) + \lambda^2\psi^{(2)}(\mathbf{r},t) + ... \tag{1.51}$$

Here λ is an order of the perturbation. The perturbation terms of the total wave-function can be expressed as a sum of basis functions for a free atom with certain amplitudes:

$$\psi^{(N)}(\mathbf{r},t) = \sum_l a_l^{(N)}(t) u_l \mathbf{r} e^{-i\omega_l t}, \tag{1.52}$$

where u is the amplitude of the basis function at the energy eigenstate l and corresponding frequency ω. The probability amplitude $a_l^N(t)$ gives a probability that to N-th order of the perturbation, the atom is in energy eigenstate l and time t. The probability amplitudes can be calculated using perturbation theory[71]:

$$a_m^{(N)}(t) = \frac{1}{i\hbar} \sum_l \int_{-\infty}^{t} dt' V_{ml}(t') a_l^{N-1}(t') e^{i\omega_{ml} t'}, \tag{1.53}$$

where

$$V_{ml} = \langle u_m | \hat{V} | u_l \rangle = \int u_m^* \hat{V} u_l dr^3 \tag{1.54}$$

are the matrix elements of the perturbation Hamiltonian, m is an index of the initial eigenstate, l is an index of the coupled eigenstate, and ω_{ml} is a frequency corresponding to the transition energy, while $'$ stands for a time derivative.

The total polarization of a medium can be determined if the dipole moment and the density of atoms (N_d) are known:

$$\boldsymbol{P} = N_d \langle \boldsymbol{p} \rangle , \tag{1.55}$$

where

$$\langle \boldsymbol{p} \rangle = \langle \psi | \hat{\boldsymbol{\mu}} | \psi \rangle \tag{1.56}$$

is an expectation value of the dipole moment operator, and ψ is the wave-function given by eq. 1.51.

Since the wave-function of the system consists of multiple power-law terms, the expectation value of the dipole moment operator will therefore also consist of multiple power-law terms. The first-order term of the expectation value of the dipole moment operator is therefore related to the linear polarization of the medium:

$$\left\langle \boldsymbol{p}^{(1)} \right\rangle = \langle \psi^{(0)} | \hat{\boldsymbol{\mu}} | \psi^{(1)} \rangle + \langle \psi^{(1)} | \hat{\boldsymbol{\mu}} | \psi^{(0)} \rangle, \tag{1.57}$$

while higher order terms, such as a second-order:

$$\left\langle \boldsymbol{p}^{(2)} \right\rangle = \langle \psi^{(0)} | \hat{\boldsymbol{\mu}} | \psi^{(2)} \rangle + \langle \psi^{(1)} | \hat{\boldsymbol{\mu}} | \psi^{(1)} \rangle + \langle \psi^{(2)} | \hat{\boldsymbol{\mu}} | \psi^{(0)} \rangle \tag{1.58}$$

are related to non-linear polarizations of the medium. Since the polarization of a medium is in general frequency-dependent, one can express the total medium polarization as a sum of polarizations caused by separate frequencies of the incident light:

$$\boldsymbol{P} = \sum_p \boldsymbol{P}(\omega_p) e^{-i\omega_p t}. \tag{1.59}$$

The linear relation of the medium polarization and the incident electric field therefore becomes:

$$P_i^{(1)}(\omega_p) = \epsilon_0 \sum_j \chi_{ij}^{(1)} E_j(\omega_p), \tag{1.60}$$

where i and j are the indices of the coupled energy levels, E_j is a projection of the amplitude of the incident light with a frequency ω_p in the polarization plane.

By combining eq. 1.60 with eq. 1.55 one can derive an expression for the first-order linear medium susceptibility[71]:

$$\chi_{ij}^{(1)}(\omega_p) = \frac{N_d}{\epsilon_0 \hbar} \sum_m \left(\frac{\mu_{gm}^i \mu_{mg}^j}{\omega_{mg} - \omega_p} + \frac{\mu_{gm}^j \mu_{mg}^i}{\omega_{mg}^* + \omega_p} \right), \tag{1.61}$$

where g is an index of the ground state, m is an index of the coupled state, μ is a dipole moment of the transition.

The second order non-linear susceptibility can be calculated if the second order dipole moment expectation value is considered (eq. 1.58)[71]:

$$\begin{aligned} \chi_{ijk}^{(2)}(\omega_p + \omega_q, \omega_q, \omega_p) = \frac{N_d}{\epsilon_0 \hbar^2} \Gamma \sum_{mn} \Bigg(& \frac{\mu_{gn}^i \mu_{nm}^j \mu_{mg}^k}{(\omega_{ng} - \omega_p - \omega_q)(\omega_{mg} - \omega_p)} \\ & + \frac{\mu_{gn}^j \mu_{nm}^i \mu_{mg}^k}{(\omega_{ng}^* + \omega_q)(\omega_{mg} - \omega_p)} \\ & + \frac{\mu_{gn}^j \mu_{nm}^k \mu_{mg}^i}{(\omega_{ng}^* + \omega_q)(\omega_{mg}^* + \omega_p + \omega_q)} \Bigg). \end{aligned} \tag{1.62}$$

Here Γ is the permutation operator. Higher-order non-linear susceptibilities can be calculated using the same approach. The calculated susceptibilities can be used A.7 to describe optical properties of a medium, such as dispersion, absorption, reflection, birefringence, etc.

In summary, the relation between the classical phenomenological refractive index and the quantum mechanical system is established. The optical properties of a medium are determined by optical transitions within the quantum mechanical system, which are described by transition matrix elements of the dipole moment operator. The complex refractive index of a medium at any instance of time t is therefore related to the distribution of charge carriers within the energy structure of a medium and the coupling of the medium energy states.

1.6 Homodyne and heterodyne detection schemes

Homodyne and heterodyne detections are methods for extracting information from a modulation of some property of an oscillating signal. The reference oscillating signal without modulations, is called *local oscillator*, while phenomenon which produces modulations of the local oscillator, or mixes with the local oscillator is called *signal*.

The *homodyne* name stands for a single frequency, meaning a signal frequency matches the local oscillator frequency. The *heterodyne* term emphasizes the fact that the signal is mixed with some other frequency such that the beating frequency matches the local oscillator frequency.

An example of the homodyne detection is the optical Michelson interferometer (Fig. 1.2). The laser beam (1) is split into two optical arms (2, 2*) which have variable lengths. The beams in both arms (3, 3*) are then again recombined and the intensity of the recombined light (4) can be monitored with a spectrometer, photodiode, camera, etc. The length difference between the two arms will cause the phase difference between electromagnetic waves in both arms, since two recombining waves will interfere. The length difference is adjusted by the moving mirror. The total intensity of the recombined light will depend on the phase difference between recombining waves. The recombined wave (4) is the local oscillator. The wave which causes the modulation of the total intensity is the signal. The change of the length between two arms transfers in the modulation of the phase between two recombining waves, and therefore in the modulation of the total intensity after recombination. The modulation of the intensity can be observed on a screen of the camera as an interference pattern.

Another example of the homodyne detection is the lock-in amplifiers, since the detection occurs at the reference frequency. Therefore the signal modulates the amplitude or the phase of the local oscillator signal, and this modulation is detected.

In the heterodyne scheme however, the detection occurs at the frequency that is a mixing product of the local oscillator and the signal. This is to shift the signal frequency range into another frequency range. For example, if some process occurs at a frequency that is too low or too high for conventional detectors, then this process can be mixed with some other frequency such that the beating product occurs at the convenient frequency range.

The heterodyning (as well as homodyning) process can also make the detection signal much stronger than the original signal since the detection signal is a product of the mixing of the original signal with the local oscillator. The resulting strength of the detected signal depends on both, the strength of the original signal, and the strength of the local oscillator. Therefore the stronger is the local oscillator signal the stronger will be the detected signal.

An example of heterodyne detection is the Morse code receiver. The received radio wave signal is mixed with the local oscillator on the receiving device. The local oscillator frequency is adjusted to be close to the frequency of the transmitted signal. The beating between the local oscillator and the signal results in shifting of the transmitted signal to lower frequencies which can be heard by a human ear.

The heterodyne detection in contrast to the homodyne detection has an intrinsic prob-

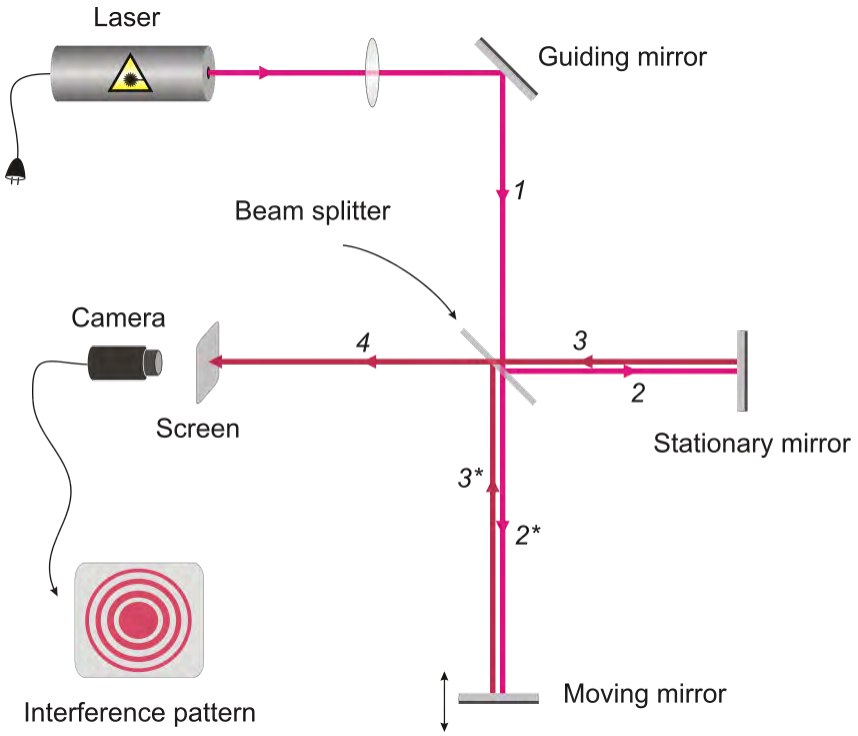

Figure 1.2: Schematic of an optical Michelson interferometer[2].

lem associated with intrinsic classical noise, such as laser intensity fluctuations, etc. Since in heterodyne and homodyne detections the detection signal is a product of the local oscillator with the signal of interest, the noise present in the local oscillator will be transferred to the mixing product. Typically the local oscillator is much stronger than the signal of interest, therefore after the mixing process, the detection signal will contain a strong noise originating from the local oscillator and not related to the signal of interest. Moreover, if the signal of interest is very weak, it may be smaller than the noise level of the detected signal. However, this problem can be solved with the *balanced* detection[77, 78]. For example, in a conventional electro-optic sampling scheme (Fig. 4.1), the detected light is split into two polarizations. The intensity of each polarization is detected by a separate photodiode. The polarizer is positioned such that intensities of light reaching each detector are equal. Instead of measuring the total intensity of the detection signal, one then measures the *difference* between intensities at each polarization. In this case, a classical noise due to the local oscillator will affect both detectors equally. Since the measured quantity is the difference between signals on each photodiode, the classical noise from the local oscillator will be subtracted. The role of the signal of interest, in this case, is a change of the polarization of light before reaching the polarizer. This approach makes the heterodyne detection to be approximately insensitive to intensity fluctuations of the local oscillator. The balancing detection however does not cancel the quantum noise, such as the shot noise due to the discrete particle nature of light. This noise will be a limiting noise factor provided perfect balancing of the detectors[67, 79].

In summary, homodyne detection is a method of detection of some phenomenon that causes modulation of the phase or frequency of another signal called a local oscillator. The heterodyne detection, on the other hand, is a method of detection of some phenomenon that is mixed with the local oscillator of a different frequency and the mixing product (beating) is detected.

1.7 Gated detection

Another approach of detecting the desired signal is based on *gating*. When the desired quantity, such as oscillating electric field interacts with medium properties of which change during the interaction, the resulting product of the interaction depends on the instance of time when the medium was altered.

An example of the gated detection is the attosecond streaking[23] or non-linear photo-conductive sampling[3] (Fig. 2.4). In attosecond streaking, the isolated XUV attosecond pulse with photon energies higher than the ionization energy of the medium ionizes the medium and creates free electrons. The free electrons can then be *streaked* to the direction of the detector. However, the streaking process can begin only from the moment when the free electrons are created. Therefore depending on the moment of ionization, with respect to the waveform of the optical streaking pulse, the total kinetic energy gained by electrons will be different.

Similarly, in non-linear photo-conductive sampling, the strong injecting pulse promotes electrons from the valence band to the conduction band based on processes described in section 1.3 of this thesis. Created quasi-free charge carriers are then displaced towards electrodes. However, the displacement can begin only from the moment when quasi-free charges are created. In both, attosecond streaking and non-linear photo-conductive sampling, the measured signal is recorded as a function of the time delay between the test pulse waveform and the gate function

$$S(\tau) \approx -\int_{-\infty}^{\infty} A(t)G(t-\tau)\,dt, \tag{1.63}$$

where t is time and S is the measured signal at the time delay between the gate G and the vector potential A of the test pulse waveform.

In this example, the medium ionization process is the gate with a duration mainly determined by the duration of the ionization process. According to the convolution theorem[80], eq. 1.63 implies that the measured signal in the frequency domain is proportional to the product of $A(\omega)$ and $G(\omega)$, therefore the spectral response of the techniques is determined by the spectral roll-off of $G(\omega)$.

In summary, the gated detection is a method of measuring physical observables in time based on the fact that observable interacts with medium properties of which are modified. The instance of time at which the medium is modified is controlled, and the net product of the interaction of the observable with the modified medium is detected.

Chapter 2

Petahertz field metrology in solids and gases

As described in the introduction section of this thesis, pulse waveform sampling is an important tool for time-resolved studies of physical processes[37, 7, 81, 82, 83, 84]. In this chapter novel concepts of pulse-waveform characterization are presented.

Section 2.1 presents a technique based on sudden excitation of charge carriers within a medium, which serves as a timing gate for the sampling of optical pulse waveforms. The semi-abrupt excitation of charge carriers and their further displacement by a test electric field can lead to a measurable current[85] which serves as an observable for the pulse waveform detection.

Section 2.2 describes another concept of the waveform sampling based on non-linear frequency mixing and further heterodyne detection. Multiple conditions for the heterodyne scheme are presented, each of which provides a detection bandwidth for sampling of optical pulse waveforms in various spectral ranges.

2.1 Non-linear photo-conductive sampling

The concept of non-linear photo-conductive sampling in solids is based on the fact that properties of a solid medium can be changed in attosecond time scale [86, 87, 7, 46, 88, 89, 90] due to linear or non-linear excitations of charge carriers within the energy structure of a medium. Such abrupt change of medium properties can be used as a temporal gate (section 1.7).

In the case of a linear excitation of a medium (attosecond streaking case), the duration of the excitation can be estimated by the duration of a pulse envelope of an exciting pulse[23, 58]. However, in the case of a non-linear excitation, the duration of the excitation process can be much shorter than the duration of an exciting pulse (Fig. 2.1).

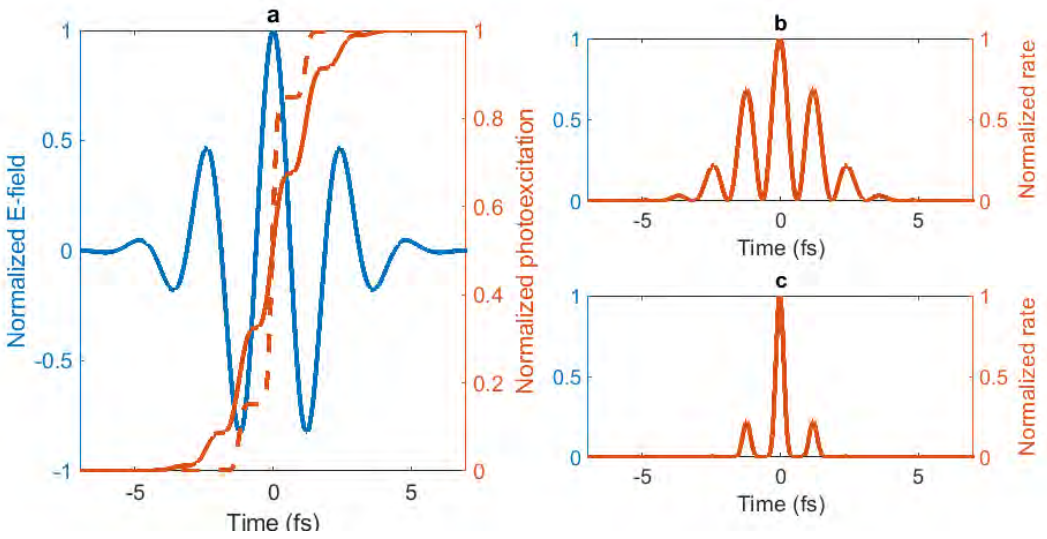

Figure 2.1: (**a**) The solid blue curve is an example pulse waveform used for the excitation of a medium. The solid orange curve is a schematic temporal profile of the time-dependent excitation of charge carriers for the case if the number of excited carriers would be proportional to the instantaneous field intensity (one photon excitation case). The dashed orange curve represents the four-photon excitation case for comparison. (**b**) Excitation rate for the linear single-photon case. (**c**) Excitation rate for the non-linear four-photon case.

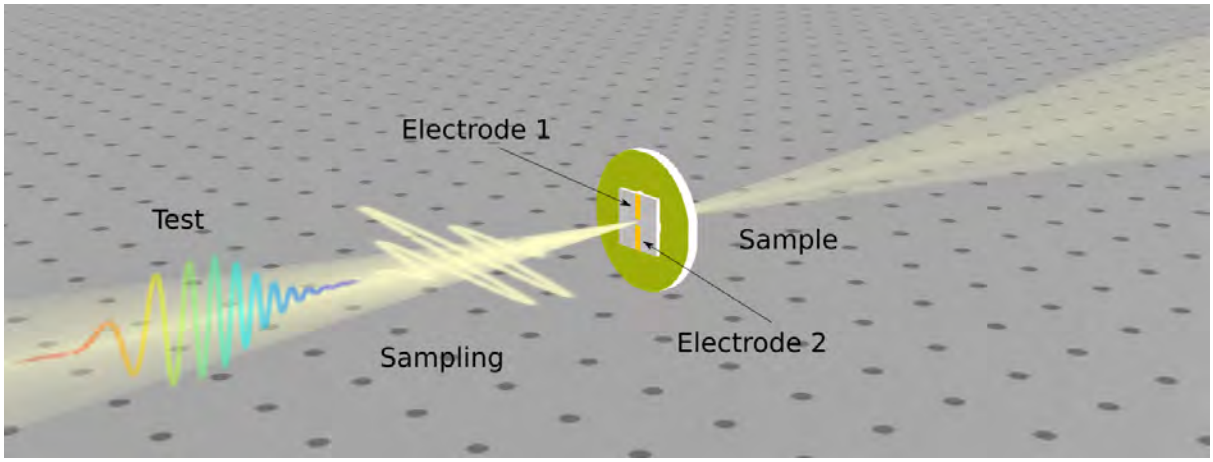

Figure 2.2: Schematic representation of the non-linear photo-conductive sampling using a solid medium.

2.1.1 Waveform sampling in solids

Fig. 2.2 shows a schematic setup of the non-linear photo-conductive sampling. The more detailed description of the optical setup is provided in the section A.2.1 of this thesis.

To employ the temporal confinement of the non-linear excitation of a medium as a gate to sample optical pulse waveforms, the few-cycle $\sim$ 2.7 fs pulse[3] (sampling) is used to

non-linearly excite the dielectric medium (Fig. 2.2). The quartz material was chosen as the sample medium in order to maximize the nonlinearity of the medium excitation process (due to the large band gap of the material). The rate of the excitation of the medium (Fig. 2.1c) will then serve as the temporal gate for the sampling process.

The pulse, waveform of which is intended to be sampled (test) is collinear with the sampling pulse. Two pulses can be delayed in time by a piezo delay stage.

The excited by the sampling pulse carriers (electrons and holes) will be displaced upon interaction with the test pulse (Fig. 2.3e). The net displacement of excited carriers will depend on the moment of the excitation, which is controlled by a time delay between injection and test pulses (Fig. 2.3d).

The net displacement of charge carriers at the end of the test pulse will create a macroscopic polarization of the medium[36]. In order to detect this polarization, a pair of metal electrodes is deposited on the surface of the quartz sample. Upon the creation of the medium polarization, the opposing shielding electric field will be created on each metal electrode. This will generate a potential difference between the electrode and the ground. The potential difference will provide an electromotive force to drive the current from the electrode to the ground or from the ground to the electrode.

The light polarizations of sampling and test pulses are orthogonal, such that the sampling pulse creates a medium polarization parallel to electrodes, in order to minimize the shielding electric field on the metal surface. On the other hand, the light polarization of the test pulse is perpendicular to the surface of electrodes, such that the medium polarization created by the test pulse is towards electrodes in order to maximize the shielding electric field on the metal.

The electrodes are connected to the pair of transimpedance amplifiers to convert the generated current into voltage with further amplification. The amplified voltage signal is then connected to the lock-in amplifier triggered at the repetition rate of the laser.

In order to increase the sensitivity of the detection, the CEP of every second pulse of the was flipped by introducing a π offset to the pulse CEP with a DAZZLER (Fastlite).

Since the inversion of the sampling waveform only flips its shape, the number of injected carriers caused by the sampling pulse remains the same. The inversion of the test pulse also only flips its waveform, however changes the sign of the net polarization created in the medium.

The lock-in detection can then be performed at half of the repetition rate of the laser to avoid the background noise originating from the strong sampling pulse and to detect only a signal caused by the net polarization created by the test pulse.

Since the process of the carrier injection is highly non-linear, by keeping the sampling pulse strong, while the test pulse weak, one can avoid significant excitation of a medium by the test pulse itself. However, since the displacement of created charge is linearly proportional to the electric field (at the weak field regime), the test pulse will still displace carriers to create a significant macroscopic polarization in the medium.

As long as these conditions are fulfilled, the total measured screening signal at each time-delay between sampling and test pulses will be proportional to a convolution of the test pulse vector potential with the gate function determined by the sampling pulse:

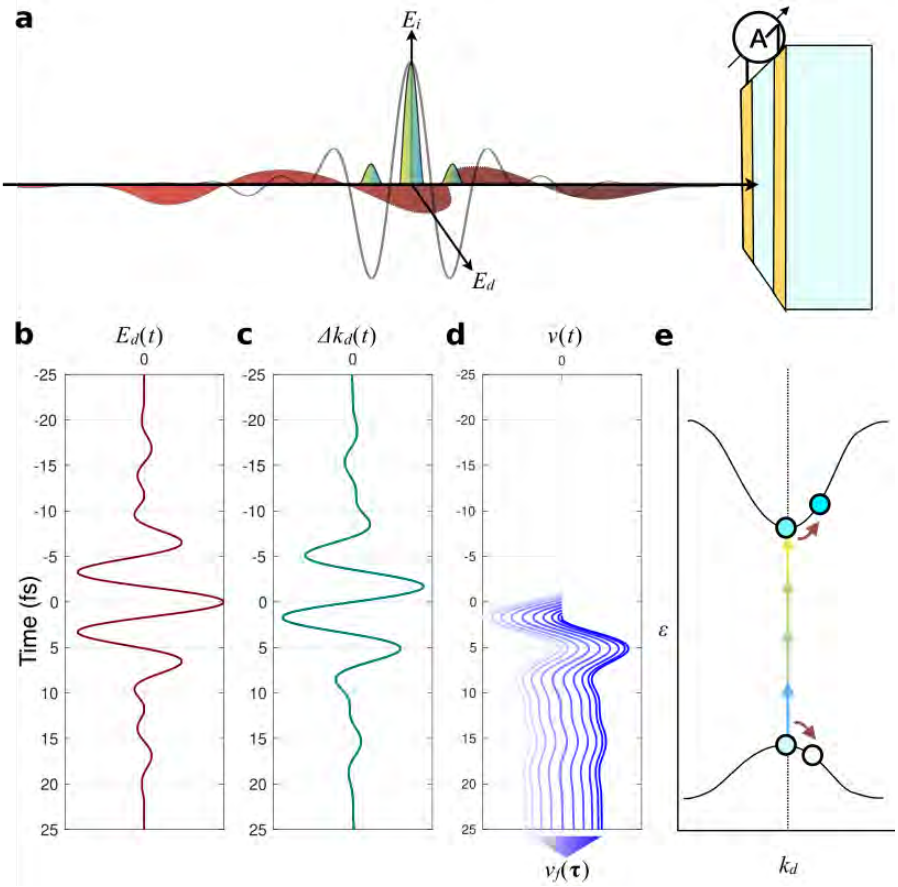

Figure 2.3: (**a**) Orthogonally polarized sampling and test fields (E_i and E_d) are focused on a dielectric medium (z-cut quartz) with deposited gold electrodes on a front surface. The gap between electrodes is adjusted to the focal spot of the incident fields. The strong, near single cycle pulse E_i induces a transition from the valence to the conduction band in the material, in the presence of orthogonally polarized test field E_d (**b**). (**c**) in an independent-particle picture, the crystal momentum offset Δk_d of an injected carrier along the horizontal direction is proportional to the time integral of the field E_d. This offset, together with band energies, determines the group velocities of charge carriers (**d**). In a semi-classical picture where photo-injection at time τ creates a wave packet with zero initial velocity, the average velocity at later times is determined by $\Delta k_d(t) - \Delta k_d(\tau)$. Therefore the average velocity of the carriers is sensitive to the time τ of the transition, which is controlled experimentally via the relative delay between E_i and E_d fields, setting the intra-band acceleration of the carriers after the photo-injection event (**e**). The measured dipole in the dielectric is proportional to the average displacement of charge carriers, which is obtained by integrating their average velocity over time. Adopted from [3].

$$S_d(\tau) = -\int_{-\infty}^{\infty} A_d(t) G(t-\tau)\, dt, \tag{2.1}$$

where $A_d(t)$ is the vector potential of the test pulse:

$$A_d(t) = \int_t^\infty E_d(t')\,dt'. \tag{2.2}$$

When the gate function $G(t-\tau)$ is confined to the time window much shorter than the duration of a half-cycle of the test field, it can be approximated by the delta function, resulting in a simplified version of the eq. 2.1:

$$S_d(\tau) \approx -\int_{-\infty}^\infty A_d(t)\delta(t-\tau)\,dt. \tag{2.3}$$

According to the eq. 2.3, the measured screening signal will depend on the vector potential of the test field from the moment of the carrier injection. Therefore when the current signal is measured at multiple time delays between sampling and test pulses, the electric field of the test pulse will be proportional to the derivative of the measured current trace:

$$E_d(t) \approx dS(d)/d\tau. \tag{2.4}$$

In order to demonstrate the validity of the non-linear NPS concept, the waveform of the NIR pulse was measured with NPS as well as with established attosecond streaking techniques, for direct comparison (Fig. 2.4). The correlation coefficient $\rho = 0.88$ and RMS field error $\epsilon = 0.48$ demonstrate a good fidelity[91] of waveform measurements obtained with two techniques (Fig. 2.4b). The difference between the two measured waveforms may be attributed to the different focusing and beam transform optics used in the two measurement systems.

Fig. 2.4 also compares the complexities of the two techniques. A very simple setup is needed for the NPS measurements, while the measurements themselves are done in ambient air. In contrast, the attosecond streaking technique requires the use of an attosecond beamline, with attosecond pulse generation as well as isolation, and photoelectron spectroscopy tools with optical components for XUV spectral range.

The agreement between two measured waveforms indicates that an attosecond streaking and NPS provide comparable attosecond timing gates, due to localization of an injection process in solids to the sub-cycle time scales.

Equation 2.1 indicates that the measured screening signal depends on the gate function. Since the shape and the magnitude of the gate function itself depends on a waveform of the sampling pulse (Fig. 2.1), thus the spectral response of the NPS technique depends on the injection pulse waveform.

To experimentally demonstrate the dependence of the NPS spectral response, sampling of the test pulse for different CEPs of the sampling arm was performed. The recorded spectral amplitudes of the measured signal were then compared for all CEP settings (Fig. 2.5). Performed TDDFT simulation demonstrates a good agreement with experimental results.

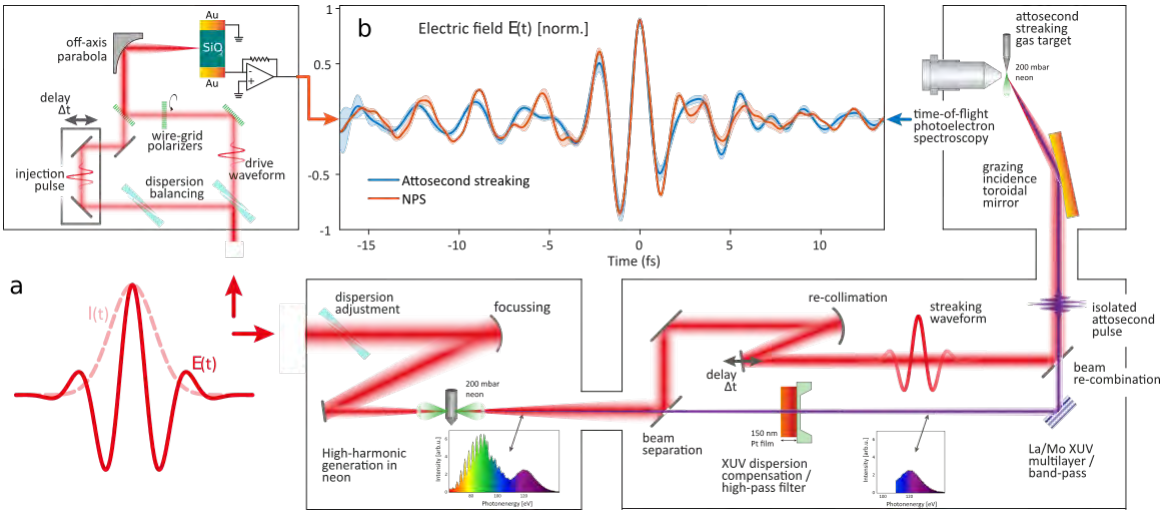

Figure 2.4: The same few-cycle laser pulse (**a**) is sent to either the NPS setup or to an attosecond beamline. The NPS setup produces time-delayed replicas of the pulse with crossed polarizations, focused onto the quartz sample with adjustable time delay, while the signal induced at the end of their interaction with the solid in an external pair of electrodes is read electronically. In the attosecond beamline, attosecond streaking is used to obtain a comparative measurement of the temporal evolution of the laser field, as it provides a broadband response in the relevant frequency range. In attosecond streaking, the laser pulse to be measured is coincident on a medium where bound electrons can be ejected by a synchronized attosecond pulse of extreme ultraviolet (XUV) light. The shift of the photoelectron energy vs. time delay allows the direct measurement of the vector potential of the laser pulse. The waveform obtained via the first-time-derivative of the energy shift of the photoelectrons emitted from a neon atom in an attosecond streaking experiment is also retrieved via NPS, returning the test field E_d, producing results that are remarkably similar given the differences between the two measurement setups (**b**). Adopted from [3].

Fig. 2.5d shows a good agreement in gate function calculations based on a TDDFT and a multi-photon (4th order) injection approaches. Since the carrier injection rate is approximately proportional to the energy deposition rate[92, 93], under the assumption of the multi-photon excitation, the gate function can be approximated by the eq. 2.5. Here n is an order of the multi-photon injection process. This approximation becomes more valid as the band-gap of a material increases.

$$G(t) \approx E_i^{2n}(t - \tau_{inj}). \tag{2.5}$$

For the case of a quartz medium and NIR sampling pulse ($\sim$ 750 nm central wavelength) used gating can be approximated by a 4th order multi-photon photo-excitation (section 1.3):

$$G(t) \approx E_i^{8}(t - \tau_{inj}). \tag{2.6}$$

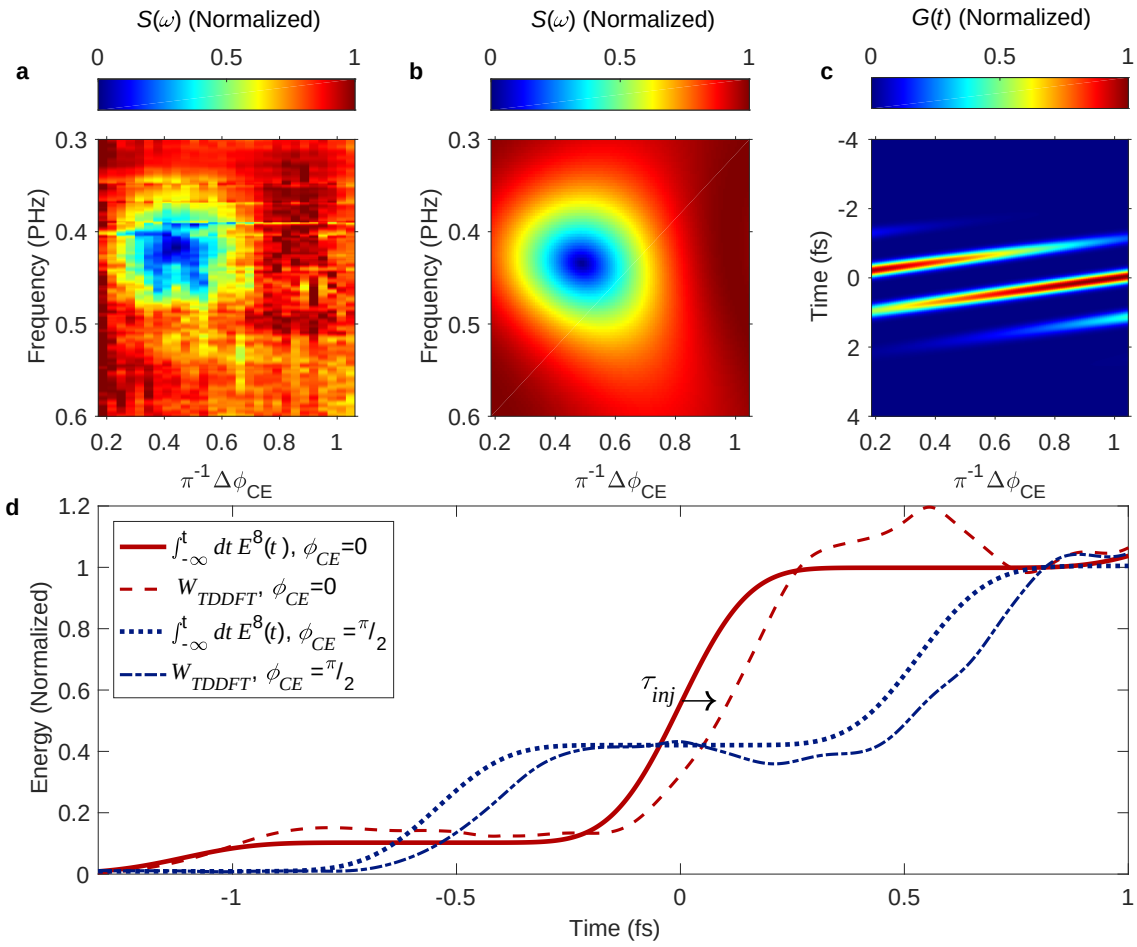

Figure 2.5: Normalized spectral response vs. CEP of the sampling pulse (**a**) shows a strong, phase-dependent minimum at the 0.42 PHz central frequency of the sampling pulse. This is consistent with a model simulation that uses $E^8(t)$ as the gating function, (**b**),(**c**). In this model, there is a single dominant photo-injection event for $\phi_{CE} = 0$, which results in a flat, unmodulated spectral response. For $\phi_{\mathrm{CE}} = \pi/2$, there are two transition events of comparable magnitude spaced by one half-cycle of the laser, as can be seen in the temporal evolution of the carrier injection rate, (**c**). The interference between these two events makes a dip appear in the normalized spectral response, (**b**), in the same region where the measured spectral response has the minimum. The ϕ_{CE}-controlled photo-injection events cause an abrupt increase of the energy deposited in the system. In **d**, a highly non-linear component of the energy is compared, calculated using the time-dependent density functional theory (TDDFT), to the time integral of $E^8(t)$. The TDDFT calculations show a slight time delay of the effective carrier injection, τ_{inj}, relative to the maximum of the laser field. Adopted from [3].

To get an actual waveform from the measured time-dependent screening signal, eq. 2.1 can be written in a frequency domain:

$$S_d(\omega) = -A_d(\omega)G(\omega) = \frac{iE_d(\omega)G(\omega)}{\omega}. \tag{2.7}$$

Knowing spectral amplitudes of the sampling pulse, absolute spectral phases, order of the multi-photon excitation, and the measured time-dependent screening signal, the actual test pulse waveform can be extracted:

$$E_d(\omega) = \frac{i\omega S_d(\omega)}{G(\omega)}. \tag{2.8}$$

The spectral response of the NPS technique for the sampling pulse waveform (Fig. 2.4b) and the quartz medium (4th order of multi-photon carrier injection) can be calculated from the TDDFT simulated energy transfer (Fig. 2.5d) by a Fourier transformation. Fig. 2.6 demonstrates a continuous detection bandwidth extending to PHz frequencies. The sampling pulse with a CEP 0 (cos pulse) leads to a relatively flat phase response up to the cut-off frequency of about 1.2 PHz. The structure of the spectral response is associated with a not perfectly 'delta-function-like' temporal shape of the gate (Fig. 2.1c and Fig. 2.5c). The eq. 2.8 also shows that as $G(\omega)$ approaches 0, the eq. 2.8 approaches infinity. Therefore to correctly extract a measured electric field, a bandpass filter should be applied to the measured data. The bandpass filter should cover a spectral region with SNR > 1.

To experimentally demonstrate the continuous detection bandwidth of the NPS technique from THz to PHz frequencies (infrared to ultraviolet wavelengths), the original test pulse was used to generate new spectral components by means of the intra-pulse difference-frequency generation, intra-pulse sum-frequency generation, or intra-pulse four-wave mixing (Fig. 2.7).

For the applicability of the technique, the signal-to-noise ratio, dynamic range, and linearity of the detection are important. Fig. 2.7b demonstrates the linearity of the detection over the broad spectral range (275 - 5300 nm) and four orders of magnitude of the peak power of the drive field.

The linearity of the detection was determined by measuring the scaling of the NPS screening signal at the central wavelength of the NIR test pulse and its second, second and a half, and third harmonics. At test field strengths from 0.001 V/Å to 1 V/Å, no harmonic distortion is present, indicating that the movement of injected charge carriers by the test field occurs within the parabolicity region of the conduction band of quartz. Starting from about 0.1 V/Å the noise level from the laser energy instabilities starts to dominate the electronic background noise, as the scaling of the signal at 2d, 2.5d, and 3d harmonics of the central wavelength is the same and linear with the test field strength.

Starting from about 1 V/Å of the test field strength, harmonic distortions appear. Mainly in the form of the third harmonic distortion, indicating that when the field strength of the test field becomes too high, the range of the movement of injected charge carriers within the conduction band of quartz exceeds the parabolicity region in the vicinity of the bottom conduction band edge. In addition, when the test pulse field strength becomes

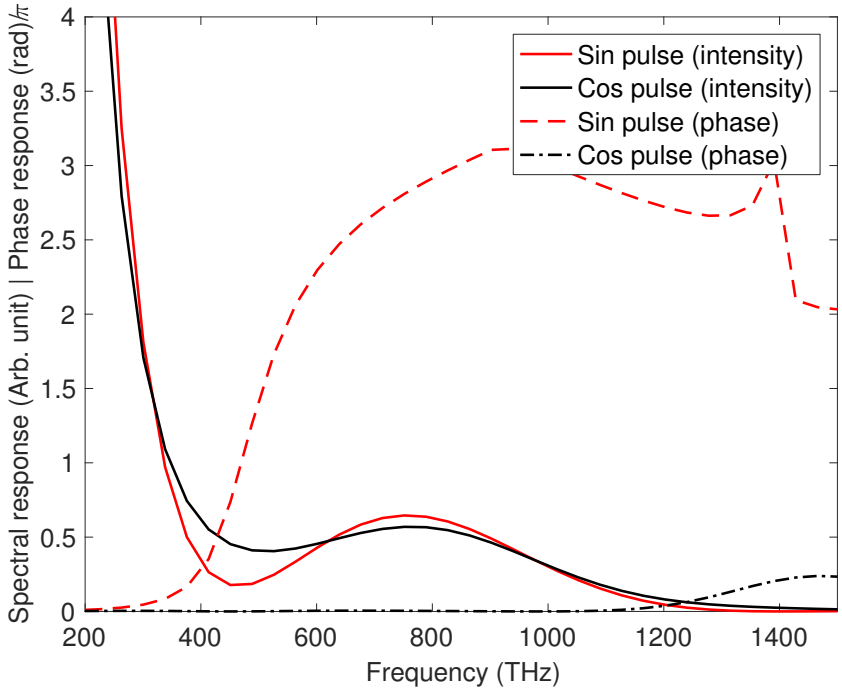

Figure 2.6: The spectral intensity and phase responses of the NPS technique for the quartz sample and experimental sampling pulse waveform (Fig. 2.4b), according to TDDFT simulation. Cos pulse corresponds to the CEP 0 of the injection waveform, while sin pulse corresponds to the CEP $\pi/2$. Adopted from [3].

comparable to a field of the sampling pulse, the test pulse by itself starts to contribute to the promotion of carriers from the valence band to the conduction band. Therefore the ratio between sampling and test pulse field strengths should be kept as large as possible.

In Fig. 2.8 the SNR can be estimated as the ratio between the signal at the central wavelength of the test pulse and the average of the spectrum outside of the bandwidth present in the test pulse spectrum.

In conclusion, the non-linear photo-conductive sampling technique using a solid medium is demonstrated. Continuous detection bandwidth with more than 1.2 PHz cut-off frequency, high dynamic range and signal-to-noise ratio provide a tool for study charged particle dynamics with attosecond time resolution. The simplicity of the experimental setup and ambient environment make the technique applicable without sophisticated attosecond beamlines, without attosecond pulse generation as well as isolation, without photoelectron spectroscopy tools and optical components for XUV spectral range.

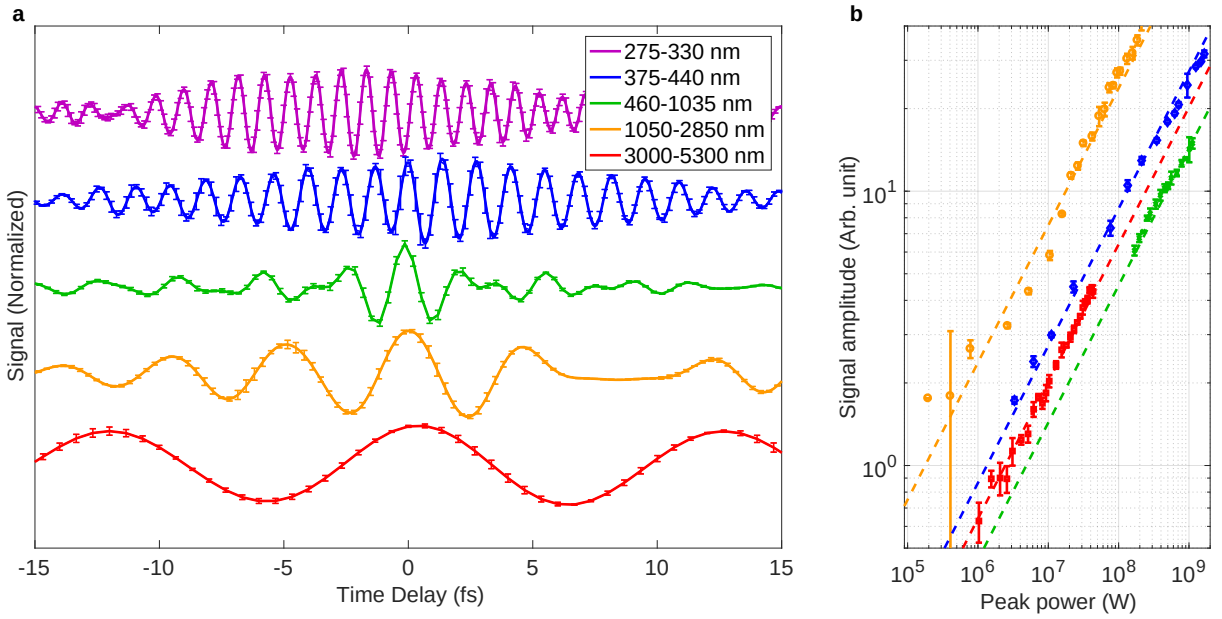

Figure 2.7: (**a**) Waveforms in different spectral ranges spanning the mid-infrared to ultraviolet, are detected by NPS, triggered by a 2.7 fs near-infrared visible pulse. The waveforms covering 3000-5300 nm and 1050-2850 nm are generated via difference frequency generation in LiNbO3 and BBO, respectively. The waveform covering 460-1035 nm is generated by the spectral broadening of a 21 fs, 790 nm pulse from a Ti:sapphire laser in a neon-filled hollow-core fiber and compressed with chirped mirrors to 2.7 fs duration (this waveform drives all other non-linear processes presented). The waveforms covering the spectral ranges 375-440 nm and 275-330 nm are both generated via sum-frequency generation in BBO, using different phase-matching conditions. The error bars represent the standard deviation of repeated measurements. (**b**) Using variable attenuation, the driving pulse energies are reduced and the signal is plotted vs. input pulse peak power, exhibiting both the linearity of the field response and its large dynamic range. The dashed lines are fitted linear field responses (i.e. scaling with $\sqrt{P}$, the square root of the peak power). The absolute positions of the lines on the vertical scale result from both the wavelength-dependent sensitivity of the measurement, which favors longer wavelengths, and the spatio-temporal properties of the frequency-converted beams. This causes the driving field strength, which determines the signal strength, to depend on more variables than power alone, but their proportionality with fixed beam parameters exhibits the linearity of the measurement. Adopted from [3].

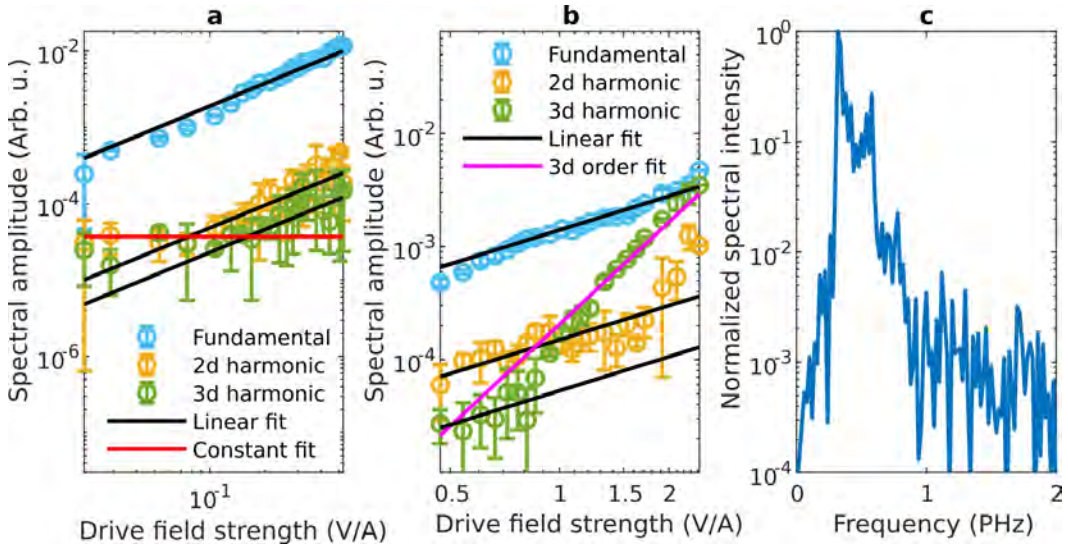

Figure 2.8: (**a**) Scaling of a measured signal at a fundamental frequency, 2d, and 3d harmonics, with the field strength of a test pulse centered at about 1.8 µm wavelength. (**b**) Scaling of a measured signal at a fundamental frequency, 2d, and 3d harmonics, with the field strength of a test pulse centered at about 750 nm wavelength. (**c**) The typical intensity signal-to-noise ratio of the NPS technique.

2.1.2 Waveform sampling in gases (ambient air)

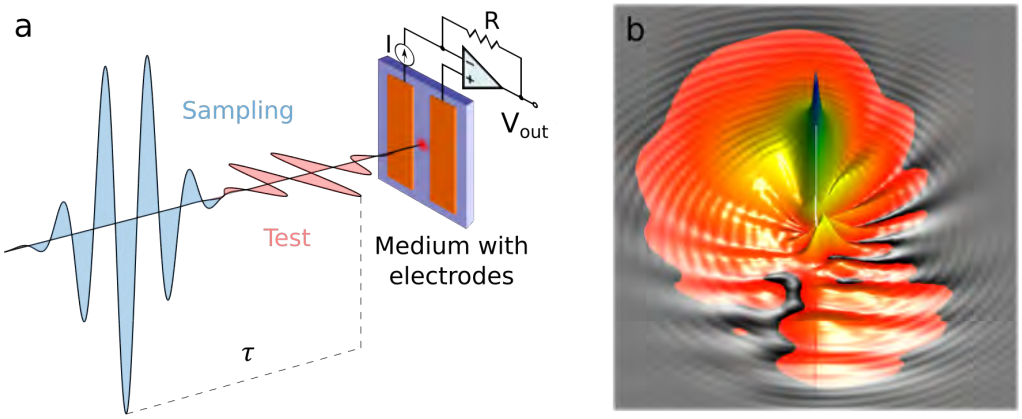

Figure 2.9: Schematic concept of the non-linear photo-conductive sampling in a gas medium (**a**), based on a symmetry breaking of an electron photonemission (**b**) due to the presence of the test pulse.

Non-linear photo-conductive sampling relies on the creation of a time gate by means of the confinement of a medium ionization within a short time window. Conceptually it is independent of a medium type (solids, gases, liquids) as long as a medium can be non-linearly ionized and produced charge carriers can be displaced by the test pulse. Although NPS in solids delivers a very compact solid-state table-top field sampling setup, a gas medium provides certain advantages:

1. Solid medium has a fixed and large charge density which provides a mean free path length typically smaller than 1 µm (section 5) due to the scattering[94]. This limits the displacement of ionized charge carriers and therefore created polarization in a medium. On the other hand, charge density and a mean free path in a gas medium can be controlled by a gas pressure. This control can be used to increase a created polarization in a medium and therefore the magnitude of a measured signal.

2. Ionization potentials of gases are typically much larger than the largest band-gaps of solids, such as in LiF or Quartz. Larger ionization potentials provide higher non-linearity of carrier injection and therefore confinement of an ionization gate to a shorter time window (Fig. 2.1b,c), which in turn, results in an increase of a detection bandwidth in comparison to solids.

3. Gas medium does not require a sophisticated sample preparation such as vapor deposition of metal electrodes on a surface of a solid sample (Fig. A.12). Essentially a piece of metal wire and ambient air medium is sufficient to perform the non-linear photo-conductive sampling.

4. Solid medium can be damaged if exposed to too strong incident light fields[95, 96], while a gas medium does not exhibit permanent damages.

5. Gas medium is much less dispersive than solids and therefore causes fewer distortions of a spectral response due to propagation effects.

6. Gases do not have surfaces and therefore do not cause reflections at interfaces which would interfere with an incident pulse, and therefore affect a spectral response of the detection.

7. The determination of a spectral response of the technique on an *ab initio* matter is much simpler in gases comparing to solids.

Fig. 2.9 shows a schematic concept of the NPS technique using gas as a sampling medium. More details are provided in the section A.2.1 of this thesis.

Two metal electrodes are positioned in an ambient air. The gap between electrodes is adjusted to match a focal spot of incident sampling and test pulses. As will be shown in the section 2.1.3, the technique does not require a pair of electrodes. A piece of a wire in the vicinity of the focused light is sufficient for sampling of optical pulse waveforms. A pair of electrodes is used to increase a signal-to-noise ratio.

Two pulses, dubbed *sampling* and *test*, were given orthogonal polarizations with a variable time delay (τ) with respect to each other. The stronger sampling pulse, which was vertically polarized, ionized ambient air, creating free electrons. Because the sampling pulse was polarized along the direction of the electrodes, it did not by itself generate a signal. The weak test pulse was polarized across the electrodes and was responsible for signal generation by displacing electrons toward one of the electrodes. As the test pulse separates electrons from positively charged ions, the emerging dipole induces image charges in the electrodes, inducing/driving a measurable current in a simple external circuit (Fig. 2.9). A transimpedance amplifier was used to provide a voltage in response to an input current[4].

The induced current can be interpreted as an imbalance in the angle-resolved photoemission of electrons in the half-planes defined by the electrodes. This asymmetry is the result of the combined action of the laser fields and the Coulomb potential of the ion on the electron, which can be simulated through a solution of the time-dependent Schrödinger equation, as shown in Fig. 2.10 for the example of a hydrogen atom. In the absence of the test field, the asymmetry is only in the direction of the sampling field, which produces a photoemission pattern that is identical in the planes of the two electrodes. In the presence of the test field, the photoemission is modified such that an asymmetry appears, resulting in a measurable potential between the electrodes. The magnitude and sign of the potential on electrodes depend on a time delay between sampling and test pulses (Fig. 2.10b,c).

The mechanism for the generation of a discernible signal from NPS in the air at ambient pressure is analogous to the application of NPS in solids: the separation of charges leading to the formation of a dipole, whose field is screened by the metal electrodes, ultimately

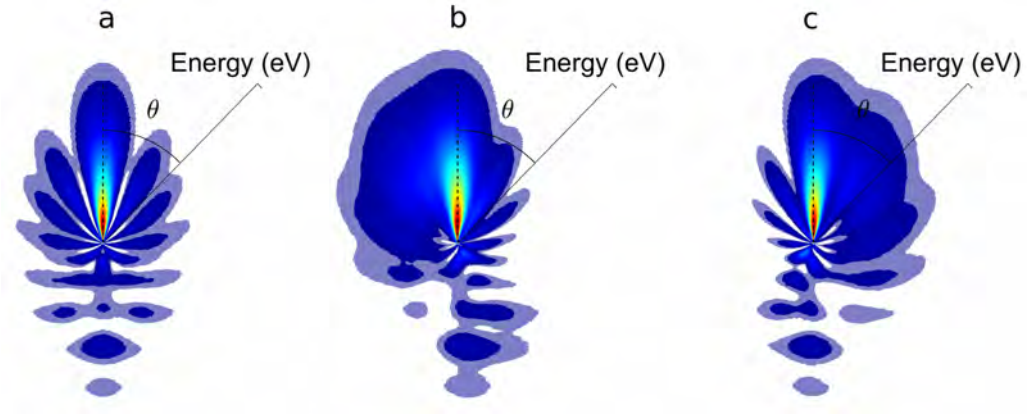

Figure 2.10: Simulated angle-resolved photoemission of electrons in a hydrogen atom for several delays between sampling and test pulses. (**a**) no time-overlap between test and sampling pulses, (**b**) photoionization of a medium at the strongest peak of a test pulse vector potential, (**c**) photoionization of a medium at a peak of a vector potential with inverted sign. Adopted from [4].

forming a current in the external circuit. By scanning the time delay between the non-linear injection of carriers (the time gate) and the field to be traced/sampled (test pulse), the electric field could be retrieved (Fig. 2.11).

In order to demonstrate the NPS detection in a gas medium, a multi-octave broadband spectral bandwidth (0.12 - 0.7 PHz) of optical frequencies was measured and compared to NPS detection in a solid medium (Fig. 2.11). The test pulse in a visible spectrum was achieved as described in section A.1 of this thesis. The NIR spectrum centered at a wavelength of about 2 µm was generated via intra-pulse DFG[97] in a Beta barium borate (BBO) crystal of type II, followed by a set of silicon and fused silica plates to block the fundamental spectrum and to compress the generated light.

The standard deviation of five measurements in both air and fused silica is represented by the shaded areas. A typical measurement time for a complete trace is several minutes.

For any electric-field measurement, it is vital to understand the relationship between the measured waveform, and the true electric field. In photoionization of atoms and molecules, a possible confounding factor is a Coulombic potential surrounding the parent ion, which will cause the free electron motion to deviate from the predictions of the strong-field approximation, according to which a signal is proportional to the vector potential of the drive field convolved with the gate function produced by the photoionization event. In order to investigate the influence of the Coulomb field of the parent ion on the measured signal, we numerically solved the TDSE in three spatial dimensions, using hydrogen as a model atom.

Using the TDSE to calculate the measured signal, assumed to be proportional to the momentum asymmetry of the resulting angle-dependent photoelectron spectrum in the direction of the test field, one can see that the signal as a function of time delay approximates the vector potential of the test field, but with a significant delay. This delay is

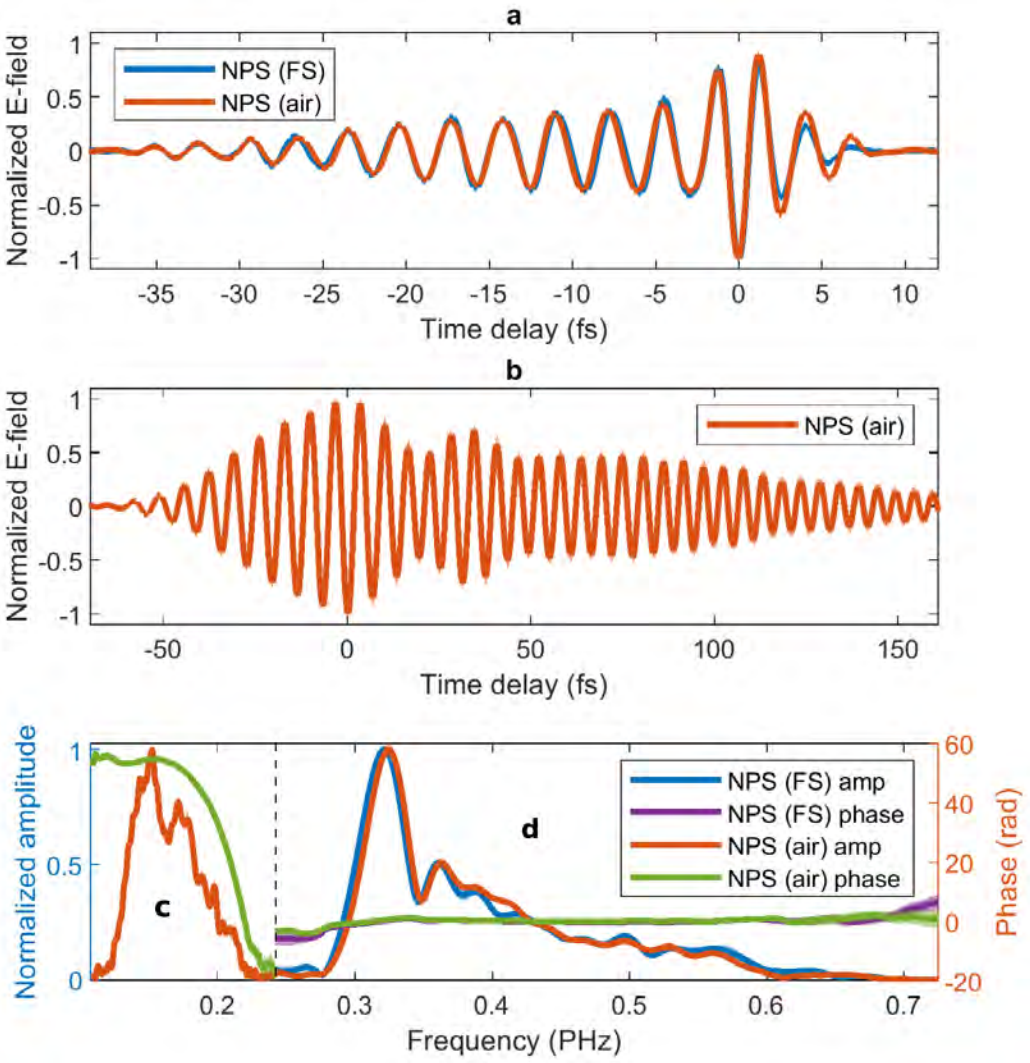

Figure 2.11: Benchmarking of measured pulse waveforms in a visible **a**, and in NIR **b** spectral ranges in the time domain, as well as in a spectral domain (**c**, **d**) using quartz and ambient air as a sampling medium.

attributed to Coulomb-laser coupling (CLC), and it agrees in magnitude with analytical theories developed for attosecond streaking [98]. To further verify this, the potential of the hydrogen ion in the simulation was replaced with a short-range spherical quantum well with a single 13.6 eV bound state. The short-range potential results in a signal that is in very good agreement with the strong-field approximation and with no appreciable delay. The effect of CLC varies in strength with the intensity of the injection field, due primarily to the injection of higher-energy electrons at higher intensities, which are less sensitive to the field of the parent ion.

The feasibility of first-principle simulations of the microscopic interaction allows for the microscopic response function to be fully characterized. This results in the spectral

amplitude and group delay variations with frequency shown in Fig. 2.12c. Appropriate phase and amplitude adjustments should be made to the measured signal, if one wishes to accurately characterize the temporal evolution of the test field in attosecond experiments. At high pressures and higher ionization rates, macroscopic effects may also affect the measurement, in terms of propagation of both pulses being measured (plasma dispersion and the Kerr effect) and the motion of the free electrons (collisions, collective plasma oscillations, and space charge) in the medium[99].

Experimentally, the optimum conditions, in which the required spectral amplitude and phase corrections are minimal, should be obtained by finding the value of the CEP which maximizes the measured signal (Fig. 2.12c). This corresponds to the condition where the photoemission gate is maximally confined to a single half-cycle of the injection field. Calculation of the Coulomb-induced phase correction is best performed using a measured injection pulse. If CEP optimization is performed experimentally, this can be obtained through standard techniques which yield the complex envelope function, such as frequency-resolved optical gating (FROG). As with other field measurement techniques, the obtained waveform is the convolution of the actual field with a gate function corresponding to the physical response of the system, whose influence must be corrected if one wishes to obtain the true electric field.

The spectral response of the detection was theoretically investigated based on solving TDSE for the case of a hydrogen atom. Fig. 2.12a shows a comparison of the ionization probability obtained from the TDSE and the measured signal. Simulation agrees well until the presence of a denser gas plasma starts to perturb the intensity scaling.

The signal is dominated by low-energy electrons, whose dynamics and interaction with the laser are influenced by the presence of the atomic/ionic potential. As in attosecond streaking experiments, where electrons are created through linear photoemission using a weak XUV pulse, the two main effects that influence the relative timing of the streaking signal are the atom-specific Wigner delay and Coulomb-laser-coupling (CLC). For low-energy electrons (below 10 eV) the magnitude of these effects on the timing is expected to be several 100 as[100, 98, 101, 102]. The electrons undergo ponderomotive motion in the relatively strong sampling field direction, while they are being accelerated by the test field, leading to a more complicated CLC in our case. Nevertheless, similar delays as in attosecond streaking are to be expected[4].

Using the TDSE to calculate the measured signal, assumed to be proportional to the momentum asymmetry of the resulting angle-dependent photoelectron spectrum in the direction of the test field, we see that the signal as a function of time delay approximates the vector potential of the test field (Fig. 2.12b).

The feasibility of first-principle simulations of the microscopic interaction allows for the microscopic response function to be fully characterized. This results in the spectral amplitude and group delay variations with frequency shown in Fig. 2.12c. Appropriate phase and amplitude adjustments should be made to the measured signal, if one wishes to accurately characterize the temporal evolution of the drive field in attosecond experiments. At high pressures and higher ionization rates, macroscopic effects may also affect the measurement, in terms of propagation of both the pulses being measured (plasma dispersion

and the Kerr effect) and the motion of the free electrons (collisions, collective plasma oscillations, and space charge) in the medium[99].

To examine the signal-to-noise ratio (SNR) and linearity of the signal with the measured field, the dependence of the signal at the fundamental frequency of the test field strength, as well as two harmonic multiples of that frequency, as a function of the test field strength was studied. This set of data allows for two important aspects of the measurement to be observed simultaneously. In the case that there is no component of the test field at the harmonic frequencies, this allows for sensitive detection of harmonic distortions that would result from nonlinearity in the detection. In the range of intensities applicable in the experiment, distortions from e.g. the test field significantly altering the ionization probability in the experiment, were absent. Such harmonics would be expected to grow with nonlinear dependence on field strength. In the case of detection of the fundamental pulse, Fig. 2.13b, the signal at the second harmonic grows linearly, indicative of linear field detection of the weak $\sim$ 400 nm signal reflected outside of the working spectral range of the chirped mirrors. A similar trend was observed when characterizing NPS in solids[3].

The SNR in the range of linear detection is above 100 in terms of intensity. This can also be seen intuitively in the logarithmically-scaled spectrum obtained via Fourier transformation of the signal shown in Fig. 2.13c obtained via Fourier transformation of the experimentally retrieved waveform (Fig. 2.11a, orange curve), where the amplitude falls abruptly outside of the transmission working spectral range band of the chirped mirror compressor.

In conclusion, a simple and versatile technique for sampling light fields at frequencies in the petahertz range: nonlinear photoconductive sampling in air. While NPS in solids has potential for future implementation within optoelectronic devices and is suitable for lower-energy injection pulses, the implementation of NPS in gas, complimentary to attosecond measurements using XUV pulses, permits a physical interpretation based on first principles. Simulations show that NPS in gases could also provide an interesting route to attosecond field-resolved spectroscopy involving low-energy electrons, e.g. for time resolving photo-ionization processes where the Coulomb interaction between an electron and its parenting ion plays the dominant role. Advantages of the NPS in solids can be summarized in terms of higher SNR, absence of sample preparation, higher ionization potential and therefore shorter confinement of an ionization-time window, significantly smaller dispersion of a gas medium, and absence of surfaces[4].

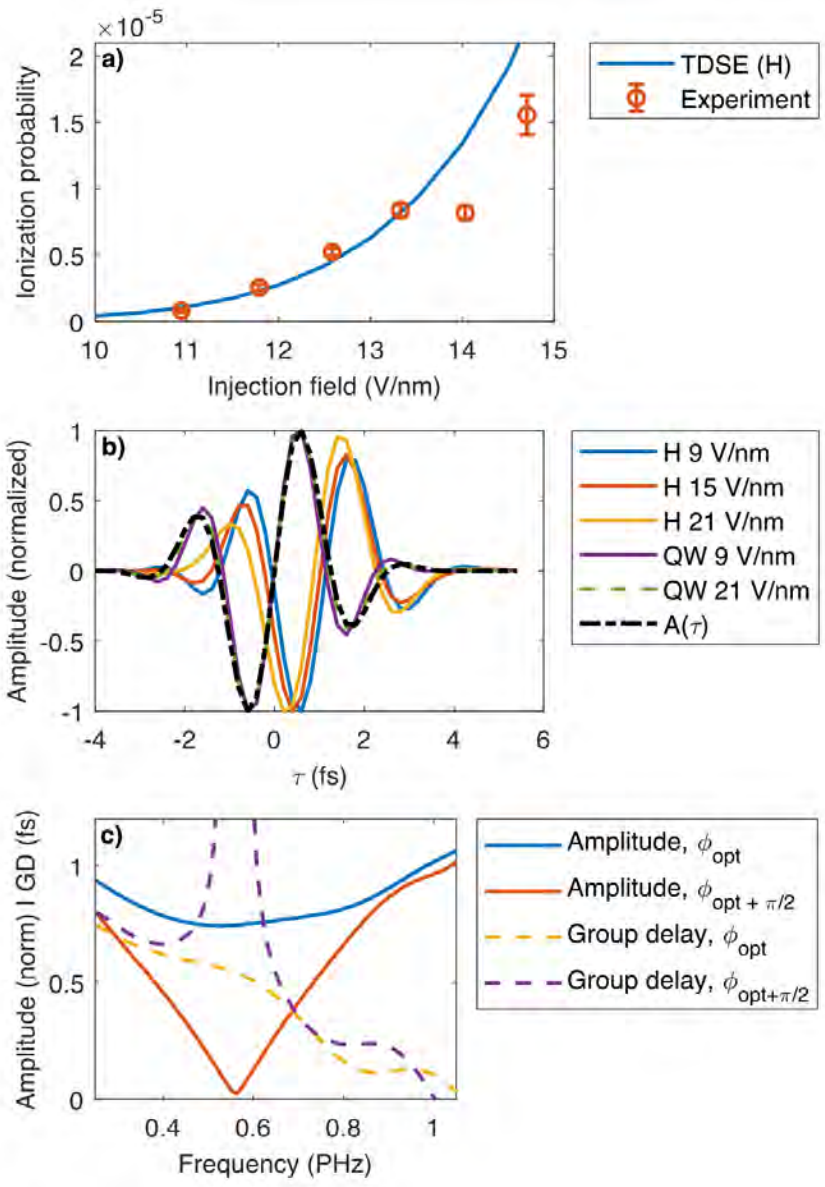

Figure 2.12: (**a**) Measured intensity scaling of the signal compared with the ionization probability for several peak strengths of the sampling field. (**b**) The measurement process is simulated as the appearance of a delay-dependent asymmetry in the angle-resolved photoelectron momentum distribution. In the presence of the atomic potential, the measurement reproduces the vector potential of the applied electric field, with a delay and phase shift caused by Coulomb-laser coupling. Performing the same simulation in an isolated spherical quantum well (QW) - a short-range potential with a single bound state of 13.6 eV binding energy - yields a similar trace, but with vanishing phase shift. Positive values of τ signify that the drive field comes before the injection pulse. (**c**) Simulated amplitude response and group delay of the measurement for the optimal CEP and the optimal CEP plus $\pi/2$, which exhibits a distinct minimum near the carrier frequency of the sampling pulse. Adopted from[4].

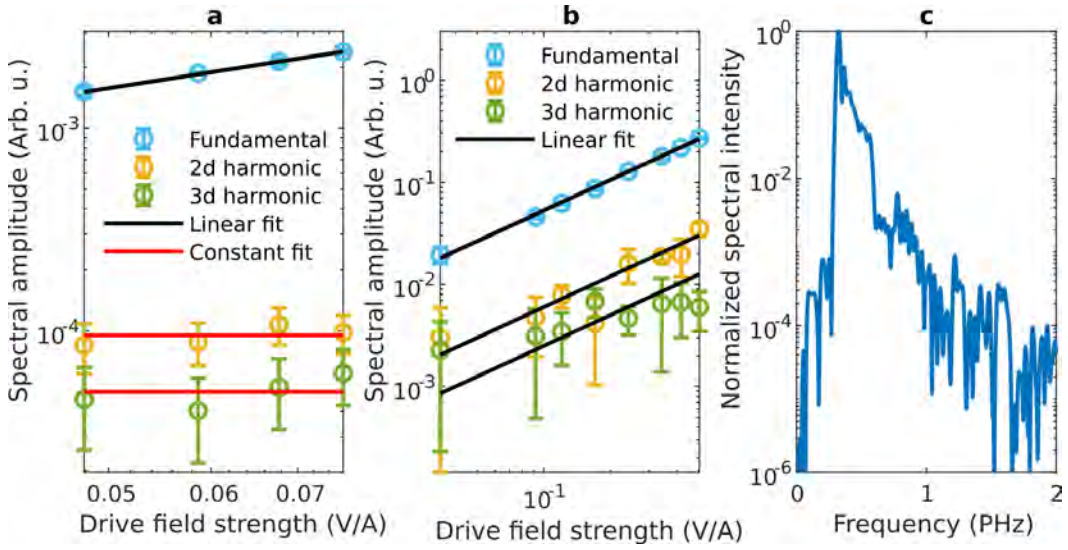

Figure 2.13: Linearity of the detection and noise level indicated by the spectral components of the waveform at 300-344 THz (fundamental), 688-733 THz (2nd harmonic), and 957-1000 THz (3rd harmonic) obtained by Fourier transformation of the measured signals at varying field strengths of visible (**a**) and NIR (**b**) test pulses. (**c**) Spectrum and spectral noise floor in the visible spectral range measured with a sampling field strength of 1.1 V/Å and a test field of 0.26 V/Å.

2.1.3 Origin and characterisation of the signal source

The measured signal from electrodes on a surface of a sample may have several origins, in particular:

1. Transport from one electrode to another
2. Modulation of an ionization yield of a medium[103]
3. Ionization of a metal surface
4. Polarization of a medium
5. Transport of ionized charge carriers to electrodes

Which regime dominates, depends on conditions such as mean free path of ionized charge carriers, charge density, etc.

The magnitude of a measured signal is proportional to a charge displacement and a number of created microscopic dipoles. Therefore maximization of a measured NPS signal, can be viewed as a maximization of a charge displacement and concentration of charge carriers. In the case of solids, not much can be done to influence these two parameters, however, a gas medium pressure allows for control both, charge displacement as well as charge concentration.

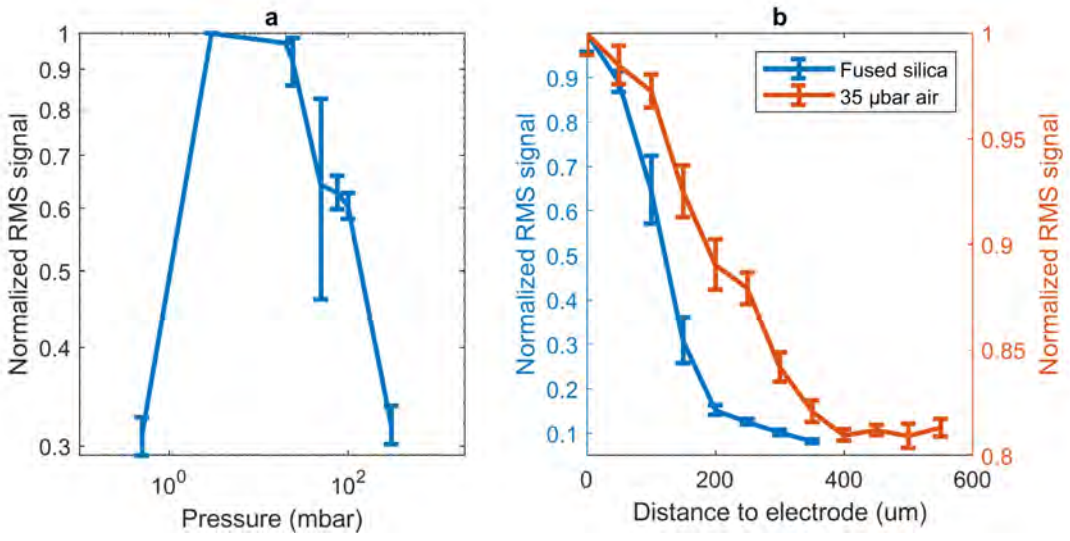

Figure 2.14: (**a**) Pressure dependence of a measured RMS signal in ambient air medium at a fixed incident light intensity. (**b**) dependence of a measured RMS on a distance to an electrode for the case of a fused silica medium and low-pressure air medium.

In order to study the influence of gas pressure on a measured NPS signal, two copper electrodes separated by a gap of about 80 µm were positioned in a small gas chamber, pressure in which was controlled. The origin of the maximum signal formation is a contribution

of three phenomena, the electron mean free path, number of charge carriers, and Coulomb interaction. The higher is the medium pressure, the more charge carriers can be created by ionization of a medium, and therefore larger medium polarization or current due to charge displacement. However the higher is the medium pressure, the less is a mean-free path of charge carrier displacement. Since the scattering is isotropic the mean free path scales as 1/p, where p is pressure[104]. On the other hand, the number of charge carriers scales linearly with a medium pressure. If the electrode distance is small enough such that most of the carriers can reach an electrode, the signal would increase linearly with the gas pressure. However, when the mean free path of charge carriers becomes comparable or smaller to the distance to an electrode, the signal becomes constant, since it is proportional to the product of a mean free path and a number of charge carriers. Therefore the signal is expected to be constant at high pressures and to start decreasing at a pressure that corresponds to the mean free path of carriers comparable to the distance to an electrode. Apart from the effects described above, at high charge carrier concentration, a Coulomb interaction between charges starts to play a role, by means of attraction of free electrons to the positively charged ions. This attraction reduces the displacement of charge carriers to a distance smaller than a mean free path, and therefore reduced measured signal. Fig. 2.14a shows a dependence of a measured signal on gas pressure. The signal has its maximum at about 5 mbar, and rolls off at higher and lower pressure. The maximum signal corresponds to a pressure when the mean free path is comparable or larger than the electrode distance. The roll-off of the signal at low pressure is due to the reduction of created charge carriers as the medium becomes less and less dense. The roll-off of the signal at high pressure is an effect of Coulomb interaction between charge carriers[104].

Fig. 2.14b demonstrates the dependence of a measured signal on a distance to an electrode. The measurement was performed using *one* electrode only. This implies that an electrode gap is *not* necessarily to conduct detection of generated currents. This also implies that the origin of an NPS signal is *not* the transport of charge carriers through the gap from one electrode to another due to the breakdown of a medium. The blue curve on Fig. 2.14b corresponds to the measurement of a signal generated in a solid medium (fused silica). A similar sharp decrease of a signal is also observed in the air at ambient pressure. The sharp roll-off of a signal is due to a small mean free path of displaced charge carriers. At low medium pressure, however (orange curve), the medium mean free path is much larger than in ambient pressure or in a solid medium. While after 400 µm the signal drops by about 90 % in a fused silica medium, it only drops by about 20 % in a low-pressure air medium.

So far, out of the list of possible origins of the signal, only transport from one electrode to another can be excluded. In order to get more insight into the mechanism of a signal, simultaneous measurement of a signal from two electrodes separated by a gap was performed. Fig. 2.15a,c shows normalized signals from both electrodes during an NPS measurement in SiO_2 medium (section 2.1.1) as well as in ambient air (section 2.1.2) medium. The signals from two separate electrodes are the same in magnitude but π out of phase. This important indication implies that the origin of a signal in a dense medium is likely due to created polarization, by means of displacement of ionized charge carriers. The created

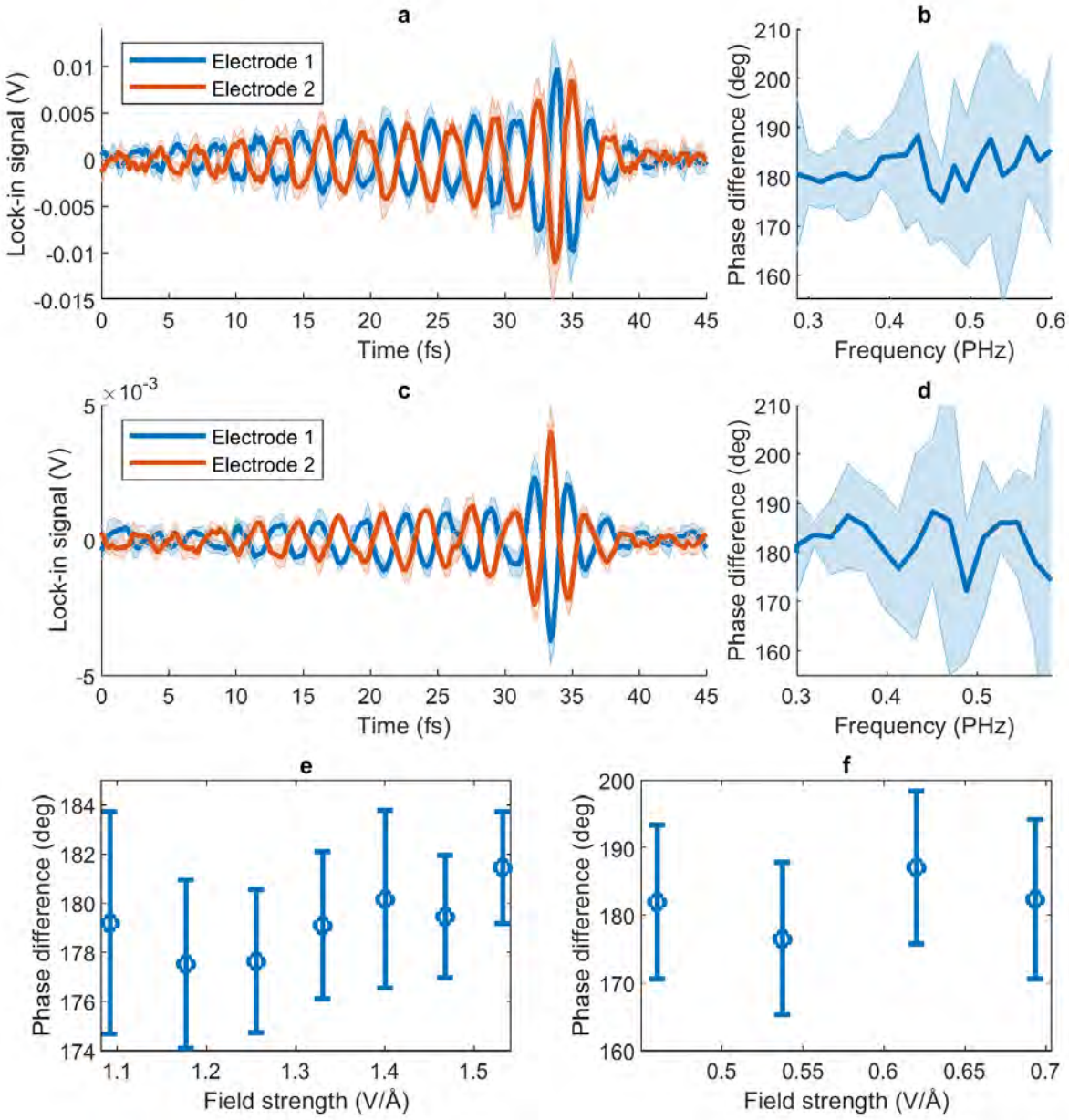

Figure 2.15: Measured pulse waveform signals recorded at two separated electrodes in fused silica (**a**) and ambient air (**c**) medium, with corresponding spectral phase differences (**b** and **d**). Dependence of a mean phase difference on sampling (**e**) and test (**f**) field strengths.

polarization then produces a screening electric field on metal electrodes. The screening field created an electromotive force, which generates current between an electrode and a

circuit ground. The origin of the π shift is due to the fact that created polarization has an equal magnitude of charge, but an opposite charge sign on each side of the crated dipole. If the generated signal would be due to modulation of an ionization yield of a medium, the electrodes would experience the same magnitude of signal modulation and would have the same phase, which is not the case. If the signal would be due to the transport of ionized charge carriers to electrodes, again the same phase of the modulated signal would be observed on both electrodes. If the signal would be due to ionization of a metal surface, the signal on both electrodes would be again in phase with each other. In addition, the signal from ionization of a metal surface would rapidly drop with the distance to an electrode. However in a low-pressure gas medium, the signal drops by only about 20 % at a distance of 400 µm to an electrode.

In summary, the origin of the NPS signal source was investigated. The origin of the signal is found to be likely due to the polarization created in a medium. The magnitude of the generated signal is found to depend on a combination of the mean free path of charge carriers and the number of created charge carriers. At a large concentration of charge carriers, an additional reduction of a signal occurs due to an increase in the influence of a Coulomb interaction between charge carriers. The Coulomb interaction reduces the displacement of charge carriers to a magnitude smaller than the mean free path of a medium, and therefore reduces created medium polarization.

2.2 Non-linear optical sampling

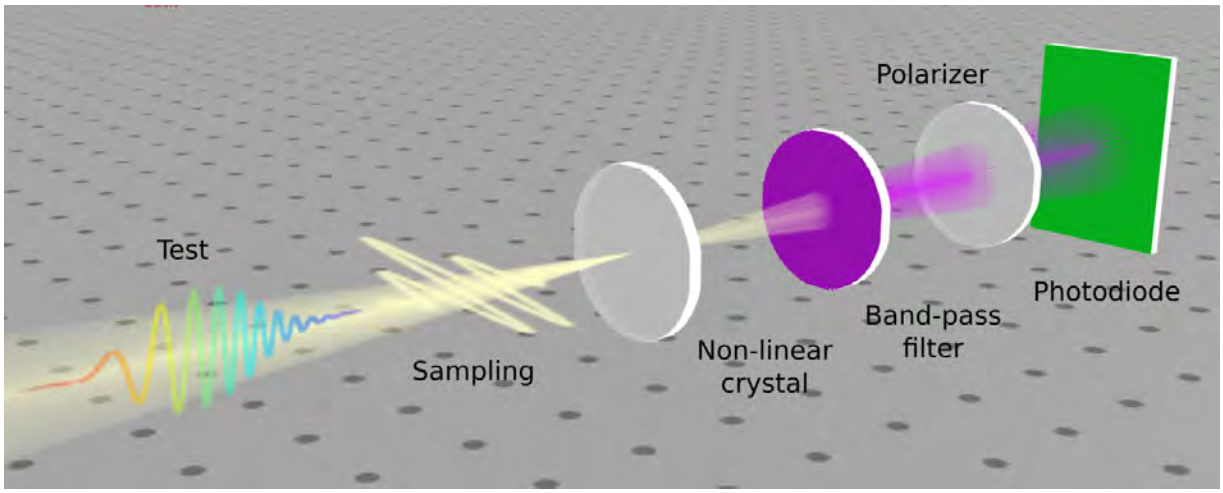

Figure 2.16: Schematic experimental setup of the non-linear optical field sampling.

As it was described in the section 2.1 of this thesis, the source of the NPS signal is a polarization created in a medium. The created polarization is then screened by metal electrodes and produces an opposing potential. Since the incident electric field changes with time, the polarization in a medium and the screening potential also change with time. Therefore in a frequency domain, the total created polarization in a medium has a certain frequency bandwidth, which can extend beyond PHz frequencies. Typical electronic devices are not fast enough to detect such fast oscillations, and therefore act as a low-pass filter. For NPS experiments described in this thesis, the transimpedance pre-amplifier (DLPCA-200, FEMTO Messtechnik) was used to convert the generated current into voltage. The settings of the pre-amplifier provided the detection bandwidth from 0 to 7 KHz. This is much smaller than the bandwidth needed to resolve the time-varying polarization in the medium caused by the interaction with an incident light at PHz-scale frequencies, and essentially limits the detection of medium polarization to quasi-DC components, or net displacement of charge carriers.

Although typical electronic devices can not directly detect oscillating at high frequencies polarization, any oscillating dipole will emit electromagnetic radiation with a frequency of its oscillation. This radiation will carry information about the created polarization in the medium[105].

If produced electromagnetic radiation occurs at frequencies photon energy of which can be detected by a conventional photo-diode, such fast dipole oscillations of the medium polarization can be detected in a form of produced light.

The total medium polarization and therefore generated electromagnetic radiation is proportional to the time delay between sampling and test pulses (section 2.1) and their waveforms. The information about the test pulse waveform can be extracted from such modulation by means of a homodyne or heterodyne detection[106, 107, 108, 109] (section

1.6).

The polarization created in a medium by a first pulse (sampling) can be considered as a local oscillator. The time-delayed polarization created due to the mixing of sampling and test pulses can be considered as a heterodyne signal. If the frequency ω of a local oscillator matches the frequency of a heterodyne signal, a spectral intensity I at this frequency will depend on the amplitudes and phases of sampling and test pulses:

$$\begin{aligned} E_{Sig} \cdot sin(\omega t + \varphi_{Sig} + \frac{\pi}{2}) \propto E_S^N \cdot sin(\omega_S t + N \cdot \varphi_S) \cdot E_T \cdot sin(\omega_T t + \varphi_T) \\ I(\omega) = [E_{LO} \cdot sin(\omega t + \varphi_{LO}) + E_{Sig} \cdot sin(\omega t + \varphi_{Sig} + \frac{\pi}{2})]^2, \end{aligned} \tag{2.9}$$

where E_{Sig}, E_{LO}, E_S, E_T are the amplitudes of the signal, local oscillator, sampling and test pulses, while φ_{Sig}, φ_{LO}, φ_S, φ_T are their phases. N is a number of photons of the sampling field involved in the mixing.

The range of frequencies that can be used as a local oscillator is provided by a spectrum of polarization created in a medium by the sampling pulse. In electro-optic sampling, for instance, the bandwidth of a local oscillator is determined by a linear polarization created by the sampling pulse in a medium. However if the sampling pulse, non-linearly (section 1.2) interacts with a medium, the local oscillator bandwidth can be *extended*.

Fig. 2.17a shows the concept of an electro-optic sampling. The sum-frequency generation between sampling and test pulses creates a heterodyne spectrum that overlaps with a fundamental spectrum of the sampling pulse which acts as a local oscillator. Since the heterodyne signal depends on a time delay between sampling and test pulses, modulation of a spectral intensity at the region of a spectral overlap contains information about the amplitude and phase of the test pulse. This concept works when a spectrum of the test pulse consists of much smaller frequencies than the sampling pulse, since in this case, the sum-frequency spectrum almost fully overlaps with the fundamental sampling spectrum. However if a spectrum of the test pulse becomes comparable to a spectrum of the sampling pulse, a significant amount of the sum-frequency bandwidth does not spectrally overlap anymore with the sampling spectrum. This results in a loss of information about the test pulse. Therefore conventional electro-optic sampling can be used to detect pulse waveforms in a spectral region of frequencies smaller than frequencies of the sampling pulse.

When the test spectrum is within the bandwidth of the sampling pulse or at higher frequencies, the sum-frequency signal does not create a spectrum that significantly overlaps with a sampling spectrum (Fig. 2.17b). In this case, a heterodyne detection condition is not fulfilled anymore and information about the test pulse can not be extracted.

However, if not the fundamental sampling spectrum, but its *second harmonic* is used as a local oscillator (Fig. 2.17c), the heterodyne condition is fulfilled and the test waveform can be again extracted. Since a second harmonic and a sum-frequency generation happen in the same non-linear medium and with the same pulses, the phase information is preserved. Fig. 2.17c shows that the local oscillator bandwidth can be extended by means of a non-linear new frequency generation. Extended local oscillator allows to fulfill the

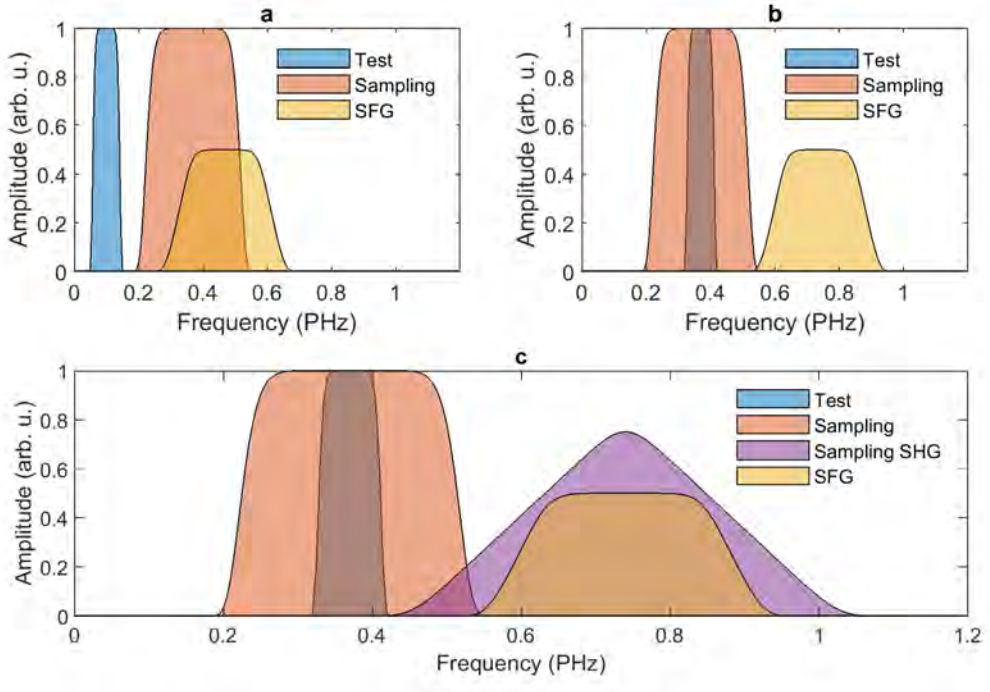

Figure 2.17: Schematic concept of the linear electro-optic sampling (**a**) and its detection bandwidth limitation (**b**). The concept of the non-linear optical sampling (**c**) based on SHG as a local oscillator and SFG as a heterodyne signal. The terms 'linear' and 'non-linear' refer to the origin of the local oscillator. In the case of electro-optic sampling, the local oscillator spectrum is a spectrum of the sampling pulse itself. In the case of the non-linear optical sampling, the local oscillator bandwidth is extended by means of a second harmonic generation.

heterodyne condition with heterodyne signals at higher frequencies and therefore perform field sampling of test pulses in a frequency range that is not accessible by a conventional electro-optic sampling.

Fig. 2.16 shows an experimental schematic setup of the non-linear optical field sampling. The detailed description of the optical experimental setup is presented in the section A.2.4 of this thesis.

The simplest case of the non-linear optical sampling is SHG + SFG channel, which allows a field sampling of the pulse waveform itself. An incident pulse is split into two arms, strong sampling:

$$E_S(t) = A_S sin(\omega t + \phi_S), \tag{2.10}$$

and weak test arm, which can be delayed with respect to the sampling arm by a time τ:

$$E_T(t) = A_T sin(\omega(t + \tau) + \phi_T). \tag{2.11}$$

A strong sampling field is incident on a non-linear medium and non-linearly generates a second harmonic which serves as a local oscillator:

$$E_{LO}(t) = \epsilon_0 \chi^{(2)} A_S^2 sin(2\omega t + 2\phi_S + \frac{\pi}{2}), \tag{2.12}$$

while both arms, delayed by the time τ, generate a sum-frequency field which serves as a heterodyne signal:

$$E_{HS}(t,\tau) = 2\epsilon_0 \chi^{(2)} A_S A_T sin(2\omega t + \omega\tau + \phi_S + \phi_T + \frac{\pi}{2}). \tag{2.13}$$

Since both, the local oscillator and the heterodyne signal occur at the same frequency ω, the intensity of the interference will depend on a time delay τ, sampling field phase ϕ_S and test field phase ϕ_T:

$$I_{LO+HS}(\tau) = I_{LO} + I_{HS} - 2\sqrt{I_{LO} I_{HS}} cos(\omega\tau + \phi_S - \phi_T). \tag{2.14}$$

If the phase of a sampling field ϕ_S is known, the delay-dependent modulation of an intensity I_{LO+HS} is proportional to a delay between two fields and the phase of the test field, therefore provides an unambiguous test waveform information.

If a heterodyne signal however originates from a different order of non-linearity, such as FWM:

$$E_{HS}(t,\tau) = 6\epsilon_0 \chi^{(3)} A_S A_S A_T sin(3\omega t + \omega\tau + 2\phi_S - \phi_T + \frac{\pi}{2}), \tag{2.15}$$

the phase of a sampling field ϕ_S is *not required to be known*, provided that the local oscillator and heterodyne signal frequencies match.

$$I_{LO+HS}(\tau) = I_{LO} + I_{HS} - 2\sqrt{I_{LO} I_{HS}} cos(\omega\tau + \phi_T). \tag{2.16}$$

This situation is analogous to conventional electro-optic sampling, where information about an absolute CEP of a sampling pulse is not required in order to sample a test waveform, since the local oscillator originates from $\chi^{(1)}$ susceptibility while the heterodyne signal from $\chi^{(2)}$ susceptibility.

The test pulse-field strength is set to be low enough such that it, by itself, does not generate a significant amount of new spectral components due to non-linear interaction with a medium, and the interaction can be considered linear. However, since the sampling pulse is strong, the non-linear mixing between sampling and test pulses will still generate a significant amount of non-linear signal.

Based on $\chi^{(2)}$ and $\chi^{(3)}$ non-linearities only, there are 6 main processes (section 1.2) which lead to generation of new spectral components, namely: OR, SHG, DFG, THG, FWM, SPM. On the other hand, there are 5 main processes that lead to the generation of the heterodyne signal: SFG, DFG, OR, FWM, XPM.

Since optical rectification creates a DC polarization field in a medium, it can not be used as an optical local oscillator, as the DC polarization field can not radiate propagating electromagnetic waves. The fundamental spectrum of a test pulse also can not be used

as a heterodyne signal. Therefore, based on $\chi^{(2)}$ and $\chi^{(3)}$ non-linearities only, in total 30 main combinations (Figs. 2.19 - 2.23) can be used for non-linear optical sampling. Any of such combinations of a local oscillator and a heterodyne signal is referred to as a *channel* in this thesis and can be used for the heterodyne detection (section 1.6) of electric fields. If a heterodyne signal is measured for various time-delays between a local oscillator and a signal, the time delay is transferred into amplitude and phase information and can be used for pulse waveform sampling as described further in sections 2.2.1 - 2.2.2 of this thesis.

To simulate the concept and model amplitude and phase spectral responses of the technique, sampling and test pulses shown in Fig. 2.18 were considered. The results of the simplest model for the infinitely thin, non-dispersing, and non-absorbing medium are presented below.

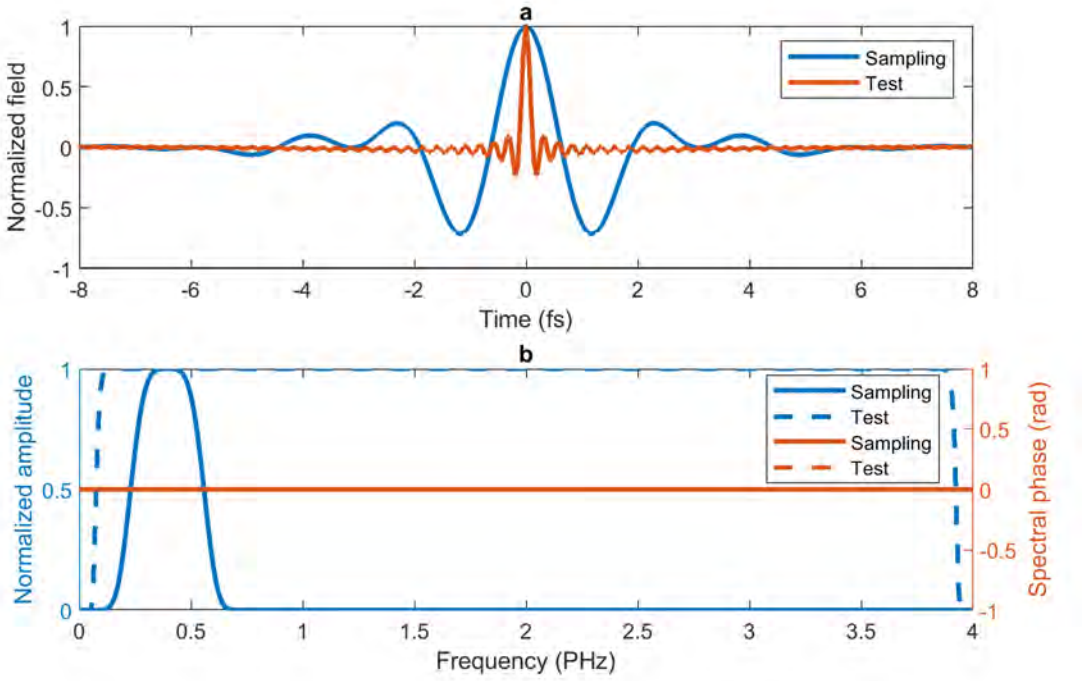

Figure 2.18: Sampling and test pulse waveforms (**a**) and their corresponding spectral amplitudes and phases (**b**) used for spectral response simulations.

Figs. 2.19 - 2.23 show calculated amplitude spectral responses for various NOS channels. The detection frequency is the one that is used to detect the modulation of the spectral intensity due to the interference of a local oscillator and a heterodyne signals. The response frequency is the frequency of the spectral response.

The important observations can be summarized as:

1. Different channels provide spectral responses for different spectral ranges, therefore certain channels or combinations of channels can be chosen for desired applications. However, if a combination of multiple channels is used for field detection, then the

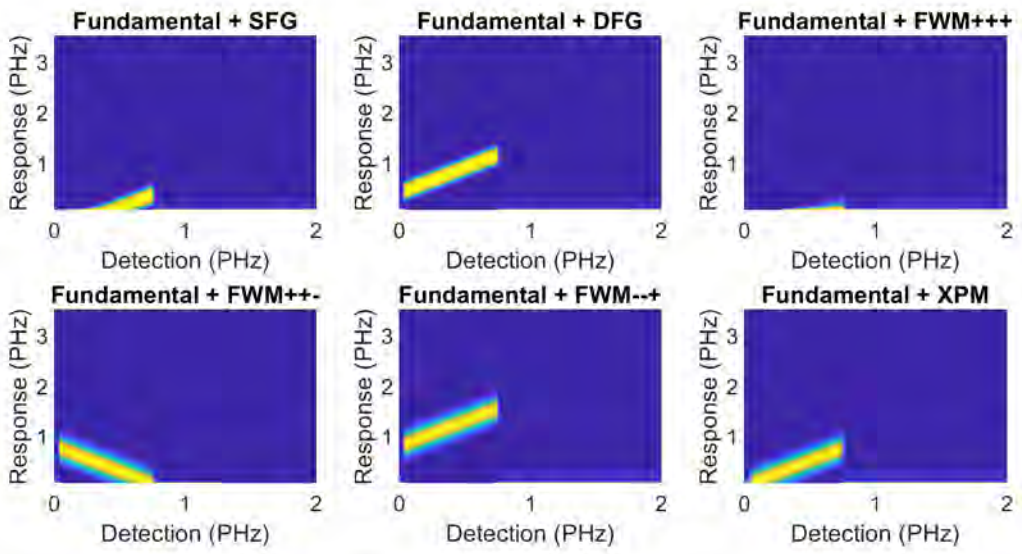

Figure 2.19: Normalized spectral amplitude responses for NOS channels based on a fundamental sampling spectrum as a local oscillator and various heterodyne signals.

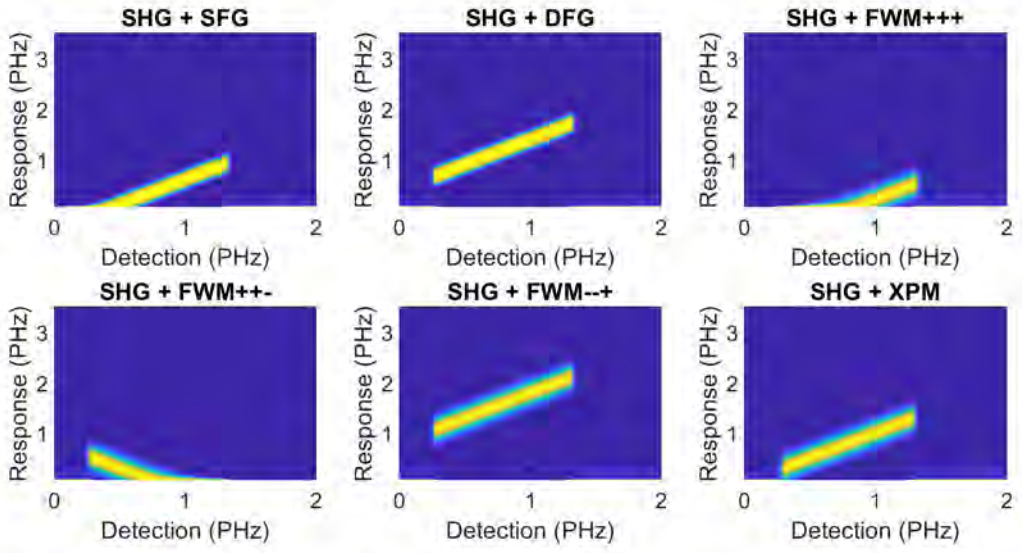

Figure 2.20: Normalized spectral amplitude responses for NOS channels based on a second harmonic from the fundamental sampling spectrum as a local oscillator and various heterodyne signals.

spectral response becomes sampling pulse intensity-dependent, as a ratio of spectral responses of different channels will vary with a field strength of a sampling pulse.

2. The spectral response bandwidth of each channel can be tailored by choosing an

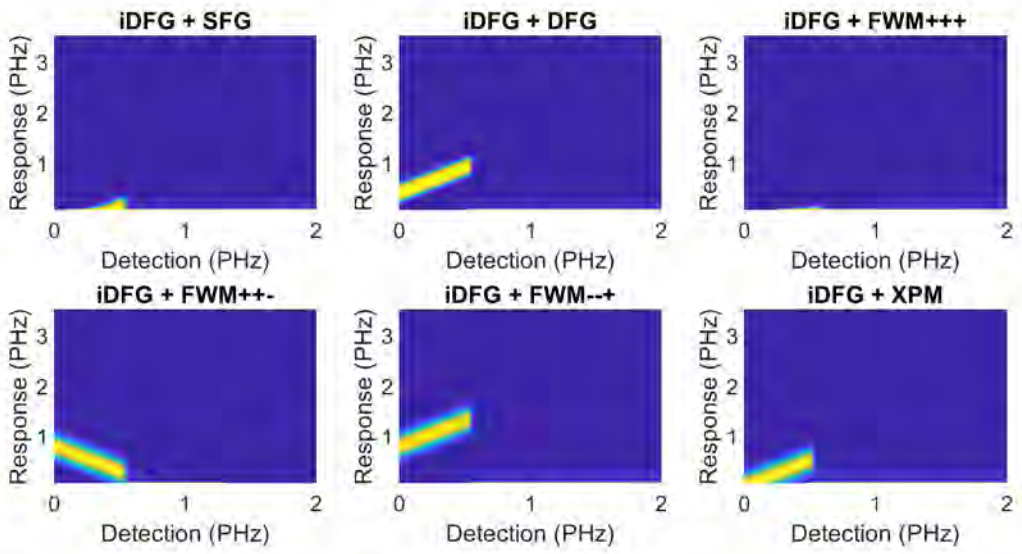

Figure 2.21: Normalized spectral amplitude responses for NOS channels based on intra-pulse difference frequency generation from the fundamental sampling spectrum as a local oscillator and various heterodyne signals.

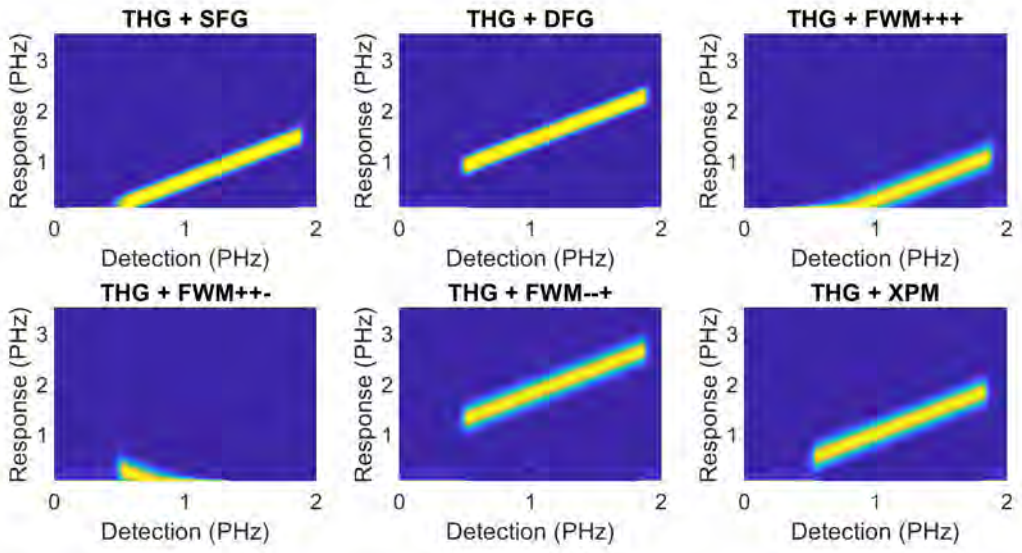

Figure 2.22: Normalized spectral amplitude responses for NOS channels based on a third harmonic of the fundamental sampling spectrum as a local oscillator and various heterodyne signals.

appropriate frequency for detection.

3. The cut-off of a spectral response bandwidth can be much higher than the highest

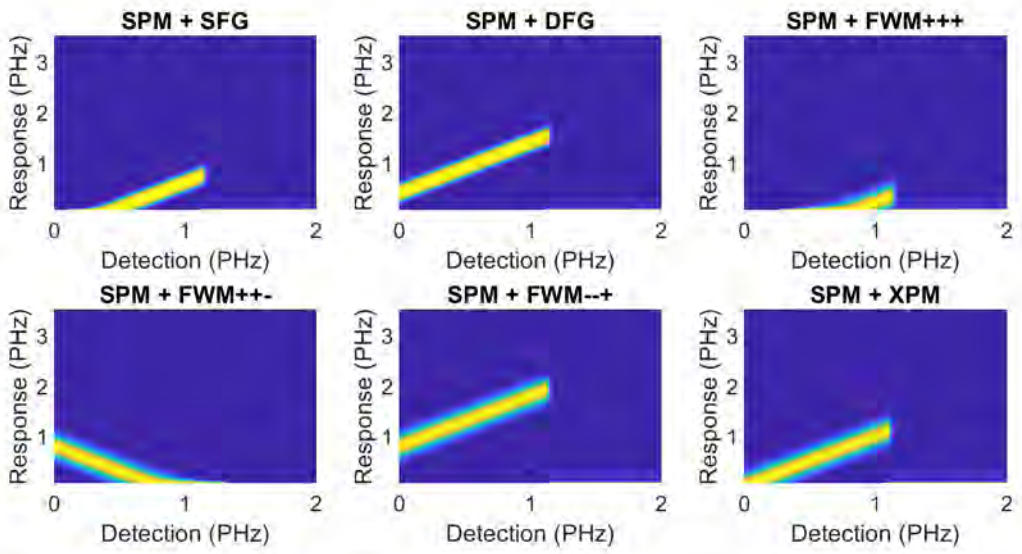

Figure 2.23: Normalized spectral amplitude responses for NOS channels based on a self-phase modulation of the fundamental sampling spectrum as a local oscillator and various heterodyne signals.

frequency of a sampling spectrum. Based on $\chi^{(3)}$ non-linearity only, a sampling pulse with a cut-off frequency of about 0.6 PHz (Fig. 2.18) allows waveform sampling of up to $\sim$ 3 PHz (Fig. 2.22).

4. The role of a local oscillator is to provide a reference for interference with a heterodyne signal. Therefore, the higher is the local oscillator frequency, the higher is a cut-off of a detection bandwidth of the channel. For instance, channels based on THG as a local oscillator allow sampling of higher frequencies comparing to channels based on SHG as a local oscillator.

The simulated phase spectral response for all channels is flat with an offset according to eqs. 2.14 and 2.16.

In the experiment however, all channels will take place simultaneously, therefore the total experimental spectral response will be a sum of spectral responses of all channels. In addition, the ratio of spectral responses, in general, depends on a field strength of the sampling pulse and values of $\chi^{(2)}$ and $\chi^{(3)}$ susceptibilities of a medium, which complicates the extraction of the experimental spectral response. Apart from that, the absorption and dispersion of pulses propagating through a medium with finite thickness will have an influence on a spectral response.

In the following section it will be shown that different channels can be separated from each other in order to obtain a simple experimental spectral response, while propagation effects can be accounted for and do not play a significant role for thin samples.

In summary, the concept of non-linear optical sampling is described. Non-linear effects within a medium can be used to create spectrally extended local oscillator and heterodyne

signals. If a local oscillator and a heterodyne signal occur at the same frequency, the time delay between sampling and test pulses results in a modulation of a spectral intensity at this frequency. This intensity dependence on a time delay contains information about the amplitude and phase of the test pulse, and therefore allows sampling of the test pulse waveform. The concept provides a fully optical method for the detection of optical pulse waveforms with PHz-scale detection bandwidth. Any non-linear medium, such as solids or gases can be used for pulse waveform sampling, as described in detail in the following section 2.2.1 of this thesis. Based on $\chi^{(1)}$, $\chi^{(2)}$ and $\chi^{(3)}$ susceptibilities only, there are about 30 channels that can be used for field sampling. Different channels provided different detection spectral amplitude bandwidths which can be tailored by choosing an appropriate detection frequency. The spectral phase response for the infinitely thin, non-dispersing, and non-absorbing medium is flat, with an offset determined by a CEP of a sampling pulse and the type of NOS channel.

2.2.1 Waveform sampling in solids

Out of all variety of channels, for practical applications, channels with large detection bandwidth, high signal-to-noise ratio, and simple spectral response are of most importance. SHG + FWM, THG + FWM, THG + SFG and THG + DFG channels are most suitable for this purpose.

If detection occurs at multiple channels simultaneously, the spectral response will be combined out of spectral responses of all involved channels, which may complicate the total spectral response of a measurement. The simplest way to reduce the number of involved channels is to use a centrosymmetric medium for detection. In this case, all channels with $\chi^{(2)}$ non-linearities become absent. Since fundamental spectrum and THG as local oscillators are well separated in the spectrum, detection in a bandwidth of a THG spectrum allows choosing channels based on THG as a local oscillator.

On the other hand, when sampling and test pulses have linear light polarizations and orthogonal to each other, polarizations of produced local oscillators and heterodyne signals will depend on the symmetry of a non-linear medium. For instance, z-cut α-quartz crystal has both $\chi^{(2)}$ and $\chi^{(3)}$ non-linearities. Although the $\chi^{(3)}$ non-linearity is essentially crystal rotation independent, the $\chi^{(2)}$ non-linear susceptibility tensor allows not only controlling a magnitude of generated second-order process, but also its polarization. This can be done by a simple rotation of a crystal. A z-cut α-quartz crystal can be positioned such that polarization of the second harmonic of a sampling pulse, which can act as a local oscillator, will be orthogonal to the polarization of a sampling pulse. On the other hand, a polarization of produced FWM between orthogonal sampling and test pulses, will be orthogonal to the sampling pulse. The produced SFG and DFG between sampling and test pulses, at this orientation of the z-cut α-quartz crystal will however be collinear with the sampling pulse. Therefore placing a polarizer after the non-linear medium allows choosing between SHG + FWM and THG + SFG + DFG channels. If the polarizer is collinear with the sampling pulse polarization, the THG + SFG + DFG channel is chosen, while if a polarizer is collinear with the test pulse, the SHG + FWM channel is chosen.

Therefore the centrosymmetric fused silica medium and z-cut α-quartz crystal, combined with a polarizer afterward, allows using THG + FWM, SHG + FWM, and THG + SFG + DFG channels separately.

Although, channels can be separated, a propagation of pulses through a medium with a finite thickness has an influence on the spectral response of the technique. In addition, the reflections at surfaces should also be considered.

Fig. 2.24 shows a typical spectral response simulated with and without propagation through a 10 µm thick z-cut α-quartz crystal and 10 µm thick fused silica glass. The propagation simulation is based on solving Maxwell's equations and described in detail in section A.8 of this thesis.

The formation of spectral responses, is illustrated in Fig. 2.25. When the z-cut α-quartz crystal is positioned such that the sampling pulse generates a second harmonic orthogonal to the fundamental polarization, two types of detection channels are formed, provided that detection occurs at a center of a second harmonic (0.8 PHz). Channel A is based on THG + SFG + DFG (Fig. 2.24b), channel B is based on SHG + FWM (Fig. 2.24c). Channel A is collinear with the test pulse polarization, while channel B is collinear with the sampling pulse polarization. The third channel can be formed in fused silica glass. When two orthogonal, sampling and test pulses are incident on the fused silica medium. The third harmonic from the sampling pulse will have a polarization of the sampling pulse. The FWM process between sampling and test pulses will, however, have a polarization of the test pulse. Placing a polarizer at 45 degrees with respect to both polarizations, projects THG local oscillator, as well as FWM heterodyne signal on one plane, and thus forms channel C based on THG + FWM interference (Fig. 2.24d). Fig. 2.25a shows spectral responses based on SFG and DFG as heterodyne signals and THG as a local oscillator (channel A), Fig. 2.25b, shows spectral responses based on FWM as heterodyne signals and SHG as a local oscillator (channel B), while Fig. 2.25c, shows spectral responses based on FWM as a heterodyne signal and THG as a local oscillator (channel C).

Since SFG and DFG processes, as well as, FWM processes occur simultaneously, the simulated spectral responses for fused silica and quartz (Fig. 2.24) consist of combined responses.

Propagation of optical pulses through a finite thickness medium causes a deviation of a spectral response comparing to the case when neither propagation nor reflections at surfaces are considered. Reflection at surfaces causes back-propagating pulses to be present in a medium together with incident pulses. At the same time, since a refractive index is wavelength dependent, the interaction of incident pulses with a front surface of a medium, causes reshaping of penetrating pulses with respect to incident pulses. Dispersion of a medium, causes a phase mismatch between propagating frequencies. Since quartz and fused silica media are not optimized for phase-matching conditions, a detection signal will originate from regions in a medium, within a coherence length. Since shorter wavelengths have smaller coherence lengths, propagation through a 10 µm fused silica or quartz medium causes reshaping of the spectral response favouring longer wavelengths. The spectral response for frequencies above 1 PHz consists of spectral fringes since coherence lengths of these frequencies are smaller than the thickness of the crystal, therefore the build-up of

non-linear generation of a heterodyne signal occurs at discrete points within the medium. A small coherence length at these frequencies also causes reduction of spectral amplitude responses, as the coherent signal does not continuously builds-up during the propagation. As can also be seen in figs. 2.24) and 2.25, the SHG + FWM and THG + FWM provide almost identical spectral responses since local oscillators (SHG and THG) only serve as a reference for the detection. However, for practical applications the SHG + FWM channel might be more favourable, since a spectral intensity of SHG can be orders of magnitude larger than a spectral intensity of THG.

When sampling and test pulses with finite spectral bandwidths take part in SFG, DFG, and FWM processes, the result is a generation of multiple new frequencies. Since simulations presented in Fig. 2.24 and 2.25 were performed by monitoring a delay-dependent change of a spectral intensity at *one* frequency only, only certain frequency out of SFG, DFG, and FWM bandwidth can be detected. This results in the formation of 'holes' and determines the shape of spectral response. Detection at frequencies different from 0.8 PHz results in reshaping of a spectral response (Fig. 2.26). For spectral responses based on DFG, SFG FWM–+ and FWM-++ heterodyne signals, increase of the detection frequency *does not* result in reshaping of the spectral response, but blue-shifting of it. On the other hand, a decrease of the detection frequency results in the red-shifting of the spectral response. Therefore the spectral response can be tailored for a particular application, simply by choosing an appropriate detection frequency. The detection based on FWM++- heterodyne signal, however, experiences a reverse dependence. The spectral response of the FWM++- channel blue-shifts as the detection frequency decreases, and red-shifts as the detection frequency increases. Figs. 2.26b-c show that when the detection frequency is increased, spectral responses from FWM++- and FWM-++ become more separated in the spectrum, and therefore form a larger hole in a total spectral response. On the other hand, when the detection frequency is decreased, spectral responses from FWM++- and FWM-++ merge more, and therefore the hole in the spectral response decreases. Hence by choosing an appropriate detection frequency one can also create a more smooth and flat overall spectral response.

The bandwidth of the spectral response is directly related to the bandwidth of the sampling pulse (Fig. 2.27). For narrow-bandwidth sampling pulses the overall spectral response is *not continuous* and consists of discrete bands. However, as the sampling bandwidth is increased, discrete bands become broader and merge, therefore providing a *continuous* spectral response covering a multi-PHz frequency range.

The delay (τ) dependent term of the eq. 2.14 allows detection of a test pulse waveform, where the strength of the detected signal is proportional to a square of LO and HS intensities ($\sqrt{I_{LO}I_{HS}}$). Since local oscillators and heterodyne signals in different channels are based on various non-linear processes, a strength of the experimentally measured signal is supposed to scale differently with field strengths of sampling and test pulses. If a local oscillator originates from a $\chi^{(2)}$ non-linearity, then the field strength of LO is proportional to E_S^2. If a heterodyne signal originates from a $\chi^{(2)}$ non-linearity, such as SFG or DFG, then HS is proportional to $E_S E_T$. Since the interfering term is proportional to a product of E_{LO} and E_{HS}, measured signal with SHG + SFG channels is expected to linearly scale

with a test field strength and to be proportional to E_S^3. Table 2.1 summarizes expected field strength dependencies for several NOS channels.

LO	HS	Scaling	Lower BW limit	Higher BW limit	$\Delta\phi_{\mathrm{CE}}$
SHG	SFG	$E_{\mathrm{T}}E_{\mathrm{S}}^3$	$\omega - \frac{3}{2}\Delta_\omega$	$\omega + \frac{3}{2}\Delta_\omega$	$-\phi_{\mathrm{S}}$
SHG	DFG	$E_{\mathrm{T}}E_{\mathrm{S}}^3$	$3\omega - \frac{3}{2}\Delta_\omega$	$3\omega + \frac{3}{2}\Delta_\omega$	ϕ_{S}
THG	SFG	$E_{\mathrm{T}}E_{\mathrm{S}}^4$	$2\omega - 2\Delta_\omega$	$2\omega + 2\Delta_\omega$	$-2\phi_{\mathrm{S}}$
THG	DFG	$E_{\mathrm{T}}E_{\mathrm{S}}^4$	$4\omega - 2\Delta_\omega$	$4\omega + 2\Delta_\omega$	$4\phi_{\mathrm{S}}$
SHG	FWM+, FWM-	$E_{\mathrm{T}}E_{\mathrm{S}}^4$	0	$2\Delta_\omega$	0
THG	FWM+	$E_{\mathrm{T}}E_{\mathrm{S}}^5$	$\omega - \frac{5}{2}\Delta_\omega$	$\omega + \frac{5}{2}\Delta_\omega$	$-\phi_{\mathrm{S}}$
THG	FWM-	$E_{\mathrm{T}}E_{\mathrm{S}}^5$	$5\omega - \frac{5}{2}\Delta_\omega$	$5\omega + \frac{5}{2}\Delta_\omega$	$5\phi_{\mathrm{S}}$
THG	XPM	$E_{\mathrm{T}}E_{\mathrm{S}}^5$	$3\omega - \frac{5}{2}\Delta_\omega$	$3\omega + \frac{5}{2}\Delta_\omega$	$-3\phi_{\mathrm{S}}$

Table 2.1: Summary of field strength and CEP dependencies based on second and third harmonic of the sampling pulse as the local oscillator. ω is the central angular frequency of the sampling pulse. Δ_ω is the bandwidth of the sampling pulse. $\Delta\phi_{\mathrm{CE}}$ is the shift of the CEP of the measured waveform relative to the actual electric field, which depends on the CEP of the sampling pulse, ϕ_{S}.

Since the measured signal is linearly proportional to complex test field E_T for all channels in the table 2.1, the test pulse spectral phase information is preserved in the detection. The local oscillator spectral phase serves as a reference for the detected spectral phase of the test pulse. Since the order of a non-linear process translates into a multiplication factor for a spectral phase, some channels experience an offset in spectral phase response. In general, spectral phase offset is determined by $\Delta\phi_{CE} = \left[N_{(LO)} - N_{(HS)}\right]\phi_S$, where $N_{(LO)}$ and $N_{(HS)}$ are orders of a non-linear processes responsible for LO and HS generation. Channels, where LO and HS originate from *different* non-linear order, $\Delta\phi_{CE} = 0$, therefore a spectral response of a spectral phase does not require information about CEP of the sampling pulse. Channels, where LO and HS originate from *the same* non-linear orders, on the other hand, require information about the CEP of the sampling pulse, in order to know an absolute test spectral phase. Table 2.1 summarizes spectral phase offsets for several channels. Although spectral responses of SHG + FWM and THG + FWM channels are practically identical, the SHG + FWM has an advantage that the CEP of the sampling pulse is not required to be known for the test field sampling, while THG + FWM channel does (table 2.1).

So far a spectral response of the NOS technique was based on an assumption that the sampling pulse is Fourier transform-limited, that is has a flat spectral phase. Experimental pulses, however, do not have a perfectly flat spectral phase. In order to experimentally demonstrate the NOS metrology concept, spectral phases of the sampling pulse were characterized with polarization gating FROG technique[38] (Fig. 2.28) technique.

As shown on Fig. 2.26, the spectral response of the detection depends on the detection frequency. In order to get a more accurate experimental spectral response of the detection, as well as to perform simulations close to experimental conditions, the spectral sensitivity of

the photodiode, as well as transmission of a bandpass filter used in experiments, were taken into account (Fig. 2.29). The photodiode spectral sensitivity was provided by ALPHALAS GmBH, while the filter transmission measurement was provided by Amelie Schulte.

Fig. 2.8 shows measured and simulated NOS detection of an ultrashort optical pulse obtained as described in section A.1 of the thesis. The detection medium was 12.344 ± 0.002 µm thick z-cut α-quartz crystal (section A.6). The simulation was performed based on a model described in section A.8. During the measurement, the quartz crystal was oriented such that a generated second harmonic polarization was perpendicular to the sampling pulse polarization, while the polarization of the sum-frequency generation was collinear with the sampling pulse polarization. After the quartz crystal, a broadband wire-grid polarizer was installed at orientation which transmits a polarization of the sampling pulse, therefore transmitting the THG, DFG, and SFG light. The wire-grid polarizer was followed by a photodiode for detection. The signal from the photodiode was feed into a lock-in amplifier (Stanford Instruments) triggered by a half-repetition rate of a laser beamline ($\sim$1.5 KHz). During the measurement, the CEP of every second pulse from the laser beamline was shifted by π, therefore providing a detectable signal at $\sim$1.5 KHz.

Good agreement between measured and simulated results confirms the validity of the model and provides an opportunity to extract an experimental spectral response of the THG + SFG + DFG channel. To extract the experimental spectral response, the sampling pulse was kept the same as for the simulation presented on Fig. 2.30, while the test pulse was chosen to be a broadband theoretical, with a flat spectral phase and CEP 0.

In order to experimentally benchmark the model and the spectral response of the THG + SFG + DFG channel, the waveform of the broadband optical pulse was sampled with NOS techniques based on THG + SFG + DFG channel as well as with established[3] NPS technique. Since NPS also has a certain spectral response function, experimental spectral responses of both, NPS and NOS were extracted from the measured spectrum and FROG phase information. Fig. 2.31 shows experimental spectral responses of NPS and NOS techniques for results of the experiment presented on Fig. 2.32. The spectral responses were calculated for CEP 0 sampling pulse. In the experiment, the CEP of both pulses was set to 0 with a solid-state light-phase detector method[89].

The extracted spectral responses were applied to the recorded NPS and NOS traces. Fig. 2.32 shows benchmarking of the pulse waveform performed with NPS, NOS, and a calibrated grating spectrometer.

Since NOS, provides a linear detection of the test pulse waveform, the THG + SFG + DFG channel is expected to scale linearly with a field strength of the test pulse. On the other hand, since the sampling pulse is responsible for the generation of the local oscillator (THG) as well as partially responsible for SFG or DFG heterodyne signal, an entire measured signal is expected to scale with the 4th order of the sampling pulse field strength (table 2.1).

Fig. 2.33a,b shows scaling of the measured signal as a function of field strength of sampling and test pulses. Excellent agreement with exponential power-law fitting confirms the validity of expected field strength dependencies.

Fig. 2.33c shows a typical SNR of the NOS measurement based on THG + SFG

channel using a very small lock-in time constant of 10 ms only. Since the measurement was performed at a half of the repetition rate of the laser (1.5 KHz), there are only about 15 optical pulses considered within 10 ms. This demonstrates an enormous sensitivity of the technique.

Non-linear photo-conductive sampling (section 2.1), relies on non-linear excitation of carriers from the valence to the conduction band. Since the temporal shape of such excitation depends on a waveform of the sampling pulse, the spectral response of the NPS technique is very CEP dependent. However NOS approach, does not rely on long-lasting modification of medium properties, therefore the spectral amplitude response is expected to be insensitive to the CEP of the incident sampling pulse. Fig. 2.34a shows dependence of measured spectral amplitudes on the CEP of interacting pulse, which agrees well with the theory. The CEP of incident pulses was varied with 'Stage II CEP stabilization' described in section A.1 of this thesis. The change of the CEP was applied to both, sampling and test pulses. Fig. 2.34c shows how does the measured time delay signal changes when a CEP of *both*, sampling and test, pulses are changed by the same amount. This again agrees with the theory (table 2.1).

Fig. 2.35 shows extracted experimental spectral response of THG + SFG + DFG channel.

As can be seen on Fig. 2.35, the spectral response of THG + SFG + DFG channel extends to PHz frequencies. The low-frequency part of the spectral response is based on a heterodyne detection of THG + SFG, while the high-frequency part of the spectral response is based on THG + DFG heterodyne detection. In order to demonstrate that THG + DFG heterodyne channel can be used for the detection of PHz frequencies, the test pulse arm was spectrally broadened as described in section A.2.4.

If the test pulse spectrum consists of frequency components in the bandwidth of the local oscillator, apart from the heterodyne detection, there will be a modulation of light intensity due to linear interference between a local oscillator and a test pulse spectrum. This modulation of intensity will vary with the time delay between sampling and test pulses and therefore will produce an additional detected signal which will not carry information about a test pulse waveform and therefore will act as background noise. However, when the polarizer is placed after the NOS crystal, such that it blocks any light polarized in a plane of the test pulse, the fundamental test pulse spectrum will be blocked and therefore will not reach a photodiode, hence preventing the linear interference signal.

Fig. 2.36 shows experimental results obtained with a sampling pulse similar to the one used for results on Fig. 2.30, but with the test pulse broadened to PHz frequencies. The typical spectral response of the THG + SFG + DFG channel (Fig. 2.35) can be seen as 3 spectral regions. From 0.2 to 0.6 PHz, the spectral response originates from a heterodyne detection of THG + SFG channel. In the region from 0.6 to 1.1 PHz the response is negligibly small, since SFG with these frequencies does not produce a heterodyne signal at the frequency of the local oscillator. The region from 1.1 to 1.5 PHz originates from a heterodyne detection of THG + DFG channel. The experimental spectrum of the test pulse (Fig. 2.36b) covers all three regions, and therefore the predicted spectral response of THG + SFG + DFG channel can be experientially tested. Fig. 2.36a shows the time-domain

signal experimentally recorded with THG + SFG + DFG channel in 12.344 ± 0.002 µm thick z-cut α-quartz crystal. Fig. 2.36b (orange curve) is an absolute spectral intensity of the time-domain signal. The NOS spectrum consists of three regions in accordance with the spectral response of the THG + SFG + DFG channel. From about 0.2 to about 0.6 PHz the measured NOS spectrum is due to THG + SFG heterodyne detection. The region between 0.6 and 1.1 PHz does not consist of a measured NOS signal, although the actual test pulse spectrum has spectral components in this spectral region. This is again in accordance with the typical spectral response of the THG + SFG + DFG channel. In the region between 1.1 and 1.4 PHz, both, spectrometer and measured NOS signal have corresponding spectral components. The inset shows a zoomed-in 1.15-1.35 PHz spectral region. A grating spectrometer signal as well as the NOS signal in a good agreement. Experimental results presented in Fig. 2.36 are in a good agreement with expected spectral response of THG + SFG + DFG channel, and therefore provide an experimental demonstration that this channel can be used for detection of PHz-scale frequencies.

The ideal NOS condition requires a test pulse field strength to be infinitely smaller than a sampling field strength. In a realistic case, however, a test pulse field strength is never infinitely small. Fig. 2.37 shows measured NOS traces for several ratios of sampling and test pulse field strengths. Sampling and test pulses in the measurement originated from CPA amplified and HCF broadened pulses from Ti:Sa based oscillator (section A.1). For measurements with a quartz crystal, a polarizer was placed collinearly to the sampling pulse polarization for THG + SFG + DFG channel. The quartz crystal was oriented such that a second harmonic from a sampling pulse had a perpendicular polarization.

Fig. 2.37 shows that as a ratio between sampling and test pulses increases, the residual artefacts of the detection reduce and become negligible small when a ratio approaches 10. Fig. 2.37b,c, however also show that when the detection is performed with a CEP alternation scheme, the residual artefacts are removed, because second-order non-linear effects are identical for CEP 0 and CEP pi incident pulses. Since in THG + SFG + DFG and SHG + FWM channels, heterodyne signal and a local oscillator originate from different non-linear orders, SFG and SHG are identical for CEP 0 and CEP π pulses, while THG and FWM provide π shifted waveforms for CEP 0 and CEP π incident sampling pulse. Hence in THG + SFG + DFG channel, the HS signal acts as stationary, while LO is flipped and the difference between flipped and non-flipped cases is measured. In SHG + FWM channel, on the other hand, the local oscillator is stationary while FWM is flipped and the difference between flipped and non-flipped cases is measured. Apart from the subtraction of residual artefacts, the CEP alternation scheme also provides about 2 times stronger signal.

In summary, the non-linear optical (NOS) concept was introduced. The non-linear term refers to non-linearly generated local oscillators, in contrast to conventional electro-optic sampling where the local oscillator originates from the fundamental spectrum of the sampling pulse. Various channels of NOS can be used for optical pulse field sampling. Three channels were described in details: THG + SFG + DFG, SHG + FWM, THG + FWM. Spectral responses of channels can be easily determined based on characterization of the sampling pulse with a spectrometer and FROG. THG + SFG + DFG channel was

analysed experimentally and benchmarked against conventional tools such as non-linear photo-conductive sampling and a grating spectrometer. The NOS detection provides a spectral response that can be tailored for a required application, simply by choosing an appropriate detection frequency. Detection of up to about 1.3 PHz frequency was demonstrated experimentally. The trigonal symmetry of the quartz medium allows sampling of a pulse waveform without π-ambiguity. Since the concept relies on perturbative non-linearities of a medium, any type of a medium that exhibit such non-linearities (solids or gas) can be used for pulse waveform sampling. These techniques present new opportunities for highly sensitive[110], time-resolved spectroscopy and field-resolved attosecond science with new wavelength ranges and systems.

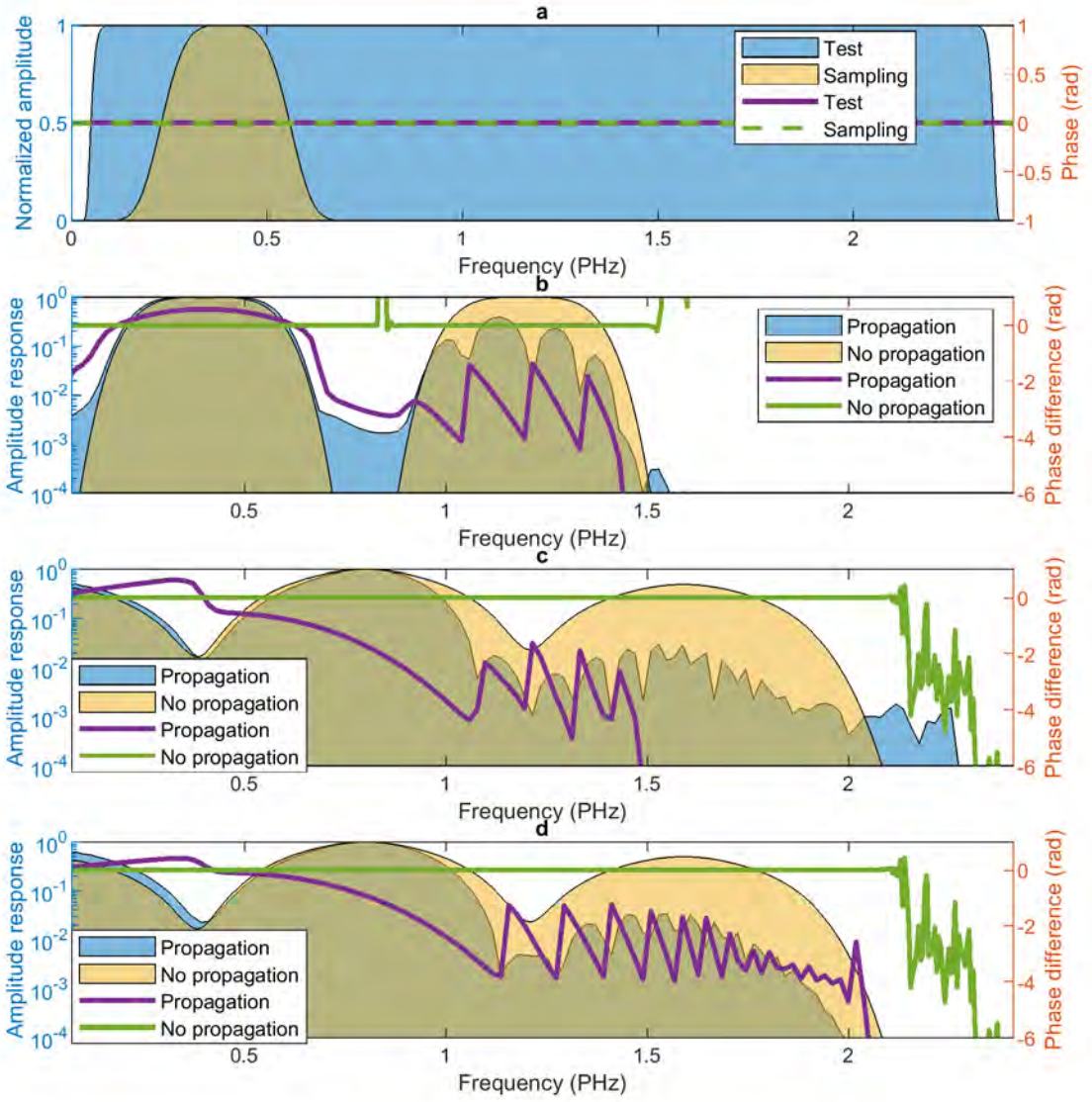

Figure 2.24: (**a**) Fourier representation of orthogonally polarized sampling and test pulses used for simulations. (**b**) and (**c**) are simulated spectral responses in a 10 µm thick z-cut α-quartz crystal oriented such that a second harmonic from the sampling pulse is orthogonal to the sampling polarization. (**b**) corresponds to the detection along with a polarization of the sampling pulse, while (**c**) corresponds to the detection along with a polarization of the test pulse. (**d**) simulated spectral response of 10 µm thick fused silica medium, followed by a polarizer at 45 degrees with respect to sampling and test polarizations. Filled areas depict normalized spectral amplitude responses, while solid lines depict spectral phase differences. The detection frequency was set to 0.8 PHz (center of the second harmonic of the sampling pulse).

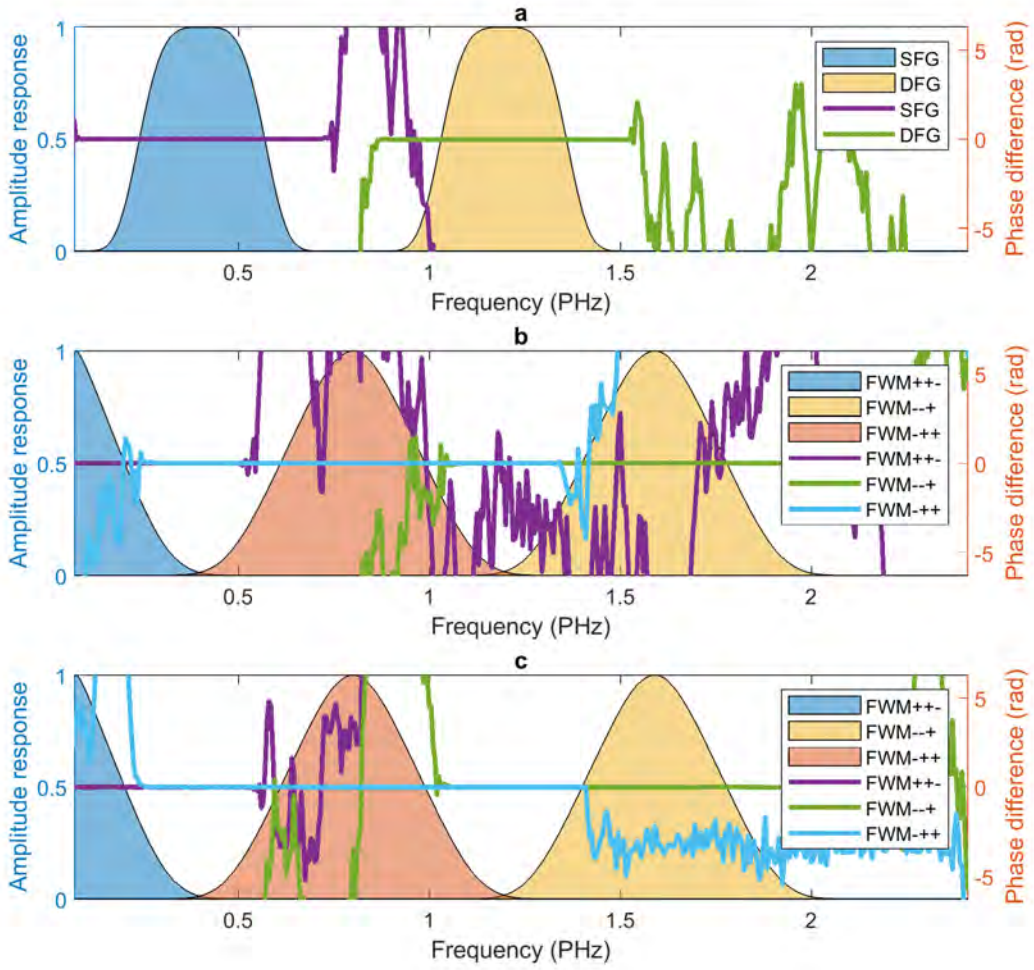

Figure 2.25: Normalized simulated spectral responses based on THG + SFG and THG + DFG channels (**a**), SHG + FWM channel (**b**), as well as THG + FWM channel (**c**). Filled areas depict normalized spectral amplitude responses, while solid lines spectral phase differences. The detection frequency was set to 0.8 PHz (center of a second harmonic of the sampling pulse).

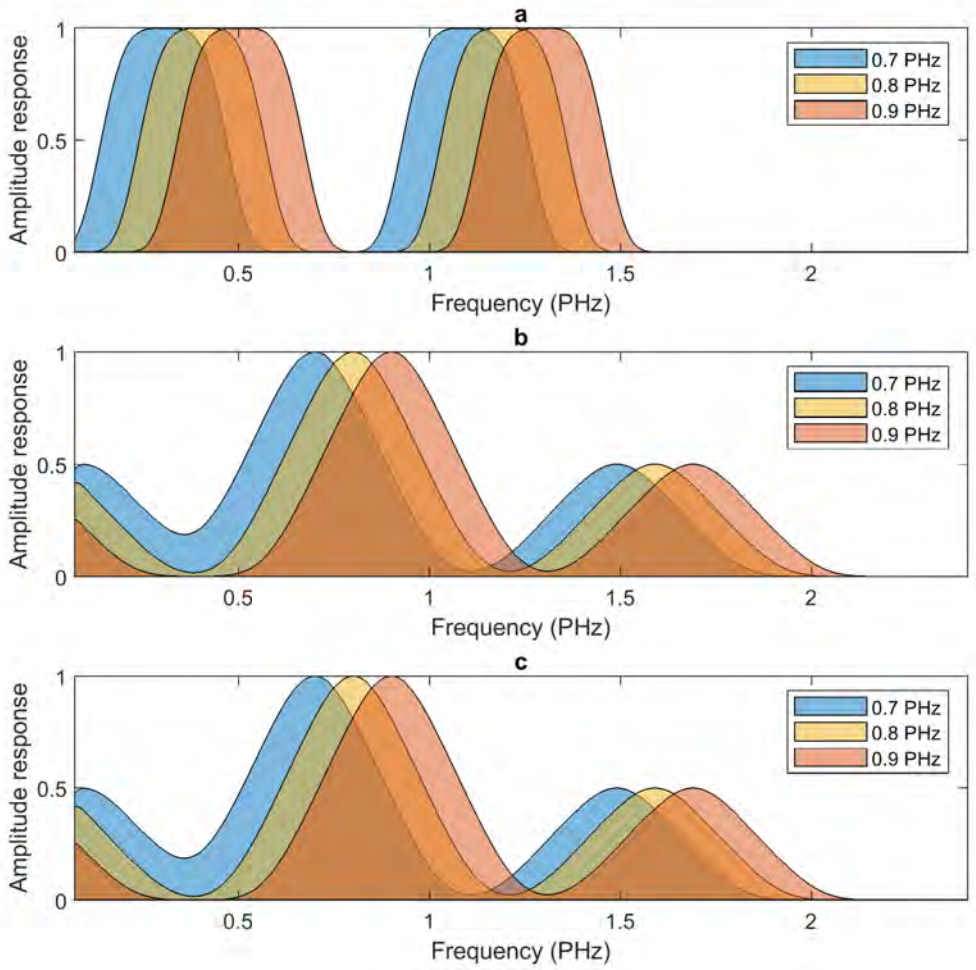

Figure 2.26: Spectral response dependence on the detection frequency for THG + SFG + DFG channel (**a**), SHG + FWM channel (**b**) and THG + FWM channel (**c**).

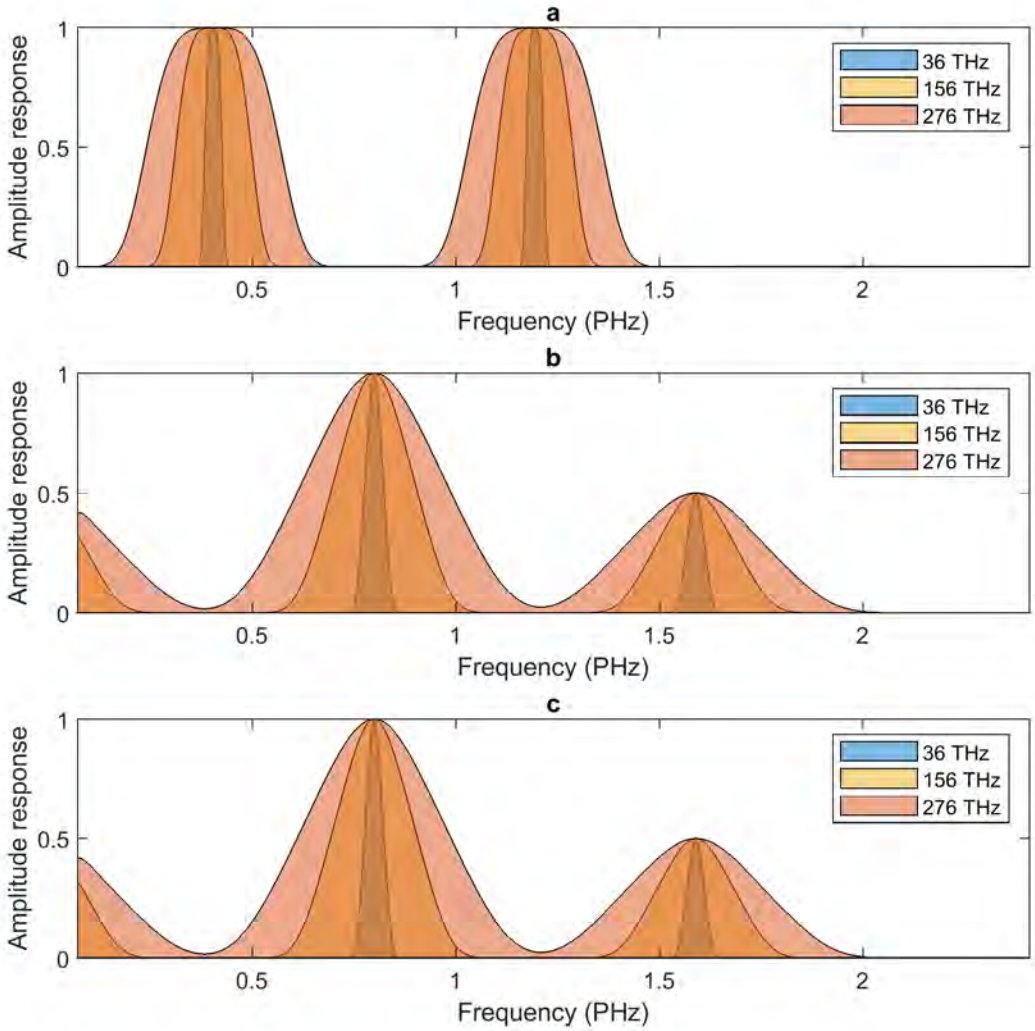

Figure 2.27: Spectral response dependence on the sampling pulse frequency bandwidth for THG + SFG + DFG channel (**a**), SHG + FWM channel (**b**) and THG + FWM channel (**c**).

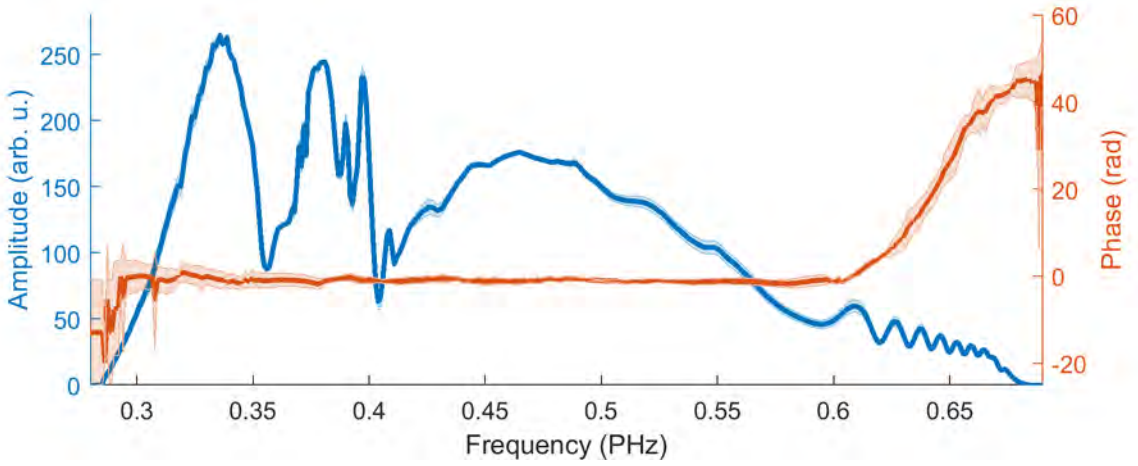

Figure 2.28: Characterization of the optical pulse used to produce sampling and test pulses for NOS detection. The constant offset of the phase was manually set, since the FROG technique does not provide information about the CEP of a pulse.

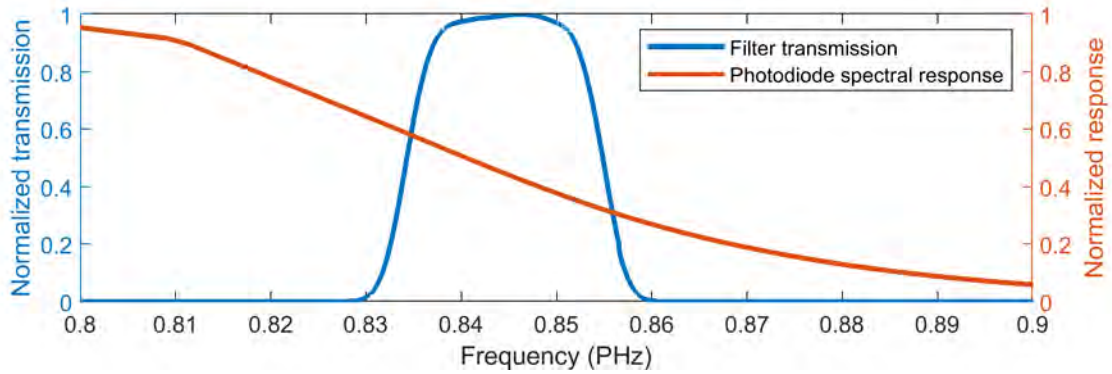

Figure 2.29: Photo-diode spectral response as well as a measured transmission of the bandpass filter used in the experiment.

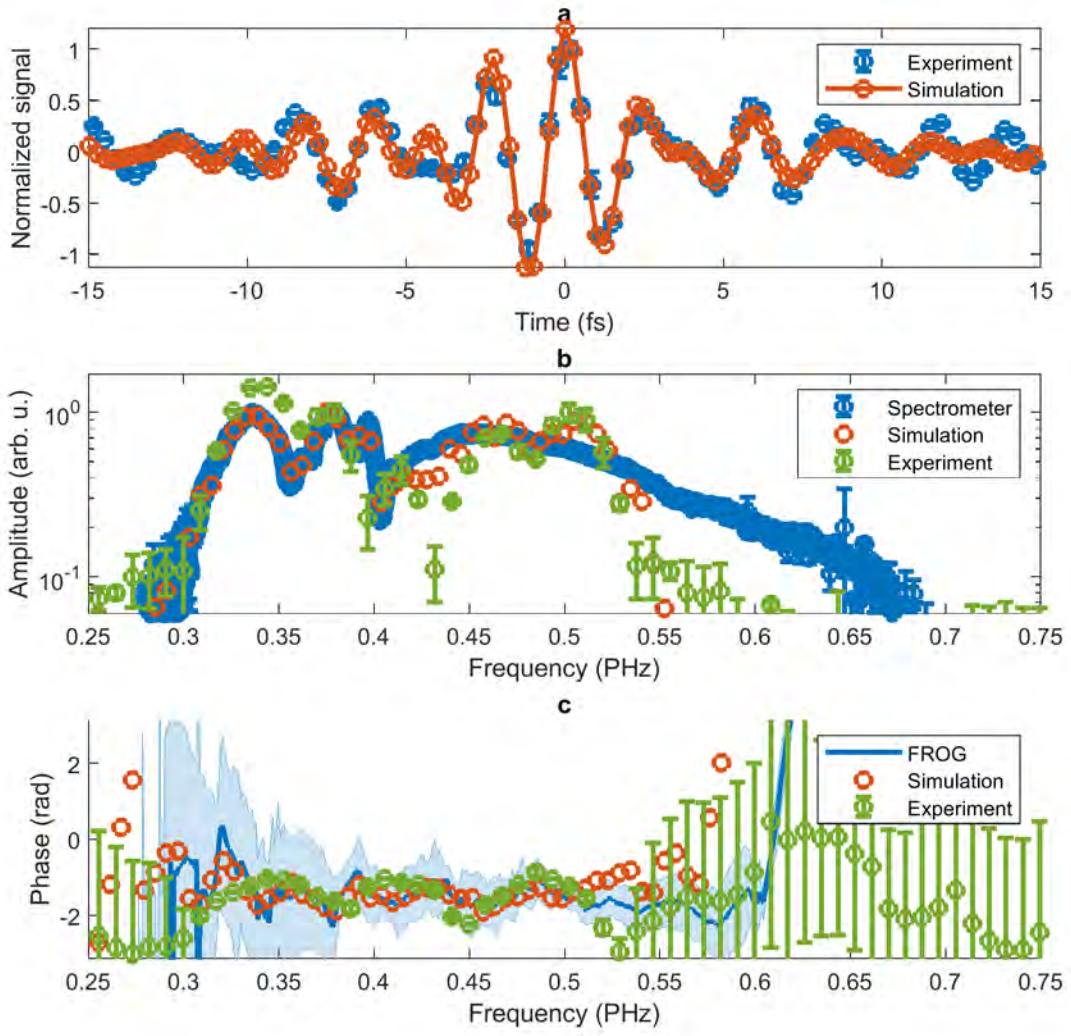

Figure 2.30: (**a**) Measured and simulated pulse waveforms based on heterodyne detection with THG + SFG channel. (**b**) measured and simulated spectral amplitudes together with the test pulse spectrum measured with a grating spectrometer. (**c**) Measured and simulated spectral phases together with a spectral phase recorded with a polarization gating FROG. Since FROG measurement does not provide the CEP information, the DC offset of spectral phases was manually set to the level of the measurement and the simulation.

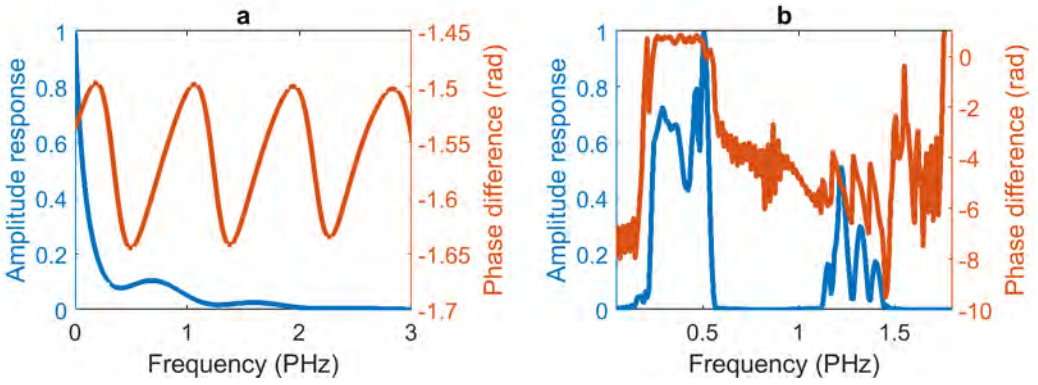

Figure 2.31: Experimental spectral responses for NPS (**a**) and NOS (**b**) calculated based on the sampling pulse spectrum (measured with a spectrometer) and the phase information extracted from the FROG measurement. The spectral response of NPS was obtained as described in section 2.1.

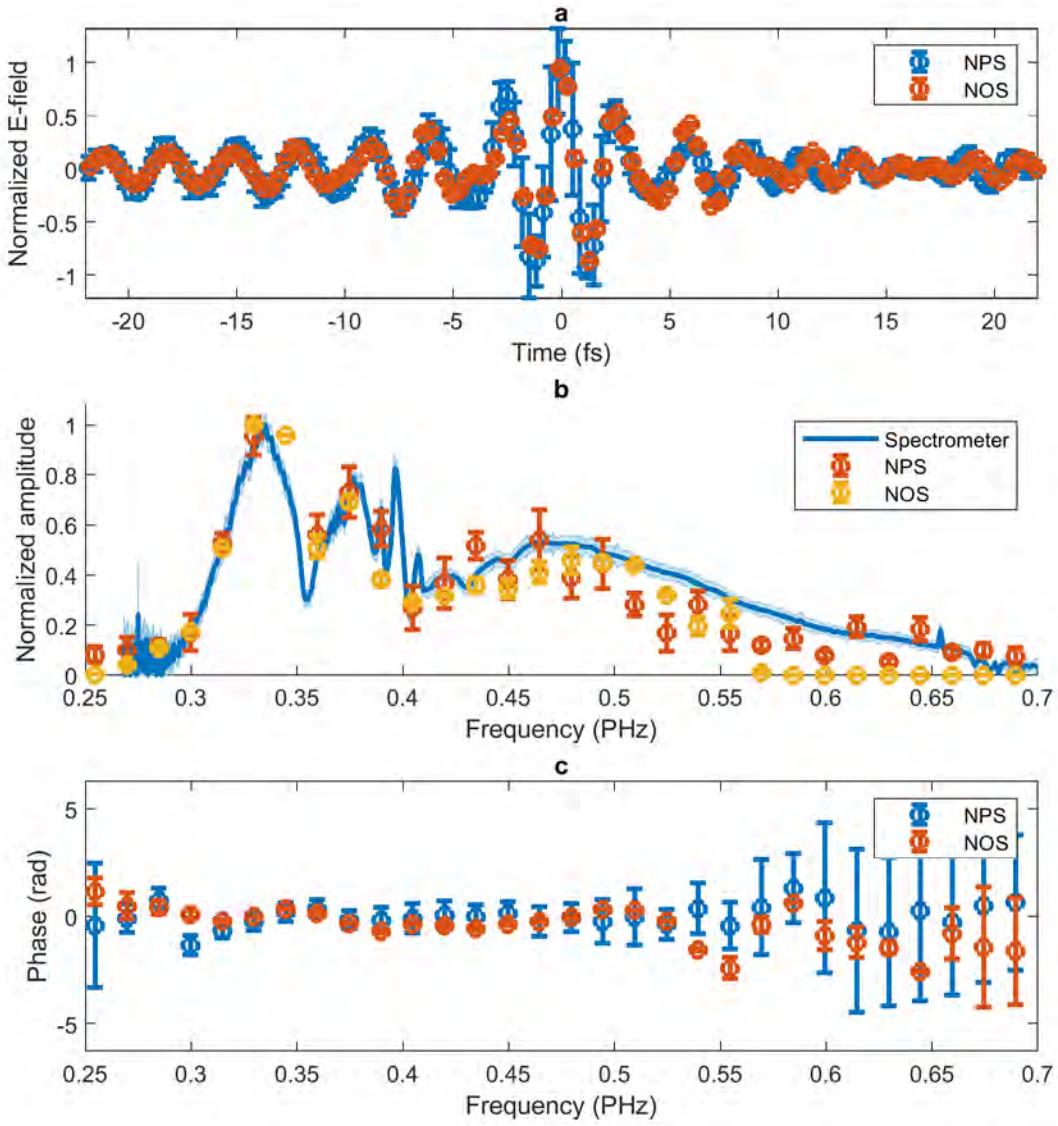

Figure 2.32: (**a**) Measured pulse waveform with NPS and NOS techniques. (**b**) Pulse waveform spectral amplitudes measured with a grading spectrometer as well as obtained by a Fourier transformation of recorded pulse waveforms. (**c**) Spectral phases of measured waveforms obtained by a Fourier transformation.

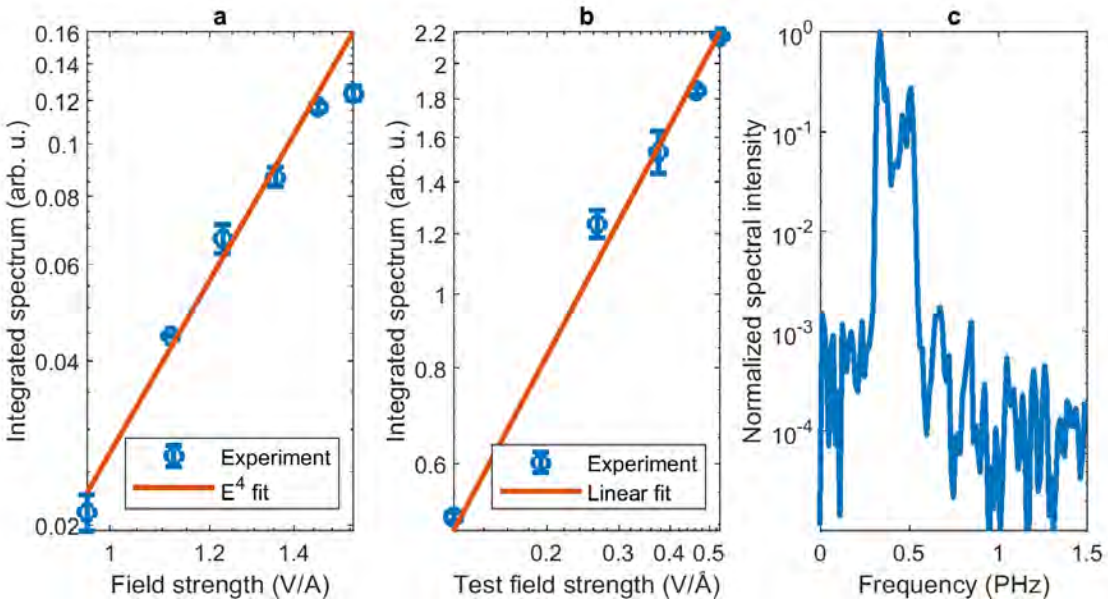

Figure 2.33: Scaling of the measured signal with field strengths of sampling (**a**) and test (**b**) pulses. (**c**) Typical SNR experimentally obtained with THG + SFG channel with 1.14 V/Å sampling field strength and 0.17 V/Å field strength of the test pulse. The data was acquired with 10 ms time constant of a lock-in amplifier, and is an average of 3 single scans.

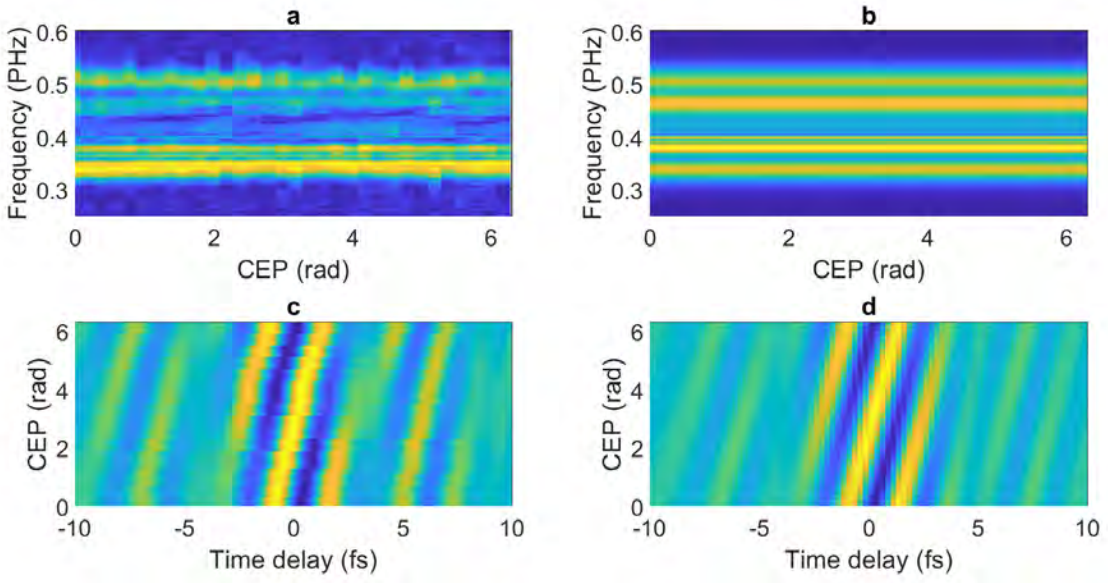

Figure 2.34: Experimental (**a**) and theoretical (**b**) dependence of recorded spectral amplitudes on a CEP of incident pulses. Experimental (**c**) and theoretical (**d**) dependence of a measured time delay signal on a CEP of both pulses.

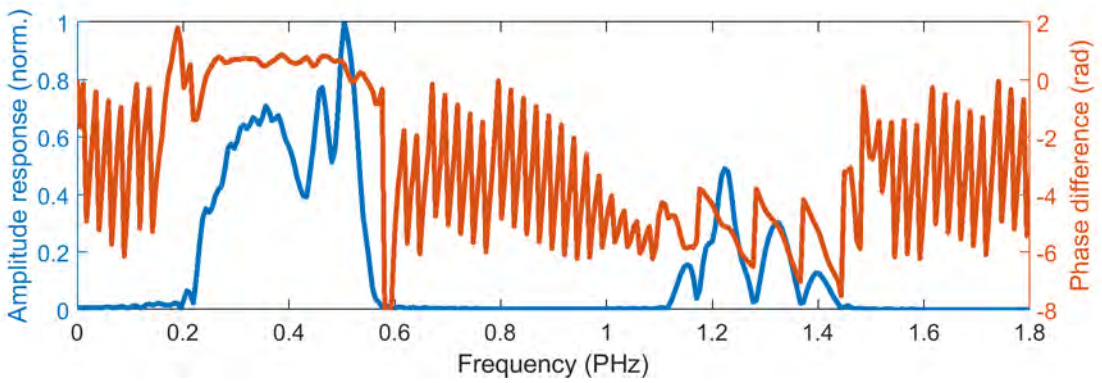

Figure 2.35: Experimental spectral response used for results in Fig. 2.30 simulated based on the characterized sampling pulse.

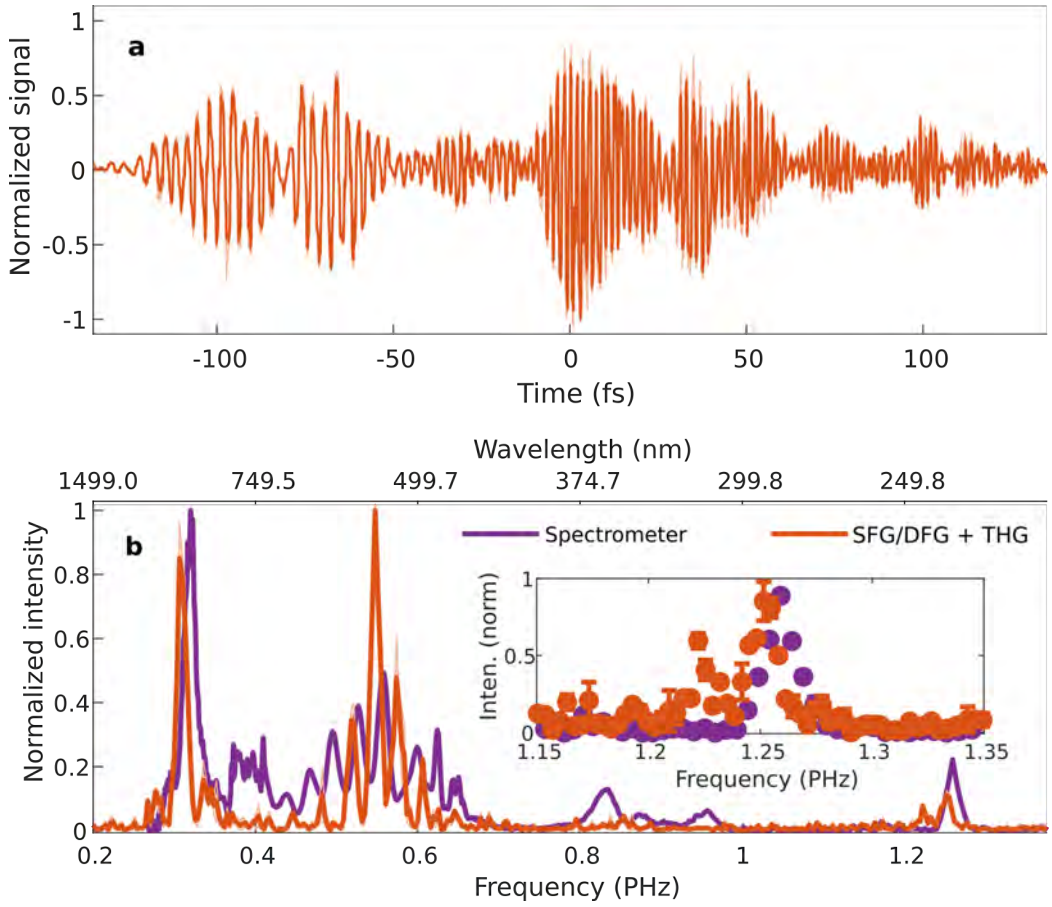

Figure 2.36: (**a**) The detected waveform contains a rapid ultraviolet oscillation, preceded by lower-frequency residual light (detected through the SFG+THG channel). (**b**) Obtaining spectral intensities via Fourier transformation allows for comparison vs. the spectrum measured by a grating spectrometer. The shaded area shows a confidence interval of one standard deviation. Adopted from [5].

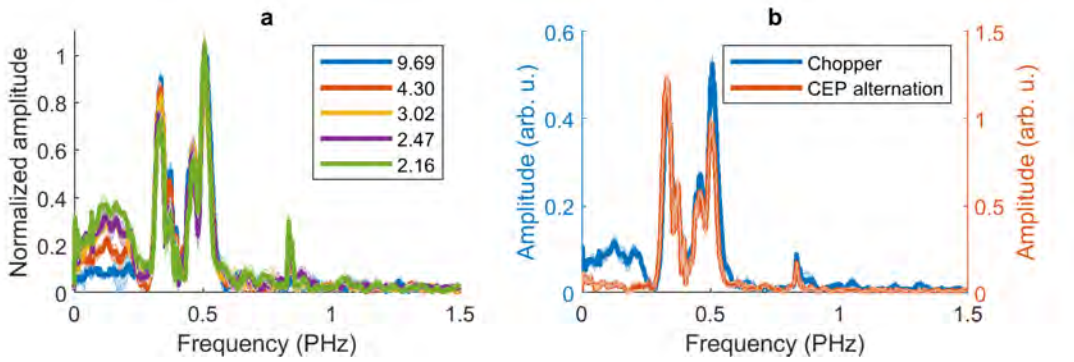

Figure 2.37: (**a**) Amplitude spectrum of measured signals for several ratios between sampling and test pulse field strengths. (**b**) Comparison of measured spectral amplitudes recorded with a CEP-alternation and mechanical chopper methods.

2.2.2 Pulse characterization with CEP-unstabilized transients

As described in section 2.2 of this thesis, non-linear optical sampling can be performed via various channels. If the channel is provided by the interference of a local oscillator and a signal originated from the same non-linear order, the time-delay measurement with unstable CEP pules will still provide a non-zero measured signal, if the source of CEP instability is the same in both, sampling and test pulses. The same source of CEP instability is a common phenomenon, when for instance one pulse is split into two arms for the pump-probe type of measurements, and therefore instabilities of the original pulse will be applied equally to both arms.

Such waveform sampling measurement can not be performed with a conventional electro-optic sampling technique, as the local oscillator (fundamental spectrum) and the signal (sum-frequency) do not originate from the same non-linearity order. Therefore the conventional electo-optic sampling based on the interference of the fundamental spectrum and a sum-frequency, can only be performed if at least the test pulse has a stabilized CEP.

The appearance of a stable waveform when measuring unstable electric fields can be understood through a detailed look at the measurement process. It emerges that the CEP of the test waveform, and the fluctuations it contains, is cancelled in the measurement through an equal and opposite contribution of the CEP of the sampling pulse. The quantity that remains is a stable waveform containing similar information to what one would obtain from a traditional pulse measurement technique but measured in a way that allows sensitivity enhancement methods from field sampling and without further post-processing with an iterative algorithm.

The relationship between the measured signal in the case of the SHG+SFG GHOST and the actual electric field can be described as follows. The SHG and SFG fields, $\tilde{E}_{\mathrm{SHG}}$ and $\tilde{E}_{\mathrm{SFG}}$, are either derived from the square of the sampling pulse, or the product of the sampling pulse with the test field. In the frequency domain, these products become the convolution between the spectra:

$$\tilde{E}_{\mathrm{SHG}}(\omega,\phi_{\mathrm{S}}) = \tilde{C}_{\mathrm{SHG}}(\omega)\int_{-\infty}^{\infty} d\omega'\,\tilde{E}_{\mathrm{S}}(\omega)e^{i\phi_{\mathrm{S}}}\tilde{E}_{\mathrm{S}}(\omega-\omega')e^{i\phi_{\mathrm{S}}} = e^{2i\phi_{\mathrm{S}}}\tilde{E}_{\mathrm{SHG}}(\omega,0), \tag{2.17}$$

$$\tilde{E}_{\mathrm{SFG}}(\omega,\phi_{\mathrm{S}},\phi_{\mathrm{T}}) = \tilde{C}_{\mathrm{SFG}}(\omega)\int_{-\infty}^{\infty} d\omega'\,\tilde{E}_{\mathrm{T}}(\omega)e^{i\phi_{\mathrm{T}}}\tilde{E}_{\mathrm{S}}(\omega-\omega')e^{i\phi_{\mathrm{S}}} = e^{i(\phi_{\mathrm{S}}+\phi_{\mathrm{T}})}\tilde{E}_{\mathrm{SFG}}(\omega,0,0), \tag{2.18}$$

where the CEPs of the sampling and test fields, ϕ_{S} and ϕ_{T}, have been written explicitly, and the complex-valued constants $\tilde{C}_{\mathrm{SHG}}(\omega)$ and $\tilde{C}_{\mathrm{SFG}}(\omega)$ are determined by the nonlinear coefficients and phase-matching properties of the nonlinear medium, as well as their subsequent filtration and focusing onto the detector.

Their combined intensity on the detector is

$$\begin{aligned} I_{\mathrm{d}}(\omega,\phi_{\mathrm{S}},\phi_{\mathrm{T}}) &\propto \left|\tilde{E}_{\mathrm{SHG}}(\omega,\phi_{\mathrm{S}})+\tilde{E}_{\mathrm{SFG}}(\omega,\phi_{\mathrm{S}},\phi_{\mathrm{T}})\right|^2 \\ &= \left|\tilde{E}_{\mathrm{SHG}}(\omega,\phi_{\mathrm{S}})\right|^2+\left|\tilde{E}_{\mathrm{SFG}}(\omega,\phi_{\mathrm{S}},\phi_{\mathrm{T}})\right|^2+ \\ &\left|\tilde{E}_{\mathrm{SHG}}(\omega,\phi_{\mathrm{S}})\tilde{E}_{\mathrm{SHG}}(\omega,\phi_{\mathrm{S}})\right|\cos\left[\phi_{\mathrm{T}}-\phi_{\mathrm{S}}+\Phi_{\mathrm{SFG}}(\omega)-\Phi_{\mathrm{SHG}}(\omega)\right], \end{aligned} \tag{2.19}$$

where $\Phi_{\mathrm{SHG}}(\omega)$ and $\Phi_{\mathrm{SFG}}(\omega)$ are the spectral phases of $\tilde{E}_{\mathrm{SHG}}(\omega,0)$ and $\tilde{E}_{\mathrm{SFG}}(\omega,0,0)$, respectively (adopted from [111]).

In a typical measurement, one would introduce a time delay to one of the fields, introducing a linear phase $\omega\tau$ in the frequency domain. The resulting modulation of the cross-term on the right-hand side of Eq. 2.19 then would trace out the measured waveform as the time delay τ was varied.

One can now see where the CEPs of the input fields enter the measurement. As mentioned previously, the SHG+SFG NOS experiences a CEP shift of $-\phi_{\mathrm{S}}$, due to the appearance of this phase in Eq. 2.19, unlike in, e. g., EOS, where all ϕ_{S} contributions cancel. Accordingly, ϕ_{S} must be known in order to determine the waveform of the test field.

However, if the phases ϕ_{S} and ϕ_{T} are the same and contain the same fluctuations (for example, if the test and sampling pulses are derived without nonlinear conversion from the same laser pulse), they cancel in Eq. 2.19, with the result that $I_{\mathrm{d}}(\omega,\phi_{\mathrm{S}},\phi_{\mathrm{T}})=I_{\mathrm{d}}(\omega,0,0)$; the measured waveform will have the same form as performing the measurement with $\phi_{\mathrm{S}}=\phi_{\mathrm{T}}=0$. This will hold even if the phase $\phi_{\mathrm{S}}=\phi_{\mathrm{T}}$ varies randomly.

In this case, the field being measured is ill-defined, and clearly the measured waveform does not correspond to it. Instead, it provides similar information compared to other techniques such as XFROG[112, 113], which provide the complex envelope of the pulse; the imaginary part of this quantity can be obtained via Hilbert transformation of the measured waveform.

One can also note that in the case where ϕ_{T} is fixed (for example, if the test field was derived from difference frequency generation), introducing a linear time dependence to ϕ_{S} results in a sinusoidal variation of the cross term in Eq. 2.19. Thus, by introducing an offset of the frequency comb of the sampling pulse, an arbitrarily fast (up to the Nyquist frequency) modulation of this signal can be introduced, enabling sensitive detection when applied to MHz-repetition-rate laser systems (adopted from [111]).

To experimentally demonstrate the concept, a NIR pulse waveform was measured with a stabilized CEP pulses using 'Stage I' and 'Stage II' stabilization modules (section A.1) using optical setup shown on Fig. A.5 and described in section A.2.4 of this thesis. The pulses were then split into two arms for the time-delay waveform sampling based on the technique described in the section 2.2.1 of this thesis. After the measurement with stabilized CEP pulses, the CEP stability was on purpose disrupted, by feeding an unsynchronized random electrical signal to the 'Stage I' CEP stabilization module and disabling the 'Stage II' module. The same pulse waveform measurement was then performed with unstabilized CEP pulses. The measurement was performed based on SHG + SFG NOS detection.

Fig. 2.38a demonstrates a test pulse waveform measurement with CEP unstabilized pulses. The results are compared to a measurement with CEP stabilized pulses, where the CEP of the sampling pulse was set to zero. Fig. 2.38b shows similar comparison between two measurements for various amounts of fused silica glass introduced in the test arm only. The introduced glass changes the CEP and dispersion of the test pulse waveform. This indicates that the measurement with CEP unstabilized pulses provides a characterization of a test pulse with an ambiguity determined by the CEP difference between sampling and test pulses.

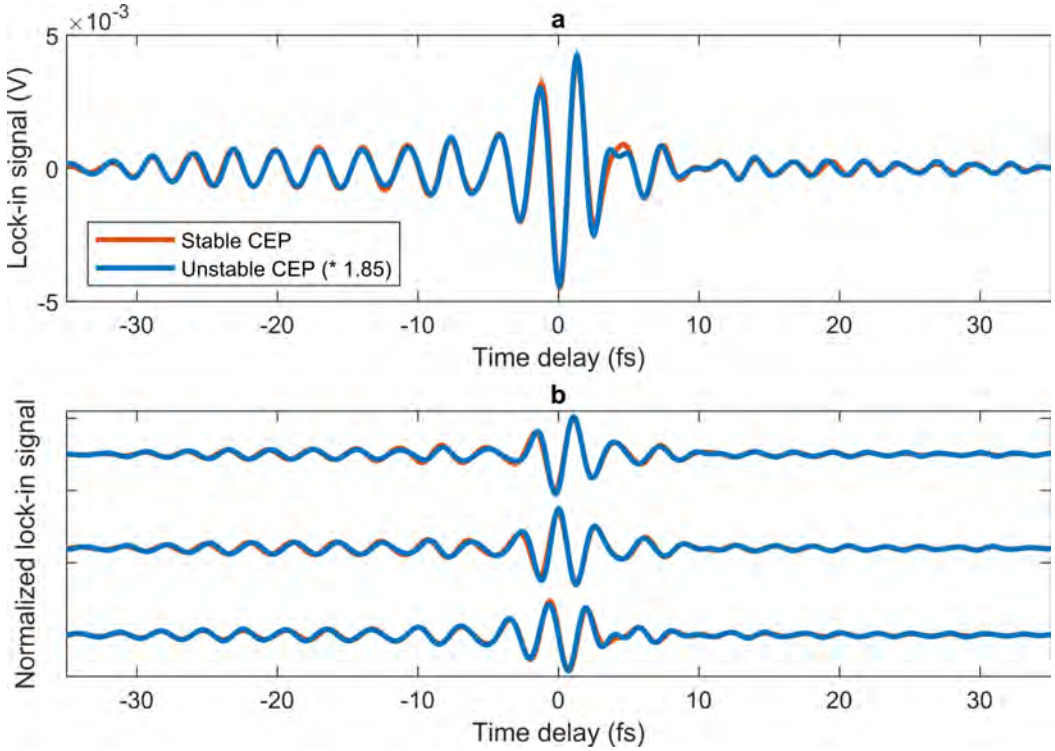

Figure 2.38: (**a**) Comparison of measurements with and without CEP stabilization of sampling and test pulses. (**b**) Similar comparison of measurements with and without CEP stabilization for various amounts of fused silica glass introduced into the test arm.

In summary, channels in which a local oscillator and a heterodyne signal originate form the same order of non-linearity allow to perform pulse characterization without CEP stabilization as long as the source of CEP instability is the same for both (sampling at test) pulses. The measurement provides a similar information as conventional techniques such as XFROG, but does not require a post-processing with an iterative algorithm. The method benefits high sensitivity due to the homodyne nature of the detection. Since the method provides optical pulse waveform sampling with CEP ambiguity, whenever only the change in the waveform is of interest, the concept can be used as a regular field resolved detection. Since a CEP stabilization of optical pulses is rather difficult and expensive procedure, the new concept therefore provides a new opportunity to perform advanced

studies with CEP-unstabilized pulses.

Chapter 3

Three-channel optical synthesizer characterization

Highly non-linear processes are very sensitive to incident electric fields of optical pulses[114, 23]. The number of excited carriers, as well as a shape of a time-dependent light-matter energy transfer, can be significantly controlled by a waveform of an incident pulse (sections 2.1, 5). The simplest way to manipulate an optical pulse waveform is by changing its carrier-envelope phase[115, 116]. However this method still provides a very limited control, therefore artificially synthesized optical waveforms are of great importance for strong-field phenomena.

This chapter describes the characterization of a high-frequency channel of a recently demonstrated optical field synthesizer[6]. The experimental characterization of the high-frequency channel allowed using it for the characterization of synthesized optical pulses with a conventional electro-optic sampling technique at frequencies approaching visible spectral range. The details of the synthesizer and electro-optic sampling based on characterized high-frequency channel constitute the core of other works described elsewhere[117, 118].

3.1 Non-linear photo-conductive sampling of the high-frequency channel

A novel concept for optical pulse waveform synthesis was recently demonstrated[6]. Two channels (CH1 and CH2) are used for pulse waveform synthesis, while the third channel (CH0) can be employed for synthesized pulse waveform characterization using conventional electro-optic field sampling. However, since the spectral response of electro-optic sampling depends on a pulse waveform, the sampling pulse waveform (CH0) has to be characterized.

Fig. 3.1 shows a schematic concept of the optical synthesizer, described in details elsewhere[6]. The laser beam-line consists of a Ti:sapphire oscillator (Rainbow 2, Spectra Physics) that provides an octave-spanning bandwidth with about ~ 750 nm central wavelength. The output from the oscillator is guided through the 'stage I CEP stabilization' module based on the feed-forward scheme[119]. CEP stable pulses are then further ampli-

fied within a 9-pass cryo-cooled Ti:sapphire chirped pulse amplifier at a repetition rate of 3 KHz, and temporally compressed using a transmission grating-based compressor yielding $\sim$ 21 fs pulses with $\sim$ 2.5 W output power. The amplified pulses are further spectrally broadened in a hollow-core fibre. The spectrally broadened pulses are compressed in a chirped mirror compressor and guided through an OPCPA system[120] resulting in 15 fs duration (FWHM of intensity) centered at about 1.8 µm.

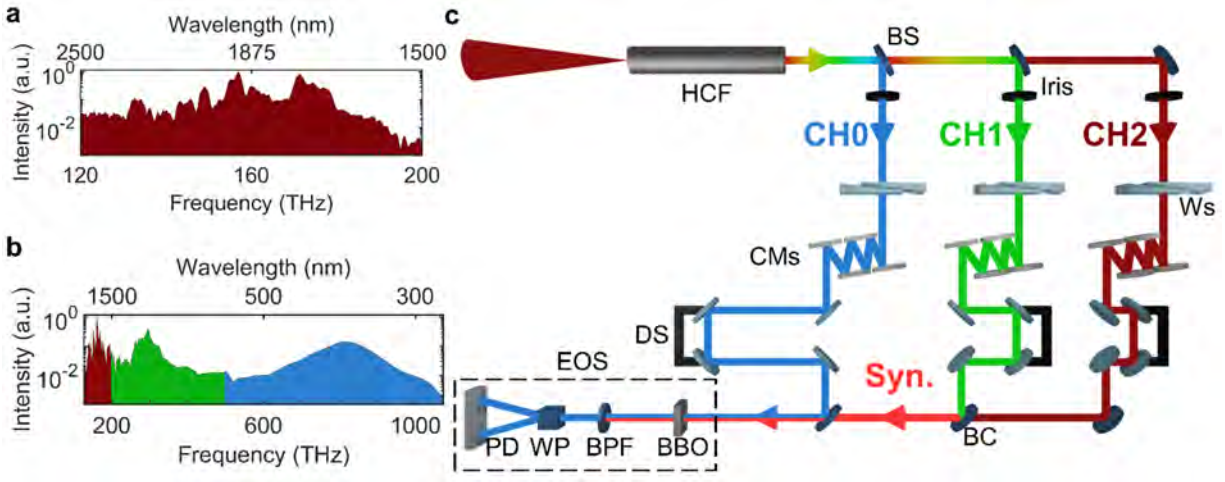

Figure 3.1: Amplified in OPCPA optical pulse with a spectrum centered at about 1.8 µm (**a**) are spectrally broadened (**b**) in a hollow-core fibre filled with ambient air. Customized beam-splitters (BS) separate the broadened spectrum into three channels (CH1, CH2 and CH0). Custom-made chirp mirrors (CMs) are used to compensate for the dispersion of air and beam splitters. Glass wedge pairs are inserted into channels to fine-tune the dispersion of pulses. Temporal and spatial overlap is achieved using delay stages (DS) and beam combiners (BC), respectively. The Wollaston prism (WP) splits the band-pass filtered (BPF) light into two orthogonally polarized beams which are sent to a pair of balanced photodiodes (PD) for detection. Adopted from [6].

In order to characterize CH0 of the synthesizer, the NPS technique was implemented. First, optical waveforms of CH1, CH2, and synthesized pulse were characterized with electro-optic sampling technique (Fig. 3.2) assuming Fourier-transform limited CH0.

From measured synthesized waveform one can extract a typical temporal profile of carrier excitation and associated injection rate shown in Fig. 3.3. The injection rate is calculated for a quartz medium assuming six photons absorption to be the dominant mechanism for the carrier's excitation.

Known carrier injection rate allows calculating a typical spectral response of NPS technique as described in details in section 2.1 of this thesis. As illustrated in Fig. 3.4 the spectral response extends beyond the frequencies of CH0 and therefore implies that the channel CH0 can be characterized with the NPS technique using synthesized pulse for the carrier excitation.

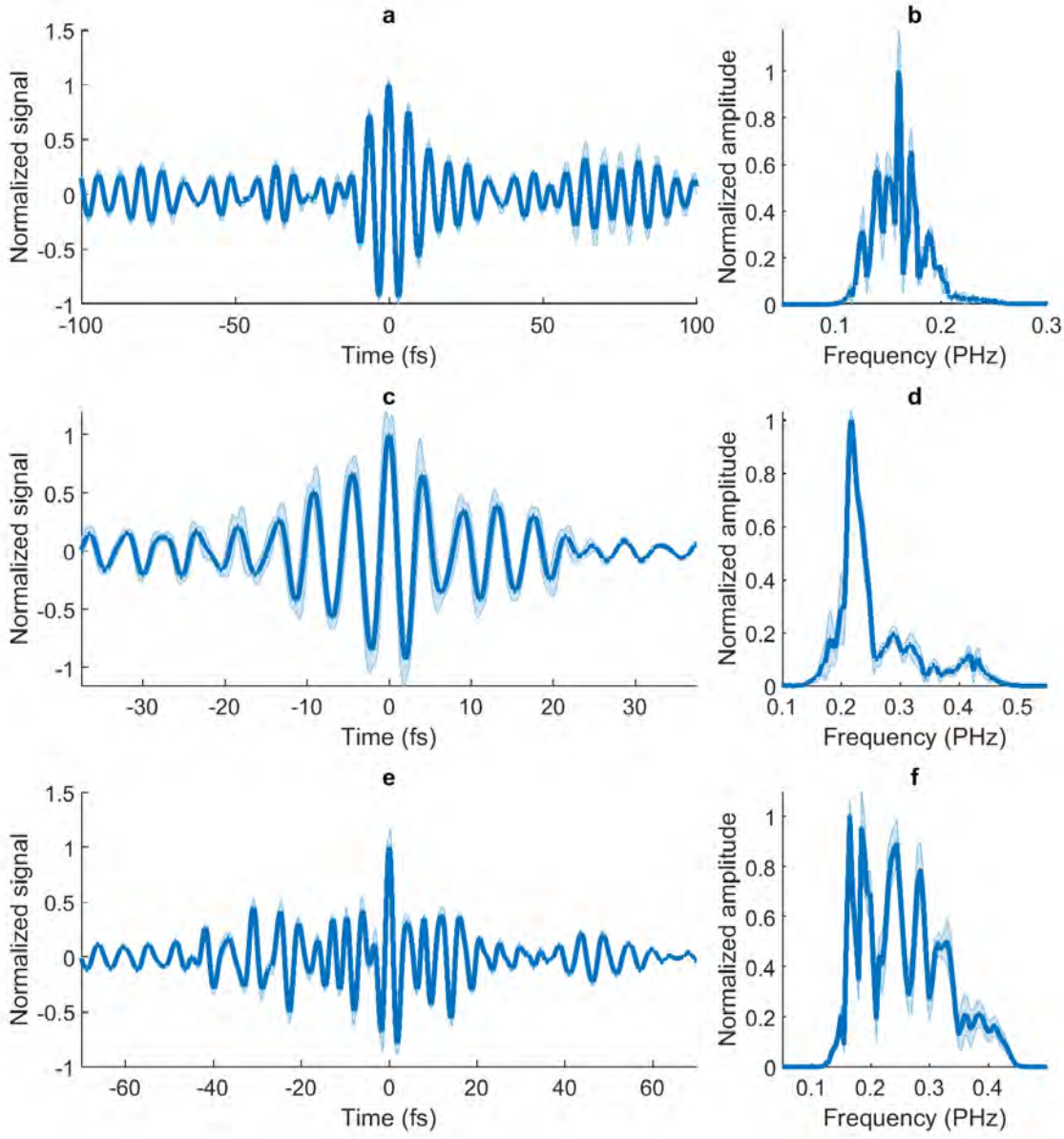

Figure 3.2: Measured optical pulse waveforms of CH2 (**a**), CH1 (**b**) as well as a synthesized pulse waveform (**c**). Sub-figures (**b**), (**d**), (**f**) show spectral amplitudes of CH2, CH1 and the synthesized pulse obtained by a Fourier transformation. The measured pulse waveforms were provided by Enrico Ridente.

Fig. 3.5b,c show experimental results of CH0 pulse measurement obtained with the NPS technique.

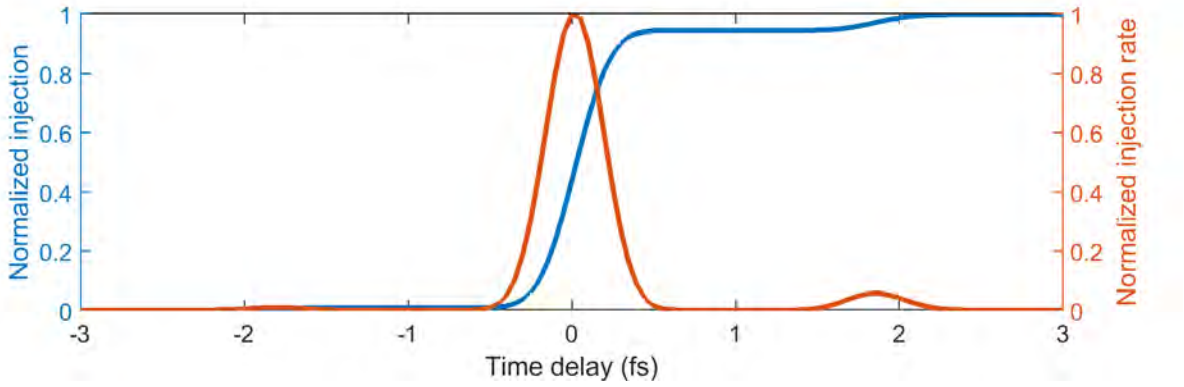

Figure 3.3: Estimated temporal carrier excitation profile as well as an excitation rate obtained with a typical synthesized pulse waveform based on six-photon absorption mechanism of carrier excitation in a quartz medium.

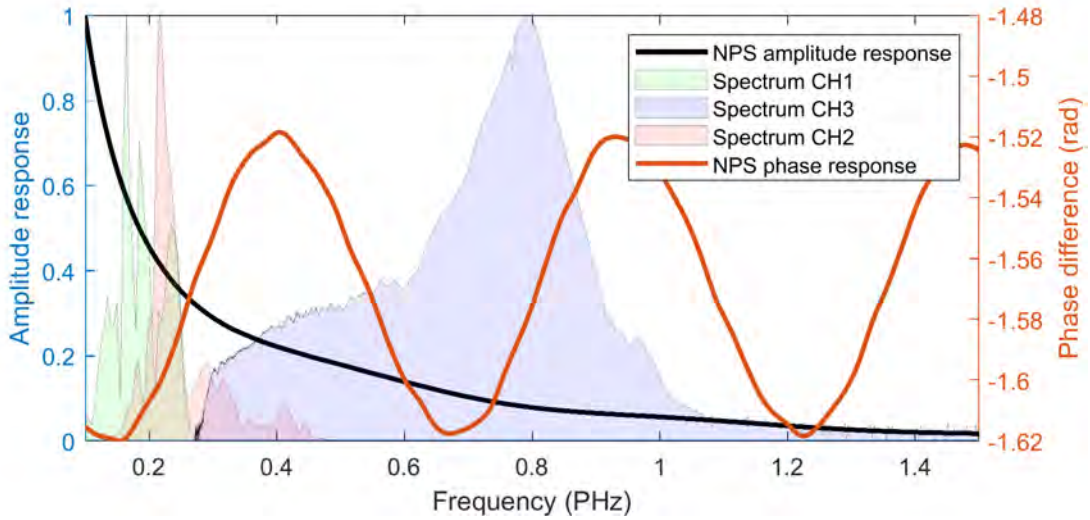

Figure 3.4: Estimated spectral amplitude and spectral phase responses obtained for the NPS detection based on a carrier excitation rate provided by a typical synthesized pulse. Shadow areas represent normalized spectral amplitudes of CH0, CH1, and CH2 channels obtained by taking a square root from the spectral intensities obtained with a grating spectrometer.

The measured pulse trance of CH0 allows the calculation of a typical spectral response of electro-optic sampling method obtained with such sampling pulse. Fig. 3.5d show calculated electro-optic sampling spectral response for the synthesizer setup presented in Fig. 3.1.

Finally, the synthesized pulse can be used to tailor a temporal carrier excitation profile and the number of excited charge carriers. In order to demonstrate such control, CH1 and CH2 were used to synthesize an optical pulse which was then focused on a quartz

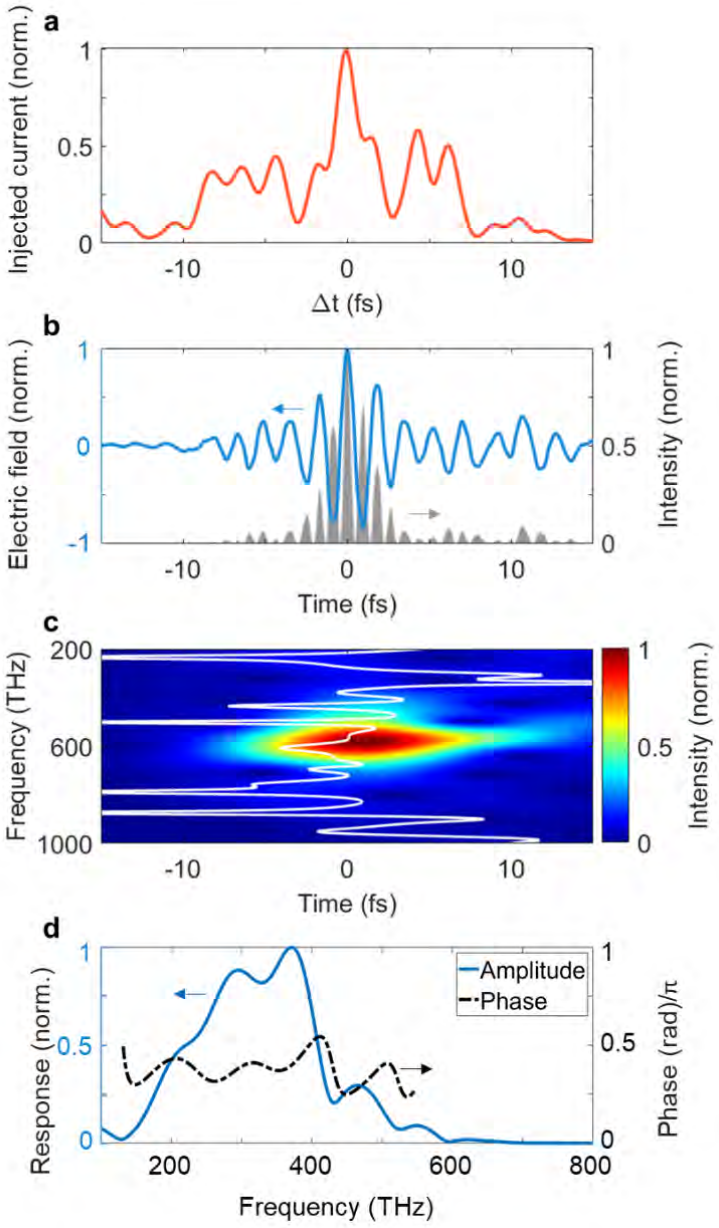

Figure 3.5: (**a**) Dependence of a measured current obtained with a synthesized pulse on a temporal delay between CH1 and CH2 used for the pulse synthesis. (**b**) Characterized optical pulse waveform of CH0 as well as intensity profile obtained with NPS technique. (**c**) spectrogram obtained by Gabor transformation of the trace in (**b**) and the group delay (white line) of the pulse in (**b**). (**c**) the response function of the EOS setup. Adopted from [6].

medium. Non-linear excitation of charge carriers provided by the incident synthesized pulse is expected to be very sensitive to the pulse waveform (section 2.1). Metal electrodes deposited on a surface of a quartz sample allow measuring a generated current due to the excitation of charge carriers. To observe a dependence of a measured current, the time delay between CH1 and CH2 was changed in a controlled manner, and the RMS current was recorded at every time delay. Fig. 3.5a shows how does a measured current depend on a time delay between CH1 and CH2 channels used for pulse synthesis. A clear dependence of a measured signal indicates that the measured current is very dependent on the incident pulse waveform. The largest magnitude of a measured current corresponds to a zero delay between CH1 and CH2 channels, which provides the shortest and most asymmetric (in its temporal E-field profile) synthesized pulse.

In summary, a two-channel optical synthesizer was characterized employing the NPS technique. Characterization of the sampling channel (CH0) allows extracting a typical experimental spectral response of the synthesizer setup. Measured pulse duration of CH0 confirms that the setup allows extending a detection bandwidth of conventional electro-optic sampling, for the first time, towards visible spectral range. As a first application, it was demonstrated that the synthesis of an optical pulse with CH1 and CH2 channels allows controlling currents inside a medium of interest. The control is achieved by means of a temporal synthesis of a pulse waveform employed for the excitation of carriers inside a sample medium.

Chapter 4

Attosecond timing of light-field-driven carrier motion

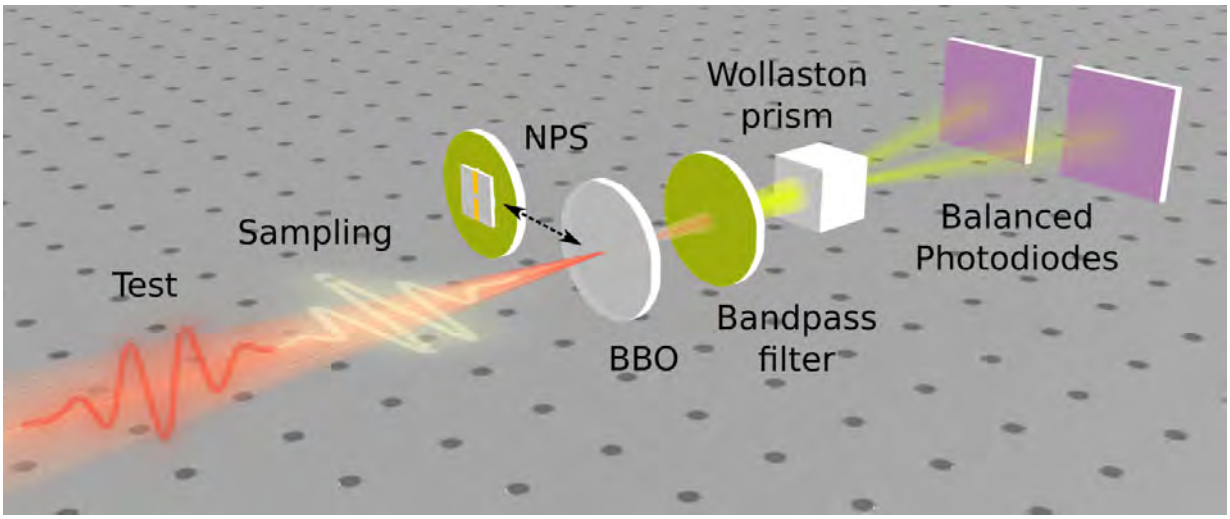

Figure 4.1: Schematic concept of an experimental setup for attosecond timing of light-field-driven carrier motion. The experimental setup, described in detail in the section A.2.2 of this thesis, consists of the test pulse waveform, which is iteratively measured with NPS and EOS techniques. Under the assumption of quasi-instantaneous response of bound charges[7], the difference between the two measured traces reveals the dynamics associated with a carrier motion within the NPS medium.

The TDDFT simulation of the time-dependent energy transfer predicts a photo-injection delay between the electric field of the sampling pulse and the rate of the energy transfer (Fig. 2.5d). This delay is therefore supposed to shift the NPS gate function in time, which will result in a measured test waveform also be shifted in time.

If the test waveform is measured with two separate techniques (Fig. 4.1), one of which involves an injection of charge carriers (NPS) while the other not, the comparison of two

measured waveforms will reveal the delay associated with injected charge carriers.

EOS field sampling technique is based on a transient modification of the medium without injection of charge carriers[67].

Temporal offsets encoded on the waveforms simultaneously measured with NPS and EOS techniques therefore provide insight into delays associated with the injected charge carriers inside the NPS medium.

To measure the photo-injection delay in quartz, the NIR pulse spectrum was down-converted by means of the intra-pulse DFG to obtain a spectrum centered at about 1.8 µm. The pulse waveform in this spectral range can be measured with a conventional EOS technique[57] as well as the NPS technique.

Type II BBO crystal of 12 µm thickness and 50 degrees phase-matching angle θ was used for the EOS detection.

Due to the small differences in the bandwidths of the two techniques, the best agreement is expected at the center of the measured pulse in the time domain. The comparison between measured waveforms (Fig. 4.2) at the center of the pulse shows a temporal delay. The delay also changes (in magnitude and sign) with the field strength of the sampling pulse.

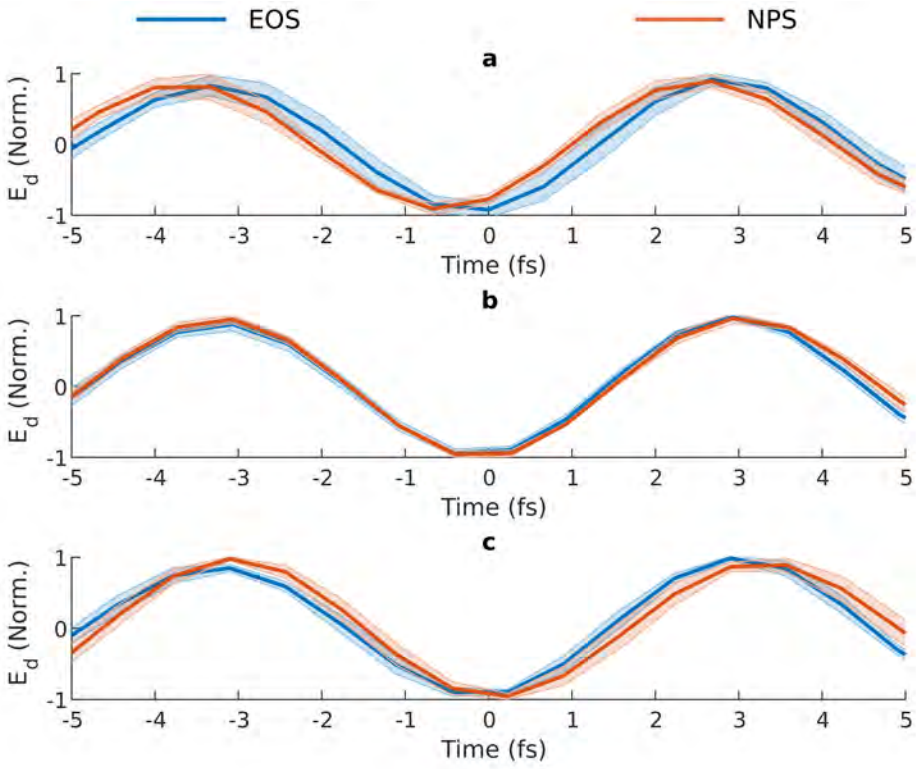

Figure 4.2: Field strength dependent temporal shift of the measured test waveform at 1.04 V/Å (**a**), 1.4 V/Å (**b**), 1.7 V/Å (**c**) field strengths of the NPS sampling pulse.

In order to explain the origin of the temporal delay, the screening of injected carriers, carrier momentum relaxation, and the onset of carrier motion was considered.

Section 4.1 discusses the influence of a plasma screening formation on observed experimental time delay.

Section 4.2 on the other hand discusses the quantum-mechanical origin of the time delay associated with non-linear excitation of charge carriers within a sample medium.

4.1 Plasma screening and momentum relaxation

Due to the propagation of sampling and test pulses inside the EOS crystal, the pulses may experience a spectral broadening due to the SPM and XPM.

In order to ensure that the EOS trace serves as a reference for the measurement, using the known sampling pulse, the EOS spectral response function was calculated by means of the non-linear wave equation, under the slowly evolving wave approximation[57]:

$$\frac{\partial E_\omega(z)}{\partial z} = ik(\omega)_\omega E_\omega(z) - \frac{i\omega}{2n(\omega)\epsilon_0 c} P_\omega^{NL}(z). \tag{4.1}$$

The equation describes an evolution of each spectral competent $E_\omega(z)$ as it propagates inside the EOS crystal. The $k(\omega)$ is a frequency dependent wavevector, $n(\omega)$ is a frequency dependent refractive index, $P_\omega^{NL}(z)$ is a non-linear polarization created in a medium at a distance z and angular frequency ω.

Under experimental conditions, the intensity inside the EOS crystal is not sufficient to produce a significant timing shift due to a spectral broadening by means of SPM and XPM. Calculated from Eq. 4.1 non-linear polarization reveals a timing shift of only about 25 as[3].

The response function for EOS was obtained by numerically propagating sampling and test pulses (with varying time delay) inside the crystal using Eq. 4.1. The delay-dependent change in a spectral intensity, after the known response curve of the photodiodes and the bandwidth of the experimental spectral filter, is then Fourier transformed to obtain a complex-valued spectrum. The ratio of the test complex spectrum and computed complex spectrum provide a response function of the EOS under the experimental conditions. This calculated spectral response function is then deconvolved from the measured EOS traces to correct the measured spectral phases and amplitudes at the input facet of the non-linear medium.

Since bulk dielectrics have relatively large dielectric constants, and the densities of injected carriers by intense laser fields can be as high as 10^{19} cm^{-3} (Fig. 4.6), the shape of an incident electric field and the shape of the electric field inside the material will differ from each other.

Each component of a field inside a material can be described as:

$$E_{trans} = E_{inc} - \frac{E_{inc} P/\epsilon_0}{4E_{inc} + P/\epsilon_0}, \tag{4.2}$$

where E_{trans} is a field on the surface of the material, transmitted through the surface. E_{inc} is the incident field. P is the linear polarization induced by the E_{trans} ($\approx -4\epsilon_0 E_{inc}$).

The total polarization of the medium $\boldsymbol{P}(t)$ due to injected carriers is proportional to the total induced current $\boldsymbol{J}(t)$ inside the material:

$$\boldsymbol{P}(t) = \int_{-\infty}^{t} \boldsymbol{J}(t')\, dt'. \tag{4.3}$$

The bold notation indicates a vector quantity. The total current $\boldsymbol{J}$ is a contribution of currents from free and bound electrons ($\boldsymbol{J} = \boldsymbol{J}_e + \boldsymbol{J}_b$). The current due to bound electrons is related to the linear refractive index and the non-linear absorption response.

The measured NPS signal will be proportional to the net polarization or a DC component of $\boldsymbol{P}(t)$.

The current from free electrons, driven by the local transmitted field E_{trans}, can be described by the classical equation of motion:

$$\nabla \boldsymbol{J_e}(t) = -N(t)\boldsymbol{E_{trans}}(t)/m^* - \gamma \boldsymbol{J_e}(t), \tag{4.4}$$

where

$$N(t) = \int_{-\infty}^{t} \omega(t')\, dt' \tag{4.5}$$

is a free carrier density, m^* is the reduced effective mass of an electron-hole pair, while γ is the momentum relaxation rate. As shown in Fig. 2.5d, the carrier injection rate $\omega(t)$ can be well approximated as

$$\omega(t) = 10^9 E_i^8(t). \tag{4.6}$$

An increase in the density of free carriers in a dielectric medium leads to a reduction of its real part of the refractive index, because the polarization induced by the free and bound carriers oppose one another (section 1.4), reducing the overall polarizability of the material. Since the density of free carriers changes during the propagation of the pulse through the material, different parts of the pulse will experience different free carrier densities and different free carrier polarizations (screening). This in turn will cause a reshaping of the interacting pulse, and a time-shift with respect to the incident pulse waveform.

Since the screening polarization depends on a carrier density and effective masses of carriers, modeling of the screening polarization depends on the time-dependent carrier density and momentum relaxation time factors, which is described by the eqs. 4.4, 4.3, 4.5, 4.6, 4.2. Since E_i and E_{inc} can be determined experimentally, modeling of the waveform reshaping and time-shift, reduces to the fitting of the momentum relaxation γ to the measured NPS waveform.

In order to determine the influence of the momentum relaxation also, the simulations of the waveform time-shift were performed for a fixed quasi-free carrier density $N(t)$ and varying momentum relaxation factor γ (Fig. 4.3)[3].

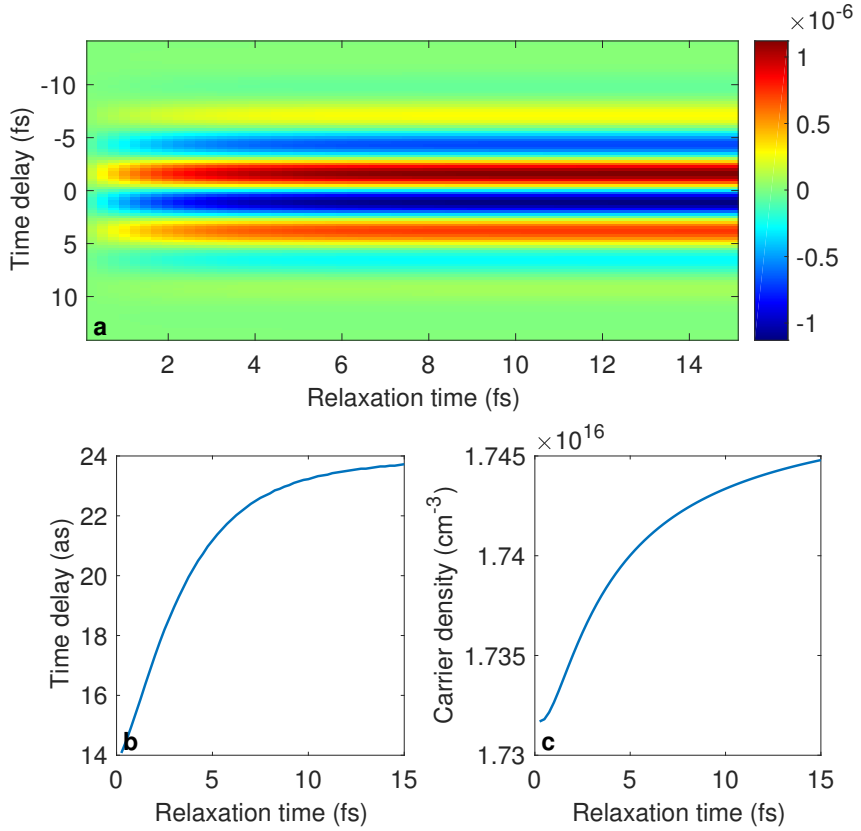

Figure 4.3: Influence of the momentum relaxation time on the time-shift of the measured with NPS test waveform. Field strength 0.5 V/Å. (**a**) Induced signal as a function of time delay between sampling and test fields and the momentum relaxation time. (**b**) Time delay of the measured waveform relative to the vector potential of the test field as a function of relaxation time. (**c**) Final carrier density as a function of the momentum relaxation time. Adopted from [3].

The reshaping of the pulse waveform and the time-shift are almost negligible and independent of the momentum relaxation time for relatively low field strength. This is because the momentum relaxation possesses a linear opposing force, as can be seen in a second term of the Eq. 4.4. Therefore the dependence on this parameter is mainly a simple rescaling of the magnitude of the current. And hence the shape of the waveform remains literally the same, but experiences a shift in time.

On Fig. 4.4 and Fig. 4.5 the time shift and reshaping of the detected waveform is simulated for various field strengths and two momentum relaxation time scales (30 fs and 0.3 fs)[3].

At a low density of injected carriers, the total polarization and the reflectivity is dominated by the polarization of bound electrons which is slightly reduced by polarization from the quasi-free electrons which is out of phase with respect to the polarization from the bound electrons. In this regime, the response of the medium is still dielectric-like.

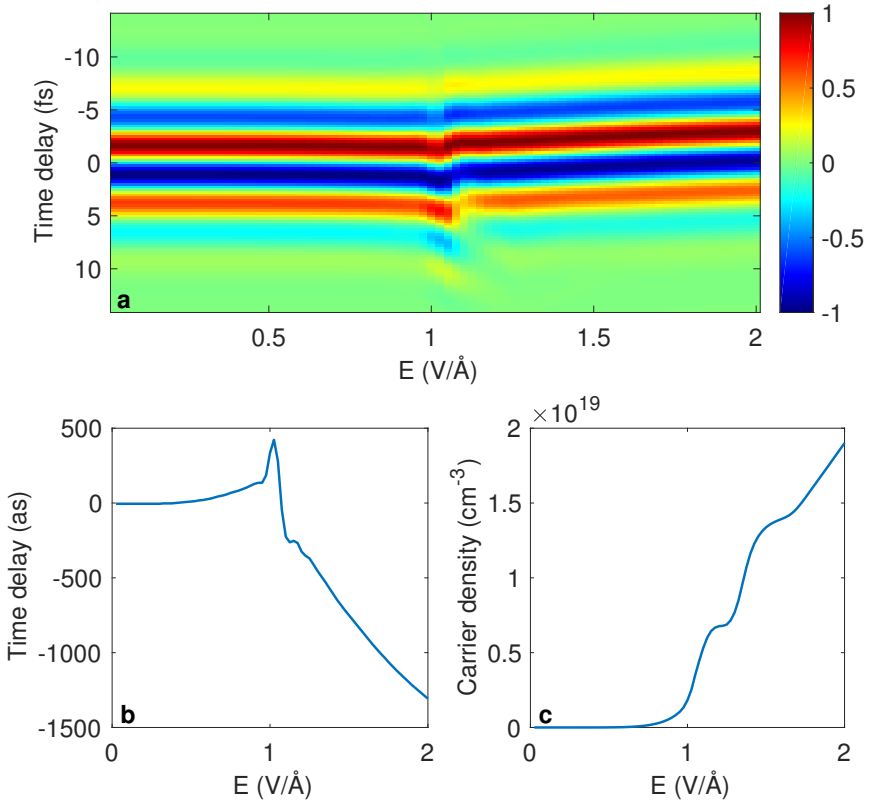

Figure 4.4: Influence of sampling field strength on detected waveform for 30 fs momentum relaxation. (**a**) Normalized induced signal as a function of time delay between sampling and test fields. (**b**) Time delay of the measured waveform relative to the vector potential of the test field as a function of an sampling field strength. (**c**) Final carrier density as a function of a sampling field strength. Adopted from [3].

At a higher density of injected carriers, the polarization from quasi-free electrons starts to dominate the polarization from bound electrons. In this regime, the response of the medium becomes Drude-like or metal-like.

At around 1.1 V/Å injection field strength, the time-dependent transition between the dielectric-like and metal-like regimes takes place. The front part of the pulse experiences the dielectric-like regime with a reduced refractive index, causing an increase of a field entering the medium. At the peak of the pulse, a significant number of carriers are injected and the medium transitions from a dielectric-like to the metal-like regime. Therefore the tail part of the pulse experiences the increase of the reflectivity and less of the field entering the medium.

Since the light intensity distribution in the focal plane is non-homogeneous, the created free carrier density is also non-homogeneous, which results in a charge of the overall time shift of the waveform due to the screening polarization. This can be taken into account by measuring the focal spot shape and performing a weighted average over the focal spot.

Fig. 4.6 shows the spatially averaged time shift of the waveform for different peak field

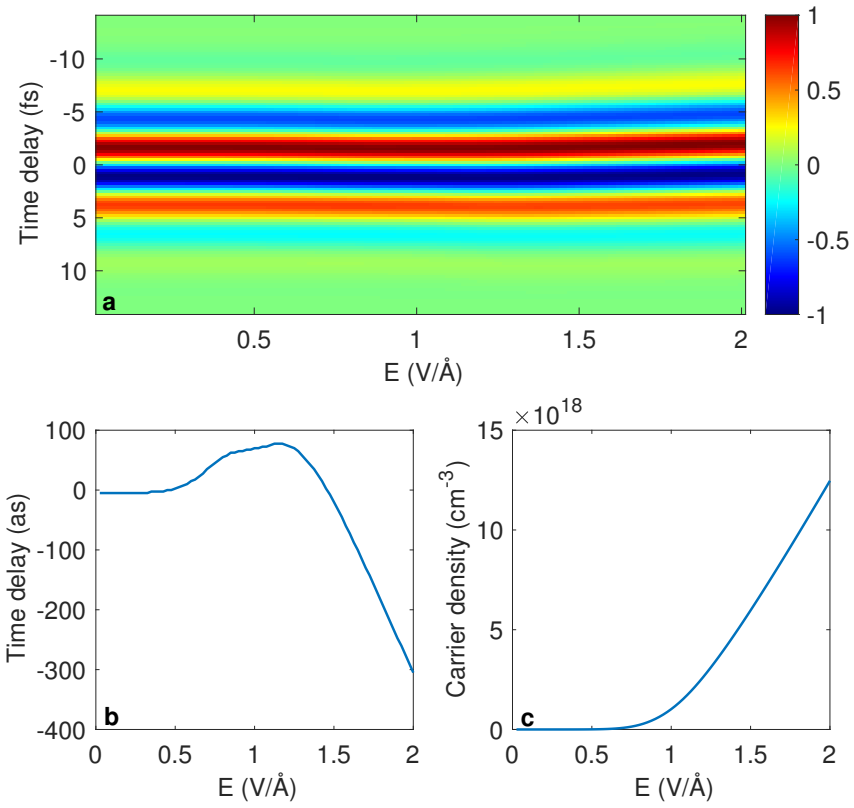

Figure 4.5: Influence of sampling field strength on detected waveform for 0.3 fs momentum relaxation. (**a**) Normalized induced signal as a function of time delay between sampling and test fields. (**b**) Time delay of the measured waveform relative to the vector potential of the test field as a function of an sampling field strength. (**c**) Final carrier density as a function of a sampling field strength. Adopted from [3].

strengths of the incident injection pulse. The effect of spatial averaging is a reduction of the overall time-shift.

Fig. 4.6a shows that the spatially averaged time-shift of the incident pulse E-field is smaller compared to the case of homogeneously injected carriers. Since excited charge carriers change the incident pulse waveform by means of introducing a time-shift and change of the transmitted spectral amplitudes, the overlap effect can be characterized by a change of the root-mean-square (RMS) value of the transmitted pulse waveform. Hence, measuring the E-field RMS change of the transmitted pulse waveform and comparing it to the theoretical model allows one to extract the density of injected carriers. Figure 4.6b shows that the typical charge carrier density due to multi-photon (section 1.3) injection by a $\sim$ 2.7 fs pulse with $\sim$ 750 nm central wavelength (section A.1) and $\sim$ 1 - 1.7 V/Å field strengths in $\sim$ 12 µm thick fused silica (section A.6) is on the order of 10^{-19} cm^{-3}.

In summary, the excitation of carriers in a medium by a strong pulse leads to a change in its optical properties. Since a non-resonant excitation is non-linearly proportional to the electric field, the time-dependent excitation of charge carriers by optical pulses depends

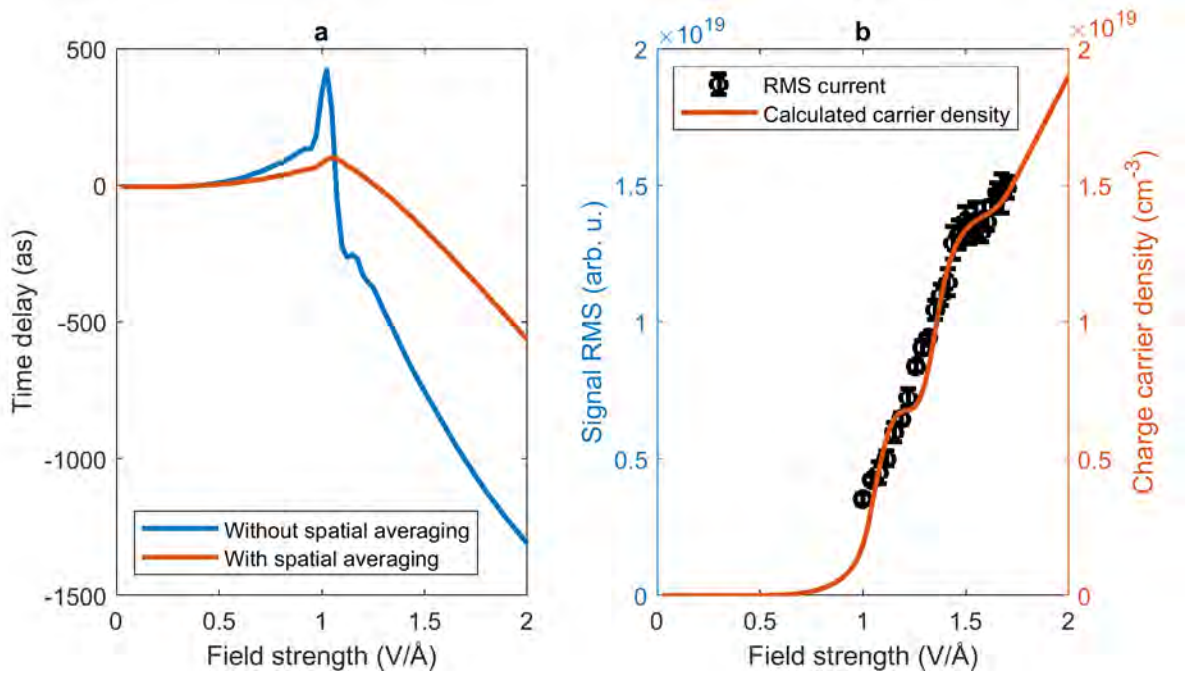

Figure 4.6: Effect of the non-homogeneous field distribution over the medium inside the focal plane on a time delay between the vector potential and the induced signal (**a**). The measured change of the pulse E-field RMS allows extracting the injected carrier concentration (**b**). Adopted from [3].

on the time-dependent evolution of the pulse electric field (pulse waveform). A relatively small number of exited carriers leads to a decrease of the real part of the refractive index and shifting of the transmitted pulse waveform to earlier times. A large number of excited carriers, on the other hand, leads to a screening effect, and therefore decrease in the transmitted electric field. From the difference between pulse waveforms propagating through the medium with and without exciting carriers, one can extract the excited carrier concentration, which depends on the field strength of the incident pulse. The typical excited carrier density due to interaction of a short pulse (section A.1 of this thesis) in a fused silica medium depends on the field strength of the incident pulse and can reach concentrations larger than 10^{-19} cm^{-3} before sample damage.

4.2 Time-delay of the high-order photon absorption

The simulation of the time delay of the waveform associated with a screening polarization agrees with the experimental time delay observed between the pulse waveform measured with NPS (at various injection field strengths) and the reference waveform measured with EOS (Fig. 4.7). The constant time offset between the simulation and experiment is present for all injection pulse field strengths. The measured time-delay offset (134 ± 93 as) is however in good agreement with the delay offset (75 as) predicted by TDDFT simulation. This suggests that the total experimental time delay is a result of the screening polarization as well as a contribution of another physical effect.

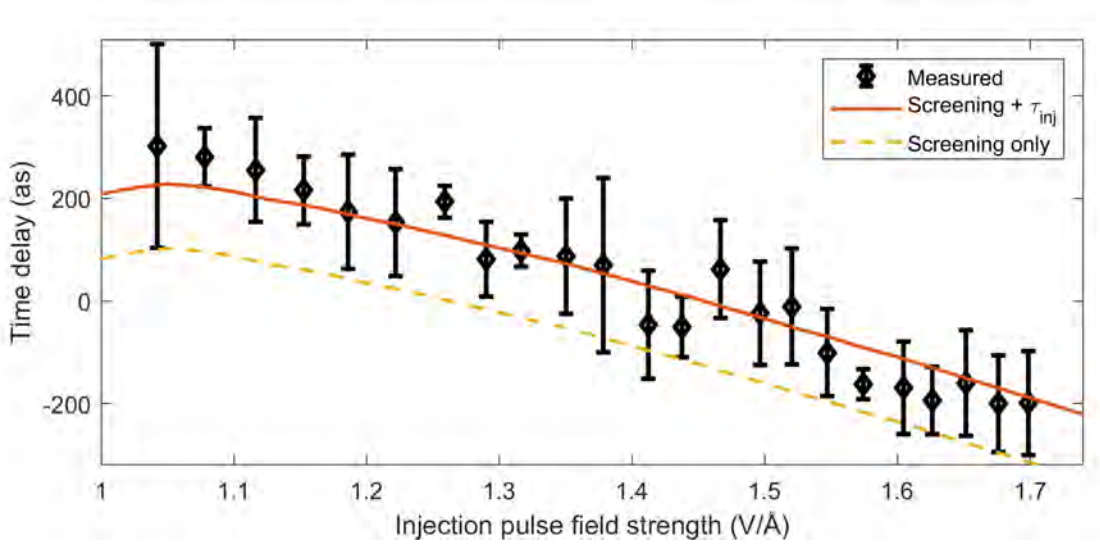

Figure 4.7: Field strength dependent time shift of the measured waveform. The measured values are compared to expectations of electric field screening by the laser-induced free carriers. Error bars represent the standard deviation of multiple measurements of the relative timing of the waveform. Adopted from [3].

Although the measured time-delay offset present in the experiment and TDDFT simulation is not well understood, it is however has a similar signature as the time-delay associated with strong-field ionization in gasses[121]. In the case of gasses, the two-photon ionization is considerably delayed relative to one-photon ionization when the same final energy in the continuum is reached. Therefore the measured time-delay offset is possibly related to the delay associated with the high-order photon absorption.

In summary, the time delay likely associated with the multiphoton nature of charge carrier excitation was measured (134 ± 93 as) experimentally and confirmed with the TDDFT simulation (75 as).

Chapter 5

Switching and modulation of the optical properties of solids

The physics behind the non-linear photo-conductive sampling (section 2.1), as well as all other ultrafast phenomena in solids[122], are based on the fact that properties of a solid medium can be modified due to light-matter energy exchange on ultrafast time scales (chapter 4). Since the NPS technique provides a detection bandwidth of up to PHz frequencies, the processes as quick as several hundred attoseconds can be resolved. When an electric field in a form of light is incident on a medium, polarization inside a medium is created, due to the work performed by the incident field. Created polarization will produce an electric field in a medium, resulting in a modification of the incident pulse electric field waveform. Therefore the modification of an incident pulse waveform contains information about polarization created in a sample medium. Since NPS allows the measurement of a pulse waveform with a couple of hundreds of attosecond temporal resolution, the dynamics of a medium polarization can be measured with the same temporal resolution. The medium polarization can occur due to a linear or non-linear[123] interactions (sections 1.2, 1.3, 1.4). The linear polarization dominates at low field strengths of the incident pulse, while non-linear polarization takes place at strong incident fields. Therefore when the transmitted (through the sample) pulse waveform is measured at low and high incident fields strengths, the difference between two measured waveforms reveals the *non-linear* polarization created in a medium.

In this chapter, the non-linear polarization and associated light-matter energy transfer are measured for several solids with various band gaps. The abruptness of the energy transfer process is studied in detail.

5.1 Material-dependent study of light-matter energy transfer

Fig. 5.1 shows a simplified concept of the experiment, described in more details in section A.2.3 of this thesis. The incident pulse (section A.1) of about 2.7 fs duration[3] and

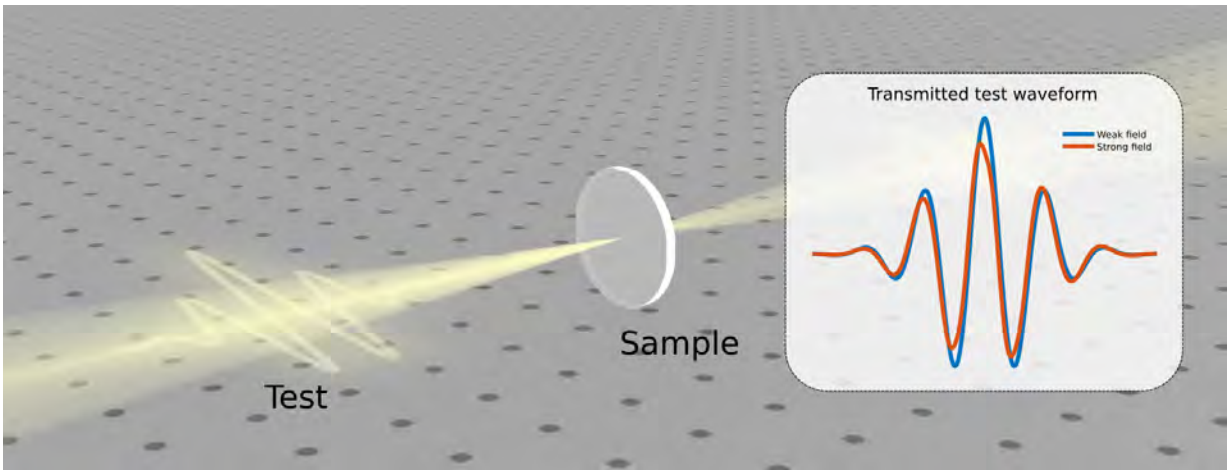

Figure 5.1: Schematic concept of the experiment. An incident test pulse is transmitted through a sample at weak and strong incident field strengths. The difference between normalized transmitted waveforms reveals information related to the non-linear polarization created in a medium.

centered at about 750 nm is incident on a sample. The transmitted pulse waveform is then measured with the NPS technique at low and high incident field strengths. The waveforms are normalized at the head of the pulse, where both reference and higher field waveforms have small electric fields, not enough to induce a significant non-linear polarization of a medium. The difference between transmitted incident pulse waveforms measured at low and high field strengths reveals the modification of the incident pulse due to created non-linear polarization in a medium.

In this experiment Si, Diamond, and SiO_2 media were investigated. Since direct band gaps of these materials differ significantly ($\sim$ 3.4 eV for silicon, $\sim$ 5.5 eV for diamond, and $\sim$ 9 eV for SiO_2), the non-linear polarization of a medium is expected to have different power-law proportionality to the incident electric field strength of an incident pulse. The higher is the order of the non-linearity, the more abrupt are the energy transfer transitions are expected.

Figs. 5.2-5.4 show measured pulse waveforms after interaction with 240 $\pm$ 15 nm silicon (Fig. 5.2), 9.18 $\pm$ 0.062 µm CVD diamond (Fig. 5.3) and 121 $\pm$ 8 nm SiO_2 samples. The investigated samples are thin, in order to minimize the effects of pulse waveform change due to propagation through the medium. The transmitted waveforms measured at low field strength are referred to as reference. The reference waveform is then compared to the measured transmitted waveform at various higher field strengths. The recorded waveforms were measured with the NPS technique as described in section 2.1 of this thesis.

The difference between two measured waveforms can be used to calculate (section 1.4) a time-dependent non-linear polarization (Figs. 5.5 - 5.7).

If a time-dependent electric field of the incident pulse and the time-dependent non-linear polarization caused by the interaction of this waveform are known, the time-dependent en-

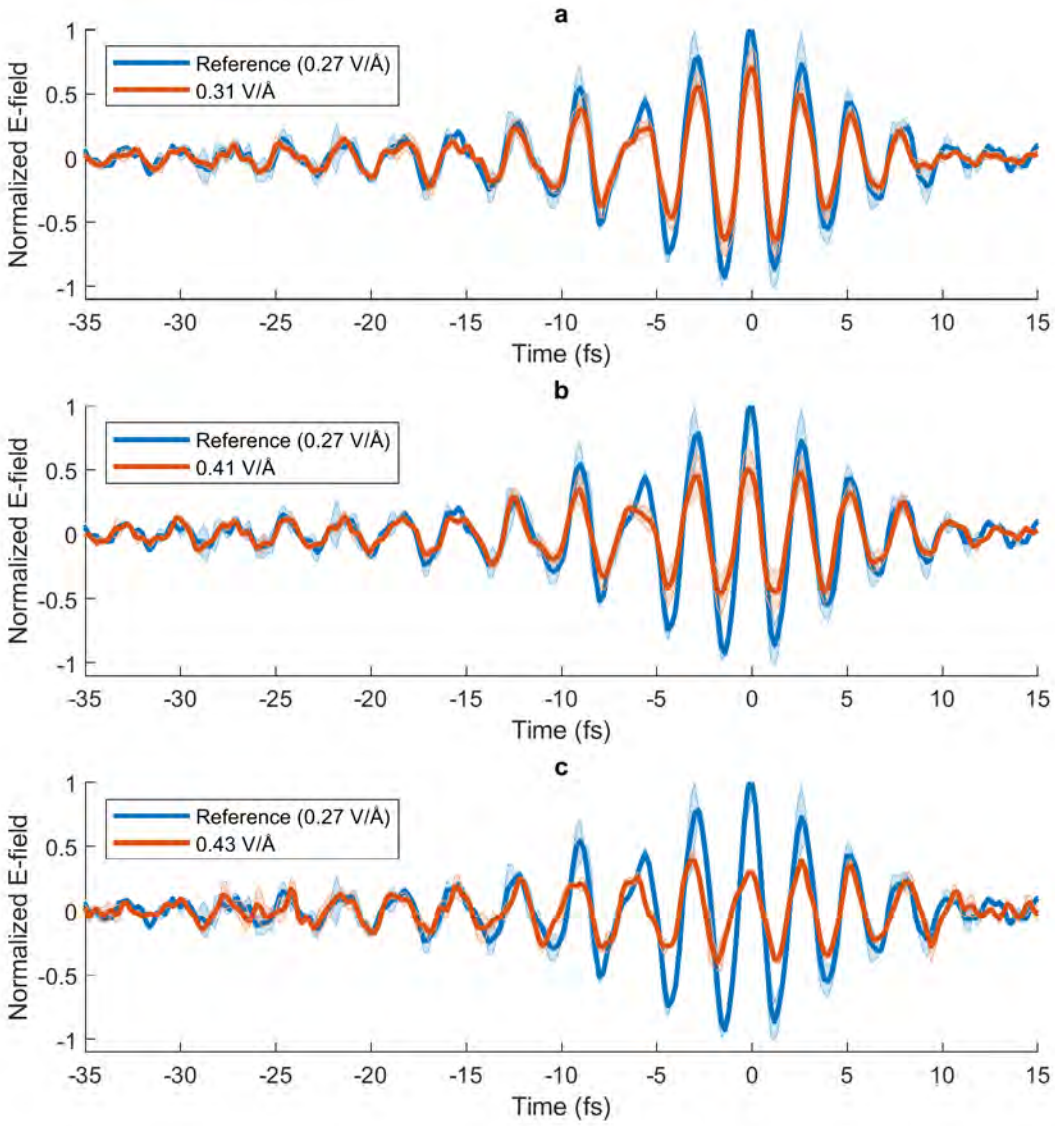

Figure 5.2: Change of measured pulse waveforms transmitted through 240±15 nm thick silicon sample at 0.31 V/Å (**a**), 0.41 V/Å (**b**) and 0.43 V/Å (**c**) incident fields strengths.

ergy transfer density can be extracted (section 1.4). In order to determine which non-linear order dominates the energy transfer, the RMS signal of the calculated time-dependent non-linear energy density was studied as a function of incident pulse field strength (Fig. 5.8). The RMS energy density was calculated as

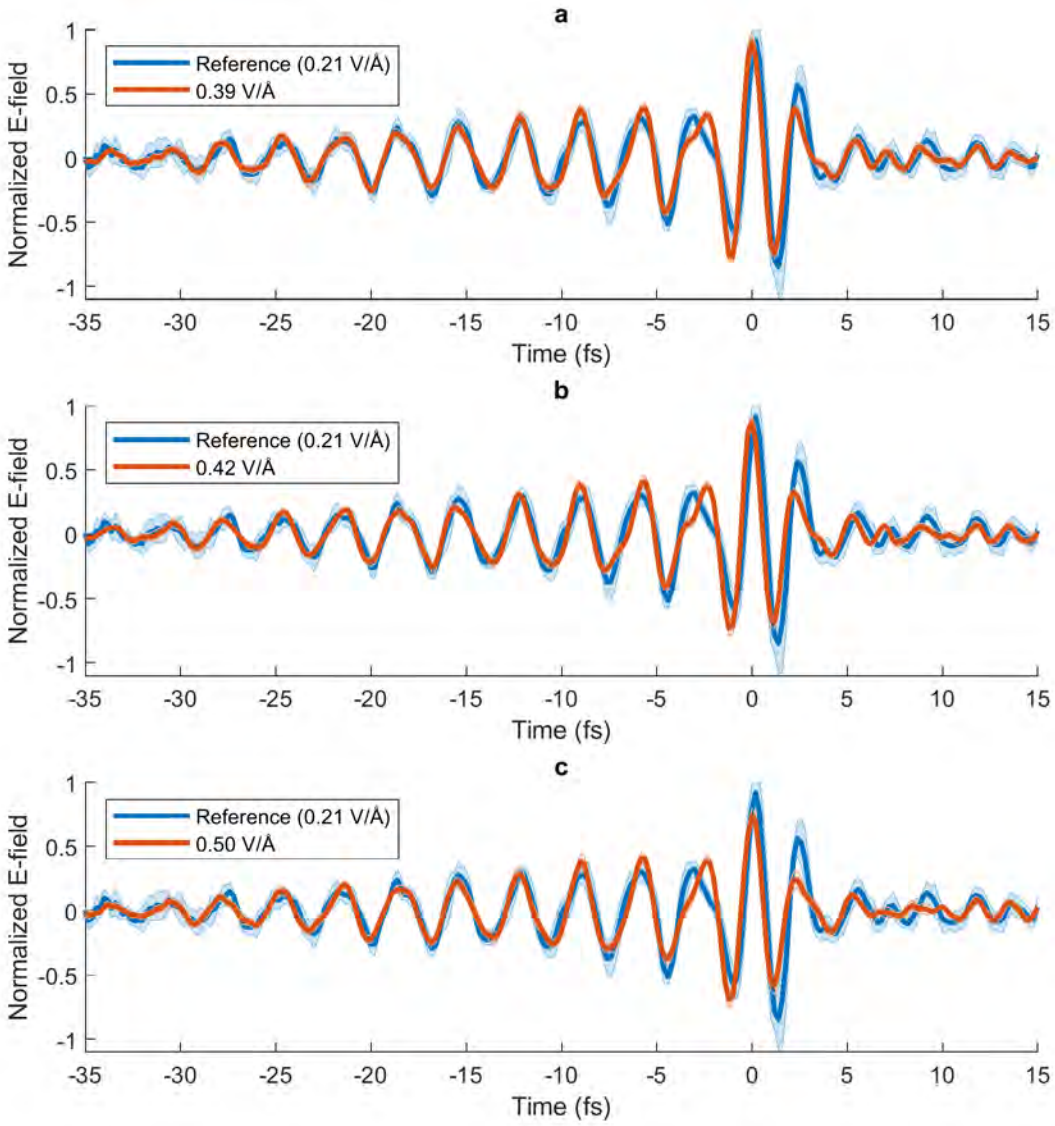

Figure 5.3: Change of measured pulse waveforms transmitted through 9.18±0.062 µm thick CVD diamond sample at 0.39 V/Å (**a**), 0.42 V/Å (**b**) and 0.50 V/Å (**c**) incident fields strengths.

$$\xi_{RMS} = \sqrt{\frac{1}{n}(\xi_{t_1}^2 + \xi_{t_2}^2 + ... + \xi_{t_n}^2)}, \tag{5.1}$$

where ξ_{RMS} is an evaluated RMS energy density, ξ_{t_n} is extracted energy density at time t_n within the measurement time window.

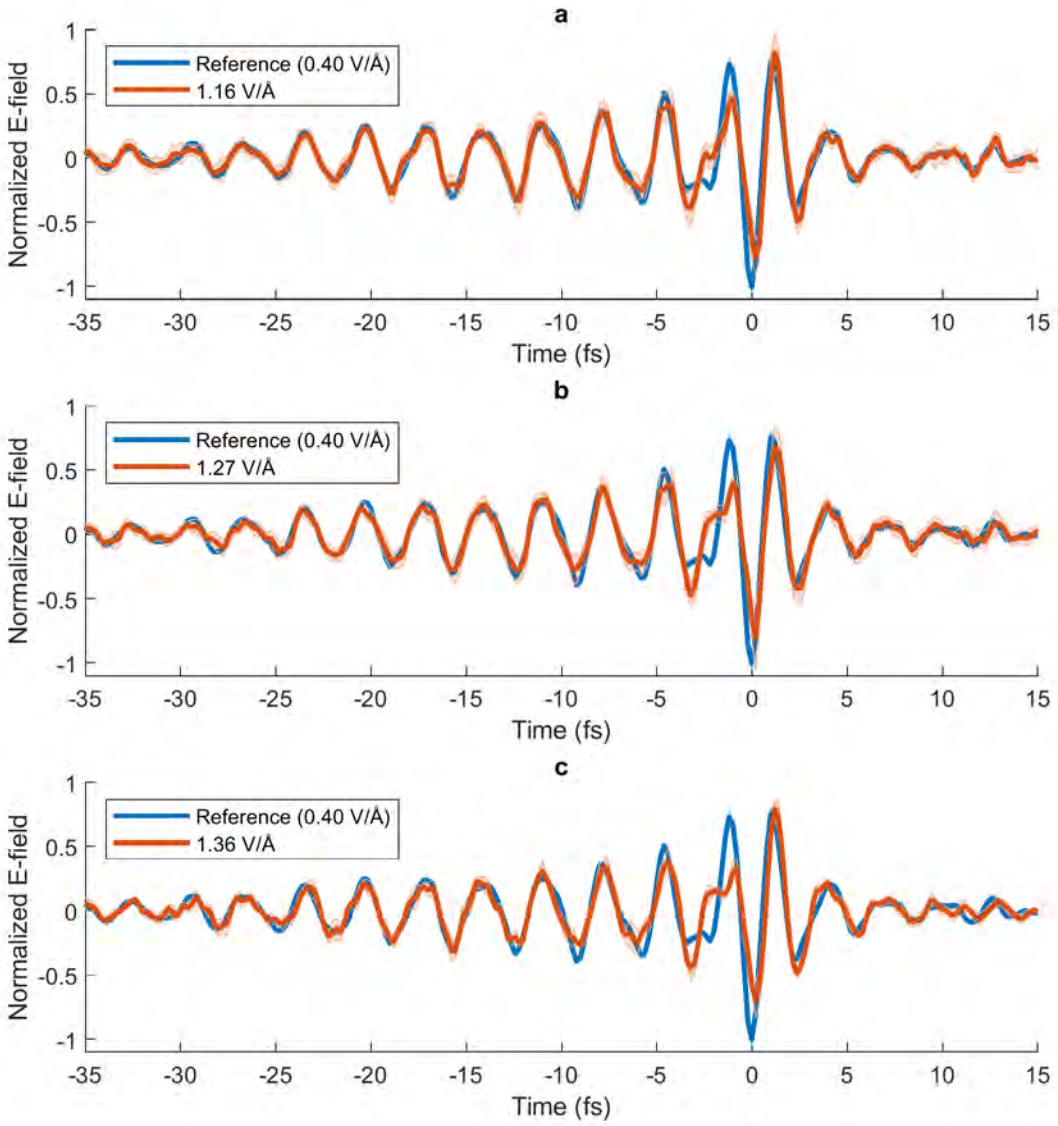

Figure 5.4: Change of measured pulse waveforms transmitted through 121±8 nm thick SiO_2 sample at 1.16 V/Å (**a**), 1.27 V/Å (**b**) and 1.36 V/Å (**c**) incident fields strengths.

Since the energy stored in the electromagnetic field of a pulse is proportional to the square of the electric field, the scaling of the RMS signal of the calculated time-dependent non-linear energy transfer is related to the number of photons that were simultaneously absorbed to cause the light-matter energy transfer. Fig. 5.8a,b indicate that energy transfer due to interaction of an incident pulse with a silicon sample is dominated by excitation of charge carriers from the valence to the conduction band by means of absorption of

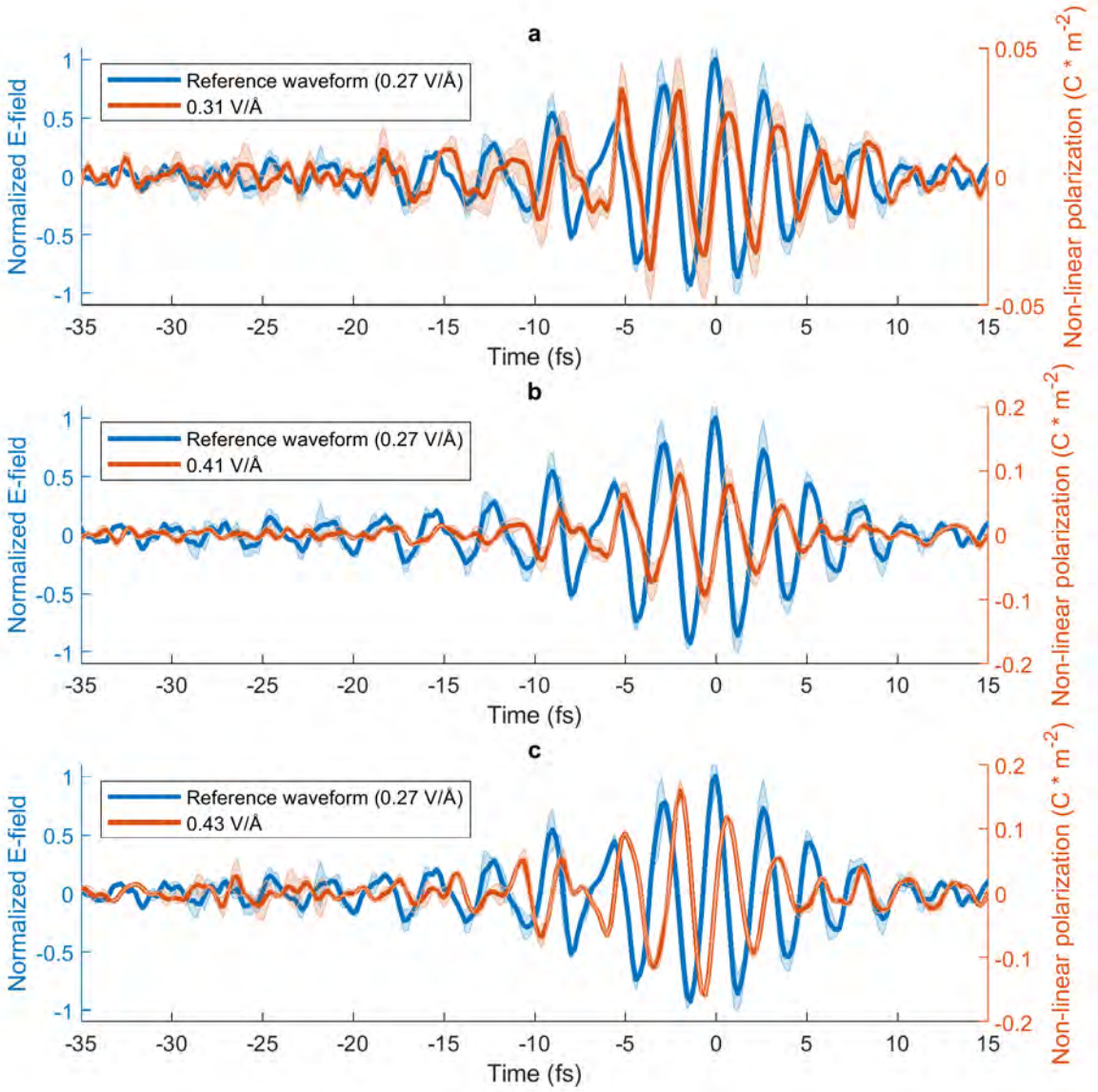

Figure 5.5: Non-linear polarizations extracted from comparison of reference and strong pulse waveforms transmitted through the silicon sample at 0.31 V/Å (**a**), 0.41 V/Å (**b**) and 0.43 V/Å (**c**) field strengths.

three photons, since E^6 scaling is observed (the carrier injection rate is approximately proportional to the energy deposition rate[92, 93]). In a similar manner, the energy transfer is dominated by the excitation of charge carriers from the valence to the conduction band in the diamond sample (Fig. 5.8c,d) due to four-photon absorption. In the SiO_2 case, however (Fig. 5.8e,f), at low field strengths the energy transfer is dominated by a third

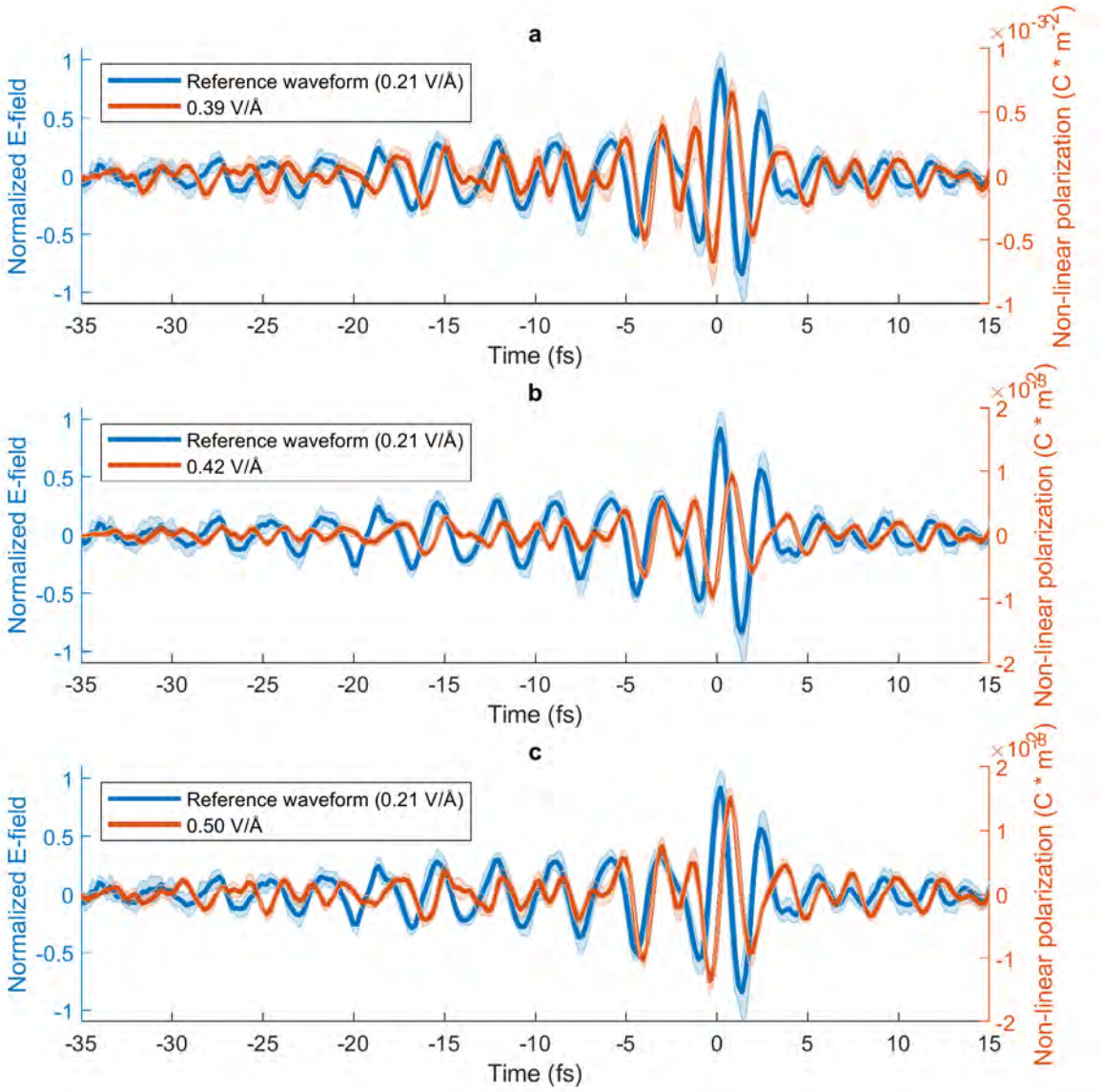

Figure 5.6: Non-linear polarizations extracted from comparison of reference and strong pulse waveforms transmitted through the diamond sample at 0.39 V/Å (**a**), 0.42 V/Å (**b**) and 0.50 V/Å (**c**) field strengths.

order non-linear polarization due to bound electrons, that is predominantly due to optical Kerr effect and third harmonic generation. At high field strengths on the other hand, the energy transfer is dominated by the excitation of charge carriers from the valence to the conduction band due to six-photon absorption.

To investigate a *switching* nature of a medium due to excitation of charge carriers

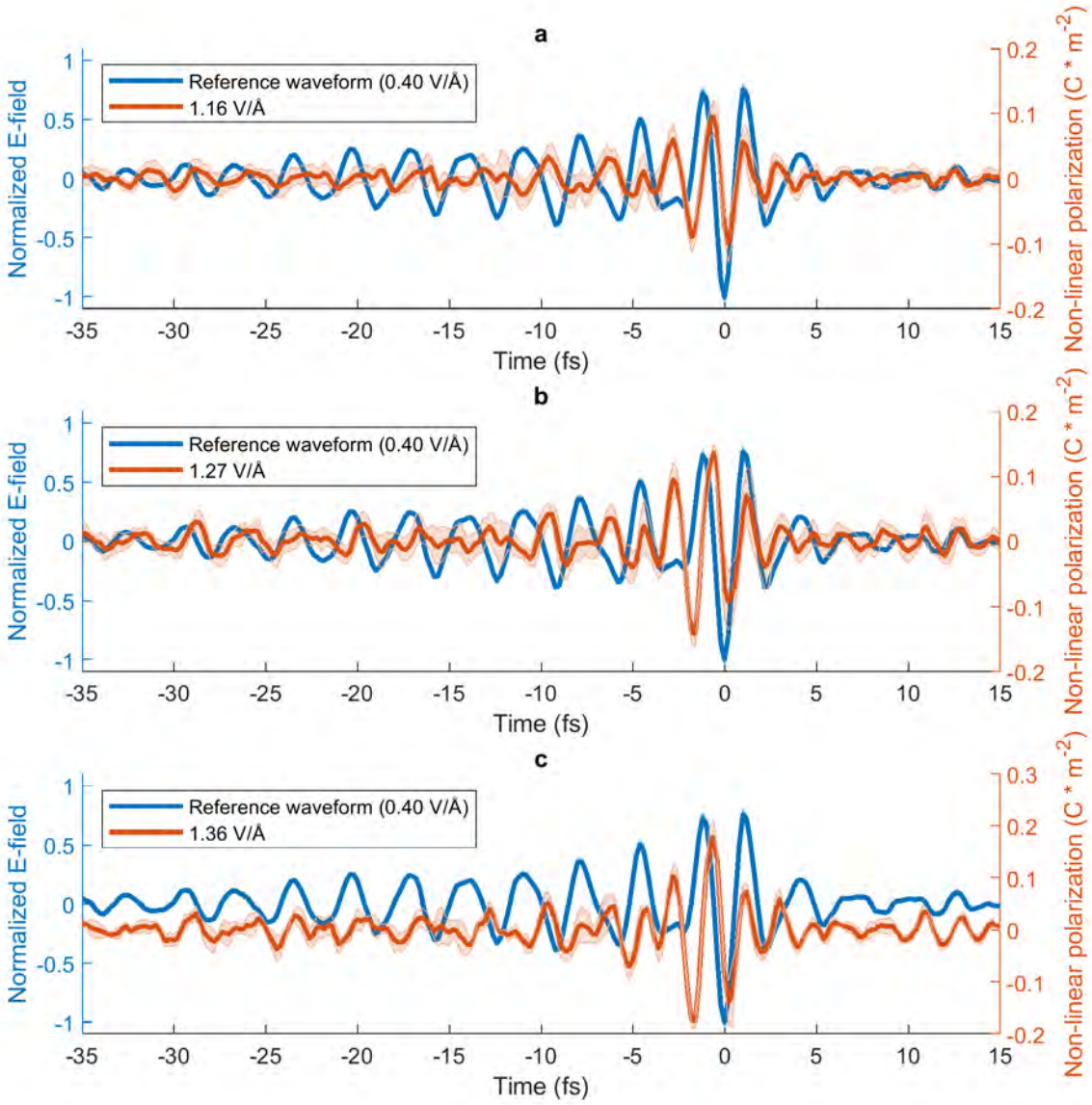

Figure 5.7: Non-linear polarizations extracted from comparison of reference and strong pulse waveforms transmitted through the SiO_2 sample at 1.16 V/Å (**a**), 1.27 V/Å (**b**) and 1.36 V/Å (**c**) field strengths.

from the valence band to the conduction band, a time-dependent energy transfer was analysed at a rather high incident field strengths. In the SiO_2 case, since the ratio between energy transfer due to bound electrons and due to injected carriers are known at any point (from the fitting of the RMS scaling), the energy transfer due to bound electrons can be subtracted from the total energy transfer to get transferred energy due to injected carriers.

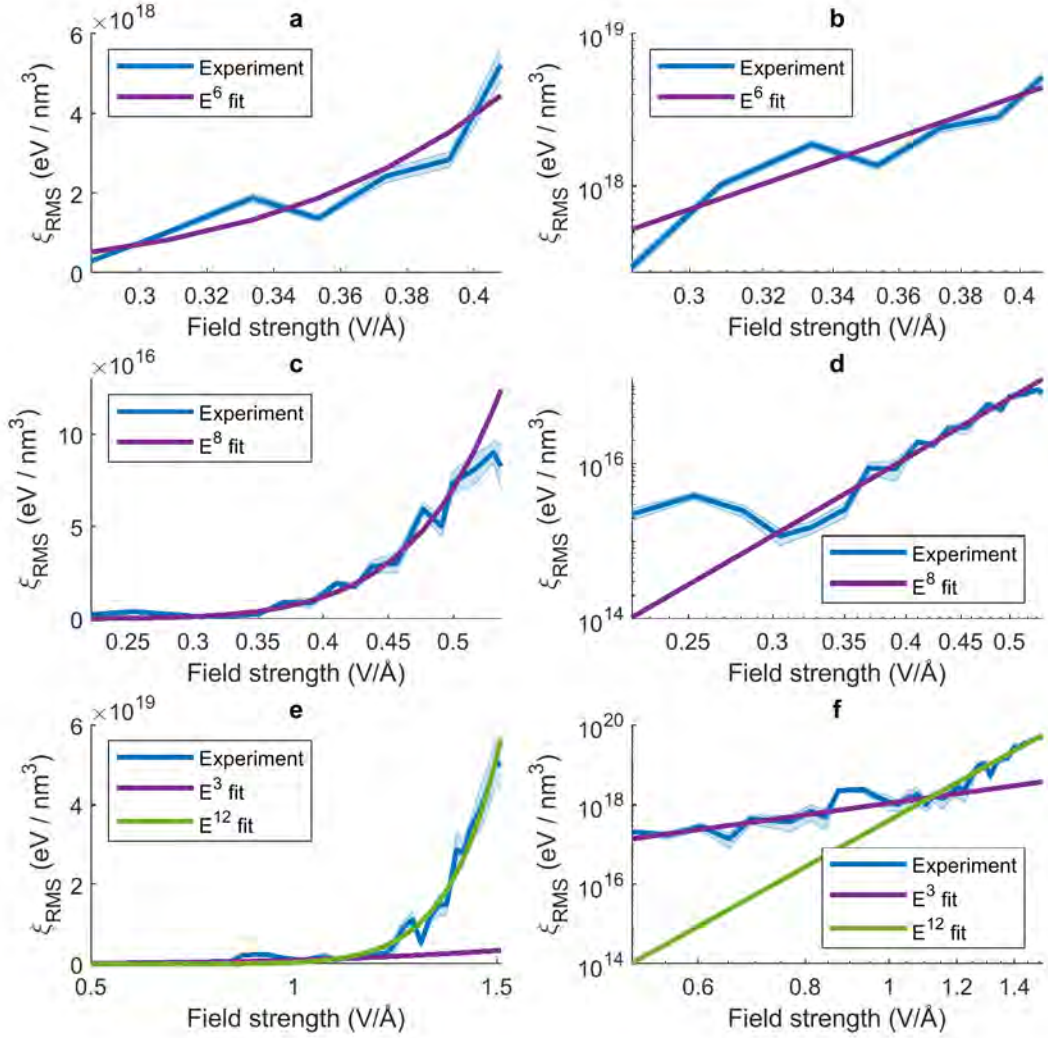

Figure 5.8: (**a**) - linear and (**b**) - logarithmic representation of the dependence of an RMS energy density on an incident pulse field strength for silicon sample. (**c**) - linear and (**d**) - logarithmic representation of the dependence of an RMS energy density on an incident pulse field strength for diamond sample. (**e**) - linear and (**f**) - logarithmic representation of the dependence of an RMS energy density on an incident pulse field strength for SiO_2 sample.

Fig. 5.9 shows time-dependent energy transfers dominated by injection of carriers into the conduction band for investigated samples. The lower is the multi-photon absorption order, the less abrupt energy transitions are observed.

In order to quantify the 'sharpness' of the energy transfer due to multi-photon injection of charge carriers, the transition that corresponds to the strongest peak of the incident

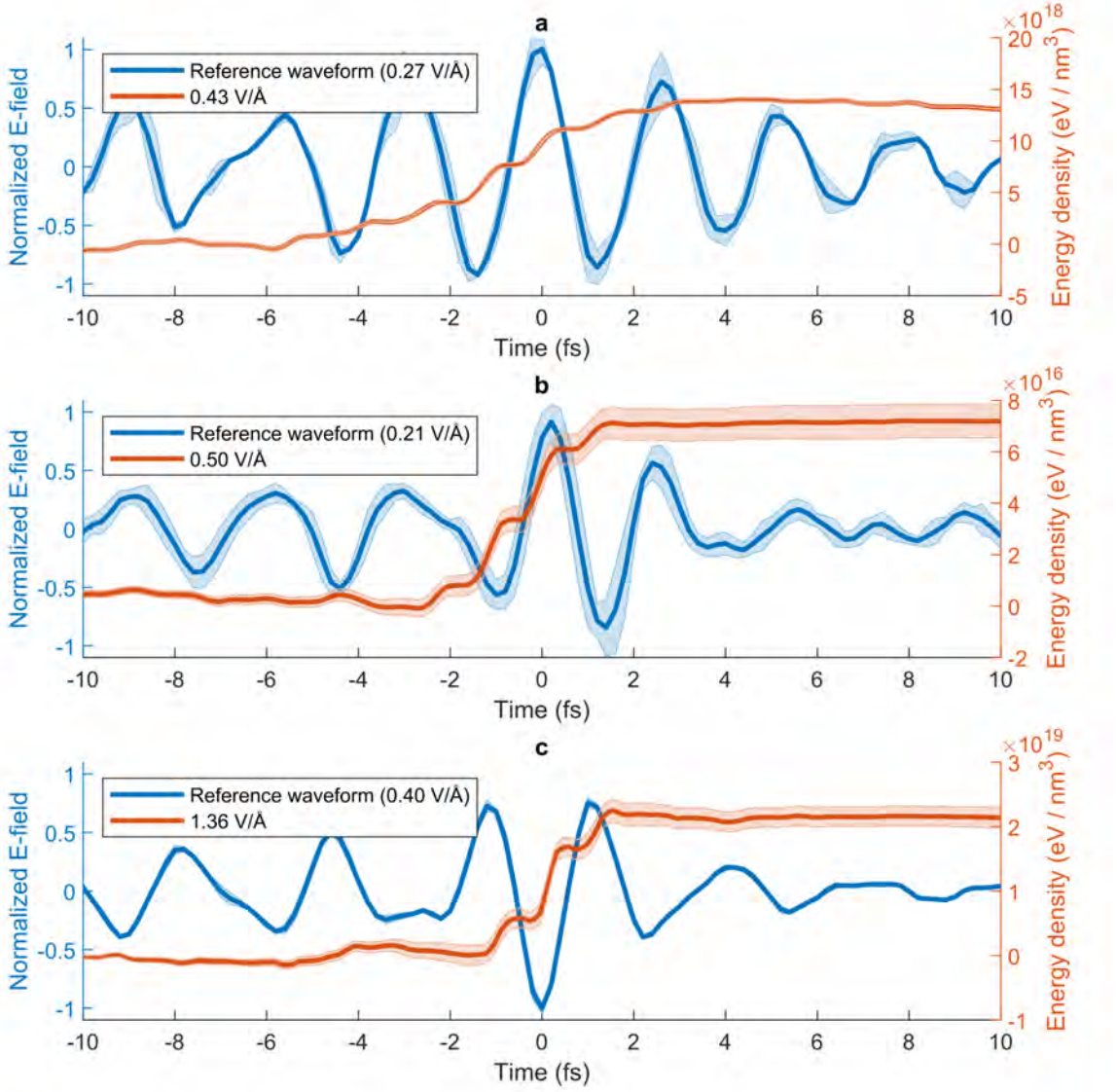

Figure 5.9: Time-dependent energy due to the non-linear component of the work performed by the incident electric field transferred to the excitation of charge carriers from the valence to the conduction band. (**a**) - silicon, (**b**) - diamond, (**c**) - SiO_2.

pulse was analyzed. Fig. 5.10a shows a normalized time-dependent energy transfer that corresponds to the strongest peak of the incident pulse. Due to a large multi-photon absorption order, the SiO_2 medium provides the sharpest transition. To quantify the time of the transition, the transition rate was calculated by taking a time derivative of the energy transfer Fig. 5.10a. The shortest transition corresponds to the SiO_2 sample with

a duration of 514±50 as (FWHM of the transition rate). Transition in diamond takes 571±10 as, while in silicon 692±25 as.

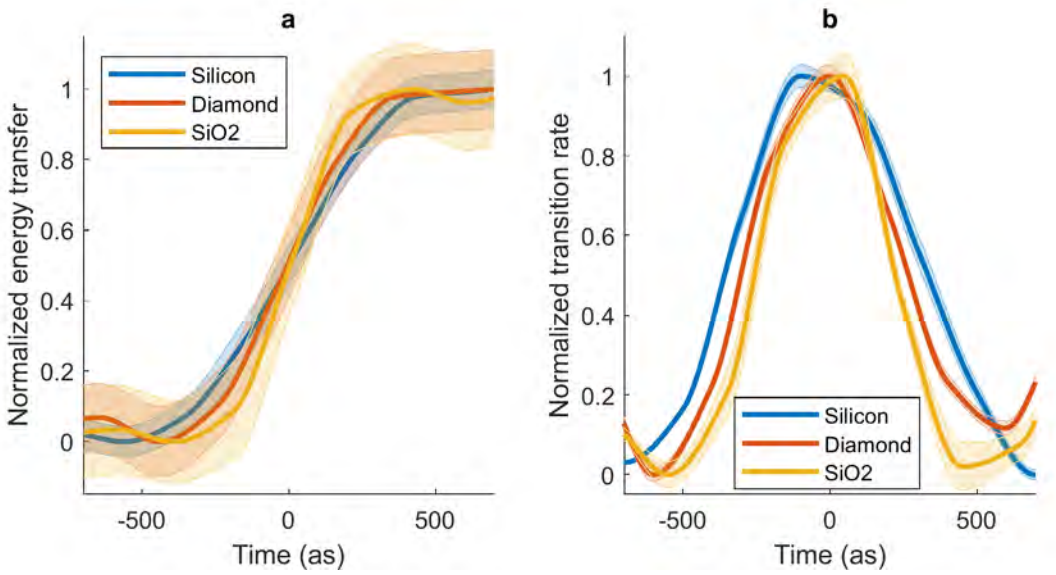

Figure 5.10: (**a**) Normalized time-dependent energy transfer due to interaction of silicon, diamond, and SiO_2 samples in the vicinity of the strongest electric field of the incident optical pulse. (**b**) Normalized time-dependent rates of transitions presented in (**a**).

As can be seen in Fig. 5.9, the excitation of charge carriers corresponds to step-like energy transfer, because excited carriers remain in the conduction band until full relaxation back to the valence band takes place. Since the process of this relaxation (recombination) is rather slow (∼ps-ms time scale[124, 125]), on a femtosecond time scale, the relaxation is negligibly small.

For the fast optoelectronic computation based on switching of a medium, it is essential that the optical properties of a medium can not only be altered quickly, but also that the medium can be brought back to its original state as quick as possible. The effect of a slow recombination of excited carriers puts a limit of a modulation of optical properties of a medium, since the return to the original state is on the order of ps-ms. However apart from a modulation of a medium due to injection of charge carriers, similar modulation can be performed due to perturbation of bound charges, such as modulation of a refractive index via perturbative medium non-linearity. In order to study a modulation of a medium based on bound electrons, regime where the energy transfer due to injected carriers is negligible small was analyzed. Such regime (Fig. 5.8) can be observed in SiO_2 medium at low incident field strengths, since the dependence of such energy transfer on the incident field strength (E^3) is much smaller than the dependence of the carriers excitation (E^{12}). Fig. 5.11a shows measured energy transfer in the regime where contribution from bound charges dominates the contribution from injection of charge carriers. The transferred energy has an *envelope-like* shape, in contrast to the carrier injection case where it has a *step-like* shape. The

pulse-like shape implies that the medium *gains* energy and then *loses* it. This process of light-matter-light energy transfer is confined in about 3.5 fs which is approximately 1 cycle of the incident pulse waveform. This implies that the optical properties of a medium are modulated within the temporal window of the energy exchange (singe the direction of the energy flow reverses).

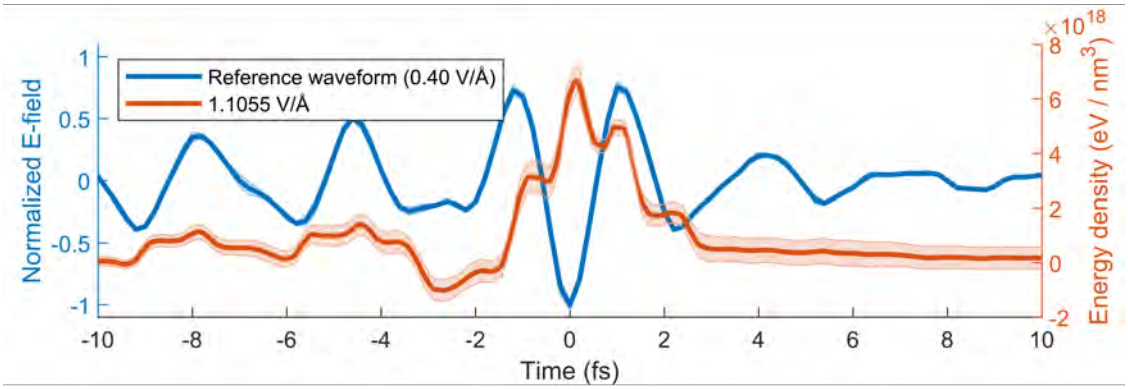

Figure 5.11: Time-dependent energy transfer due to interaction of SiO_2 sample with an incident pulse in the regime where energy transfer due to bound charge carriers dominates.

In summary, a time-resolved light-matter interaction between few-cycle laser pulses centered at about 750 nm wavelength and several solids were studied. The solids were chosen to provide three, four, and six-photon non-linear off-resonant excitations of charge carriers. The transition times associated with a non-linear energy transfer due to excitation of carriers as well as due to non-linear polarization of bound charge carriers with a half-cycle were found to be 692±25 as in silicon, 571±10 as in diamond sample, and 514±50 as in SiO_2 sample. For considered experimental conditions, in silicon and diamond samples the non-linear energy exchange is dominated by the injection of charge carriers into the conduction band. In the SiO_2 medium, two non-linear energy exchange regimes were identified. At high incident pulse field strengths, the non-linear energy exchange is dominated by excitation of charge carriers, and therefore can be used for ultrafast switching of medium properties. At lower incident pulse field strengths the non-linear energy exchange is dominated by transient non-linear response of bound charges. The energy exchange due to interaction with bound charges is confined to about one cycle of the incident field, and therefore can be used for ultrafast modulation of medium optical properties.

Chapter 6

Attosecond control of the optical properties of solids

Chapter 5 describes the study of the non-linear polarization created due to interaction of a medium with strong incident pulses. The light-matter interaction causes an energy exchange between an incident light and a medium. The time-dependent energy exchange within one half-cycle can be confined to a time window of several hundreds attoseconds. Such confinement provides an attosecond switching gate for modification of optical and electronic[52] properties of a medium. Ultrafast switching of the optical properties can be used to induce localized changes on optical pulse waveforms and therefore for pulse waveform manipulation. These tailored changes can also be considered as a piece of information that can be transmitted and further read out by a pulse waveform measurement. The amount of such information that can be stored on a pulse waveform is therefore determined by a temporal confinement of the localized changes. In addition, controlled laser fields have recently led to many important studies in the interaction of light with solids[126, 65, 127, 128]. Hence understanding optical-field response of solids to sub-cycle photo-injection is essential for advancing optoelectronics towards faster computations.

In chapter 5, a single pulse was used to modify and test the properties of several media, therefore the switching event was synchronized with the waveform of the incident pulse, and occurred at a fixed time (strongest parts of the pulse) with respect to the pulse waveform. This provides a very limited control, since the same pulse is responsible for the photo-excitation and probing of the medium.

This problem can be solved when two pulses interact with a medium. The first pulse (injection) is set to be strong to modify properties of a medium and to provide the switching gate by a non-linear interaction with a medium. The second pulse (test) is set to be weak, such that its interaction with the sample medium is linear, and therefore by itself, the test pulse does not photo-excite charge carriers from the valence to the conduction band, but can *test* the modification of the medium response induced by the injection pulse. The time delay of the injection[129] pulse with respect to the test pulse is equivalent to the time delay of the switching gate with respect to the test pulse. The measured transmitted waveform of the test pulse, at various delays with respect to the injection pulse, therefore

provides information about the non-equilibrium dynamics that perturbs the linear optical response of a medium.

To study and use the switching dynamics of the optical properties for pulse waveform manipulation, the sample medium was altered *during* the presence of the test pulse at various delays. The results of the study are described in section 6.1.

6.1 Optical-field response of solids to sub-half-cycle photo-injection

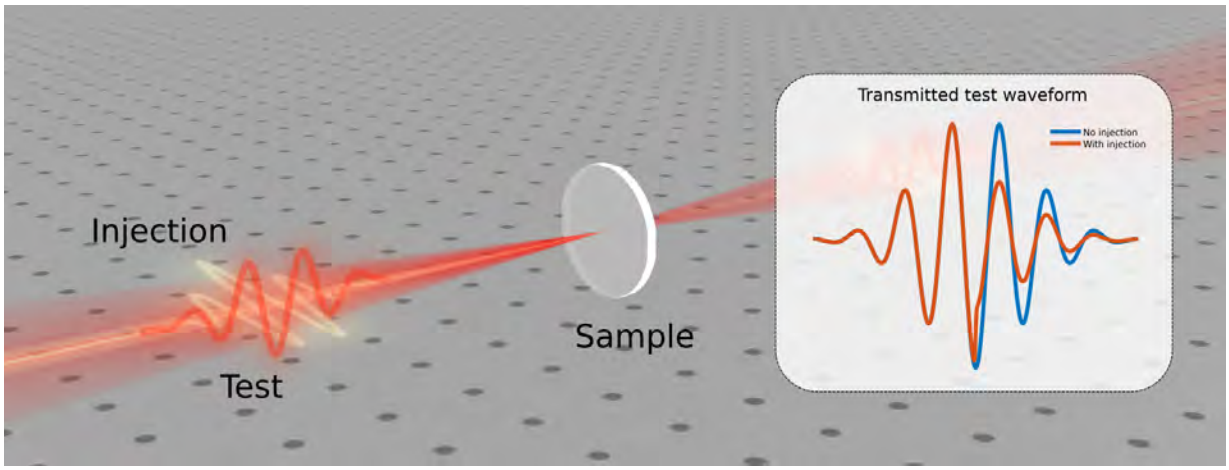

Figure 6.1: Schematic concept of the experiment. Injection pulse modifies properties of the sample during a propagation of the test pulse through it. Depending on the time of the photo-injection, the transmitted test waveform exhibit different modifications of its pulse waveform.

The non-linear interaction of an intense laser pulse with a medium can confine the event of 'switching' to a fraction of the pulse. The switching event[22] can be transient (as in the case of the optical Kerr effect) or non-transient due to inter-band excitation of charge carriers. Such an extreme temporal confinement of photo-injection also leaves a solid in a highly non-equilibrium state that will determine a non-equilibrium optical properties.

Attosecond temporal resolution as well as the high sensitivity of the heterodyne field detection approach (sections 2.2) allow the study of very fast processes with high precision. To exploit these advantages the fast non-equilibrium dynamics of charge carriers during and after photo-excitation was studied. Fig. 6.1 shows a schematic concept of the experiment. Injection pulse transiently modifies properties of a sample medium, while the test pulse experiences modification of its transmitted pulse waveform due to sudden changes of the linear response of a medium.

A $\sim$ 3 fs linearly-polarized near-infrared injection pulse was used for a photo-excitation of silicon and fused-silica samples by a multiphoton absorption. A weak $\sim$ 12 fs test pulse

is transmitted through the sample medium at various delays with respect to the injection pulse. The 2.2 µm central wavelength of the test pulse corresponds to an oscillation period of 7.5 fs, therefore the photo-injection event is well confined to a single half-cycle of the test field. The relatively long period of the test field is beneficial for studying light-driven electron motion. To decouple this motion from photo-injection, the pump and test pulses were polarized orthogonally to each other[130]. The detailed description of the experimental setup is provided in section A.2.5 of this thesis.

Fig. 6.2 shows typical test and injection pulses used in the experiment. As can be noticed, most of the energy of the injection pulse is confined within a half-cycle of the test pulse. Since the two most important processes responsible for the change of optical properties (Kerr effect and carrier injection) are non-linearly proportional to the incident injection electric field, the confinement of the switching gate responsible for the transition from unperturbed medium to perturbed is confined within a *sub-half-cycle* duration of the test pulse.

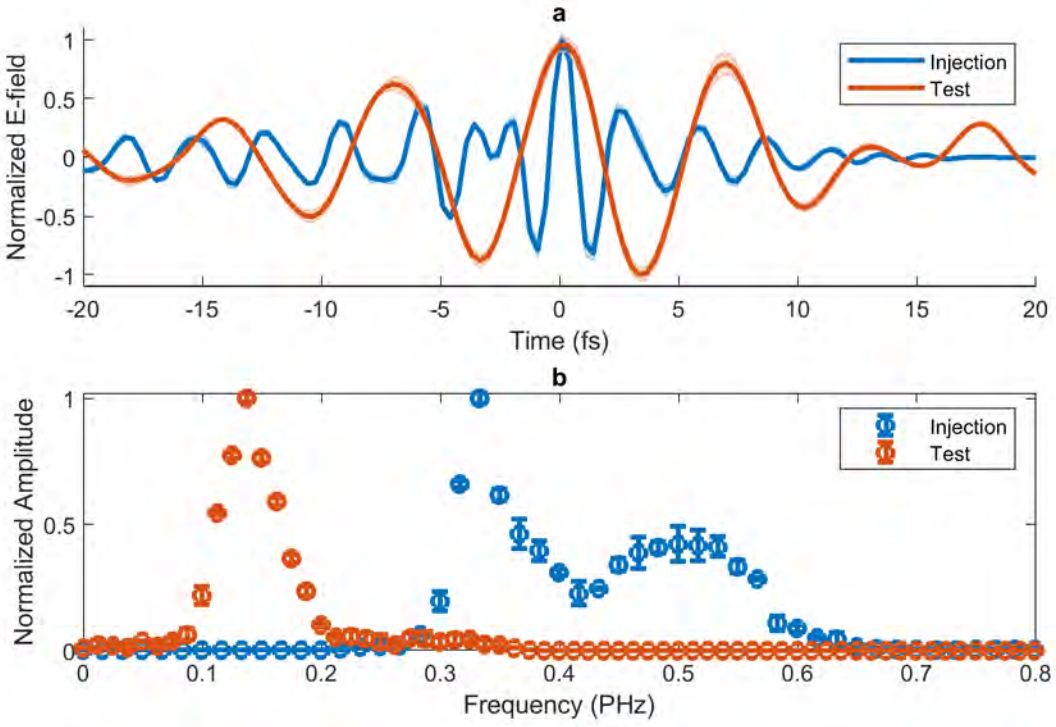

Figure 6.2: (**a**) Typical injection and test pulse waveforms used in the experiment. (**b**) Spectral amplitudes of injection and test pulses obtained by a Fourier transformation of pulse waveforms.

Fig. 6.3a shows test pulse waveforms transmitted through Si sample at several delays with respect to the injection pulse. In the first case the injection of carriers occurs long before the arrival of the test pulse (-130.8 fs). In this case the entire test pulse waveform

travels through the modified medium, and therefore the entire test pulse waveform is affected. In the second case, the injection occurs *during* the propagation of the test pulse through the medium. In this case the head of the test waveform travels through the non-modified medium while the tail of the test pulse travels though the modified medium. From the comparison of the reference and modified waveforms one can see that modified waveform experiences a phase shift (injection of charge carriers creates an electron-hole plasma, thus reducing the real part of the refractive index). The modified waveform also exhibits an attenuation of the transmitted electric field (injection of charge carriers causes an absorption). The pulse waveform modifications can be related to the changes of real and imaginary parts of the medium refractive index. The phenomenological model of the time-dependent refractive index developed within the frame of this study is in an excellent agreement with experimental results (Fig. 6.3c,d).

Since the injection time window is confined to the duration smaller than the half-cycle of the test pulse, even a small change of the time delay between two pulses causes dramatic difference in the measured test waveform change. Such conditions also imply that injection at zero-crossings of the test pulse may impose different changes to the test pulse waveform comparing to injection at the peaks of the test pulse waveform (Fig. 6.3b). As can also be seen on Fig. 6.3b, the significant changes in the measured difference occur only within a very short time window of the carrier injection.

Fig. 6.3c shows changes in the test pulse waveform by slicing the injection pulse through the test pulse. The mechanism can be seen as *light-matter-light* interaction. The injection pulse induces semi-instantaneous changes in the *linear* optical properties of the sample medium. The modification of optical properties of the sample medium induce changes on the transmitted test pulse waveform. When the medium properties can be controlled in time, so is the transmitted test pulse waveform can be controlled in time. The experimental setup therefore can also be seen as a switching device for *tailoring* of pulse waveforms.

Quasi-abrupt changes in the test waveform seen on Fig. 6.3c imply a quasi-abrupt changes in the optical properties of a sample medium, which can be now measured directly.

The real part of the refractive medium is mainly responsible for the dispersion of a meadium, while the imaginary part for the absorption (section 1.4). The dispersion of a medium would normally reshape the optical pulse, however if the sample is thin, and the medium dispersion is small, then the time-shift of the test pulse waveform is expected to approximate a change of the real part of the refractive index, while the change of the field magnitude to approximate the change of the imaginary part of the refractive index.

To extract this information positions of zero-crossings and magnitudes of the test pulse waveform peaks were measured versus the time delay between the test and injection pulses.

Fig. 6.4 shows measured test pulse waveform as well as zero-crossing/peak-magnitude analysis for several peaks and zero-crossings of the test field. It can be concluded that since various zero-crossings as well as field peaks (of different magnitude and sign) provide the same results, the interaction of the test pulse with the sample medium is linear and the test pulse merely probes changes in a medium induced by the injection pulse.

In order to confirm that the measured temporal shifts of zero-crossings as well as magnitude changes of peak fields are indeed provide an information about very first dynamics

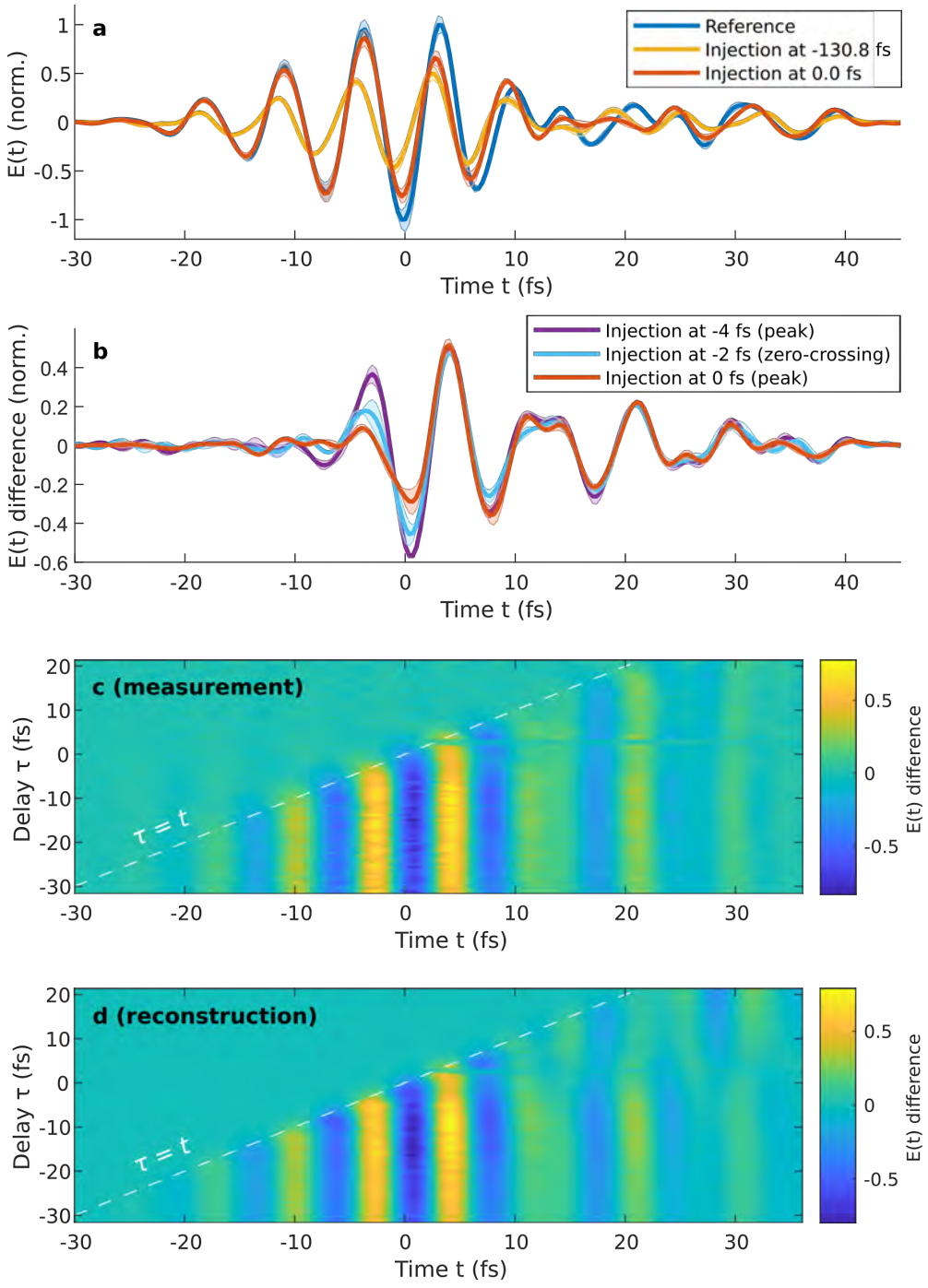

Figure 6.3: (**a**) Measured test pulse waveform signal transmitted though a Si sample at two delays with respect to the injection pulse. (**b**) Difference between reference and modified waveforms for the injection occurring within a vicinity of a zero-crossing and peaks of the test pulse waveform. (**c**, **c**) Time dependent changes of the test waveform vs injection time.

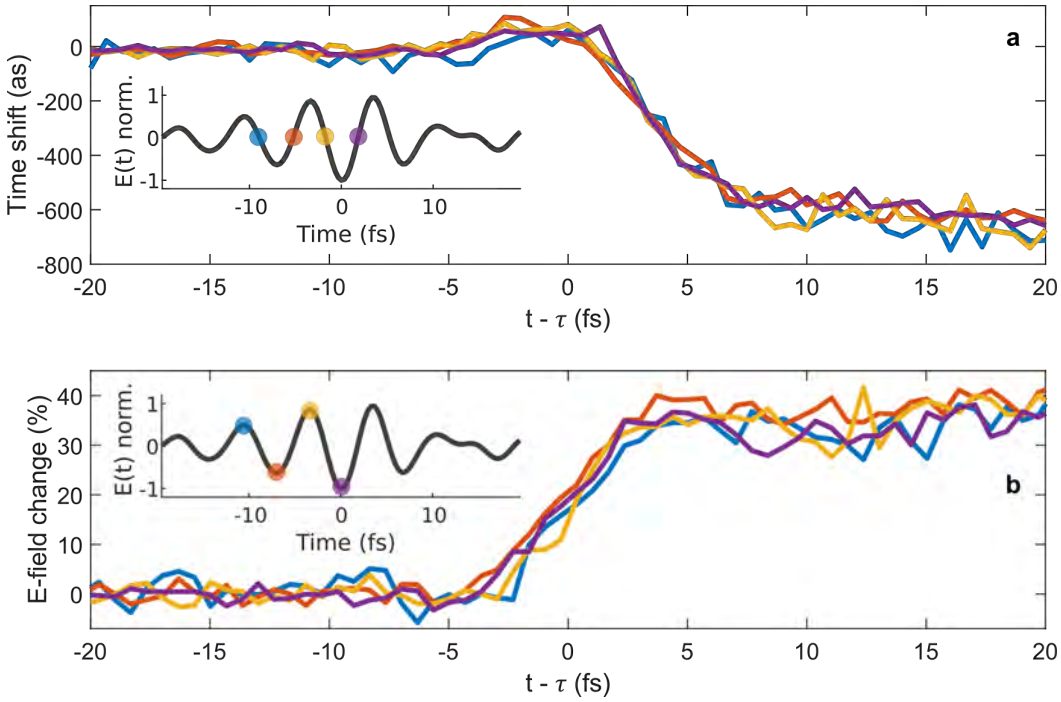

Figure 6.4: (**a**) Injection-delay dependent time shift of several zero-crossings. (**b**) Injection-delay dependent E-field magnitude change of several peaks. t is time, while τ is a delay with respect to the time of a zero-crossing or a E-field peak. The insets show reference test waveform transmitted through a sample without injected charge carriers. The markers on the reference waveform show which zero-crossings and peaks were considered for the analysis.

of the medium refractive index modifications, the process was theoretically modelled as described in more detail in [130]. Fig. 6.5 shows experimental results based on zero-crossings shifts and peak fields magnitude change (evaluated by averaging over four half peaks and four zero-crossings) of the test waveform together with a time-dependent refractive index extracted by the theoretical model. The solid lines are the theoretical results obtained by applying the same analysis to the reconstructed waveforms. The shaded green area represents an injection pulse envelope obtained from the measured injection pulse waveform presented on Fig. 6.2. By comparison of left and right panels on Fig. 6.5 one can conclude that the temporal shift of zero-crossings exhibits very similar temporal evolution as the real part of the refractive index. On the other hand, the change of the peak field magnitudes provides a similar information as a temporal evolution of the imaginary part of the refractive index. Hence, the analysis of zero-crossings and peak magnitudes delivers a new and very simple method for study of the dynamics of the non-equilibrium properties of a medium with a temporal resolution determined by a measurement technique.

As can also be seen on Fig. 6.5, the switching of the refractive index due to photo-excitation is more abrupt in fused silica medium in comparison to silicon. This can be

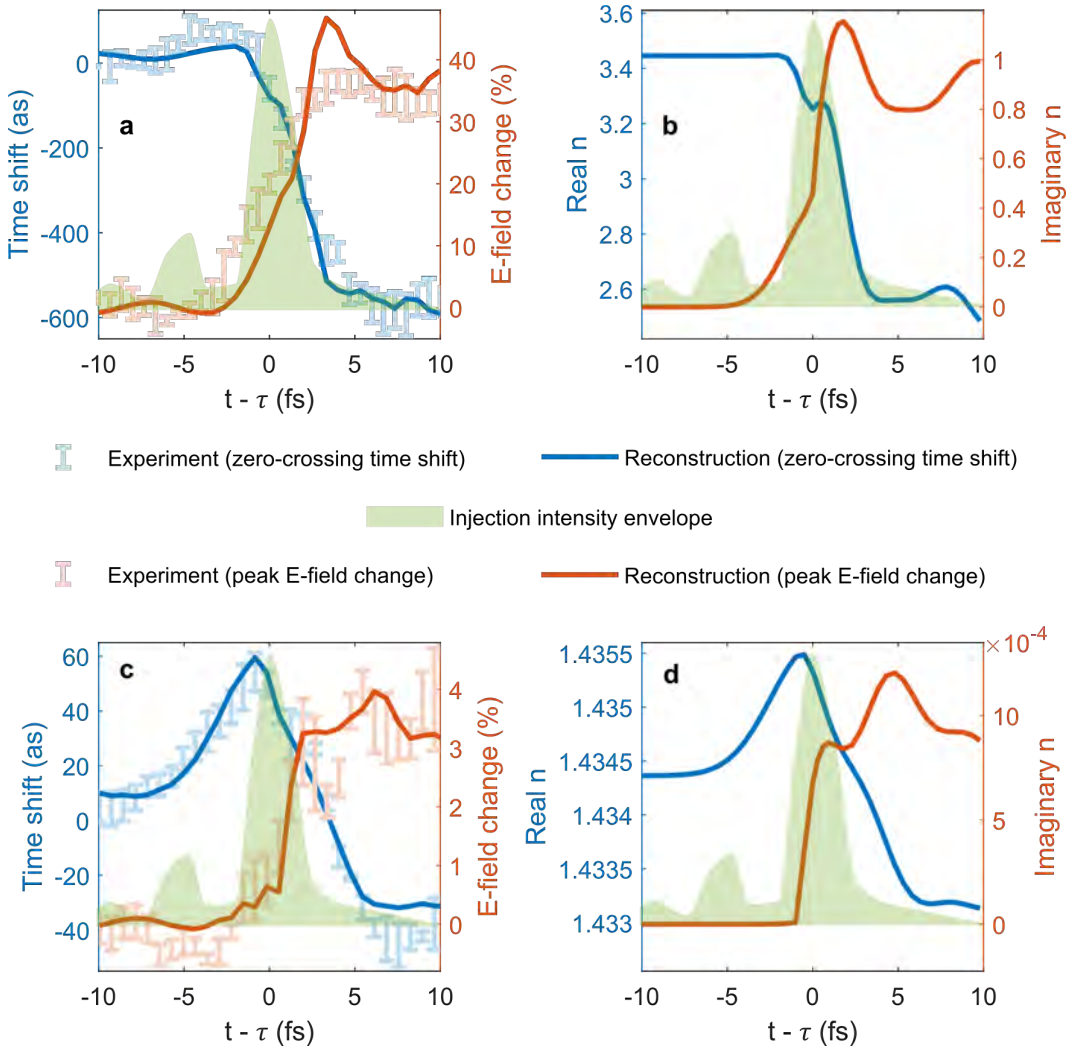

Figure 6.5: Zero-crossings phase shift and peaks E-field change as a function of injection delay for silicon (**a**) and fused silica (**c**) samples. Reconstructed real and imaginary parts of the time-dependent refractive index for silicon (**b**) and fused silica (**c**) samples.

understood considering that the number of photons required to promote a charge carrier from the valence to the conduction band in fused silica is larger than in silicon. Therefore the photo-excitation in fused silica is more non-linear with respect to the injection pulse field, and hence the event of the photo-excitation is more confined in time. On the other hand, the induced concentration of charge carriers in silicon is expected to be much larger than in fused silica, therefore the overall changes of the optical properties in silicon are much larger in comparison to fused silica.

The transient increase of the real part of the refractive index presented on Fig. 6.5 is associated with the optical Kerr effect. The transient Kerr effect dominates the formation of non-equilibrium optical properties, until the plasma contribution takes over.

Fig. 6.5 also demonstrates that the formation of the modified refractive index takes longer than the duration of the event of photo-injection. This is particularly evident in the case of fused silica, where photo-injection is expected to be largely confined to the half wave cycle, i.e. to an interval of ≤ 1 fs, as also supported by the sharp change in the imaginary part of the refractive index. However, the formation of the perturbed refractive index is not completed even 5 fs later. When a light pulse propagates over an infinitesimally small distance, the time-dependent change of its electric field is approximately proportional to the time-dependent electric current that the pulse induces in the medium. Even if all the free charge carriers emerged instantaneously, this would not lead to an abrupt change in the transmitted waveform. Distortions would build up during the time that it takes electrons to gain momentum due to the acceleration by the test field[130].

After the formation of the non-equilibrium refractive index, the dynamics does not stop. Fig. 6.6 shows zero-crossings/peak-fields analysis of the experimental results extended to a larger time window. Since this analysis provides similar information as a temporal evolution of real and imaginary parts of the non-equilibrium refractive index (Fig. 6.5), the results suggest that the real part of the refractive index keeps decreasing, while imaginary part keeps increasing (after the photo-excitation took place). This can be understood in terms of the 'thermalization' part of the non-equilibrium dynamics. After quasi-abrupt photo-excitation of charge carriers, multiple states within the band structure get occupied forming a non-equilibrium charge distribution. As the time goes, the non-equilibrium distribution would evolve towards an equilibrium Fermi-Dirac distribution[131]. This step involves intraband relaxation of charge carriers towards the edges of conduction and valence bands. As the electrons and holes relax to the band edges, their effective masses increase. This results in subsequent changes of the medium refractive index[132].

In the following, the influence of the actual moment of the photo-excitation with respect to the transmitted test pulse waveform is studied. In particular, the addressed questions is whether it make a difference if the charge carriers are photo-injected at the peaks of the electric field of the test pulse or at zero-crossings. To answer this question experimentally, the event of photo-excitation must be confined within sub-*half* cycle of the test pulse. This is because two adjacent zero-crossings or peaks of the pulse waveform are separated by a *half-cycle* of the test field. In the present experiment the photo-excitation event is confined to the half-cycle of the test pulse (Fig. 6.2), therefore this condition is automatically fulfilled.

To experimentally observe the influence of the moment of carrier photo-injection, the energy loss of the test pulse is evaluated for all time delays between injection and test pulses. Fig. 6.7 shows that the energy loss of the test pulse clearly depends on the moment of the photo-excitation of a medium. The later the photo-excitation takes place the larger part of the pulse travels through the medium with unperturbed optical properties. In addition to this overall trend, the loss of the test pulse energy oscillates with a period of a half-cycle of the test pulse. This phenomenon can be clearly observed for fused silica sample, where the photo-injection event is largely confined to a single half-cycle of the test pulse. By itself, a sudden turn-on of absorption explains neither the oscillatory behaviour of the energy loss in Fig. 6.7b, nor the timing of these oscillations with respect to the test field.

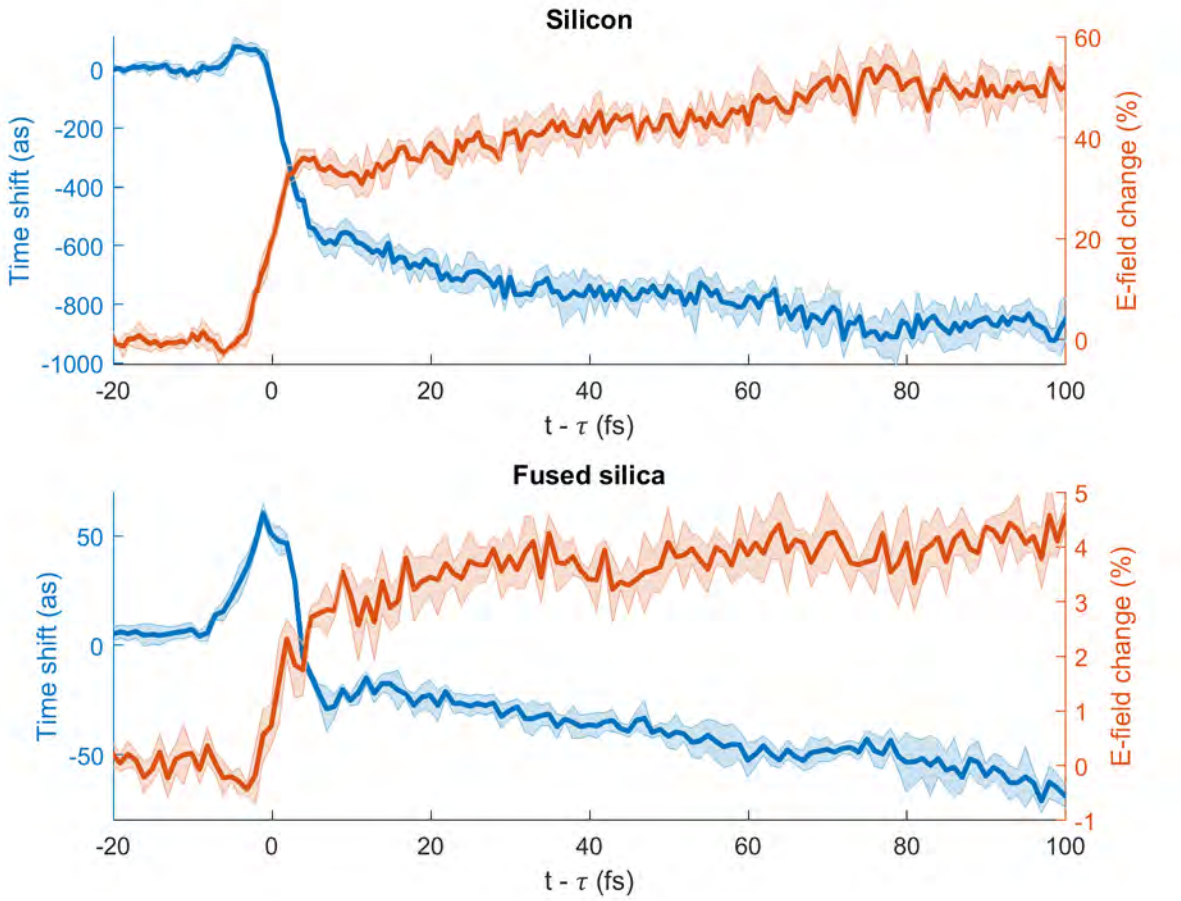

Figure 6.6: Temporal shift of zero-crossings as well as change of the peak field magnitudes as a function of the delay between injection and test pulses.

However, the observed modulations can be explained with the consideration of the energy flow from the test pulse to the kinetic energy of charge carriers[130]. The classical motion of a free electron can be estimated with a Drude-like model, where an electron's velocity obeys Newton's second law with a friction term:

$$\frac{dv}{dt} = -\frac{e}{m}E(t) - \gamma v(\tau), \tag{6.1}$$

where m is the electron effective mass, e is the elementary charge, E is the electric field of the test pulse, while γ is the momentum relaxation rate. Under the assumption that all charge carriers are created at time τ and with initial velocity, on average, zero, the Eq. 6.1 can be solved with the initial condition $v(\tau) = 0$. The test field interacting with the electron therefore performs work:

$$W(\tau) = -e \int_{\tau}^{\infty} E(t)v(t)\,dt. \tag{6.2}$$

When this work is positive, the test pulse loses energy due to classical acceleration of photo-injected charge carriers. The modelled results represented by a solid orange curve on Fig. 6.7 exhibit a very good qualitative agreement with experimentally measured test pulse energy losses. In the model described by Eq. 6.1 and 6.2, the momentum relaxation rate of $\gamma = 0.5$ 1/fs for used for the silicon medium, while $\gamma = 0.25$ 1/fs was used for fused silica medium. For fused silica, this very simple model very well reproduces both the overall trend and the sub-cycle modulation of the energy loss. According to this model, the modulation depth decreases as the relaxation rate increases, which suggests one of the possible reasons why no visible modulation was observed with the silicon sample: due to the higher concentration of charge carriers, the momentum-relaxation[133] rate in those measurements was probably larger than that in the measurements on fused-silica. There is, however, another likely reason: as opposed to fused silica, several half-cycles of the pump pulse photo-injected charge carriers in silicon, which necessarily makes sub-cycle effects less pronounced[130].

In summary, the formation of the modified optical properties in silicon and fused silica was measured with attosecond temporal resolution. It was show that non-linear mutliphoton excitation of charge carriers within a solid medium can be used as a quasi-abrupt switch of optical properties forming a modified refractive index. The abruptness and confinement of the switching event was studied in detail. For both media, the time dependence of the real and imaginary parts of the refractive index was closely matched by the temporal shift of the zero-crossings and rescaling of the test pulse peaks magnitudes. The measurements show that a fast photo-injection event does not necessarily cause an equally fast distortion of the test field, the distortion builds up as the charge carriers acquire momentum due to the interaction with the field[130]. The switching of optical properties of a medium can be used to control and manipulate optical pulse waveforms. This could provide a simple route towards transient optical field-synthesis. When the transition of the switching process becomes within a time window shorter than a half-cycle of the test pulse, one enters the regime where the actual moment of the injection plays as an additional important factor. When the injection takes place in a vicinity of zero-crossings of the test waveform, the substantial amount of energy is transferred to the classical acceleration of charge carriers. Therefore the control of the switching event in combination with a transmitted test pulse provides a light-matter-light scheme towards manipulation of optical pulse waveforms and material properties at ultrafast time scales.

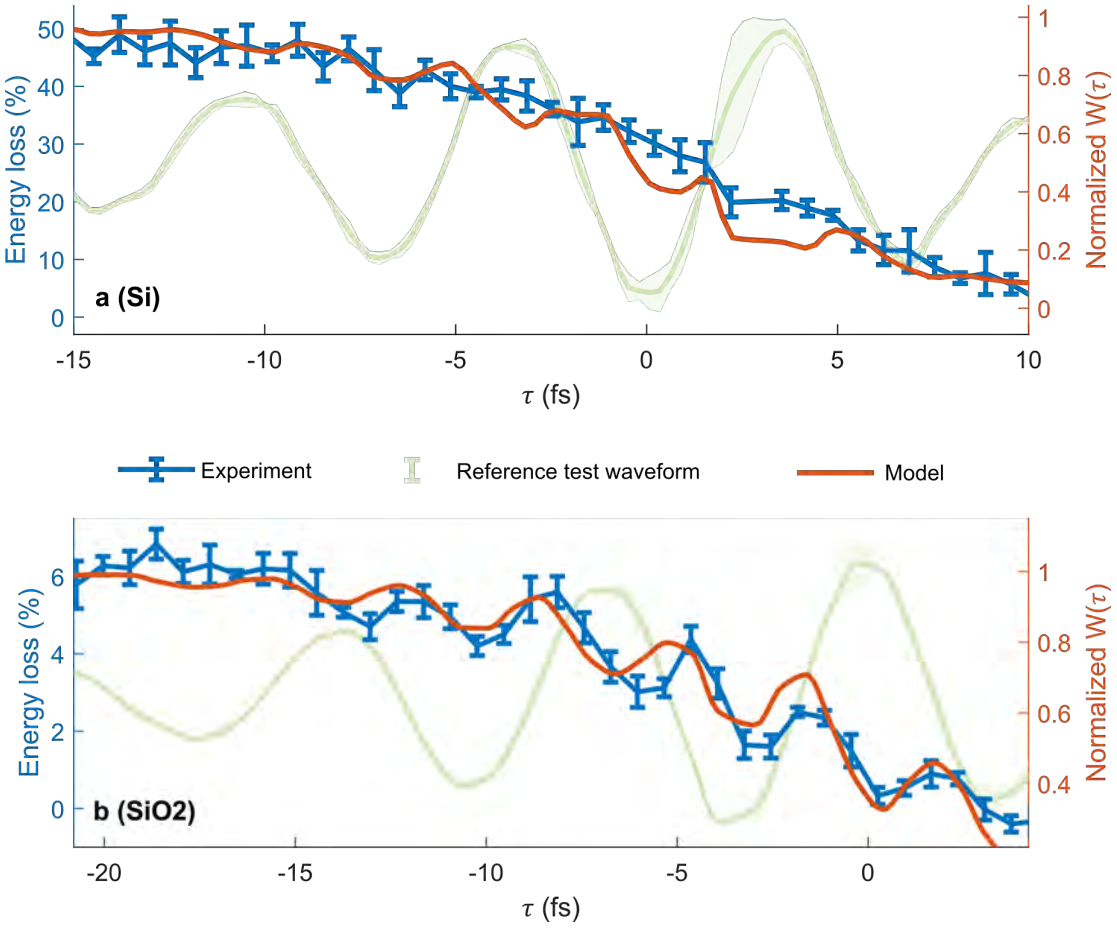

Figure 6.7: Loss of the test pulse energy as a function of injection delay.

Chapter 7

Conclusion

This dissertation introduced novel concepts for petahertz-scale pulse waveform sampling. The techniques allow performing time-resolved studies of ultrafast processes with attosecond temporal resolution, petahertz-scale detection bandwidth, and high sensitivity. Inexpensive and simple experimental setups make the technology widely accessible for a variety of scientific and commercial applications without sophisticated vacuum experimental beamlines. Pulse waveform characterization with CEP unstabilized pulses is demonstrated.

The origin of a signal source for non-linear photo-conductive sampling was studied in detail. It was found that the primary source of the signal is a medium polarization created in a medium. The gas medium can be used for the optimization of the signal. The strongest signal in the air medium is observed at several mbar pressure.

A high-frequency channel of a novel optical synthesizer was characterized with a non-linear photo-conductive sampling technique. It was found that such optical channel can be used for electro-optic sampling of synthesized waveforms approaching, for the first time, visible spectral range.

The time delay associated with a plasma formation and high order non-linear excitation of charge carriers was studied experimentally and supported with the theoretical model.

Switching and modulation of electronic and optical properties of solids were demonstrated for materials with various band gap energies. The energy deposition within one half-cycle of the experimental pulse was found to be confined (full width of the half maximum of the transition) to about 690 as in silicon, 570 as in diamond, and 510 as in fused silica media. It was demonstrated that at low incident pulse field strengths, the light-matter energy exchange can be dominated by the optical Kerr effect. Since this effect is transient, it can be used for modulation of a medium response. One the other hand, charge carrier photo-excitation can be used for ultrafast switching of medium properties.

The very first moments of the formation of the non-equilibrium optical properties due to photo-excitation were studied in detail for silicon and fused silica solids. It was shown that non-linear multi-photon excitation of charge carriers within a solid medium can be used as a quasi-abrupt switch of optical properties forming a modified refractive index. The response of the medium with modified properties was found to be non-instantaneous, as it builds up while the charge carriers acquire momentum due to the interaction with the field.

The dynamics of the medium properties continues after the event of photo-excitation. The dynamics of the real and imaginary parts of the refractive index exhibit different trends associated with the thermalization of the non-equilibrium charge distribution. For both media, the time dependence of the real and imaginary parts of the refractive index was closely matched by the temporal shift of the zero-crossings and rescaling of the test pulse peaks magnitudes. This provides a very simple method to study non-equilibrium refractive index dynamics with sub-cycle temporal resolution.

It was demonstrated that the switching of optical properties of a medium can be used to control and manipulate optical pulse waveforms. This could provide a simple route towards transient field-synthesis. When a transition of the switching process becomes within a time window shorter than a half-cycle of the test pulse, the time delay between the switching event and the test pulse can be used to control the light-matter energy exchange. When the injection takes place in a vicinity of zero-crossings of the test waveform, the substantial amount of energy is transferred to the classical acceleration of charge carriers within the medium. The control of the switching event in combination with a transmitted test pulse provides a light-matter-light scheme towards manipulation of optical pulse waveforms and material properties at ultrafast time scales.

-

Appendix A

Apendix

A.1 Laser beam-line

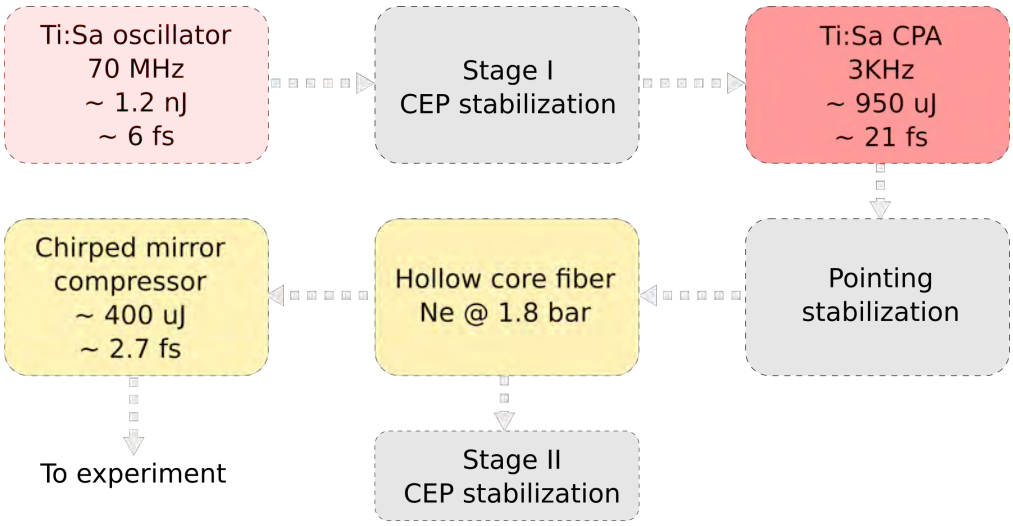

Figure A.1: Diagram of the experimental beam-line

Fig. A.1 shows a schematic of the laser beam-line[59, 119] used for experiments presented in this thesis. Ti:sapphire oscillator (Rainbow 2, Spectra Physics) provides an octave-spanning bandwidth with about $\sim$ 750 nm central wavelength. The output from the oscillator is guided through the 'stage I CEP stabilization' module based on the feed-forward scheme[119]. CEP stable pulses are then further amplified within a 9-pass cryo-cooled Ti:sapphire chirped-pulse amplifier at a repetition rate of 3 KHz, and temporally compressed using a transmission grating-based compressor yielding $\sim$ 21 fs pulses with $\sim$ 2.5 W output power. The amplified pulses are further spectrally broadened in a hollow-core fiber filled with neon gas (1.8 bar pressure) resulting in a spectral broadening to a bandwidth of about 400 - 1100 nm. The chirped mirror compressor consisting of 3 pairs of chirped mirrors in combination with about 6 mm of fused silica glass and 50 cm of air

is then used to compress the broadened spectrum to about $\sim$ 2.7 fs (FWHM) duration pulse[3]. The pulse duration is based on the intensity envelope of the complex-valued analytic wave, whose real part is the electric field measured by NPS, and the imaginary part is the Hilbert transform of the field. The compressed pulses are then guided to an experimental setup for further experiments. The small fraction of spectrally broadened light is reflected from the Brewster window of the hollow core fibre sealing and guided to the 'Stage II CEP stabilization'. The 'Stage II stabilization' is based on the f-to-2f technique as described in details elsewhere[134].

A.2 Optical schematics of experimental setups

A.2.1 Non-linear photo-conductive sampling in solids and gasses

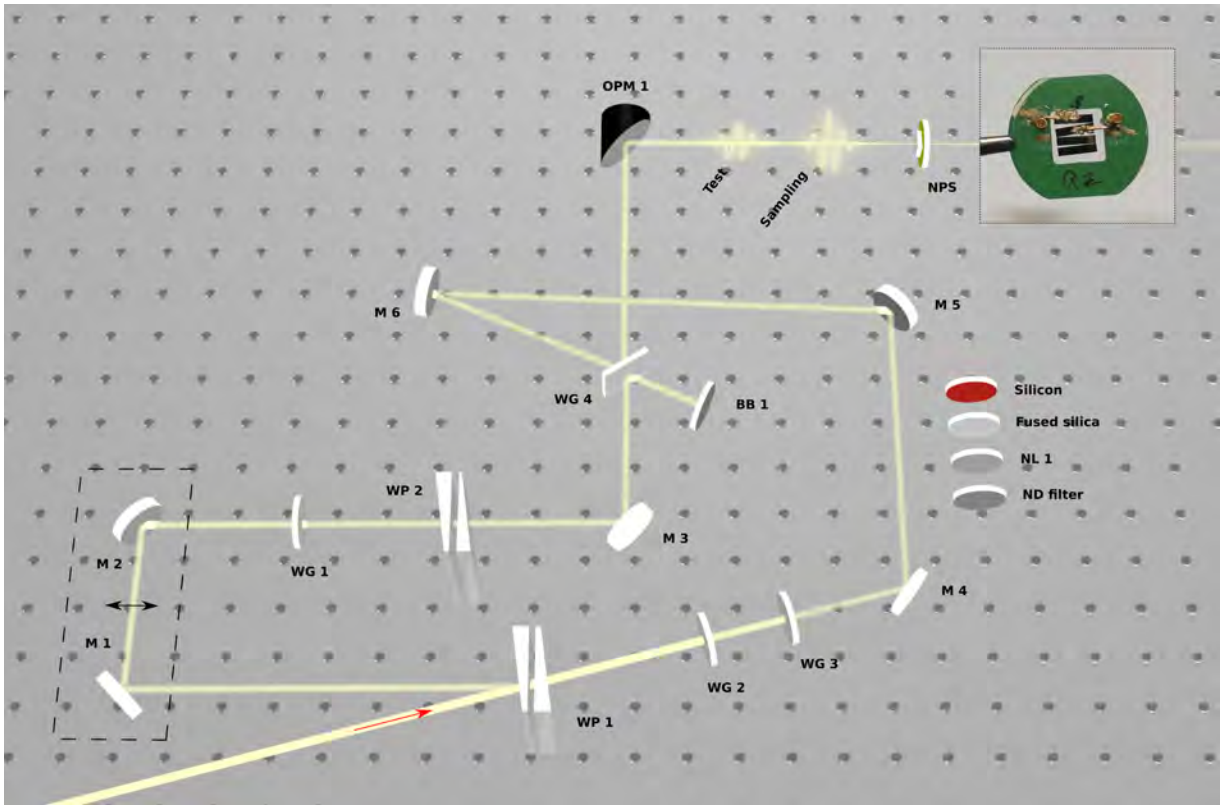

Figure A.2: Optical setup for non-linear photo-conductive sampling in solids and gasses. For NPS detection in gas, a solid sample is replaced by a pair of copper metal electrodes.

The input laser beam is split into two arms by taking a reflection from a front surface of the first wedge in the wedge pair WP 1. The reflected beam (sampling arm) is guided through a delay stage consisting of a retro-reflector M 1 and M 2 protected silver mirrors mounted on a closed-loop piezo stage (PX 200, Piezosystems Jena).

Silicon, fused silica, non-linear crystal (NL 1), and natural density filter (ND filter) windows can be optionally installed in the transmitted beam (test arm) for the generation and compression of new spectral components.

The wire-grid polarizers WG 1 - WG 3 are used to adjust the energies of test and sampling pulses, while fused silica wedge pairs (WP 1, WP 2) fine-tune the compressions and the CEPs of the pulses[89].

Both arms are then recombined by a wire-grid polarizer WG 4, which is set to transmit the sampling arm and reflect the test arm polarizations. The orthogonally polarized pulses are focused on the NPS detector by a protected silver off-axis parabolic mirror OPM 1.

The beam block BB 1 is used to block the residual light after the polarizer WG 4, while the plane-protected silver mirrors M 3 - M 6 are used for beam guiding.

Non-linear photo-conductive sampling in the gas medium was performed by replacing the solid-state NPS detector with two copper wires separated by a gap matching the focus spot (Fig. A.13). For the case of measurements not in ambient pressure, two metal electrodes were mounted inside a small vacuum chamber filled with a gas at a set pressure.

A.2.2 Attosecond timing of light-field-driven carrier motion

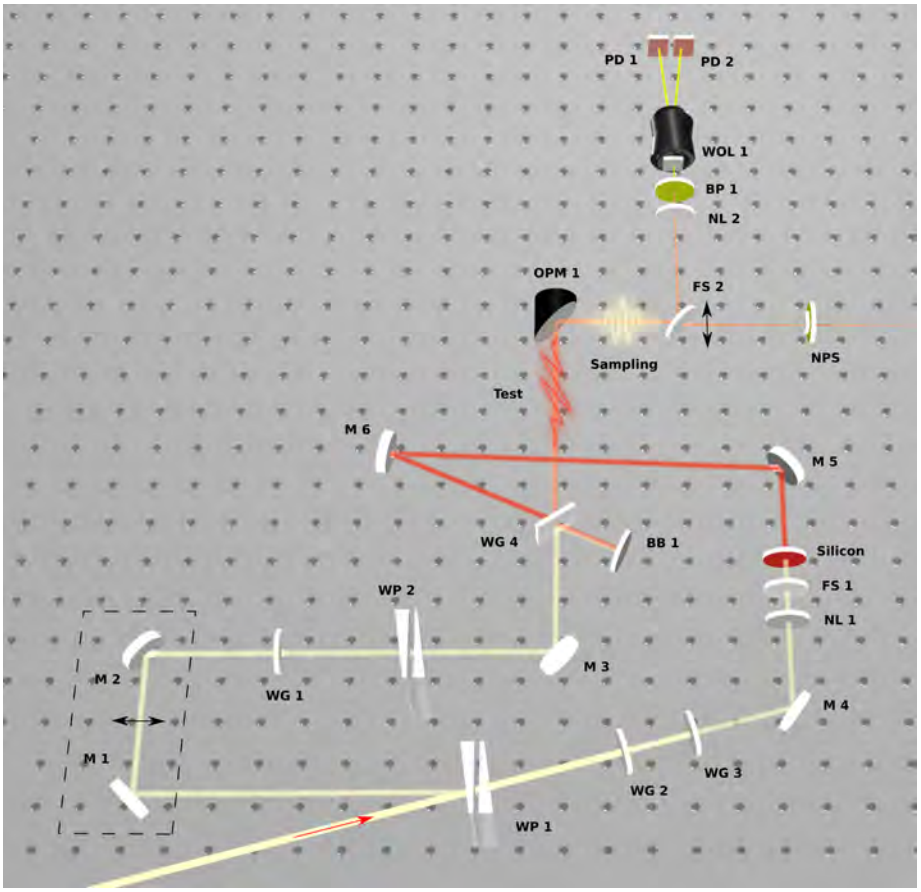

Figure A.3: Optical setup for attosecond timing of light-field-driven carrier motion.

The input laser beam is split into two arms by taking a reflection from the front surface of the first wedge in the wedge pair WP 1. The reflected beam (sampling arm) is guided through a delay stage consisting of a retro-reflector M 1 and M 2 protected silver mirrors mounted on a closed-loop piezo stage (PX 200, Piezosystems Jena).

The small diameter ($\sim$ 4 mm) and a high energy ($\sim$ 350 µJ) of the collimated laser beam provide enough intensity for the intra-pulse DFG process in a non-linear crystal (12.4 µm thick type II BBO, θ = 50 deg) NL 1. The set of silicon and fused silica windows are

used for compression of the generated NIR spectrum centered at a wavelength of about 1.8 µm. The silicon window also blocks the incident fundamental spectrum by absorption. The wire-grid polarizers WG 1 - WG 3 are used to fine-tune the energies of test and sampling pulses, while fused silica wedge pairs (WP 1, WP 2) fine-tune the compressions and the CEPs of pulses. Both arms are then recombined by a wire-grid polarizer WG 4, which is set to transmit the sampling arm and reflect the test arm polarizations. The orthogonally polarized pulses are then focused by a protected silver off-axis parabolic mirror OPM 1.

The fused silica plate FS 2 can be moved out of the beam for the test pulse waveform detection with NPS or moved in, for the test pulse waveform detection with EOS. Thin 12.4 µm thick type II BBO crystal ($\theta = 50$ deg) is used to generate a sum-frequency between sampling and test pulses which is then filtered by a bandpass filter BP 1 and transmitted through the Wollaston prism WOL 1 for the balanced detection with GaP photodiodes PD 1 and PD 2.

The beam block BB 1 is used to block the residual light after the polarizer WG 4, while plane protected silver mirrors M 3 - M 6 are used for beam guiding.

A.2.3 Switching and modulation of optical properties in solids

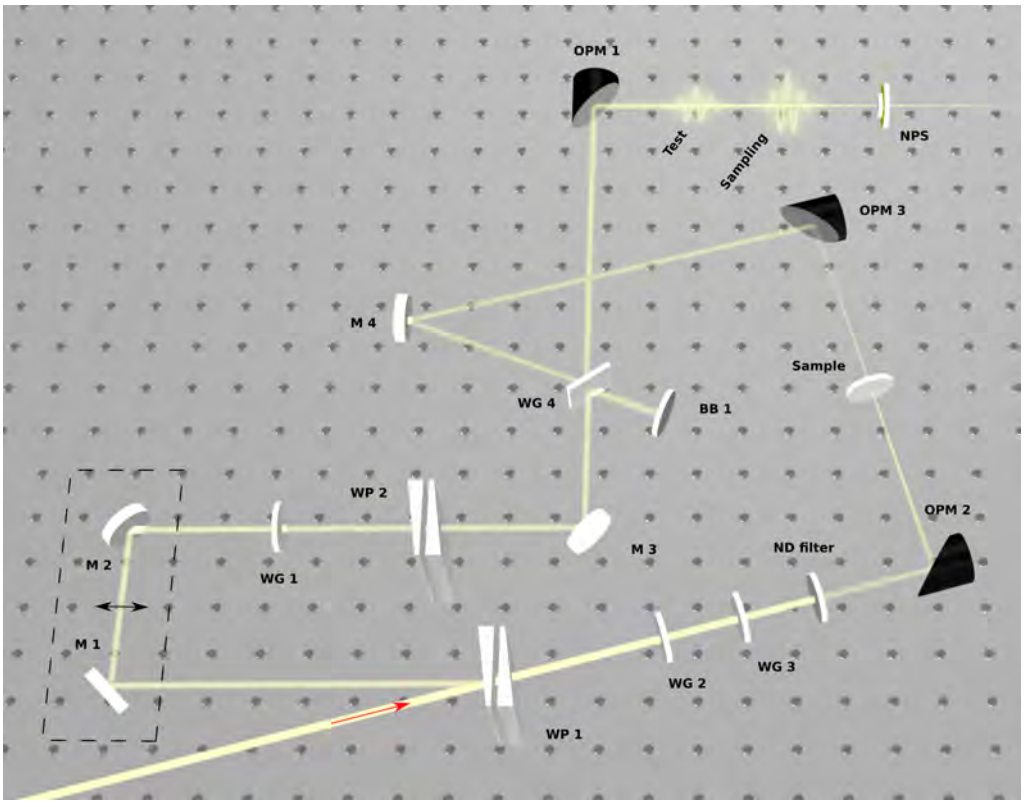

Figure A.4: Optical setup for switching and modulation of optical properties in solids.

The input laser beam is split into two arms by taking a reflection from the front surface

of the first wedge in the wedge pair WP 1. The reflected beam (sampling arm) is guided through a delay stage consisting of a retro-reflector M 1 and M 2 protected silver mirrors mounted on a closed-loop piezo stage (PX 200, Piezosystems Jena).

The off-axis protected silver parabolic mirror OPM 2 focuses the test arm on the sample, which is then further collimated by a protected silver off-axis parabolic mirror OPM 3.

The wire-grid polarizers WG 1 - WG 3 are used to set the energies of test and sampling pulses, while fused silica wedge pairs (WP 1, WP 2) fine-tune the compressions and the CEPs of pulses. Both arms are then recombined by a wire-grid polarizer WG 4, which is set to transmit the test arm and reflect the sampling arm polarizations. The orthogonally polarized pulses are then focused on the NPS detector by a protected silver off-axis parabolic mirror OPM 1.

The beam block BB 1 is used to block the residual light after the polarizer WG 4, while plane protected silver mirrors M 3 - M 6 are used for beam guiding.

A.2.4 NOS characterization and benchmarking

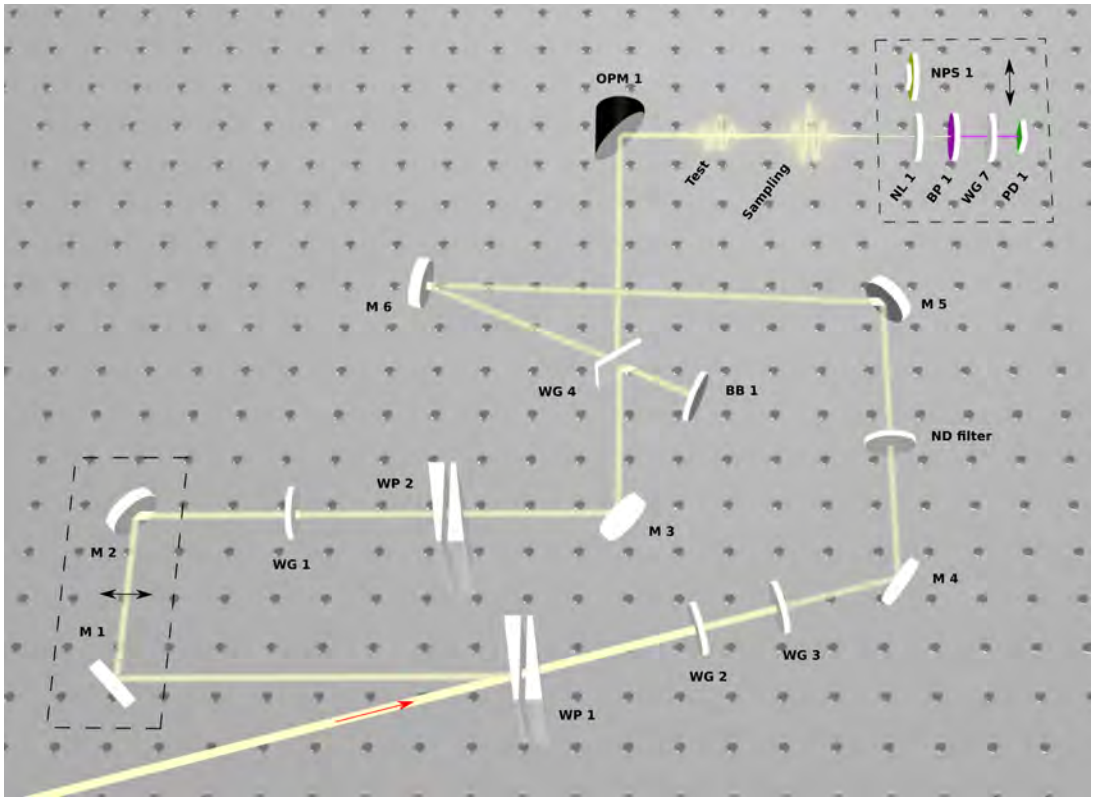

Figure A.5: Optical setup for NOS detection and characterization, as well as for the NOS-NPS benchmarking in the visible spectral range.

The input laser beam is split into two arms by taking a reflection from the front surface of the first wedge in the wedge pair WP 1. The reflected beam (sampling arm) is guided

through a delay stage consisting of a retro-reflector M 1 and M 2 protected silver mirrors mounted on a closed-loop piezo stage (PX 200, Piezosystems Jena).

The wire-grid polarizers (WG 1 - WG 3) are used to set the energies of test and sampling pulses, while fused silica wedge pairs (WP 1, WP 2) fine-tune the compressions and the CEPs of pulses. Both arms are then recombined by a wire-grid polarizer WG 4, which is set to transmit the test arm and reflect the sampling arm polarizations. The orthogonally polarized pulses are then focused by a protected silver off-axis parabolic mirror OPM 1 for the NPS or NOS detection. The quartz crystal ($\sim$ 12.34 µm thick, z-cut) NL 2 is used to generate a local oscillator and a signal, which are then filtered by a bandpass filter BP 1 and the wire-grid polarizer WG 5. The light is then detected by a photodiode.

The beam block BB 1 is used to block the residual light after the polarizer WG 4, while plane protected silver mirrors M 3 - M 6 are used for beam guiding.

The reflective UVFS natural density filter (ND filter) is used for the test arm attenuation.

The broadband NOS detection was performed with a setup presented on Fig. A.6. The protected aluminum off-axis parabolic mirror OPM 2 focuses the beam on a BBO crystal (100 µm thick type II, $\theta = 29.2$ deg) NL 1 to generate new spectral components down to 235 nm. The fundamental light with the newly generated spectrum is re-collimated by a protected aluminum off-axis parabolic mirror OPM 3.

Both arms are then recombined in a wire-grid polarizer WG 4 and focused with a protected aluminum off-axis parabolic mirror to the NOS detection setup.

Plane protected silver mirror M 3 and a plane protected aluminum mirror M 6 are used for the beam guiding.

The wire-grid polarizer WG 5 ensures the linear polarization of the test arm after interaction with a BBO crystal NL 1.

A.2.5 Attosecond control of the optical properties of solids

The input laser beam is split into two arms by taking a reflection from the front surface of the first wedge in the wedge pair WP 1. The reflected beam (injection arm) is guided through a delay stage consisting of a retro-reflector M 1 and M 2 protected silver mirrors mounted on a closed-loop piezo stage (PX 200, Piezosystems Jena).

The third optical arm (sampling arm) is created by taking a reflection from a thin (200 µm thick) UVFS window FS 2. The reflected light is guided through a delay stage consisting of a retro-reflector M 6 and M 7 protected silver mirrors mounted on a closed-loop piezo stage (PX 200, Piezosystems Jena).

The wire-grid polarizers WG 1, WG2, WG 3, WG 5 are used to set the energies of the test, injection, and sampling pulses, while fused silica wedge pairs WP 1, WP 2, WP 3 to fine-tune the compressions and the CEPs of the pulses.

The off-axis protected silver parabolic mirror OPM 2, focuses the test arm on a nonlinear crystal (BiBo, 0.8 mm thick, $\theta = 10.3$ deg) NL 1, for the intra-pulse DFG process. The set of silicon and fused silica plates (Si, FS 1) is used for the compression of the newly generated NIR spectrum and for blocking the fundamental spectrum by absorption

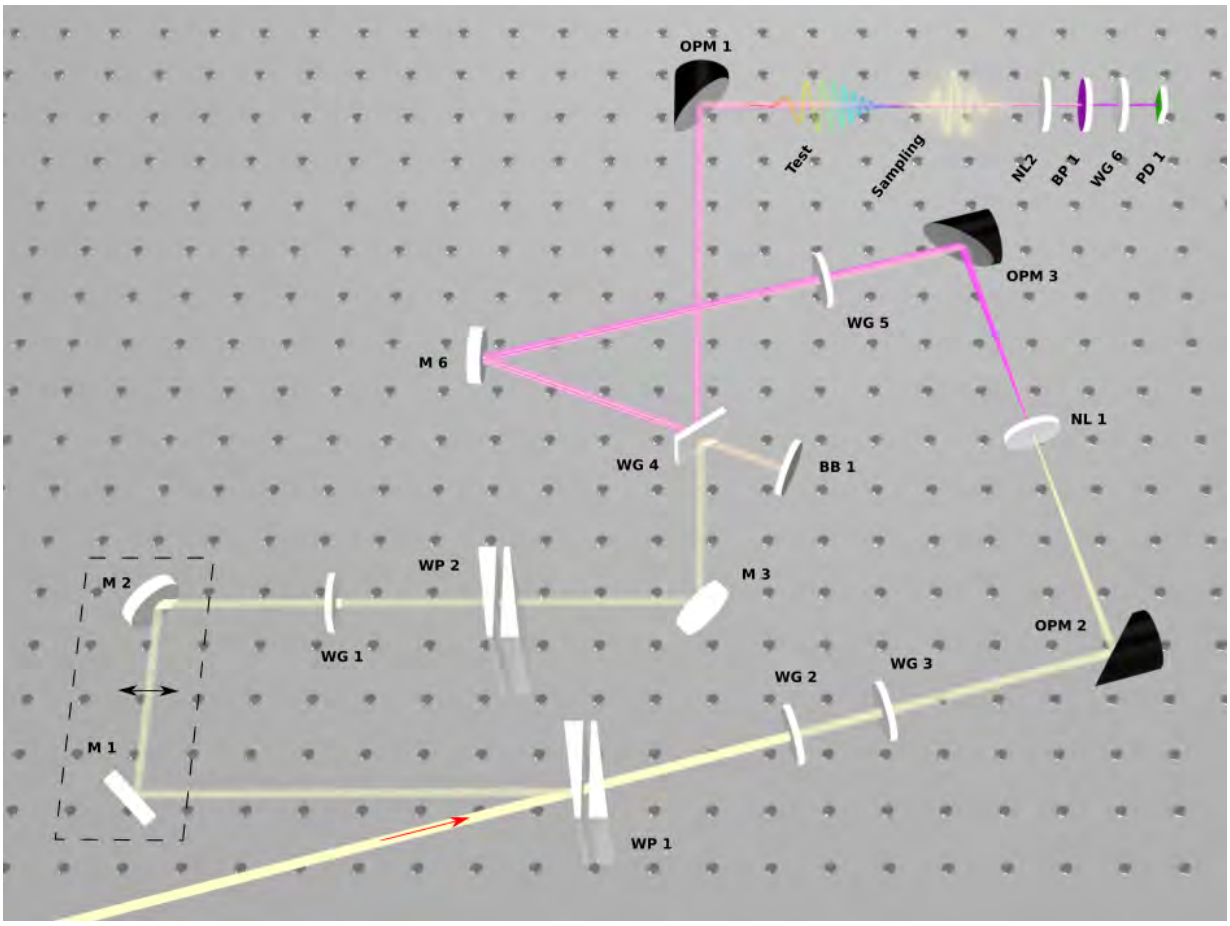

Figure A.6: Optical setup for broadband NOS detection.

in silicon. The generated and compressed NIR light is further collimated by a protected gold off-axis parabolic mirror OPM 3.

Injection and test arms are recombined by a wire-grid polarizer WG 4, which is set to transmit the injection arm and reflect the test arm polarizations. The orthogonally polarized pulses are focused by a protected silver off-axis parabolic mirror OPM 1 on the sample, and further re-collimated by a protected silver off-axis parabolic mirror OPM 4. The mirror OPM 4 has a hole at its optical axis, to prevent the injection arm from propagating further, as well as to increase the contrast of the waveform changes. The collimated beam is guided by a protected silver mirror M 10 to the wire-grid polarizer WG 6, for the recombination with the sampling arm.

Beam blocks BB 1 and BB 2 are used to block the residual beam after the recombining polarizers WG 4 and WG 6. The beam block BB 3 blocks the injection arm after the mirror OPM 4.

The quartz crystal ($\sim$ 12.34 µm thick, z-cut) NL 2 provides a local oscillator and a signal which are further filtered by a bandpass filter BP 1 and a wire-grid polarizer WG 7. The light is then further detected by a photodiode PD 1.

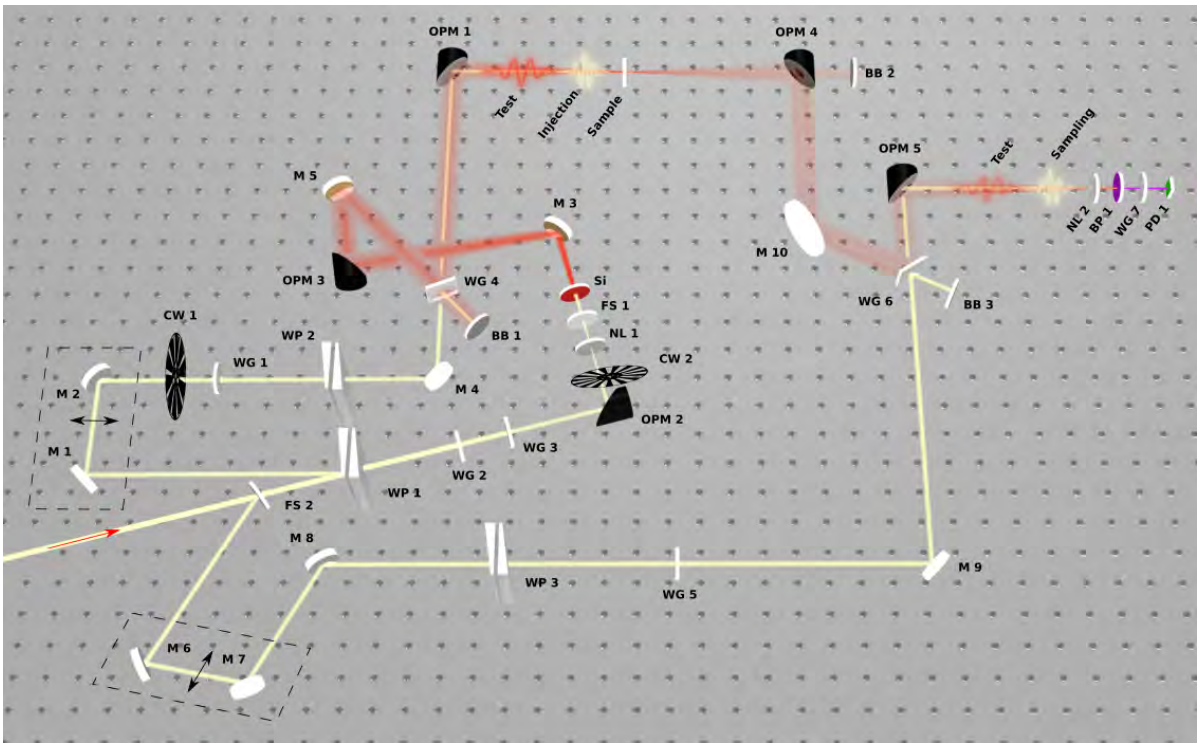

Figure A.7: Optical setup for the ultrafast relaxation dynamics and sub-half-cycle control of optical properties in solids.

Protected gold plane mirrors M 3 and M 5 as well as protected silver plane mirrors M4, M8, M9, and M 10 are used for the beam guiding.

Chopper wheels CW 1 and CW 2 provide the sequence of pulses used for the semi-simultaneous detection scheme described in chapter A.3.1 of this thesis.

A.3 Data acquisition

For the experiments involving NPS technique and described in chapters 2, 4, 5, the current signal from each electrode was first converted into voltage with further amplification by a transimpedance amplifier (DLPCA-200, FEMTO Messtechnik). The amplified voltage signal was then connected to a dual-phase lock-in amplifier (SR-830, Stanford Research Systems), triggered by an electrical signal synchronized with half of the repetition rate of the laser.

The EOS detection discussed in chapters 2 and 4, was performed with two GaP photodiodes connected to produce a current signal proportional to an energy of light incident on each photodiode. The differential output from two photodiodes was connected to a dual-phase lock-in amplifier (SR-830, Stanford Research Systems), triggered by an electrical signal synchronized with half of the repetition rate of the laser.

In the NOS detection, discussed in chapter 2, a photodiode produces a current signal proportional to the light intensity incident on the photodiode. The current signal was first converted into voltage with further amplification by a transimpedance amplifier (DLPCA-200, FEMTO Messtechnik). The amplified voltage signal was then connected to a dual-phase lock-in amplifier (SR-830, Stanford Research Systems), triggered by an electrical signal synchronized with half of the repetition rate of the laser.

Experiments with three optical arms, described in chapter 6 were performed with the semi-simultaneous pulse waveform detection described in the chapter A.3.1 of this thesis.

The measured signal from the lock-in amplifier or an oscilloscope was read by software on a computer via GPIB interface (National Instruments).

A.3.1 Semi-simultaneous detection scheme

Field sampling measurements based on a modification of the pulse waveform due to the interaction with a sample, properties of which are modified, require to measure the reference and modified waveforms for comparison.

Since the waveform sampling requires measuring some observable at multiple time delays between pump and probe pulses, the actual sampling of the waveform usually takes minutes or hours, depending on the measuring technique, pulse stability, temporal and spectral resolutions, etc.

For instance, if the typical pump-probe study of the dynamics of some physics process requires measuring a pulse waveform transmitted through an unperturbed sample. Then the properties of the sample are modified, and transmitted pulse waveform though the modified sample is measured. The difference between the two measured waveforms contains information about the modification of sample properties. If a measurement of a pulse waveform takes one minute, then the entire experiment would take about 2 minutes, assuming that the properties of the sample can be changed instantly. Since any measurement is exposed to various sources of noise, two minutes would correspond to the accumulation of noise with a spectral bandwidth from about 8 mHz (lower cut-off frequency) to infinity.

Since amplitudes of many sources of noise, such as pink noise, are inversely proportional to a frequency, an increase of a lower cut-off frequency will significantly reduce the total noise present in a measurement.

An increase of a lower noise cut-off frequency requires to decrease a total measurement time, with the ideal situation to be when the reference and modified waveforms are measurement *semi-simultaneously*.

The semi-simultaneous detection can be achieved when instead of a sequential measurement of a total reference waveform followed by a measurement of a total modified waveform, *each point* of waveforms is measured sequentially.

In the experiment described in chapter 6 of this thesis, three optical arms are used. The injection arm controls the properties of the sample medium by exciting it with an optical pulse. The pulse in the test arm is used to probe these changes in the medium by propagation through the excited or not-excited sample. The sampling arm provides a gate that can be delayed with respect to the test arm to sample its waveform.

The chopper wheels are placed inside the first and second arms rotating at 1/3 of a repetition rate of the laser. The duty cycle of the wheel in the first arm is set to 1/3, while the duty cycle of the wheel in the second arm is set to 2/3. Such configuration provides the following sequence of pulses from three arms:

First arm	1	0	0
Second arm	1	1	0
Third arm	1	1	1

Here '1' indicates that the pulse is present, while '0' indicates that the pulse is blocked by the chopper wheel.

This sequence of pulses is delivered to the measuring device such as a photo-diode. The

generated by a photodiode current signal can then be further amplified and converted to a voltage by means of a transimpedance amplifier (DLPCA-200, FEMTO Messtechnik). The output from a transimpedance amplifier would provide a time-domain train of voltage signals (Fig. A.8a). Such voltage signal can be guided to a boxcar integrator (SR200, Stanford Research Systems) which provides a DC output for each of the single voltage pulses (Fig. A.8b). The output from the boxcar integrator can be digitized with an analog-to-digital converter or simply measured with a conventional oscilloscope.

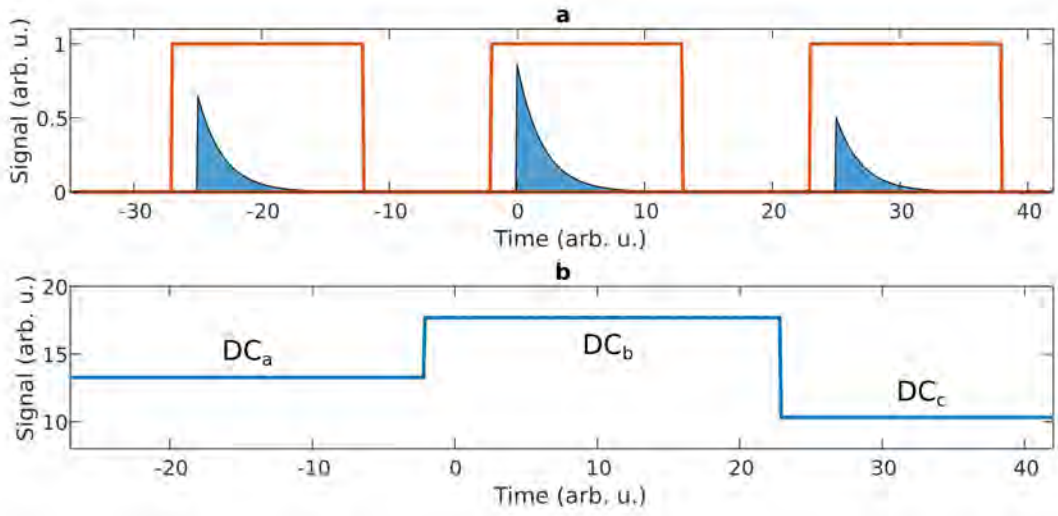

Figure A.8: Schematic representation of a transimpedance amplifier output (blue area) for 3 consequent pulses (**a**), and corresponding output from a boxcar averager (**b**). The orange color in (**a**) represent a measurement time window set for the boxcar averager.

If a first arm pulse does not change any properties of the sample medium, then there is no influence of the first arm on the measurement and DC_a and DC_b outputs are identical.

If however the first arm pulse changes the sample medium, then the second arm pulse will be different when the first arm pulse is present, thus DC_a and DC_b outputs will be different. The difference between DC_a and DC_b outputs corresponds to a difference in the probe waveform due to the change of the sample properties. In this configuration of the measurement, the first arm pulse should be blocked after the sample and prevented from reaching the detector. In this case, only the sample is affected by a first arm pulse, but not the detector.

The measurement of a signal related to the field at each point of the reference waveform will be $DC_a - DC_c$, while the measurement of the signal related to the field at each point of the modified waveform will be $DC_b - DC_c$.

Since the measurement at each point of the reference and modified waveforms requires measuring only 3 consequent pulses, such measurement is exposed to the noise occurring only during the time between measurement of first and third pulses. In our 3 KHz repetition rate laser system, this noise duration corresponds to about 666 µs. This duration

implies that the measurement of the reference and modified waveforms experience virtually the same noise, which will be subtracted when one calculates a difference. The lower cut-off frequency of the noise bandwidth in the measurement of the difference between reference and modified waveforms can therefore be as high as 1.5 KHz. This lower cut-off frequency is much higher than the 8 mHz frequency considered in the example, and therefore significantly reduces the overall noise of a measurement. Such reduction of noise significantly improves the sensitivity of the detection and therefore allows studying processes that produce very weak signals.

A.4 Samples for chapter 5

In order to extract non-linear polarizations, transferred energies, and charge displacements described in chapter 5 of this thesis, precise sample thickness information is required.

A time-domain field-resolved sampling of optical pulse waveform provides a useful tool for sample thickness measurement. When a medium is introduced into a laser beam path, the pulse waveform will be shifted in time and attenuated in spectral amplitudes. Both effects are described by refractive indices of the material and sample thickness. Since refractive indices of various materials are well known and modeled by Sellmeier equations, comparing measured pulse waveforms with and without samples allows to precisely determine sample thickness by modelling the propagation.

To determine a sample thickness, optical pulse waveforms with and without a sample were measured in time-domain with NPS technique (apart from silicon sample, the thickness of which was measured as described in section A.5). The measured pulse waveform without a sample was then used to theoretically propagate it through the sample of various thicknesses. The propagation of an optical pulse through a medium can be modelled as

$$E_p(t) = \mathcal{F}^{-1}\left[\mathcal{F}(E_i(t)) \cdot T_1 \cdot T_2 \cdot e^{ikd}\right], \tag{A.1}$$

where E_p and E_i are propagated and incident waveforms, $\mathcal{F}$ and $\mathcal{F}^{-1}$ are Fourier transform and inverse Fourier transform operators, T_1 and T_2 are field transmission at front and back surfaces, t is time, d is a samples thickness, and $k = n\omega/c$ is a wave vector.

The back-reflected pulses can be modelled with

$$E_b(t, N) = \mathcal{F}^{-1}\left[\mathcal{F}(E_i(t)) \cdot T_1 \cdot T_2 \cdot R_1^N \cdot R_2^N \cdot e^{ik(1+2N)d}\right], \tag{A.2}$$

where N is a number of a back reflection, while R_1 and R_2 are reflections at front and back surfaces.

If a frequency-dependent refractive index n is known (Sellmeier equations), transmissions T_1 and T_2 as well as reflections R_1 and R_2 can be calculated using Fresnel equations[135] for electric field.

The modelled sample thickness is fitted such that the difference between modelled and measured waveforms is minimized. Fig. A.9 show measured and modelled pulsed waveforms considering 20 back-reflections.

Table A.1 summarizes extracted thicknesses of samples.

Sample №	Material	Thickness
1	Polycrystalline CVD diamond	$9.18 \pm 0.062\ \mu m$
2	Amorphous fused silica	$121 \pm 8\ nm$
3	Crystalline $\langle$ 100 $\rangle$ Si	$240 \pm 15\ nm$

Table A.1: Samples and their measured thicknesses.

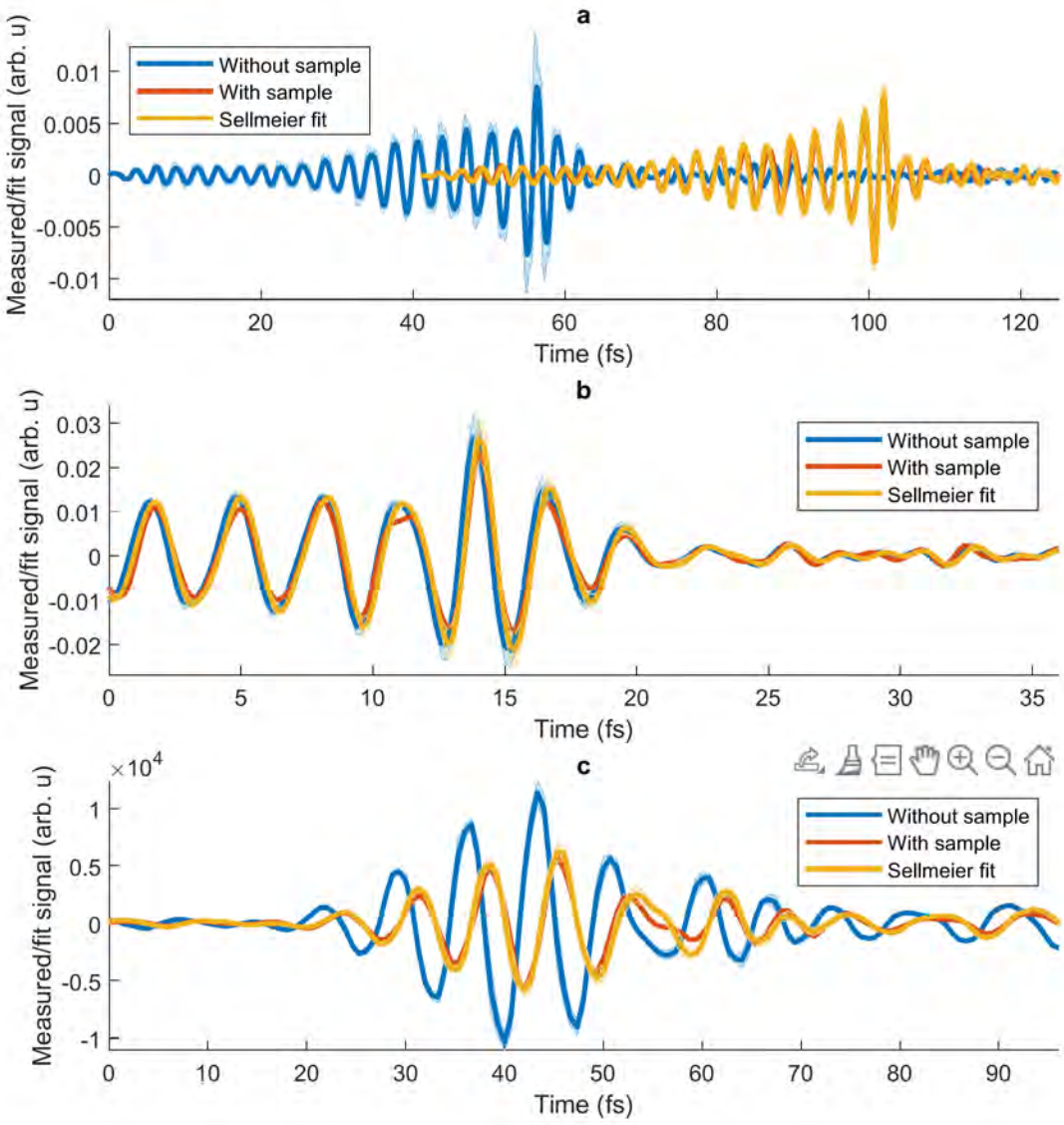

Figure A.9: Measured and modelled pulse waveforms for 9.18 ± 0.062 µm thick diamond (**a**), 121 ± 8 nm thick SiO2 (**b**) and 240 ± 15 nm silicon (**c**) samples.

A.5 Samples for chapter 6

Similar to chapter 5, in order to study the dynamics of optical properties in solids, precise unperturbed sample thicknesses have to be known.

Thicknesses of samples used in the experiment described in chapter 6 were measured as described in section A.4 of this thesis.

Fig. A.10 shows measured and modelled pulse waveforms considering 20 back-reflections. The pulse waveforms were measured with NOS technique described in chapter 2.2 of this thesis.

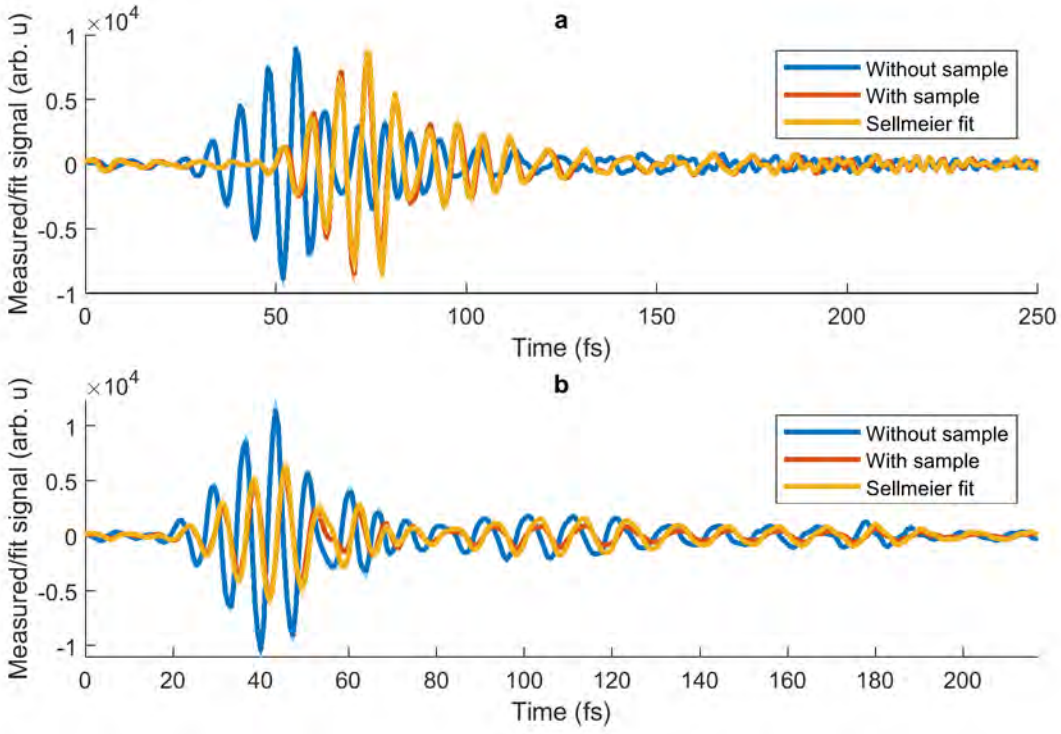

Figure A.10: Measured and modelled pulse waveforms for 12.82 ± 0.082 µm thick fused silica (**a**) and 240 ± 15 nm silicon (**b**) samples.

Table A.2 summarizes extracted thicknesses of samples used in experiments described in chapter 6 of this thesis.

Sample №	Material	Thickness
1	Amorphous fused silica	12.82 ± 0.082 µm
2	Crystalline ⟨ 100 ⟩ Si	240 ± 15 nm

Table A.2: Samples and their measured thicknesses.

A.6 Samples for NOS

Measurement of sample thicknesses by fitting a propagated waveforms in the time domain, although precise, exposed to drifts of pulse waveforms. Since measurement of a single pulse waveform usually takes a couple of minutes, the error in extracted thicknesses is proportional to the total time required to record the waveforms. However, if a sample is not too thick and not too thin, such that spectral fringes due to back-reflected pulses can be resolved with a spectrometer, a sample thickness can be measured more accurately as described further. Fig. A.11a and A.10a correspond to a thickness measurement performed with a spectrometer as well as with field resolved detection. Both methods provide the same information, however, the precision of extracted thickness is better in measurement with a spectrometer.

In order to precisely determine a spectral response of NOS technique (section 2.2 of this thesis), the propagation effects within a sampling medium should be considered. For this purpose, the precise thickness of the non-linear medium should be known. The thickness of a solid medium can be determined with a conventional spectrometer and a broadband light source. As an optical pulse propagates through a solid medium, the reflection at surfaces will take place. Some of the back-reflected pulses will travel in the same direction as the incident pulse but will be delayed due to propagation through the medium. Multiple pulses in the time domain will result in spectral fringes, which can be measured with a spectrometer. The total transmission of a medium, taking into account reflections at the surfaces can be determined[136] as

$$T(n,\omega,d) = \frac{1}{cos\left(\frac{\omega}{c}nd\right) - \frac{i}{2}\left(n+\frac{1}{n}\right) sin\left(\frac{\omega}{c}nd\right)}, \tag{A.3}$$

where T is an intensity transmission, n is a real-valued refractive index of a frequency ω, c is a speed of light and d is a sample thickness.

To precisely measure the thicknesses of z-cut α-quartz crystal and fused silica glass samples, the intensity spectrum of a broadband pulse (section A.1 of this thesis) was measured with and without samples (Fig. A.11). The spacing of fringes was then modeled with eq. A.3 and frequency-dependent refractive index based on Sellmeier equation for a considered medium. The calculated sample thickness is the one that provides the best agreement of fringe positions in the experiment.

The thin fused silica glass samples were provided by Valley Design Corp., while thick z-cut α-quartz crystal samples were provided by MTI Corporation, and further polished to reduce the thickness.

In summary, thicknesses of solid samples for NOS technique were measured and used for further evaluation of the spectral response considering propagation effects.

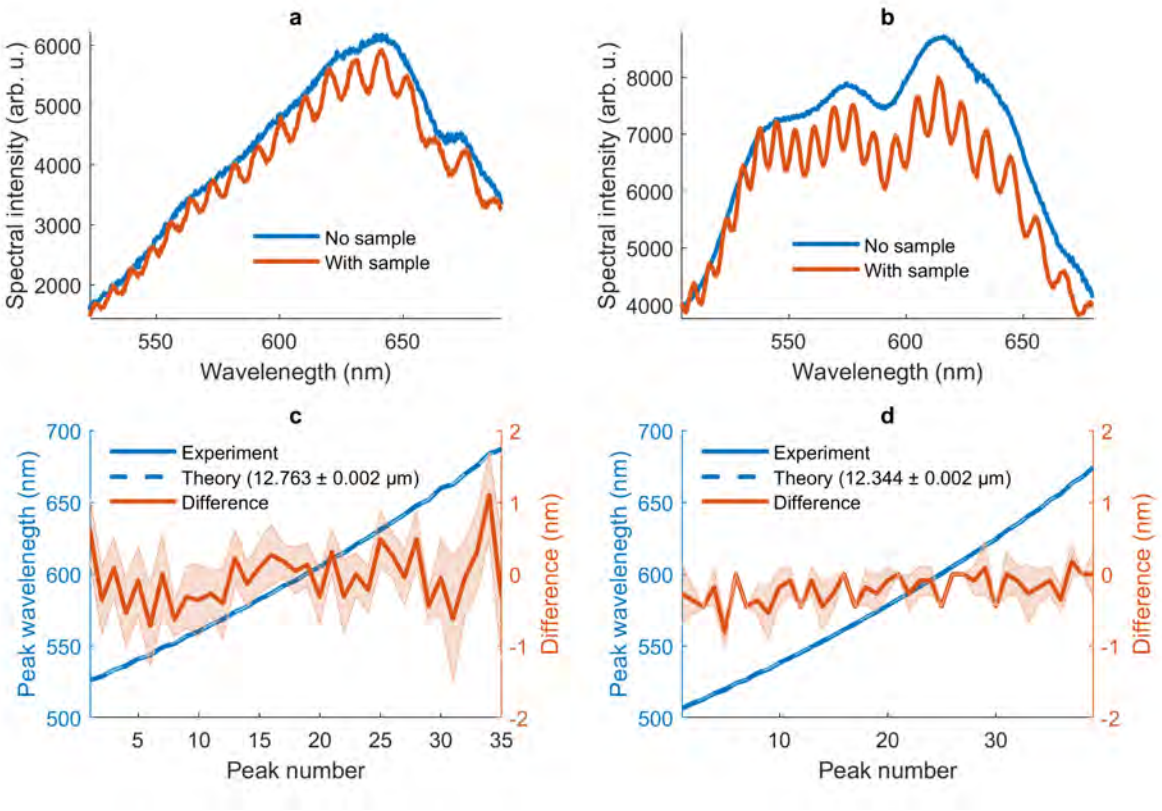

Figure A.11: Measured change of spectral intensities with amorphous fused silica (**a**) and z-cut α-quartz crystal samples (**b**). Positions of spectral fringes allow extraction of thicknesses for fused silica (**c**) and quartz (**d**) samples.

A.7 Samples for NPS

Several sample concepts for experiments involving the NPS technique have been developed and fabricated.

The fabrication of NPS samples was performed by means of the metal vapour deposition on a substrate material covered by a mask with a structure of intended electrode geometry.

The fabrication of masks simplifies the sample preparation as well as allows the precise fabrication of different electrode geometries.

Fig. A.12 shows designed and fabricated samples used in the experiments described in this thesis. The intermediate chromium layer of 5 nm thickness is used between the surface of a substrate material and a layer of 100 nm thick gold. The chromium layer is used to improve the overall bonding of metal electrodes with a sample surface. The deposited electrodes are then connected to the female crimp pins (Allectra GmBH) on the round PCB board of 1 inch diameter with a conductive silver paste and copper wires. Each pin on the PCB boards can then be connected to a coaxial cable with a male crimp connector on one side and a BNC connection on the other side. The BNC sides of the cables can then be used for measurement of a signal from each electrode by means of conventional devices such as a lock-in amplifier, oscilloscope, etc.

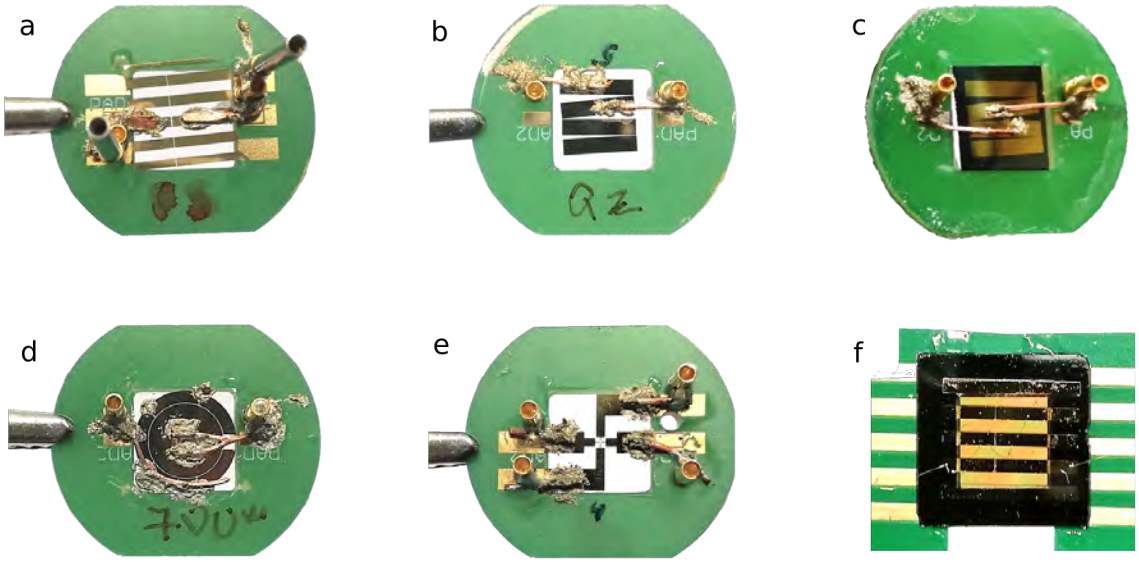

Figure A.12: Typical NPS samples with a linear electrode geometry and a fixed electrode gap size (**a**), adjustable gap size (**b**), circular electrode geometry and a fixed gap size (**d**), two pairs of electrodes (**e**), electrodes deposited on a multi-layer structure (**c**) and electrodes deposited on a thin-film substrate (**f**).

Sample geometry illustrated on Fig. A.12a was used for experiments described in sections 4,6, 2.1.1, 2.1.2, 2.1.3 and 2.2.1 of this thesis.

Fig. A.12a, illustrates that the NPS device can be implemented not only on bulk

substrates, but also on free-standing thin films.

The concept of samples with two pairs of electrodes (Fig. A.12e) was used for characterization of pulse polarization as well as absolute CEP detection[137]. In short, four electrodes allow the measurement of a screening polarization in two orthogonal planes, and therefore the sampling of optical pulses which do not possess a linear polarization.

Fig. A.12c demonstrates that the NPS device can be made out of a bulk medium, or out of a tailored medium as described in details elsewhere[138].

The samples can then be mounted in a conventional 1 inch holder or on a rotational mount (Fig. A.13a).

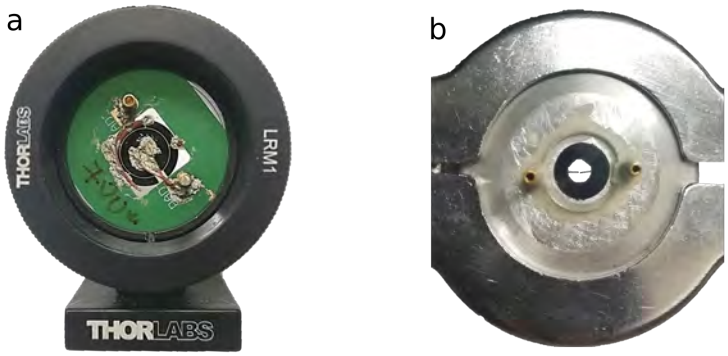

Figure A.13: Typical NPS sample installation in holders used for experiments in a solid (**a**) and gas (**b**) medium.

For NPS measurements in a gas medium, two copper wires are soldered to the male crimp pins which are then connected to female pins and can be mounted either on a PCB board (ambient air medium) or mounted inside a vacuum chamber for measurements with a controlled pressure (Fig. A.13).

A.8 Maxwell-equations model with propagation effects

Propagation effects, such as dispersion, absorption, phase mismatch, etc., influence the spectral response of the NOS detection. These effects were modeled by numerically solving Maxwell's equations on a one-dimensional grid.

Since the dispersion of the refractive index is a deciding factor in the coherent build-up of the signals of interest, it is important that it is kept as accurate as possible, including all dispersion orders. This is somewhat atypical for a time-domain calculation, and naive application of the refractive index from a Sellmeier equation found in the literature may lead to non-physical results, as they are typically the summation of a number of Lorentzian resonances, matched only to the real part of the refractive index. However, in the time domain, the refractive index of the material is contained in a response function, which must obey causality. Single Lorentzian resonances, although their resulting polarizations can be calculated quite efficiently in the time domain, typically lead to large inaccuracies in the absorption beneath the band-gap of typical solids.

In the model, an appropriate time-domain response function is found by first placing a series of absorption bands in the frequency domain and then calculating the resulting refractive index through the Kramers-Krönig relations, which guarantees that the resulting function will obey causality. The refractive index is matched to literature values in a nonlinear least-squares fitting. There is some freedom in choosing the length of the response function, but typically it contains 3000-15000 points, with a time step of 6 attoseconds (0.25 atomic units). This means that the history of the electric field must be stored at each point on the grid which contains the crystal. In other words, previous values of the electric fields must be stored in order to calculate the new ones. Additionally, the histories of the linear and nonlinear polarizations are stored at each point.

The linear polarization is calculated as a convolution of the field history with the response function, meaning its value at time t is given by

$$P^{(1)}(t) = \int_{-t_L}^{t} dt'\, \chi^{(1)}(t) E(t-t'), \tag{A.4}$$

where t_L is the (finite) length of the response function $\chi^{(1)}(t)$.

The nonlinear polarizations can be calculated from the convolution of the field with a separate set of response functions, which can differ for different orientations of each instance of the field.

For the second-order polarization:

$$P_k^{(2)}(t) = \int_{-t_L}^{t} dt'\, \chi_{jk}^{(2)}(t) E_j(t-t') \int_{-t_L}^{t'} dt''\, \chi_{ij}^{(2)}(t) E_i(t-t''). \tag{A.5}$$

For the third order polarization:

$$P_\ell^{(3)}(t) = \int_{-t_L}^{t} dt'\, \chi_{k\ell}^{(3)}(t) E_k(t-t') \int_{-t_L}^{t'} dt''\, \chi_{jk}^{(3)}(t) E_j(t-t') \int_{-t_L}^{t''} dt'''\, \chi_{ij}^{(3)}(t) E_i(t-t''') \tag{A.6}$$

The subscripts of the fields and polarizations indicate the direction of the field within the material and, in general, must be summed over all combinations. As a significant simplification, the same response function is employed by deriving from the linear response, for the nonlinear terms, with a weighting determined by the susceptibility tensors of the crystal, thus approximating the dispersion of the nonlinear coefficients by Miller's rule.

The values of the polarization in the given directions come from summing over the elements of the nonlinear tensors, which are then normalized by the known linear susceptibility $\chi^{(1)}$ at a frequency of interest ω_0. The normalization factor, $\chi^{(1)}$, can be extracted from a measured or calculated refractive index by means of Eq. (A.7).

$$n(\omega_0) = \sqrt{1 + \chi^{(1)}(\omega_0)}. \tag{A.7}$$

The full polarization is calculated using the full tensor nature of the third and second-order nonlinearities, meaning that 14 separate polarizations are calculated for the two polarization components at each time step and contribute to the final polarization, which serves as a driving term in Maxwell's equations. The calculation of the nonlinear polarization is by far the most numerically intensive step in the propagation.

The full propagation is performed using numerically evaluated spatial derivatives that are accurate to sixth order in the spatial grid step. Convergence checks were performed such that the dispersion and transmission of broadband pulses up to 1 PHz frequency are transmitted with numerical dispersion accounting for < 0.001 of the actual dispersion. The model was developed by Nicholas Karpowicz.

Appendix B

Data Archiving

All the data and programming scripts used for the evaluation and analysis of results presented in this thesis are stored on the data archive server of the Max Planck Computing and Data Facility: *archive.mpcdf.mpg.de*.

The archive consists of separate folders for each figure that illustrates experimental or simulation results presented in this thesis. The containing sub-folders store all relevant raw data as well as programming scripts used for the analysis and plotting.

Bibliography

[1] T. Tamaya, A. Ishikawa, T. Ogawa, and K. Tanaka. Diabatic mechanisms of higher-order harmonic generation in solid-state materials under high-intensity electric fields. *Physical Review Letters*, 116(1), January 2016.

[2] Maren Mohler. Georg August Universität Göttingen. Das michelson-interferometer. Accessed: 2020-12-26.

[3] Shawn Sederberg, Dmitry Zimin, Sabine Keiber, Florian Siegrist, Michael S. Wismer, Vladislav S. Yakovlev, Isabella Floss, Christoph Lemell, Joachim Burgdörfer, Martin Schultze, Ferenc Krausz, and Nicholas Karpowicz. Attosecond optoelectronic field measurement in solids. *Nature Communications*, 11(1):430, Jan 2020.

[4] Dmitry Zimin, Matthew Weidman, Johannes Schötz, Matthias F. Kling, Vladislav S. Yakovlev, Ferenc Krausz, and Nicholas Karpowicz. Petahertz-scale nonlinear photoconductive sampling in air. *Optica*, 8(5):586, April 2021.

[5] Dmitry Zimin, Vladislav S. Yakovlev, and Nicholas Karpowicz. Ultra-broadband photonic sampling of optical waveforms. *Nature Photonics, NPHOT-2021-07-00821, Submitted*, July 2021.

[6] Enrico Ridente, Mikhail Mamaikin, Najd Altwaijry, Dmitry Zimin, Vladimir Pervak Matthias F. Kling, Matthew Weidman, Ferenc Krausz, and Nicholas Karpowicz. Electro-optic characterization of synthesized infrared-visible light fields. *Nature Photonics, NPHOT-2021-02-00180, Submitted*, February 2021.

[7] A. Sommer, E. M. Bothschafter, S. A. Sato, C. Jakubeit, T. Latka, O. Razskazovskaya, H. Fattahi, M. Jobst, W. Schweinberger, V. Shirvanyan, V. S. Yakovlev, R. Kienberger, K. Yabana, N. Karpowicz, M. Schultze, and F. Krausz. Attosecond nonlinear polarization and light–matter energy transfer in solids. *Nature*, 534(7605):86–90, Jun 2016.

[8] Gordon E. Moore. Cramming more components onto integrated circuits, reprinted from electronics, volume 38, number 8, april 19, 1965, pp.114 ff. *IEEE Solid-State Circuits Society Newsletter*, 11(3):33–35, September 2006.

[9] Kyung Taec Kim, Chunmei Zhang, Andrew D. Shiner, Bruno E. Schmidt, François Légaré, D. M. Villeneuve, and P. B. Corkum. Petahertz optical oscilloscope. *Nature Photonics*, 7(12):958–962, November 2013.

[10] J. Schoetz, Z. Wang, E. Pisanty, M. Lewenstein, M. F. Kling, and M. F. Ciappina. Perspective on petahertz electronics and attosecond nanoscopy. *ACS Photonics*, 6(12):3057–3069, November 2019.

[11] Yujia Yang, Marco Turchetti, Praful Vasireddy, William P. Putnam, Oliver Karnbach, Alberto Nardi, Franz X. Kärtner, Karl K. Berggren, and Phillip D. Keathley. Light phase detection with on-chip petahertz electronic networks. *Nature Communications*, 11(1), July 2020.

[12] N. A. Gershenfeld and I. L. Chuang. Bulk spin-resonance quantum computation. *Science*, 275(5298):350–356, January 1997.

[13] Samuel L. Braunstein and Peter van Loock. Quantum information with continuous variables. *Reviews of Modern Physics*, 77(2):513–577, June 2005.

[14] J. L. O'Brien. Optical quantum computing. *Science*, 318(5856):1567–1570, December 2007.

[15] T. D. Ladd, F. Jelezko, R. Laflamme, Y. Nakamura, C. Monroe, and J. L. O'Brien. Quantum computers. *Nature*, 464(7285):45–53, March 2010.

[16] Frank Arute, Kunal Arya, Ryan Babbush, Dave Bacon, Joseph C. Bardin, Rami Barends, Rupak Biswas, Sergio Boixo, Fernando G. S. L. Brandao, David A. Buell, Brian Burkett, Yu Chen, Zijun Chen, Ben Chiaro, Roberto Collins, William Courtney, Andrew Dunsworth, Edward Farhi, Brooks Foxen, Austin Fowler, Craig Gidney, Marissa Giustina, Rob Graff, Keith Guerin, Steve Habegger, Matthew P. Harrigan, Michael J. Hartmann, Alan Ho, Markus Hoffmann, Trent Huang, Travis S. Humble, Sergei V. Isakov, Evan Jeffrey, Zhang Jiang, Dvir Kafri, Kostyantyn Kechedzhi, Julian Kelly, Paul V. Klimov, Sergey Knysh, Alexander Korotkov, Fedor Kostritsa, David Landhuis, Mike Lindmark, Erik Lucero, Dmitry Lyakh, Salvatore Mandrà, Jarrod R. McClean, Matthew McEwen, Anthony Megrant, Xiao Mi, Kristel Michielsen, Masoud Mohseni, Josh Mutus, Ofer Naaman, Matthew Neeley, Charles Neill, Murphy Yuezhen Niu, Eric Ostby, Andre Petukhov, John C. Platt, Chris Quintana, Eleanor G. Rieffel, Pedram Roushan, Nicholas C. Rubin, Daniel Sank, Kevin J. Satzinger, Vadim Smelyanskiy, Kevin J. Sung, Matthew D. Trevithick, Amit Vainsencher, Benjamin Villalonga, Theodore White, Z. Jamie Yao, Ping Yeh, Adam Zalcman, Hartmut Neven, and John M. Martinis. Quantum supremacy using a programmable superconducting processor. *Nature*, 574(7779):505–510, October 2019.

[17] E. Knill. Quantum computing with realistically noisy devices. *Nature*, 434(7029):39–44, March 2005.

[18] C. A. Ryan, O. Moussa, J. Baugh, and R. Laflamme. Spin based heat engine: Demonstration of multiple rounds of algorithmic cooling. *Physical Review Letters*, 100(14), April 2008.

[19] Gopalakrishnan Balasubramanian, Philipp Neumann, Daniel Twitchen, Matthew Markham, Roman Kolesov, Norikazu Mizuochi, Junichi Isoya, Jocelyn Achard, Johannes Beck, Julia Tissler, Vincent Jacques, Philip R. Hemmer, Fedor Jelezko, and Jörg Wrachtrup. Ultralong spin coherence time in isotopically engineered diamond. *Nature Materials*, 8(5):383–387, April 2009.

[20] J. Takeda, K. Nakajima, S. Kurita, S. Tomimoto, S. Saito, and T. Suemoto. Time-resolved luminescence spectroscopy by the optical kerr-gate method applicable to ultrafast relaxation processes. *Physical Review B*, 62(15):10083–10087, October 2000.

[21] M. Kozák, J. McNeur, K. J. Leedle, H. Deng, N. Schönenberger, A. Ruehl, I. Hartl, J. S. Harris, R. L. Byer, and P. Hommelhoff. Optical gating and streaking of free electrons with sub-optical cycle precision. *Nature Communications*, 8(1), January 2017.

[22] D. H. Auston, K. P. Cheung, and P. R. Smith. Picosecond photoconducting hertzian dipoles. *Applied Physics Letters*, 45(3):284–286, August 1984.

[23] Ferenc Krausz and Misha Ivanov. Attosecond physics. *Rev. Mod. Phys.*, 81:163–234, Feb 2009.

[24] M Ferray, A L'Huillier, X F Li, L A Lompre, G Mainfray, and C Manus. Multiple-harmonic conversion of 1064 nm radiation in rare gases. *Journal of Physics B: Atomic, Molecular and Optical Physics*, 21(3):L31–L35, February 1988.

[25] X. F. Li, A. L'Huillier, M. Ferray, L. A. Lompré, and G. Mainfray. Multiple-harmonic generation in rare gases at high laser intensity. *Physical Review A*, 39(11):5751–5761, June 1989.

[26] P. B. Corkum. Plasma perspective on strong field multiphoton ionization. *Physical Review Letters*, 71(13):1994–1997, September 1993.

[27] M. Lewenstein, Ph. Balcou, M. Yu. Ivanov, Anne L'Huillier, and P. B. Corkum. Theory of high-harmonic generation by low-frequency laser fields. *Physical Review A*, 49(3):2117–2132, March 1994.

[28] Shambhu Ghimire, Anthony D. DiChiara, Emily Sistrunk, Pierre Agostini, Louis F. DiMauro, and David A. Reis. Observation of high-order harmonic generation in a bulk crystal. *Nature Physics*, 7(2):138–141, December 2010.

[29] Georges Ndabashimiye, Shambhu Ghimire, Mengxi Wu, Dana A. Browne, Kenneth J. Schafer, Mette B. Gaarde, and David A. Reis. Solid-state harmonics beyond the atomic limit. *Nature*, 534(7608):520–523, June 2016.

[30] F. Langer, M. Hohenleutner, U. Huttner, S. W. Koch, M. Kira, and R. Huber. Symmetry-controlled temporal structure of high-harmonic carrier fields from a bulk crystal. *Nature Photonics*, 11(4):227–231, March 2017.

[31] Tran Trung Luu, Zhong Yin, Arohi Jain, Thomas Gaumnitz, Yoann Pertot, Jun Ma, and Hans Jakob Wörner. Extreme–ultraviolet high–harmonic generation in liquids. *Nature Communications*, 9(1), September 2018.

[32] Jie Li, Xiaoming Ren, Yanchun Yin, Kun Zhao, Andrew Chew, Yan Cheng, Eric Cunningham, Yang Wang, Shuyuan Hu, Yi Wu, Michael Chini, and Zenghu Chang. 53-attosecond x-ray pulses reach the carbon k-edge. *Nature Communications*, 8(1), August 2017.

[33] Thomas Gaumnitz, Arohi Jain, Yoann Pertot, Martin Huppert, Inga Jordan, Fernando Ardana-Lamas, and Hans Jakob Wörner. Streaking of 43-attosecond soft-x-ray pulses generated by a passively CEP-stable mid-infrared driver. *Optics Express*, 25(22):27506, October 2017.

[34] M. Hentschel, R. Kienberger, Ch. Spielmann, G. A. Reider, N. Milosevic, T. Brabec, P. Corkum, U. Heinzmann, M. Drescher, and F. Krausz. Attosecond metrology. *Nature*, 414(6863):509–513, November 2001.

[35] E. Goulielmakis. Direct measurement of light waves. *Science*, 305(5688):1267–1269, August 2004.

[36] Agustin Schiffrin, Tim Paasch-Colberg, Nicholas Karpowicz, Vadym Apalkov, Daniel Gerster, Sascha Mühlbrandt, Michael Korbman, Joachim Reichert, Martin Schultze, Simon Holzner, Johannes V. Barth, Reinhard Kienberger, Ralph Ernstorfer, Vladislav S. Yakovlev, Mark I. Stockman, and Ferenc Krausz. Optical-field-induced current in dielectrics. *Nature*, 493(7430):70–74, December 2012.

[37] Martin Schultze, Elisabeth M. Bothschafter, Annkatrin Sommer, Simon Holzner, Wolfgang Schweinberger, Markus Fiess, Michael Hofstetter, Reinhard Kienberger, Vadym Apalkov, Vladislav S. Yakovlev, Mark I. Stockman, and Ferenc Krausz. Controlling dielectrics with the electric field of light. *Nature*, 493(7430):75–78, December 2012.

[38] D.J. Kane and R. Trebino. Characterization of arbitrary femtosecond pulses using frequency-resolved optical gating. *IEEE Journal of Quantum Electronics*, 29(2):571–579, 1993.

[39] C. Iaconis and I. A. Walmsley. Spectral phase interferometry for direct electric-field reconstruction of ultrashort optical pulses. *Optics Letters*, 23(10):792, May 1998.

[40] Jonathan R. Birge, Richard Ell, and Franz X. Kärtner. Two-dimensional spectral shearing interferometry for few-cycle pulse characterization. *Optics Letters*, 31(13):2063, July 2006.

[41] M. Drescher, M. Hentschel, R. Kienberger, M. Uiberacker, V. Yakovlev, A. Scrinzi, Th. Westerwalbesloh, U. Kleineberg, U. Heinzmann, and F. Krausz. Time-resolved atomic inner-shell spectroscopy. *Nature*, 419(6909):803–807, October 2002.

[42] N. Dudovich, O. Smirnova, J. Levesque, Y. Mairesse, M. Yu. Ivanov, D. M. Villeneuve, and P. B. Corkum. Measuring and controlling the birth of attosecond XUV pulses. *Nature Physics*, 2(11):781–786, October 2006.

[43] M. Uiberacker, Th. Uphues, M. Schultze, A. J. Verhoef, V. Yakovlev, M. F. Kling, J. Rauschenberger, N. M. Kabachnik, H. Schröder, M. Lezius, K. L. Kompa, H.-G. Muller, M. J. J. Vrakking, S. Hendel, U. Kleineberg, U. Heinzmann, M. Drescher, and F. Krausz. Attosecond real-time observation of electron tunnelling in atoms. *Nature*, 446(7136):627–632, April 2007.

[44] M. Schultze, K. Ramasesha, C. D. Pemmaraju, S. A. Sato, D. Whitmore, A. Gandman, J. S. Prell, L. J. Borja, D. Prendergast, K. Yabana, D. M. Neumark, and S. R. Leone. Attosecond band-gap dynamics in silicon. *Science*, 346(6215):1348–1352, December 2014.

[45] M. Ossiander, F. Siegrist, V. Shirvanyan, R. Pazourek, A. Sommer, T. Latka, A. Guggenmos, S. Nagele, J. Feist, J. Burgdörfer, R. Kienberger, and M. Schultze. Attosecond correlation dynamics. *Nature Physics*, 13(3):280–285, November 2016.

[46] Florian Siegrist, Julia A. Gessner, Marcus Ossiander, Christian Denker, Yi-Ping Chang, Malte C. Schröder, Alexander Guggenmos, Yang Cui, Jakob Walowski, Ulrike Martens, J. K. Dewhurst, Ulf Kleineberg, Markus Münzenberg, Sangeeta Sharma, and Martin Schultze. Light-wave dynamic control of magnetism. *Nature*, 571(7764):240–244, June 2019.

[47] Eleftherios Goulielmakis, Zhi-Heng Loh, Adrian Wirth, Robin Santra, Nina Rohringer, Vladislav S. Yakovlev, Sergey Zherebtsov, Thomas Pfeifer, Abdallah M. Azzeer, Matthias F. Kling, Stephen R. Leone, and Ferenc Krausz. Real-time observation of valence electron motion. *Nature*, 466(7307):739–743, August 2010.

[48] M. Lucchini, S. A. Sato, A. Ludwig, J. Herrmann, M. Volkov, L. Kasmi, Y. Shinohara, K. Yabana, L. Gallmann, and U. Keller. Attosecond dynamical franz-keldysh effect in polycrystalline diamond. *Science*, 353(6302):916–919, August 2016.

[49] Shambhu Ghimire, Georges Ndabashimiye, Anthony D DiChiara, Emily Sistrunk, Mark I Stockman, Pierre Agostini, Louis F DiMauro, and David A Reis. Strong-field and attosecond physics in solids. *Journal of Physics B: Atomic, Molecular and Optical Physics*, 47(20):204030, 2014.

[50] Dmitry Zimin. Generation and characterization of 12th harmonic out of 1025nm femtosecond yb:yag laser. Technical report, Deutsches Elektronen-Synchrotron, DESY, Hamburg, 2015.

[51] T. T. Luu, M. Garg, S. Yu. Kruchinin, A. Moulet, M. Th. Hassan, and E. Goulielmakis. Extreme ultraviolet high-harmonic spectroscopy of solids. *Nature*, 521(7553):498–502, May 2015.

[52] M. Garg, M. Zhan, T. T. Luu, H. Lakhotia, T. Klostermann, A. Guggenmos, and E. Goulielmakis. Multi-petahertz electronic metrology. *Nature*, 538(7625):359–363, October 2016.

[53] Isabella Floss, Christoph Lemell, Georg Wachter, Valerie Smejkal, Shunsuke A. Sato, Xiao-Min Tong, Kazuhiro Yabana, and Joachim Burgdörfer. Ab initio multiscale simulation of high-order harmonic generation in solids. *Physical Review A*, 97(1), January 2018.

[54] Jian Lu, Eric F. Cunningham, Yong Sing You, David A. Reis, and Shambhu Ghimire. Interferometry of dipole phase in high harmonics from solids. *Nature Photonics*, 13(2):96–100, December 2018.

[55] Q. Wu and X.-C. Zhang. Free-space electro-optic sampling of terahertz beams. *Applied Physics Letters*, 67(24):3523–3525, December 1995.

[56] D. Grischkowsky, Søren Keiding, Martin van Exter, and Ch. Fattinger. Far-infrared time-domain spectroscopy with terahertz beams of dielectrics and semiconductors. *Journal of the Optical Society of America B*, 7(10):2006, October 1990.

[57] Sabine Keiber, Shawn Sederberg, Alexander Schwarz, Michael Trubetskov, Volodymyr Pervak, Ferenc Krausz, and Nicholas Karpowicz. Electro-optic sampling of near-infrared waveforms. *Nature Photonics*, 10(3):159–162, Mar 2016.

[58] R. Kienberger, E. Goulielmakis, M. Uiberacker, A. Baltuska, V. Yakovlev, F. Bammer, A. Scrinzi, Th. Westerwalbesloh, U. Kleineberg, U. Heinzmann, M. Drescher, and F. Krausz. Atomic transient recorder. *Nature*, 427(6977):817–821, Feb 2004.

[59] A L Cavalieri, E Goulielmakis, B Horvath, W Helml, M Schultze, M Fieß, V Pervak, L Veisz, V S Yakovlev, M Uiberacker, A Apolonski, F Krausz, and R Kienberger. Intense 1.5-cycle near infrared laser waveforms and their use for the generation of ultra-broadband soft-x-ray harmonic continua. *New Journal of Physics*, 9(7):242–242, jul 2007.

[60] Ronald Ulbricht, Euan Hendry, Jie Shan, Tony F. Heinz, and Mischa Bonn. Carrier dynamics in semiconductors studied with time-resolved terahertz spectroscopy. *Reviews of Modern Physics*, 83(2):543–586, June 2011.

[61] Dmitry Zimin. Strong-field interaction of solids with terahertz and infrared radiation. Master's thesis, 2016.

[62] J. Itatani, F. Quéré, G. L. Yudin, M. Yu. Ivanov, F. Krausz, and P. B. Corkum. Attosecond streak camera. *Physical Review Letters*, 88(17), April 2002.

[63] J. Itatani, J. Levesque, D. Zeidler, Hiromichi Niikura, H. Pépin, J. C. Kieffer, P. B. Corkum, and D. M. Villeneuve. Tomographic imaging of molecular orbitals. *Nature*, 432(7019):867–871, December 2004.

[64] M. F. Kling. Control of electron localization in molecular dissociation. *Science*, 312(5771):246–248, April 2006.

[65] A. L. Cavalieri, N. Müller, Th. Uphues, V. S. Yakovlev, A. Baltuška, B. Horvath, B. Schmidt, L. Blümel, R. Holzwarth, S. Hendel, M. Drescher, U. Kleineberg, P. M. Echenique, R. Kienberger, F. Krausz, and U. Heinzmann. Attosecond spectroscopy in condensed matter. *Nature*, 449(7165):1029–1032, October 2007.

[66] J. A. Valdmanis, G. Mourou, and C. W. Gabel. Picosecond electro-optic sampling system. *Applied Physics Letters*, 41(3):211–212, August 1982.

[67] A. Leitenstorfer, S. Hunsche, J. Shah, M. C. Nuss, and W. H. Knox. Detectors and sources for ultrabroadband electro-optic sampling: Experiment and theory. *Applied Physics Letters*, 74(11):1516–1518, March 1999.

[68] James Clerk Maxwell. VIII. a dynamical theory of the electromagnetic field. *Philosophical Transactions of the Royal Society of London*, 155:459–512, December 1865.

[69] David J. Griffiths. *Introduction to Quantum Mechanics (2nd Edition)*. Pearson Prentice Hall, 2nd edition, April 2004.

[70] Bahaa E A Saleh and Malvin Carl Teich. *Fundamentals of photonics; 2nd ed.* Wiley series in pure and applied optics. Wiley, New York, NY, 2007.

[71] Robert W. Boyd. *Nonlinear Optics, Third Edition*. Academic Press, Inc., USA, 3rd edition, 2008.

[72] L V Keldysh. Ionization in the field of a strong electromagnetic wave. *Zh. Eksperim. i Teor. Fiz.*, Vol: 47, 11 1964.

[73] Wolfgang Demtröder. *Laser Spectroscopy 1*. Springer Berlin Heidelberg, 2014.

[74] M. Th. Hassan, T. T. Luu, A. Moulet, O. Raskazovskaya, P. Zhokhov, M. Garg, N. Karpowicz, A. M. Zheltikov, V. Pervak, F. Krausz, and E. Goulielmakis. Optical attosecond pulses and tracking the nonlinear response of bound electrons. *Nature*, 530(7588):66–70, February 2016.

[75] Charles Kittel. *Introduction to Solid State Physics*. Wiley, 8 edition, 2004.

[76] Grosso Giuseppe and Pastori Parravicini. *Solid state physics : 2 ed.* Elsevier, USA, 2 ed. edition, 2016.

[77] H. R. Carleton and W. T. Maloney. A balanced optical heterodyne detector. *Applied Optics*, 7(6):1241, June 1968.

[78] Horace P. Yuen and Vincent W. S. Chan. Noise in homodyne and heterodyne detection. *Optics Letters*, 8(3):177, March 1983.

[79] Michael Porer, Jean-Michel Ménard, and Rupert Huber. Shot noise reduced terahertz detection via spectrally postfiltered electro-optic sampling. *Optics Letters*, 39(8):2435, April 2014.

[80] Wikipedia contributors. Convolution theorem — Wikipedia, the free encyclopedia, 2021. [Online; accessed 5-February-2021].

[81] Martin Dressel, Natalia Drichko, Boris Gorshunov, and Andrei Pimenov. THz spectroscopy of superconductors. *IEEE Journal of Selected Topics in Quantum Electronics*, 14(2):399–406, 2008.

[82] M. Beck, M. Klammer, S. Lang, P. Leiderer, V. V. Kabanov, G. N. Gol'tsman, and J. Demsar. Energy-gap dynamics of superconducting NbN thin films studied by time-resolved terahertz spectroscopy. *Physical Review Letters*, 107(17), October 2011.

[83] A. Tomasino, A. Parisi, S. Stivala, P. Livreri, A. C. Cino, A. C. Busacca, M. Peccianti, and R. Morandotti. Wideband THz time domain spectroscopy based on optical rectification and electro-optic sampling. *Scientific Reports*, 3(1), October 2013.

[84] T. J. Huisman, R. V. Mikhaylovskiy, J. D. Costa, F. Freimuth, E. Paz, J. Ventura, P. P. Freitas, S. Blügel, Y. Mokrousov, Th. Rasing, and A. V. Kimel. Femtosecond control of electric currents in metallic ferromagnetic heterostructures. *Nature Nanotechnology*, 11(5):455–458, February 2016.

[85] Takuya Higuchi, Christian Heide, Konrad Ullmann, Heiko B. Weber, and Peter Hommelhoff. Light-field-driven currents in graphene. *Nature*, 550(7675):224–228, September 2017.

[86] Agustin Schiffrin, Tim Paasch-Colberg, Nicholas Karpowicz, Vadym Apalkov, Daniel Gerster, Sascha Mühlbrandt, Michael Korbman, Joachim Reichert, Martin Schultze, Simon Holzner, Johannes V. Barth, Reinhard Kienberger, Ralph Ernstorfer, Vladislav S. Yakovlev, Mark I. Stockman, and Ferenc Krausz. Optical-field-induced current in dielectrics. *Nature*, 493(7430):70–74, Jan 2013.

[87] Alexander V. Mitrofanov, Aart J. Verhoef, Evgenii E. Serebryannikov, Julien Lumeau, Leonid Glebov, Aleksei M. Zheltikov, and Andrius Baltuška. Optical detection of attosecond ionization induced by a few-cycle laser field in a transparent dielectric material. *Phys. Rev. Lett.*, 106:147401, Apr 2011.

[88] Martin Schultze, Krupa Ramasesha, C.D. Pemmaraju, S.A. Sato, D. Whitmore, A. Gandman, James S. Prell, L. J. Borja, D. Prendergast, K. Yabana, Daniel M. Neumark, and Stephen R. Leone. Attosecond band-gap dynamics in silicon. *Science*, 346(6215):1348–1352, 2014.

[89] Tim Paasch-Colberg, Agustin Schiffrin, Nicholas Karpowicz, Stanislav Kruchinin, Özge Sağlam, Sabine Keiber, Olga Razskazovskaya, Sascha Mühlbrandt, Ali Alnaser, Matthias Kübel, Vadym Apalkov, Daniel Gerster, Joachim Reichert, Tibor Wittmann, Johannes V. Barth, Mark I. Stockman, Ralph Ernstorfer, Vladislav S. Yakovlev, Reinhard Kienberger, and Ferenc Krausz. Solid-state light-phase detector. *Nature Photonics*, 8(3):214–218, Mar 2014.

[90] Tim Paasch-Colberg, Stanislav Yu. Kruchinin, Özge Sağlam, Stefan Kapser, Stefano Cabrini, Sascha Muehlbrandt, Joachim Reichert, Johannes V. Barth, Ralph Ernstorfer, Reinhard Kienberger, Vladislav S. Yakovlev, Nicholas Karpowicz, and Agustin Schiffrin. Sub-cycle optical control of current in a semiconductor: from the multiphoton to the tunneling regime. *Optica*, 3(12):1358–1361, Dec 2016.

[91] Christophe Dorrer and Ian A. Walmsley. Accuracy criterion for ultrashort pulse characterization techniques: application to spectral phase interferometry for direct electric field reconstruction. *J. Opt. Soc. Am. B*, 19(5):1019–1029, May 2002.

[92] Georg Wachter, Christoph Lemell, Joachim Burgdörfer, Shunsuke A. Sato, Xiao-Min Tong, and Kazuhiro Yabana. Ab initio simulation of electrical currents induced by ultrafast laser excitation of dielectric materials. *Phys. Rev. Lett.*, 113:087401, Aug 2014.

[93] Isabella Floss, Christoph Lemell, Georg Wachter, Valerie Smejkal, Shunsuke A. Sato, Xiao-Min Tong, Kazuhiro Yabana, and Joachim Burgdörfer. Ab initio multiscale simulation of high-order harmonic generation in solids. *Phys. Rev. A*, 97:011401, Jan 2018.

[94] Syed Naeem Ahmed. Interaction of radiation with matter. In *Physics and Engineering of Radiation Detection*, pages 65–155. Elsevier, 2015.

[95] C. Fourment, B. Chimier, F. Deneuville, D. Descamps, F. Dorchies, G. Duchateau, M.-C. Nadeau, and S. Petit. Ultrafast changes in optical properties of SiO2 excited by femtosecond laser at the damage threshold and above. *Physical Review B*, 98(15), October 2018.

[96] B. C. Stuart, M. D. Feit, A. M. Rubenchik, B. W. Shore, and M. D. Perry. Laser-induced damage in dielectrics with nanosecond to subpicosecond pulses. *Physical Review Letters*, 74(12):2248–2251, March 1995.

[97] Hanieh Fattahi, Alexander Schwarz, Sabine Keiber, and Nicholas Karpowicz. Efficient, octave-spanning difference-frequency generation using few-cycle pulses in simple collinear geometry. *Optics Letters*, 38(20):4216, October 2013.

[98] Renate Pazourek, Stefan Nagele, and Joachim Burgdörfer. Attosecond chronoscopy of photoemission. *Reviews of Modern Physics*, 87(3):765–802, August 2015.

[99] J. Schötz, B. Förg, W. Schweinberger, I. Liontos, H. A. Masood, A. M. Kamal, C. Jakubeit, N. G. Kling, T. Paasch-Colberg, S. Biswas, M. Högner, I. Pupeza, M. Alharbi, A. M. Azzeer, and M. F. Kling. Phase-matching for generation of isolated attosecond XUV and soft-x-ray pulses with few-cycle drivers. *Physical Review X*, 10(4), October 2020.

[100] Misha Ivanov and Olga Smirnova. How accurate is the attosecond streak camera? *Physical Review Letters*, 107(21), November 2011.

[101] Alexandra S. Landsman and Ursula Keller. Attosecond science and the tunnelling time problem. *Physics Reports*, 547:1–24, January 2015.

[102] Ossama Kullie. Tunneling time in attosecond experiments and the time-energy uncertainty relation. *Physical Review A*, 92(5), November 2015.

[103] Seung Beom Park, Kyungseung Kim, Wosik Cho, Sung In Hwang, Igor Ivanov, Chang Hee Nam, and Kyung Taec Kim. Direct sampling of a light wave in air. *Optica*, 5(4):402–408, Apr 2018.

[104] Johannes Schoetz, Ancyline Maliakkal, Johannes Bloechl, Dmitry Zimin, Zilong Wang, Philipp Rosenberger, Meshaal Alharbi, Abdallah M Azzeer, Matthew Weidman, Vladislav S Yakovlev, Boris Bergues, and Matthias F Kling. The emergence of macroscopic currents in photoconductive sampling of optical fields. *Nature Communications, NCOMMS-21-17770, Submitted*, May 2021.

[105] Nicholas Karpowicz, Jianming Dai, Xiaofei Lu, Yunqing Chen, Masashi Yamaguchi, Hongwei Zhao, X.-C. Zhang, Liangliang Zhang, Cunlin Zhang, Matthew Price-Gallagher, Clark Fletcher, Orval Mamer, Alain Lesimple, and Keith Johnson. Coherent heterodyne time-domain spectrometry covering the entire "terahertz gap". *Applied Physics Letters*, 92(1):011131, 2008.

[106] Amit Beer, Dror Hershkovitz, and Sharly Fleischer. Iris-assisted terahertz field-induced second-harmonic generation in air. *Optics Letters*, 44(21):5190, October 2019.

[107] Kirill A. Grishunin, Nikita A. Ilyin, Natalia E. Sherstyuk, Elena D. Mishina, Alexey Kimel, Vladimir M. Mukhortov, Andrey V. Ovchinnikov, Oleg V. Chefonov, and Mikhail B. Agranat. THz electric field-induced second harmonic generation in inorganic ferroelectric. *Scientific Reports*, 7(1), April 2017.

[108] Jianming Dai, Xu Xie, and X.-C. Zhang. Detection of broadband terahertz waves with a laser-induced plasma in gases. *Physical Review Letters*, 97(10), September 2006.

[109] Xiaofei Lu and X.-C. Zhang. Balanced terahertz wave air-biased-coherent-detection. *Applied Physics Letters*, 98(15):151111, April 2011.

[110] C. Riek, D. V. Seletskiy, A. S. Moskalenko, J. F. Schmidt, P. Krauspe, S. Eckart, S. Eggert, G. Burkard, and A. Leitenstorfer. Direct sampling of electric-field vacuum fluctuations. *Science*, 350(6259):420–423, October 2015.

[111] Dmitry Zimin, Vladislav S. Yakovlev, Nicholas Karpowicz, and Ferenc Krausz. Pulse characterization with cep-unstabilized transients. *In preparation*, July 2021.

[112] Baatarchuluun Tsermaa, Byung-Kwan Yang, Myung-Whun Kim, and Jin-Seung Kim. Characterization of supercontinuum and ultraviolet pulses by using xfrog. *J. Opt. Soc. Korea*, 13(1):158–165, Mar 2009.

[113] S. Linden, H. Giessen, and J. Kuhl. XFROG: new method for amplitude and phase characterization of ultraweak ultrashort pulses. In *Technical Digest. Summaries of Papers Presented at the Conference on Lasers and Electro-Optics. Conference Edition. 1998 Technical Digest Series, Vol.6 (IEEE Cat. No.98CH36178)*. IEEE, 1998.

[114] Giulio Maria Rossi, Roland E. Mainz, Yudong Yang, Fabian Scheiba, Miguel A. Silva-Toledo, Shih-Hsuan Chia, Phillip D. Keathley, Shaobo Fang, Oliver D. Mücke, Cristian Manzoni, Giulio Cerullo, Giovanni Cirmi, and Franz X. Kärtner. Sub-cycle millijoule-level parametric waveform synthesizer for attosecond science. *Nature Photonics*, 14(10):629–635, July 2020.

[115] Peter M. Goorjian and Steven T. Cundiff. Nonlinear effects on the carrier-envelope phase. *Optics Letters*, 29(12):1363, June 2004.

[116] Szabolcs Hack, Sándor Varró, and Attila Czirják. Carrier-envelope phase controlled isolated attosecond pulses in the nm wavelength range, based on coherent nonlinear thomson-backscattering. *New Journal of Physics*, 20(7):073043, jul 2018.

[117] Olga Razskazovskaya. *Infrared waveform synthesis for applications in attosecond science*. PhD thesis, Ludwig Maximilian University of Munich, 2017.

[118] Enrico Ridente. *Few-cycle optical waveforms for transient molecular fingerprinting*. PhD thesis, Ludwig Maximilian University of Munich, 2021.

[119] Tim Paasch-Colberg. *Ultrafast, optical-field-induced currents in solid-state materials*. PhD thesis, Technische Universität München, 2014.

[120] Mikhail Mamaikin. *Time-Resolved Microscopy ofNear-Infrared to Visible Waveforms*. PhD thesis, Ludwig Maximilian University of Munich, 2020.

[121] Lucas J. Zipp, Adi Natan, and Philip H. Bucksbaum. Probing electron delays in above-threshold ionization. *Optica*, 1(6):361–364, Dec 2014.

[122] P. Gaal, W. Kuehn, K. Reimann, M. Woerner, T. Elsaesser, and R. Hey. Internal motions of a quasiparticle governing its ultrafast nonlinear response. *Nature*, 450(7173):1210–1213, December 2007.

[123] Alexej Pashkin, Alexander Sell, Tobias Kampfrath, and Rupert Huber. Electric and magnetic terahertz nonlinearities resolved on the sub-cycle scale. *New Journal of Physics*, 15(6):065003, June 2013.

[124] Thomas P. Weiss, Benjamin Bissig, Thomas Feurer, Romain Carron, Stephan Buecheler, and Ayodhya N. Tiwari. Bulk and surface recombination properties in thin film semiconductors with different surface treatments from time-resolved photoluminescence measurements. *Scientific Reports*, 9(1), March 2019.

[125] I. N. Volovichev, G. N. Logvinov, O. Yu. Titov, and Yu. G. Gurevich. Recombination and lifetimes of charge carriers in semiconductors. *Journal of Applied Physics*, 95(8):4494–4496, April 2004.

[126] G. Vampa, T. J. Hammond, M. Taucer, Xiaoyan Ding, X. Ropagnol, T. Ozaki, S. Delprat, M. Chaker, N. Thiré, B. E. Schmidt, F. Légaré, D. D. Klug, A. Yu. Naumov, D. M. Villeneuve, A. Staudte, and P. B. Corkum. Strong-field optoelectronics in solids. *Nature Photonics*, 12(8):465–468, June 2018.

[127] Tim Paasch-Colberg, Stanislav Yu. Kruchinin, Özge Sağlam, Stefan Kapser, Stefano Cabrini, Sascha Muehlbrandt, Joachim Reichert, Johannes V. Barth, Ralph Ernstorfer, Reinhard Kienberger, Vladislav S. Yakovlev, Nicholas Karpowicz, and Agustin Schiffrin. Sub-cycle optical control of current in a semiconductor: from the multiphoton to the tunneling regime. *Optica*, 3(12):1358, November 2016.

[128] O. Schubert, M. Hohenleutner, F. Langer, B. Urbanek, C. Lange, U. Huttner, D. Golde, T. Meier, M. Kira, S. W. Koch, and R. Huber. Sub-cycle control of terahertz high-harmonic generation by dynamical bloch oscillations. *Nature Photonics*, 8(2):119–123, January 2014.

[129] F. Schlaepfer, M. Lucchini, S. A. Sato, M. Volkov, L. Kasmi, N. Hartmann, A. Rubio, L. Gallmann, and U. Keller. Attosecond optical-field-enhanced carrier injection into the GaAs conduction band. *Nature Physics*, 14(6):560–564, March 2018.

[130] Dmitry Zimin, Nicholas Karpowicz, Muhammad Qasim, Matthew Weidman, Ferenc Krausz, and Vladislav S. Yakovlev. 1-femtosecond-scale drude-lorentz response in photoexcited solids. *In review*, July 2021.

[131] On the theory of quantum mechanics. *Proceedings of the Royal Society of London. Series A, Containing Papers of a Mathematical and Physical Character*, 112(762):661–677, October 1926.

[132] Muhammad Qasim, Michael S. Wismer, Manoram Agarwal, and Vladislav S. Yakovlev. Ensemble properties of charge carriers injected by an ultrashort laser pulse. *Physical Review B*, 98(21), December 2018.

[133] W. Kuehn, P. Gaal, K. Reimann, M. Woerner, T. Elsaesser, and R. Hey. Coherent ballistic motion of electrons in a periodic potential. *Physical Review Letters*, 104(14), April 2010.

[134] Martin Schultze. *Attosecond real time observation of ionization and electron-electron interactions*. PhD thesis, Ludwig Maximilian University of Munich, 2008.

[135] Wikipedia contributors. Fresnel equations — Wikipedia, the free encyclopedia, 2021. [Online; accessed 27-February-2021].

[136] Wikipedia contributors. Transfer-matrix method (optics) — Wikipedia, the free encyclopedia, 2020. [Online; accessed 11-January-2021].

[137] Maximilian Kubullek. Cep measurement of circularly polarised laser pulses in fused silica. Master's thesis, Ludwig Maximilian University of Munich, 2018.

[138] Najd A. Altwaijry. Optimising strong field-induced currents in solids using wave propagation effects. Master's thesis, Ludwig Maximilian University of Munich, 2018.

Acknowledgements

I would like to express immense gratitude to all colleagues and friends with whom we shared time in the institute and outside. Without you, it would not be possible to successfully achieve all goals of this dissertation. In particular:

- Nick Karpowicz for being a brilliant scientist and a wonderful supervisor. Your knowledge and teaching abilities brought me to a higher scientific level and helped to achieve the results presented in this thesis.
- Ferenc Krausz for the opportunity to be a part of the cutting-edge research. Your scientific ideas and suggestions were always essential in all studies.
- Martin Schultze for being a wonderful co-leader of the group. Your scientific advice and humor were motivating me to achieve goals.
- Vladislav Yakovlev for theoretical support and in-depth scientific discussions. It helped me to learn and experience all beauty and challenges of the theoretical approach.
- Shawn Sederberg for being an amazing researcher and a project partner. Your approach towards scientific goals taught me the structural and efficient way of research.
- Hanieh Fatahi for wonderful discussions, events, and fun.
- Florian Siegrist, Marcus Ossiander, Olga Razskazovskaya, Clemens Jakubait, Matthew Weidman for being great long-term colleagues.
- Michail Mamaikin, Enrico Ridente, Mohammad Qasim, Julia Gessner, Keyhan Golliari, Simon Reiger, Najd Altwaijry, Amelie Schulte, Michael Heynck, Anton Trainer for all projects, events and fun we had. Especially the table tennis experience.
- Katarzyna Danielewicz and Malte Kremser for your support with the preparation of essential items for the research.

- Anton Horn, Tobias Kleinhenz, and Lukas Schuster for wonderful technical support.
- Frau Wild, Kerstin Schmidt-Buchmann, and all administration of the 'International Max Planck Research School for Advanced Photon Science' for the great and professional organization of the school workflow.
- Julia Obermeier and her team for delicious lunches and Nachschlag.
- Gertrud Müller and Christina Hofer for the help with a translation of the abstract :)
- All other colleagues and friends with whom we had common projects or other activities during my Ph.D. studies, and whom I forgot to mention above.